Theoretical study of topological defects in the ferroic material Cu2OSeO3

Houssam Sabri

université PARIS-SACLAY

Theoretical study of topological defects in the ferroic material Cu_2OSeO_3

Étude théorique des défauts topologiques dans le matériau ferroique Cu_2OSeO_3

Thèse de doctorat de l'université Paris-Saclay

École doctorale n°573 : interfaces : matériaux, systèmes, usages (INTERFACES)
Spécialité de doctorat : Physique
Graduate School : Physics. Référent : CentraleSupélec

Thèse préparée dans le **Laboratoire SPMS, CentraleSupélec**, sous la direction de **Igor KORNEV**, professeur à CentraleSupélec, Université Paris-Saclay

Thèse soutenue à Gif-sur-Yvette, le 14 Avril 2023, par

Houssam SABRI

Composition du jury

Membres du jury avec voix délibérative

Pierre-Eymeric JANOLIN Professeur, CentraleSupélec - Université Paris-Saclay	Président & Examinateur
Bertrand DUPÉ Chercheur Qualifié FNRS Nanomat/Q-mat/CESAM, Université de Liège	Rapporteur & Examinateur
Nikolay PERTSEV Senior Researcher , Ioffe Institut	Rapporteur & Examinateur
Grégory GENESTE Directeur de Recherche, CEA-DAM, Laboratoire Matière en Conditions Extrêmes	Examinateur
Yousra NAHAS Research Professor, University of Arkansas	Examinatrice
Alexander TAGANTSEV Professeur Émérite - Swiss Federal Institute of Technology (EPFL), Institute of Materials Science	Examinateur

THESE DE DOCTORAT
NNT : 2023UPAST066

université PARIS-SACLAY

ÉCOLE DOCTORALE
Interfaces:
matériaux, systèmes, usages

Titre : Étude théorique des défauts topologiques dans le matériau ferroique Cu_2OSeO_3
Mots clés : Multiferroiques, skyrmions, défaut topoligiques, calculs *ab-initio*.

Résumé : Ces dernières années, un intérêt croissant s'est manifesté pour une nouvelle classe de matériaux émergents qui présentent des propriétés topologiques protégées par certains principes physiques fondamentaux. Ces matériaux ont suscité un intérêt important en raison de leur potentiel d'utilisation dans les futurs dispositifs électroniques, entre autres applications. Cependant, leurs études théoriques restent difficiles en raison de leur nature complexe et multi-échelle. L'objectif est étudier théoriquement les défauts topologiques dans les matériaux multiferroïques, en particulier dans le Cu_2OSeO_3 multiferroïque. Dans cette étude, nous avons développé et utilisé des outils analytiques et informatiques nécessaires pour comprendre et modéliser le comportement de phénomènes complexes et multi-échelles en présence de défauts topologiques dans les matériaux multiferroïques. Nous nous sommes notamment concentrés sur les propriétés thermodynamiques de diverses phases dans le multiferroïque Cu_2OSeO_3, y compris les mécanismes de transition de phase et le diagramme de phase champ magnétique-température. L'étude examinera également la caractérisation de différents défauts topologiques hébergés par le matériau, tels que les skyrmions magnétiques et les défauts ponctuels, ainsi que l'interaction entre eux en utilisant une approche analytique et des calculs de premiers principes tels que les calculs de la théorie de la fonctionnelle de la densité et les simulations de Monte Carlo de l'hamiltonien effectif. Les résultats de cette étude ont fourni de nouvelles connaissances sur les propriétés et le comportement des matériaux multiferroïques avec des défauts topologiques en général et en particulier dans le Cu_2OSeO_3, ainsi que sur le rôle des défauts ponctuels dans la stabilité et l'instabilité de la phase de réseau de skyrmions.

Title : Theoretical study of topological defects in the ferroic materials Cu_2OSeO_3
Keywords : Multiferroics, skyrmions, topological defects, *ab-initio* calculations.

Abstract : In recent years, there has been a growing interest in a class of materials that exhibit topological properties. These materials have generated significant interest due to their potential for use in future electronic devices, among other applications. However, their theoretical studies remain challenging due to their complex and multi-scale nature. The aim is to focus on the theoretical studies of topological defects in multiferroic materials, specifically in the multiferroic Cu_2OSeO_3 .

In this study we developed and utilized analytical and computational tools necessary to understand and model the behavior of complex and multi-scale phenomena in the presence of topological defects in multiferroic materials. Specifically,we have focused on the thermodynamic properties of various phases in the multiferroic Cu_2OSeO_3 , including phase transition mechanisms and the magnetic field-temperature phase diagram. The study will also examine the characterization of different topological defects hosted by the material, such as magnetic skyrmions and point defects and the interaction between them using an analytical approach and first-principles calculations such as density functional theory calculations and effective Hamiltonian Monte Carlo simulations.

The results of this study provides new insights into the properties and behavior of multiferroic material with topological defects in general and in particular in Cu_2OSeO_3 as well as elucidating the role of point defects in stability and instability of skyrmion lattice phase.

"Rather than love, than money, than fame, give me truth. "

Henry David Thoreau, Walden

"It is the peculiar and perpetual error of the human understanding to be more moved and excited by affirmatives than by negatives "

Francis Bacon, Novum Organum

"Physics is like sex: sure, it may give some practical results, but that's not why we do it "

Richard P. Feynman

Acknowledgements

So That's it , this was the period of my life called the "Ph.D" . 37 months of work indeed (plus minus some messing around), but also three years of very rich human experiences. I have met so many people, encountered many highs and ups along this journey, that made me who I am today. Before anything else, I would like to thank the jury members for sparing some of their time to examine and evaluate my work.

Nonetheless, none of this would exist without my supervisor Pr. Igor Kornev whom effort and help cannot be summed in just words. I owe a huge part of this work and my knowledge in physics, (and also coding in C++ and Fortran) to Igor and especially for the "quick ones" questions that have no quick answers, and no matter how much I would thank him it would not suffice. Thank you Igor !!

I would also be thankful and grateful, first to Pierre-Eymeric Janolin, for being the first one to host to toddler me in this lab, 5 years ago, I am very grateful to his remarks, critics and also methodical style of work, since it shaped me into being who I am today, my first steps in research were made under your supervision, I want to also thank Brahim Dkhil, AKA the cool dad of the group for his remarks and suggestions. I want to also thank all the colleagues starting with Milad, Jiacheng ("NON!! you will not get an extended acknowledgment JC18 !! wink wink "), Zechao, Shenglan, Minghai, Jingye, Gaëlle, Matthieu, Giulio ("Mon Amic"), Long("Jackie"), Ran, Igor G., Dania, Francesco, Wafa, Daniel, and all the PhD students and postdocs that were in my first days in the lab (Vitoria, Henri, Pavan, Léonard)

Je remercie également tout l'équipe des ITAs du laboratoire SPMS, Pascale G. et Fabienne et les discussions inachevables de la salle de café, Agnès, Nicolas, Vincent, Thierry, Maxime, Christine B. , Luis, Xavier, je tiens aussi à remercier énormement Céline et Christine V pour toute leurs patience et aide administrative, ainsi que Pascale S. et Eugénie. Une pensée également au chercheurs

permanents également tout d'abord par le nouveau directeur du SPMS Hichem Dammak et l'ancien directeur Guilhem Dezanneau ainsi que Jean-Michel Gilet, Pietro Cortona et Pierre Becker ("Grand-Pierre").

Finally to end this part I want to thank my familyn for all the support and encouragement they gave me during my studies and this period. They unconditional support is was helped me to made it till here, especially the best mother in the world (I know I'm biased), since without her sacrifice I wouldn't be in this place, I know that you'll feel proud. I want to also thank my brother and sister, for bearing the stubborn bossy older brother that I am, a deep thought to my late father who made me love science and nourished the sense of scientific curiosity since childhood. At last, but not least, I want to deeply thank my wife for being by my side and supporting me during this quest and bearing a spoiled me with shenanigans during the last phase of thesis, thank you again.

Houssam SABRI
18 November 2022; 18h10

Contents

List of Figures

List of Tables

List of Abbreviations

MCS Monte Carlo Sweeps

DFT Density Functional Theory

DMI Dzyaloshinskii-Moriya Interaction

SOC Spin-Orbit Coupling

LDA Local Density Approximation

GGA Generalized Gradient Approximation

PAW Projector Augmented Wave

PBC Periodic Boundary Condition

CSO Copper Oxide Selinite Cu_2OSeO_3

FM Ferromagnetic

AF Antiferromagnetic

SkL Skyrmion Lattice

FD Fluctuation Disordered

LP Lifshitz Point

TCP Tricritical Point

SSL Spiral Spin Liquid

For my late father Mohamed Sabri
(1965-2010)
To my mother Amina, my brother
Ridouane and sister Imane
To my wife Fatima-Zahra

Introduction

FERROICS constitute a class of materials possessing peculiar properties. They were discovered more than 70 years ago among the complex oxides compounds, and these materials owe undeniable importance for fundamental physics and state-of-the-art technological applications. The main characteristic of these materials, namely the coexistence of several types of ferroic orders, leads to the possibility of establishing coupling between different order parameters. And so far, despite numerous investigations, the study of topological defects in ferroic materials remains an open topic.

Topological defects arise in a wide variety of condensed matter systems, and due to their nature related to the topological properties, they have surged interest in the field of spintronics. The robustness of devices based on topological defects, especially skyrmions, gained the attention of the condensed matter community in the last decade. Their robustness against continuous mechanical deformations and defects directly results from their topological stability. Henceforth the need for extensive studies of the topological solitons in magnetic materials, which include vortices, hedgehogs, and Skyrmions [1]. Magnetic skyrmions are a prominent example of topological spin textures, they can be described as circular spin textures with spin up on the edge of the circle and spin down in the center, and they are anticipated to allow for the existence of discrete magnetic states which are significantly more energetically stable (per unit volume) than their single-domain counterparts. For this reason, it is envisioned that magnetic skyrmions may be used as bits to store information in future memory and logic devices.

One of the materials that host these topological defects is the copper oxide selenite Cu_2OSeO_3, a chiral magnet of the B20 magnets family that crystallizes in the cubic space group $P2_13$ exhibit the same features of the B20 magnets [2]. However, this crystal is the only insulator in this family of chiral magnets that displays a multiferroic behavior with a magnetoelectric coupling [3, 4]; this may give rise

to the ferroelectric counterpart topological solitons, and also the manipulation of skyrmions with an electric field [5].

It is the purpose of this work to study the stability and existence, and topological properties of topological solitons in multiferroic material Cu_2OSeO_3, by proposing a microscopical model based on local interaction and symmetry, which are included in the effective Hamiltonian model that accounts for various interaction in Cu_2OSeO_3, as well as, the calculation of the strength of those interactions from DFT based calculation. The next step is to solve the effective Hamiltonian relying on Monte Carlo simulations. This study will provide us with the thermodynamical equilibrium properties as a function of temperature and external excitation. Consequently, the main goal of this study is " To develop efficient analytical and computational tools for modeling and studying topological defects in ferroic materials and, in particular, studying various topological entities existing in Cu_2OSeO_3."

The manuscript is organized into two parts: the first part contains three chapters about the general background and the physics in multiferroics magnetic materials and solitons and the employed methods, and the second part focuses on the results of Monte Carlo simulations in Cu_2OSeO_3.

- **Chapter 1** :This chapter constitutes an overview of ferroic materials, starting with magnetic materials, the exchange mechanism, and the different interactions in magnetic orders. We also discuss the Landau theory of phase transition and a brief review of multiferroic materials, their types, and mechanisms.
- **Chapter 2** This chapter provides us with different types of possible solitons in ferroics. It includes the mathematical description of the various "trivial" solitons, the types of possible topological defects, and how to quantify the topological charge. The chapter starts with a brief overview of the history and application of topological defects, and it ends with a short description of an exotic phase found in magnetic material, the spin liquid state.
- **Chapter 3** This chapter gives a general overview of the theoretical background of the employed methods: Density Functional Theory (DFT), the construction of the effective Hamiltonian used in Monte Carlo simulations, and a brief primer on Monte Carlo simulations and the Metropolis algorithm.

- **Chapter 4** : This chapter collects the main results obtained from Monte Carlo simulations and focuses on the thermodynamical properties of Cu_2OSeO_3, which includes a brief, finite-size scaling, the strength of magnetic interactions, magnetoelastic coupling and also provides us with different domains of stability of magnetic phases which include magnetic skyrmions phase, helical state, and general phase diagram as well as a possible spiral spin liquid phase. The chapter ends with the main results of this part, which is the (B, T) phase diagram of Cu_2OSeO_3.
- **Chapter 5** This chapter focuses on the topological properties of the magnetic phase and topological defects in Cu_2OSeO_3. It also includes some analytical expressions for quantifying the topological charges of point defects, skyrmions, and 3D hopfions-like solitons, as well as exploring the dynamics of point defects and their role in the annihilation of skyrmions. In this chapter, we analyze the coexistence of the different topological defects in the Cu_2OSeO_3.

Part I

General Background

Chapter 1

Ferroic materials

1.1 Magnetic order and magnetic materials

The ferroic materials refer to ones that exhibit a ferroic order (magnetization $\mathbf{M}_i$, polarization $\mathbf{P}_i$, deformation η_{ij} and toroidal moment $\mathbf{T}_i$) which is switchable with the application of external stimuli (magnetic field $\mathbf{H}_i$, electric field $\mathbf{E}_i$ ...).

Ferromagnets refer to materials with ferromagnetic order that display spontaneous magnetization $\mathbf{M}_s$ without any applied magnetic field. This spontaneous magnetization results from the order of the microscopic magnetic moments $\mathbf{m}_i$ in which they are aligned in a parallel direction. In the case of a ferromagnetic monodomain, there is only one axis for magnetization. Therefore, the possible states for the remanent magnetization M_r and $-M_r$ and going from one of these states to the other require applying a magnetic field. This behavior is depicted in the hysteresis loop of Fig. 1.1 where the magnetization reverses at the coercive field H_c.

1.1.1 Magnetic moment and magnetization

The magnetization of the system is governed by the order of magnetic moments, which originates from the magnetic properties of the electronic configuration of its atoms. The magnetic moment of an electron comes from two contributions, the orbital angular momentum magnetic moment $\mathbf{L}$:

$$\mathbf{m}_L = -(\frac{e}{2m_e})\mathbf{L} \tag{1.1}$$

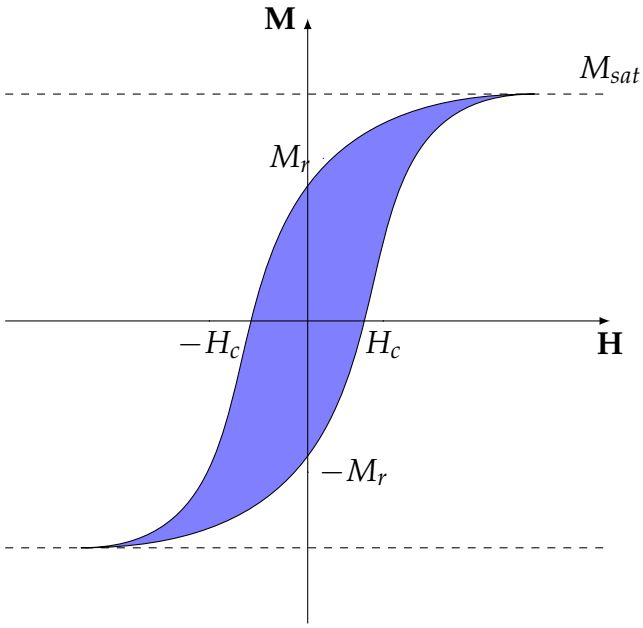

FIGURE 1.1: The $M - H$ hysteresis loop for ferromagnets with coercive field H_c and remanent magnetization M_r

Where its z-component is quantized as :

$$m_{l_z} = -\frac{\mu_B}{\hbar} m_l \tag{1.2}$$

And also the second part is the spin magnetic moment :

$$\mathbf{m}_S = -g_S \mu_B \mathbf{S} \tag{1.3}$$

Here we have $\mu_B = e\hbar/2m_e$ the Bohr magneton, g_S the Landé g-factor ($g_S \simeq 2$ for the electron), m_l is the magnetic quantum number, and $\mathbf{S}$ the spin of the electron, the total magnetic moment of the atom is given then by the total angular momentum quantum number $\mathbf{J} = \mathbf{L} + \mathbf{S}$:

$$\mathbf{m} = g_J \mu_B \frac{\mathbf{J}}{\hbar} \tag{1.4}$$

Ferromagnetic materials exhibit thermodynamical behavior in which the macroscopic total magnetization $\mathbf{M}$, which is defined as the mean order of the microscopic magnetic moments of atoms $\mathbf{m}_i$ in a volume V :

$$\mathbf{M} = \frac{1}{V} \sum_i \mathbf{m}_i \tag{1.5}$$

undergoes a phase transition from the disordered paramagnetic phase (at high temperatures) to the ordered phase (at low temperatures). This phase transition is described within the Landau phenomenological theory of phase transitions [6], as we will see later in this chapter.

1.1.2 Origin of magnetic moment

1.1.2.1 Isolated atom

The magnetic moment of an atom is associated with the orbital moment and intrinsic magnetic moment, known as the spin of its electrons. Let us start with an isolated atom. The possible state for a single electron can be characterized entirely by four quantum numbers, n the principal quantum number, l the orbital-angular-momentum quantum number, m_l the eigenvalue of the z-component of the orbital angular momentum, and m_s the spin quantum number, associated with the z–component of the spin angular momentum. We will now discuss how an isolated atom accommodates multiple electrons. We will use the Russel-Saunders coupling scheme [7] for the addition of multiple momenta; for example, for spin momenta, we have $\mathbf{S} = \sum_i \mathbf{S}_i$ where S is the algebraic value of total spin, the same also applies for orbital momenta of electrons $\mathbf{L}_i$. The energy of the orbitals depends only on n, and l [8].

In the ground state, an isolated atom will fill in first the orbitals with the lowest energies while respecting Pauli's exclusion principle. In our case, two electrons cannot have all the same four quantum numbers. Hund's rules give priority within each subshell: Electrons must occupy the orbitals that maximize the spin. This rule means that the orbitals of a subshell l are each occupied with one electron, of parallel spins, before doubling the occupancy of each orbital to permit the minimization of Coulomb interaction between electrons. The total angular momentum is given by $J = |L - S|$ if the subshell is less than half-full, or $J = L + S$ if it is more than half-full. When the subshell is half-full, $L = 0$, and $J = S$. These differences in the total angular momentum are caused by a relativistic effect called spin-orbit coupling, which we will discuss later in this chapter [9].

1.1.2.2 Localized magnetism

In the previous section, the primary assumption of the isolated atom is that external electrostatic potential is spherical (nucleus potential), however in a solid, the surrounding potential from neighbor atoms is non-spherical, and the observed magnetic moment in solids is often completely different from that in an isolated atom. To understand the origin of the permanent magnetic moment of some solids, we use the same picture as in isolated atoms. Some elements can retain their magnetic moments when in a solid, because angular momentum comes from inner incomplete sub-shells whose electrons are not involved in the bonding of the crystal. Those elements are said to possess localized magnetism since all the electrons responsible for the magnetic moment are well localized in their respective crystal sites. This type of mechanism is the main mechanism of magnetism in insulators. Nonetheless, the observed magnetic moment in solids often differs from that in an isolated atom [10].

1.1.2.3 Itinerant magnetism

In metallic systems, the conduction electrons sometimes give rise to magnetism, as the 3d electrons in iron, cobalt, and nickel. In such systems, the Coulomb interaction produces a spin-dependent band shift when the system is below T_c. The simplest model that describes itinerant magnetism is Hubbard model [11]

$$\mathcal{H} = -\sum_{ij,\sigma} t_{ij} c^{\dagger}_{i\sigma} c_{j\sigma} + U \sum_{i} n_{i\uparrow} n_{i\downarrow} \tag{1.6}$$

$c^{\dagger}_{i\sigma}$ is the creation operator of an electron with spin σ on-site i while $c_{j\sigma}$ annihilate an electron with spin σ on-site j, $n_{i\sigma} = c^{\dagger}_{i\sigma} c_{i\sigma}$ is the spin-density operator for spin σ on-site i and t_{ij} is the hopping integral containing both the kinetic energy and the crystal potential. It is associated with the probability of an electron hopping from the site i to j. In this model, electrons are considered to interact among themselves only when on the same site, where they feel the screened effective Coulomb potential given by the parameter U, thus giving a good approximation of metallic systems since the Coulomb interaction is strongly screened. Within the mean-field approximation, the Hubbard model can be solved with the Hartree-Fock method, leading to a similar form of the Stoner criterion for stability of the

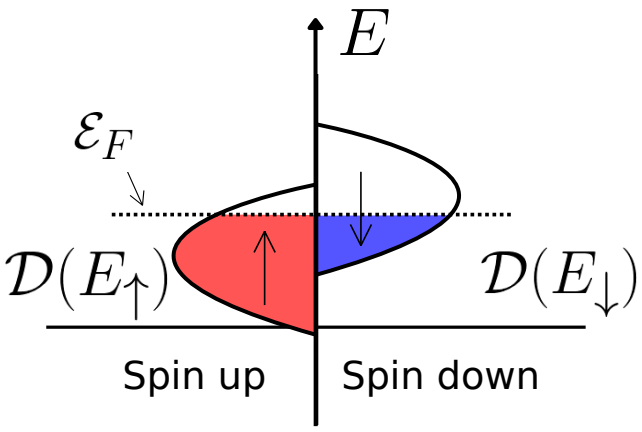

FIGURE 1.2: A schematic band structure for the Stoner model of ferromagnetism

ferromagnetic state [12].

$$U\mathcal{D}(\mathcal{E}_F) > 1 \tag{1.7}$$

Where $\mathcal{D}(\mathcal{E}_F)$ is the density of state at the Fermi energy $\mathcal{E}_F$, the system can lower its energy by creating an imbalance in the number of up and down spins as depicted in Fig.1.2, thereby favoring ferromagnetic state [9].

1.1.3 Exchange mechanisms : Heisenberg exchange

The type of ordering of the magnetic moments and the transition's critical temperature T_c depends on the strength, sign, and type of interactions between the dipoles. In 1928, Heisenberg [13] and Dirac [14] developed the basic concept of the quantum-mechanical exchange interaction, known now as the Heisenberg exchange Hamiltonian.

Let us consider a system of two paramagnetic ions with one unpaired electron each (Copper ion as an example). We also suppose the ions are fixed with interatomic distance R_{ab}. The Hamiltonian is expressed as :

$$\mathcal{H} = \mathcal{H}_a + \mathcal{H}_b + \mathcal{H}_{ab} \qquad \mathcal{H}_a = \frac{\mathbf{p}_1^2}{2m_e} - \frac{1}{4\pi\epsilon_0}\frac{Ze^2}{r_1} \qquad \mathcal{H}_b = \frac{\mathbf{p}_2^2}{2m_e} - \frac{1}{4\pi\epsilon_0}\frac{Ze^2}{r_2} \tag{1.8}$$

$\mathcal{H}_a, \mathcal{H}_b$ are the Hamiltonians of electrons 1 and 2 in the field of core a and b. The solutions of the Schrodinger equation are the atomic orbitals ϕ_a and ϕ_b where :

$$\mathcal{H}_a\phi_a(\mathbf{r}_1) = E_a\phi_a(\mathbf{r}_1) \qquad \mathcal{H}_b\phi_b(\mathbf{r}_2) = E_b\phi_b(\mathbf{r}_2) \tag{1.9}$$

and the interaction Hamiltonian $\mathcal{H}_{ab}$ has the form :

$$\mathcal{H}_{ab} = \frac{1}{4\pi\epsilon_0}\left(\frac{Z^2e^2}{R_{ab}} - \frac{Ze^2}{r_{1b}} - \frac{Ze^2}{r_{2a}} + \frac{e^2}{r_{12}}\right) \tag{1.10}$$

The first term corresponds to the Coulomb repulsion of the two ions. The second and third represent the attractive potential between electron 1 and ion b and electron 2 and ion a, and the last term is the mutual Coulomb repulsion between the two electrons 1 and 2. In addition to the atomic orbitals, the wavefunction has

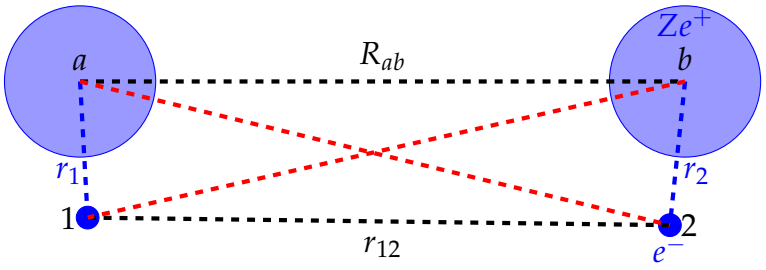

FIGURE 1.3: Two-center with two electrons system

a spin dependency, which emerges from the Pauli exclusion principle (the anti-symetrization of many electrons wavefunction). Since the spin-orbit coupling is small compared to Coulomb interaction, then in our case with two electrons, we have four states for two spins :

$$|\uparrow\uparrow\rangle \qquad |\uparrow\downarrow\rangle \qquad |\downarrow\uparrow\rangle \qquad |\downarrow\downarrow\rangle \tag{1.11}$$

Thus, we can make a linear combination based on total spin $\mathbf{S}$ and its projection on the quantization axis S_z. In the case of a singlet state ($S = 0$), we have the possible state :

$$\frac{1}{\sqrt{2}}(|\uparrow\downarrow\rangle - |\downarrow\uparrow\rangle) \tag{1.12}$$

and in the case of the triplet state ($S = 1$), we have

$$|\uparrow\uparrow\rangle, \qquad \frac{1}{\sqrt{2}}(|\uparrow\downarrow\rangle + |\downarrow\uparrow\rangle), \qquad |\downarrow\downarrow\rangle \tag{1.13}$$

With S_z respectively is (1, 0, -1) if we denote E_T and E_S the energies of the triplet and singlets state, respectively, and the difference between those energies is what determines which parallel alignment is favored ($S = 0$ or $S = 1$). And we express

those energies in the compact form :

$$E_T = \mathcal{C} - \mathcal{J} \qquad E_S = \mathcal{C} + \mathcal{J} \tag{1.14}$$

where $\mathcal{C}$ is the Couloumb energy :

$$\mathcal{C} = \frac{E_S + E_T}{2} = \langle \phi_a(\mathbf{r}_1)\phi_b(\mathbf{r}_2)| \frac{e^2}{r_{12}} |\phi_a(\mathbf{r}_1)\phi_b(\mathbf{r}_2)\rangle \tag{1.15}$$

and $\mathcal{J}$ is the exchange energy :

$$\mathcal{J} = \frac{E_S - E_T}{2} = \langle \phi_a(\mathbf{r}_1)\phi_b(\mathbf{r}_2)| \frac{e^2}{r_{12}} |\phi_a(\mathbf{r}_2)\phi_b(\mathbf{r}_1)\rangle \tag{1.16}$$

To construct the spin Hamiltonian that will be used in the following, we must recall that the electron spin operator satisfies $\mathbf{S}^2 = S(S+1) = \frac{3}{4}$ then for our case with two electrons, we have :

$$\mathbf{S}^2 = (\mathbf{S}_1 + \mathbf{S}_2)^2 = \frac{3}{2} + 2\mathbf{S}_1 \cdot \mathbf{S}_2 \tag{1.17}$$

Since $\mathbf{S}^2$ has the eigenvalue $S(S+1)$ the operator $\mathbf{S}_1 \cdot \mathbf{S}_2$ has the value $-\frac{3}{4}$ in the singlet state and $\frac{1}{4}$ in the triplet state which gives :

$$\mathcal{H}_{spin} = \frac{1}{4}(E_S + 3E_T) - (E_S - E_T)\mathbf{S}_1 \cdot \mathbf{S}_2 \tag{1.18}$$

If we redefine the zero of energies as $\frac{1}{4}(E_S + 3E_T)$ then we can write the Heisenberg spin Hamiltonian as:

$$\mathcal{H}_{spin} = J\mathbf{S}_1 \cdot \mathbf{S}_2 = (E_T - E_S)\mathbf{S}_1 \cdot \mathbf{S}_2 \tag{1.19}$$

This Hamiltonian can be generalized for the case of N interacting spins as :

$$\mathcal{H}_{Heisenberg} = \sum_{i<j} J_{ij}\mathbf{S}_i \cdot \mathbf{S}_j \tag{1.20}$$

We can observe that depending on the sign of J, the system's ground state is either the triplet state or singlet state. This favored state decides whether we have a ferromagnetic ordering (parallel spins) or antiferromagnetic ordering (antiparallel spins) [15, 16].

1.1.4 Spin-orbit coupling interactions

1.1.4.1 Single ion anisotropy

In the condition of total quenching of angular momentum, which is the case of solid insulators, we have $\langle\psi_0|\,\mathbf{L}\,|\psi_0\rangle = 0$ the spin-orbit perturbation $\mathcal{H}_{SO} = \lambda\mathbf{L}\cdot\mathbf{S}$ has no contribution in first-order perturbation theory. However, in the second-order perturbation theory, there might be an effect regardless of the spin state.

$$\mathcal{H}_S^{ani} = |\lambda|^2 \sum_n \frac{\langle 0|\,L_\mu\,|n\rangle\,\langle n|\,L_\nu\,|0\rangle}{E_0 - E_n} S_\mu S_\nu = S_\mu \Lambda_{\mu\nu} S_\nu \tag{1.21}$$

Where $\Lambda_{\mu\nu}$ is a symmetric second-rank tensor that depends on the ordering of excited orbitals and crystalline symmetry. This symmetric tensor can be decomposed into a scalar, and a traceless symmetric second-rank tensor, the combination of three eigenvalues of $\Lambda_{\mu\nu}$, corresponds to a trivial constant. For high crystalline symmetries (cubic and tetrahedral), the quadratic contribution is null, and the smallest anisotropic term is on the form [17]:

$$\mathcal{E}_{ani}^{cub} = \mathcal{K}(S_x^4 + S_y^4 + S_z^4) \tag{1.22}$$

Another rule is if the local environment possesses mirror planes, the principal axis must lie in or perpendicular to them.

1.1.4.2 Dzyaloshinskii-Moriya Interaction

Collinear orderings are not the only type of configuration in ferromagnets. In materials with strong spin-orbit coupling, an interaction emerges that is the Dzyaloshisnkii-Moriya interaction (DMI) is a crucial ingredient for magnetic chiral textures.

Dzyaloshinskii in 1958 [18] introduced the phenomenological theory to explain the weak ferromagnetism in some antiferromagnets. The analysis was based on symmetry arguments since the DMI is an antisymmetric exchange that exists only when symmetry inversion is lacking. Two years later, Moriya [19] demonstrated microscopically that the DM interaction arises from the second-order perturbation to spin-orbit coupling (SOC). The DMI has the form:

$$\mathcal{H}_{DMI} = \sum_{ij} \mathbf{D}_{ij} \cdot \mathbf{S}_i \times \mathbf{S}_j \tag{1.23}$$

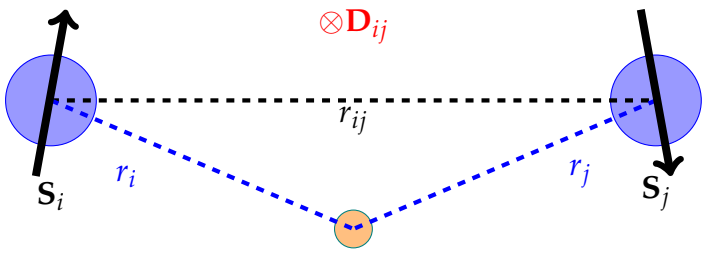

FIGURE 1.4: a DMI generated by indirect exchange for the triangle composed of two atomic spins and an atom with a strong SOC ,describing the Fert-Levy model [20] that explains interfacial DMI.

Where we can define $\mathbf{D}_{kl} = (\boldsymbol{\xi}_k - \boldsymbol{\xi}_l)$ and :

$$i\boldsymbol{\xi}_k = -\lambda \sum_{n_l} \left[\frac{\langle 0_l 0_k | \, \mathbf{L}_k \, | n_l 0_k \rangle \, \langle n_l 0_k | \, \hat{\mathbf{J}} \mathbf{S}_k \cdot \mathbf{S}_l \, | 0_l 0_k \rangle}{E_{0_k 0_l} - E_{n_k 0_l}} \right] \tag{1.24}$$

One can clearly see that the interaction vanishes for $\xi_k = \xi_l$. Therefore the existence relies on the chemical environment of two ions and symmetry considerations. The symmetry of neighboring ions dictates the magnitude and direction of the vector $\mathbf{D}_{ij}$. Let us consider two fixed spins in points A and B, where point C is bisecting AB. Thus the symmetry rules on DMI imply that

- If C is a symmetry inversion center then $\mathbf{D}_{ij} = 0$.
- If a mirror plane perpendicular to AB passes through C then $\mathbf{D}_{ij} \perp AB$
- If there is a mirror plane passing through A and B then $\mathbf{D}_{ij} \perp$ mirror plane
- If a two-fold rotation axis $\mathbf{R}$ is perpendicular to AB through C then $\mathbf{D}_{ij} \perp \mathbf{R}$
- If there is a n-fold axis ($n \geq 2$) along AB then $\mathbf{D}_{ij} \parallel AB$

1.1.5 Exchange mechanisms in insulators

In this subsection, we study the mechanisms, origin, and nature of exchange interaction in magnetic insulator compounds. The insulating magnetic materials are made of paramagnetic cations (metallic cations) and diamagnetic anions, which will be called ligands, that constitute the main structure of the crystal. Within the system, the paramagnetic ions occupy the site with a certain symmetry. The structure of the ligands determines the electronic structure of the metallic

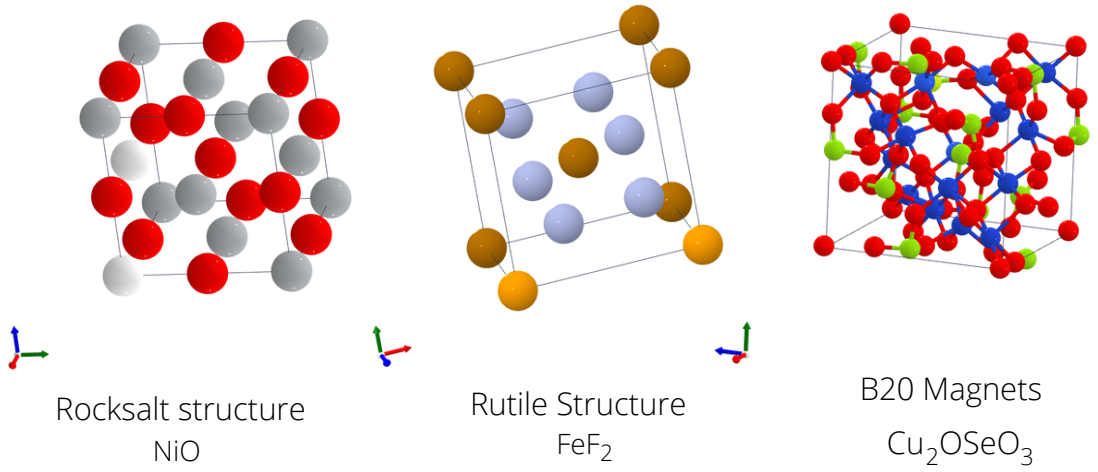

FIGURE 1.5: Examples of magnetic insulators

cations. Moreover, these diamagnetic ions have a mediating effect regarding the coupling between spins of paramagnetic cations.

The anions structure, which is called the diamagnetic matrix, determines the character of the valence shell of paramagnetic ions. Although paramagnetic ions exhibit their strong magnetic coupling, the magnitude of some coupling cannot be attributed to only the direct exchange mechanism. Thus, the indirect exchange mechanism, which involves the cation-anion-cation unit or metal-ligand-metal unit ($M_1 - L - M_2$)[21], plays a significant role. In the following, we'll consider the electrons orbitals as localized, with some mixing with diamagnetic ligand ions orbitals. The zeroth order of ground state configuration will be constituted of singly occupied orbitals ϕ_m of the paramagnetic ions and doubly occupied s, p valence orbitals of diamagnetic ligand ϕ_l. The basis includes empty orbitals ϕ_μ, ϕ_λ respectively for metal and ligand orbitals [22]. Three mechanisms govern the indirect exchange. The first involves one electron transfer called the **direct kinetic exchange** in which the interaction is written as :

$$\mathcal{H}_{tr} = -\sum_{m_1 m_2} \frac{|t_{m_1 m_2}|^2}{U} \frac{1}{2}(1 - 4\mathbf{S}_{m_1} \cdot \mathbf{S}_{m_2}) = Cte - \sum_{m_1 m_2} \frac{-2|t_{m_1 m_2}|^2}{U}(\mathbf{S}_{m_1} \cdot \mathbf{S}_{m_2}) \tag{1.25}$$

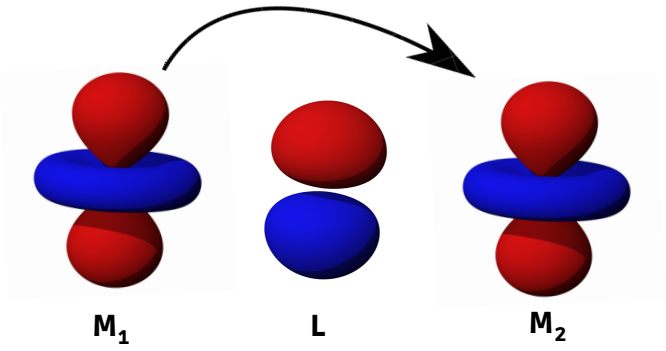

FIGURE 1.6: Representation of the kinetic exchange interaction that involve one-electon transfer

where $t_{m_1 m_2}$ is hopping parameter between m_1 and m_2 (Fig. 1.6) the singly occupied (SO) metallic orbitals, U is the on-site Coulomb repulsion that approximate energy involved in the transfer $m_1 \rightarrow m_2$. The second type of exchange interaction in magnetic insulators is the **polarization exchange** in which the spin-polarization contribution involves a virtual excitation of the electron in SO ϕ_{m_1} to an empty orbital ϕ_μ, along with excitation of an electron from the doubly occupied (DO) orbital ϕ_l to ϕ_{m_1}, the effective interaction is written as :

$$\mathcal{H}_{pol} = -\sum_{m_1 m_2 l \mu} \frac{J_{lm_1}^{m_1\mu}(J_{lm_2}^{m_2\mu})^*}{\varepsilon_\mu - \varepsilon_l}\frac{1}{2}(1 - 4\mathbf{S}_{m_1}\cdot\mathbf{S}_{m_2}) = Cte - 2\sum_{m_1 m_2} J_{eff}^{pol}(\mathbf{S}_{m_1}\cdot\mathbf{S}_{m_2}) \tag{1.26}$$

Where $\varepsilon_\mu - \varepsilon_l$ is the energy difference between orbitals. The sign of J_{eff}^{pol} is determined by $J_{lm_1}^{m_1\mu} = \langle\phi_{m_1}\phi_l|\,\mathcal{H}_{12}\,|\phi_l\phi_{m_1}\rangle$ and $(J_{lm_2}^{m_2\mu})^*$. Predicting the sign of the J_{eff}^{pol} is not possible without an analysis of relative symmetry of the involved orbitals. Finally the third type of exchange in magnetic insulators involves two electrons excitation contribution which is written as :

$$\mathcal{H}_{supeex} = Cte + 2\sum_{m_1 m_2}\left\{\sum_l \frac{\left|G_{ll}^{m_1 m_2}\right|^2}{\Delta E(ll \rightarrow m_1 m_2)} + 2\sum_\mu \frac{\left|G_{\mu\mu}^{m_1 m_2}\right|^2}{\Delta E(\mu\mu \rightarrow m_1 m_2)}\right\}(\mathbf{S}_{m_1}\cdot\mathbf{S}_{m_2}) \tag{1.27}$$

Where $G_{ll}^{m_1 m_2} = \langle\phi_{m_1}\phi_{m_2}|\,\mathcal{H}_{12}\,|\phi_l\phi_l\rangle$. This mechanism stabilizes the antiferromagnetic state.

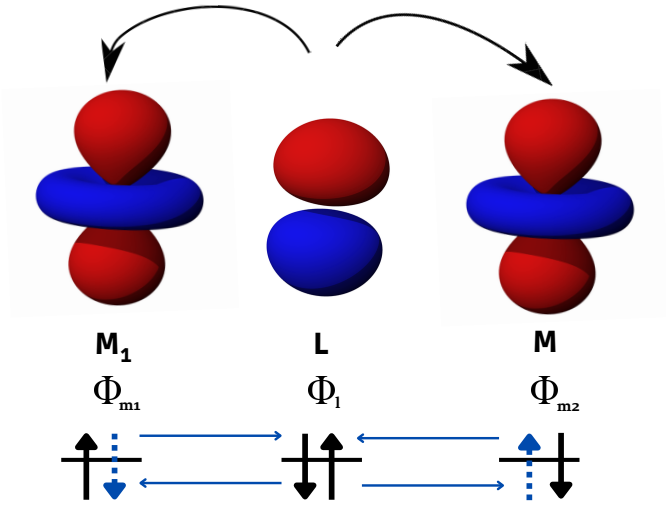

FIGURE 1.7: Representation of the superexchange interaction that involve two-electron transfer

The first term represents the process of two electrons making a virtual transition from DO orbitals ϕ_l to an adjoining SO orbitals one each ϕ_{m_1} and ϕ_{m_2}, the second term denotes a virtual transition of two electrons from ϕ_{m_1} and ϕ_{m_2} to a non-degenerate empty orbital ϕ_μ. This mechanism is depicted in Fig.1.7

1.2 Phase transitions in ferroics

1.2.1 Landau theory

The fascinating thing about Landau's theory is that it gives a good description of the phase transitions under a few simple assumptions about the order parameter. The free energy of the system completely determines the physics at thermodynamic equilibrium. The free energy $\mathcal{F}$ is a functional that must be invariant under the operations of the symmetry group of the high-temperature disordered phase. While $\mathcal{F}$ is a complex function of the order parameter φ (magnetization, polarization, ...), however, since $\langle\varphi\rangle = 0$ at $T > T_c$ the free energy can be expressed as a function of local free energy density $f(T, \varphi(\mathbf{r}))$ the simplest form for

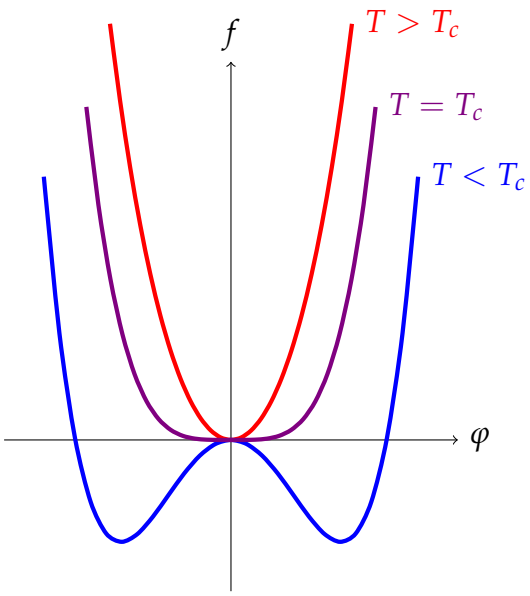

FIGURE 1.8: The Landau free energy density $f(T,\varphi) = \frac{1}{2}r\varphi^2 + u\varphi^4$ as a function of order parameter φ at $T > T_c$, $T = T_c$ and $T < T_c$.

the free energy functional is

$$\mathcal{F} = \int \mathrm{d}\mathbf{r} f(T,\varphi(\mathbf{r})) + \int \mathrm{d}\mathbf{r} \frac{1}{2} c(\nabla\varphi(\mathbf{r}))^2 \tag{1.28}$$

Where c is a phenomenological coefficient. f is then expanded in power series of φ, where above T_c we must have $\langle\varphi\rangle = 0$ when h the conjugate field (magnetic field, electric field ...) is zero. Thus the linear term of the expansion is nil, and the expansion has the form :

$$f(T,\varphi) = \frac{1}{2}r\varphi^2 - w\varphi^3 + u\varphi^4 + \dots \tag{1.29}$$

The terms of the above equation must all be invariant under the operation of the symmetry group of the high-temperature phase, so in most cases, the odd terms may vanish. The r,w, and u coefficients can, in principle, depend on temperature. If the expansion is stopped at given power of φ, then it should be even with a positive coefficient to ensure the boundedness of φ at the equilibrium state.

1.2.2 Phase transition in magnetic materials

1.2.2.1 Second order phase transitions

In magnetic materials, the order parameter, as seen in the first section, is magnetization. Thus, in such systems, the free energy must be invariant under time reversal since φ changes sign under time reversal. This means that odd terms in the expansion must vanish, and only the even terms remain in the Landau expansion of the free energy density. The expansion can be written then (to the 4th order) as

$$f(T,\varphi) = \frac{1}{2}r\varphi^2 + u\varphi^4 \tag{1.30}$$

Typically, the free energy density contains higher order terms, but it's acceptable to approximate the series up to fourth order in the order parameter as long as the parameter remains small. In order for the system to be thermodynamically stable (i.e. the order parameter is bounded at the energy minimum), the coefficient of the highest even power of the parameter must be positive, denoted by $u > 0$ in this case. To simplify matters, we assume that u is independent of temperature, denoted by $u(T) = u$, and we approximate the temperature dependence of r with the linear approximation $r(T) \simeq a(T - T_c)$, where r changes sign at the critical temperature, T_c. Finally, with these assumptions in place, we minimize f with respect to φ in the presence of the conjugate field h.

$$\frac{\partial f}{\partial \varphi} = r\varphi + 4u\varphi^3 = h \tag{1.31}$$

When $h = 0$ the solutions are

$$\varphi = 0 \qquad T > T_c \tag{1.32}$$

$$\varphi = \pm\sqrt{\frac{-r}{4u}} = \pm\sqrt{\frac{a(T_c - T)}{4u}} \qquad T < T_c \tag{1.33}$$

Thus the mean field theory predicts a second order phase transition with

$$\varphi \sim |T - T_c|^\beta \qquad \beta = 1/2 \tag{1.34}$$

Where β is called a *critical exponent* and controls the temperature dependence of φ at vicinity of T_c. From the free energy, one can compute the specific heat as :

$$C_v = -T\frac{\partial^2 f}{\partial T^2} = \frac{a^2}{8u}T \qquad T < T_c \tag{1.35}$$

$$C_v = 0 \qquad T > T_c \tag{1.36}$$

The last equation gives the specific heat part associated with the ordering establishment. The total specific heat includes additional analytic components that originate from degrees of freedom not related to the ordering. As a result, one should anticipate a smoothly varying background in conjunction with the previous term. Regarding the susceptibility, we calculate it as follows:

$$\chi = \frac{\partial \varphi}{\partial h} = \frac{1}{r} \qquad T < T_c \tag{1.37}$$

$$\chi = \frac{1}{2|r|} \qquad T > T_c \tag{1.38}$$

The last equation implies that $\chi \sim |T - T_c|^{-\gamma}$ where γ is the susceptibility exponent. It's worth noting that the jump in the specific heat is connected to the discontinuity in the second derivative of the free energy, which is a distinguishing feature of a second-order phase transition.

1.2.2.2 First-order phase transition

Landau's theory is applicable for investigating first-order phase transitions as well. There are two distinct approaches, one for systems that are symmetric under a change in the sign of the order parameter and one for systems that are not. Since magnetic systems are studied here, the expansion consists of only even terms. However, in other ferroic materials (ferroelectrics as example), odd terms may also be present. In magnetic systems, a first-order phase transition can occur if the quartic coefficient $-u_4$ is negative. However, since the stability of the solution necessitates a positive highest-order coefficient, we must extend the expansion to the sixth order as seen in Fig.1.9.

$$f(T, \varphi) = \frac{1}{2}r\varphi^2 - u_4\varphi^4 + u_6\varphi^6 \tag{1.39}$$

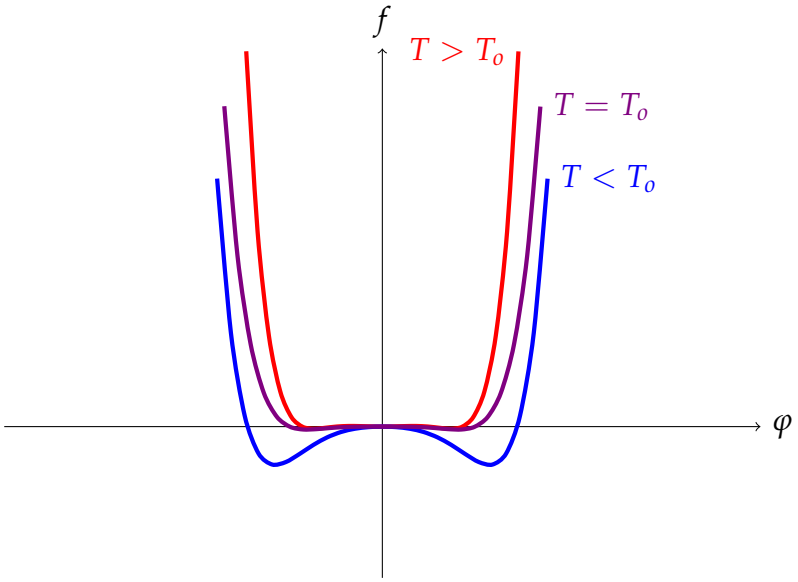

FIGURE 1.9: The Landau free energy density $f(T,\varphi) = \frac{1}{2}r\varphi^2 - u_4\varphi^4 + u_6\varphi^6$ as a function of order parameter φ at $T > T_o$, $T = T_o$ and $T < T_o$.

Where $r = a(T - T_o)$ and T_o is a temperature where r changes sign, this temperature is not T_c as we will show next. In this scenario, there is no critical point, and thus the concept of a *critical temperature* can be misleading. We proceed with the analysis of the density of free energy in two steps. We first analyze the behavior at $T > T_o$. We have convex terms φ^2 and φ^6 (trend toward positive value) and a concave term φ^4, thus for very high temperature above T_o there is only one minimum at $\varphi = 0$, as the temperature is decreased, local minima arise at $\varphi = \varphi_o \neq 0$ which became the global minima at $T < T_o$ due to φ^2 changing sign. When the temperature surpasses T_o, the global minimum of the system cannot change continuously from φ_o to 0. Instead, at a specific temperature T_*, the minima at $\varphi = 0$ and φ_o will become degenerate, resulting in an abrupt transition between the two minima depending on whether the system is cooled or heated. The minimization of free energy density with respect to order parameter yields the following transition temperature T_*

$$T_* = T_o \pm \frac{u_4^2}{3au_6} \tag{1.40}$$

and we have

$$\varphi = 0 \qquad T > T_* \tag{1.41}$$

$$\varphi = 0; \varphi = \pm\sqrt{\frac{2u_4 \pm \sqrt{4u_4^2 - 6ru_6}}{6u_6}} \qquad T_o < T < T_* \tag{1.42}$$

$$\varphi = \pm\sqrt{\frac{2u_4 \pm \sqrt{4u_4^2 - 6ru_6}}{6u_6}} \qquad T < T_o \tag{1.43}$$

A further demonstration that the transition is first-order, we can show that the free energy for this order parameter is continuous at the transition temperature T_* but its first derivative is discontinuous, leading to an abrupt change in entropy which can be reflected as a non zero latent heat.

1.2.3 Phase transition in magnetic systems

For small magnetization $\mathbf{M}$ the free energy F is written :

$$F(T, \mathbf{M}) = F_0 + a(T)\mathbf{M}^2 + \frac{b(T)}{2}\mathbf{M}^4 + ... \tag{1.44}$$

The coefficient $b(T)$ is positive and varies slowly with temperature around the transition's critical temperature T_c. On the other hand, the coefficient $a(T)$ changes its sign with temperature and cancels at T_c. Doing a Taylor expansion around T_c, yields $a(T) = \alpha_0(T - T_c)$, and for $T > T_c$ the minimum of the free energy with respect to magnetization is achieved for $\mathbf{M} = 0$. However, as $T < T_c$, the $a(T)$ coefficient becomes negative, and the new minimum of the free energy is :

$$\frac{\partial F}{\partial \mathbf{M}} = 2\alpha_0(T - T_c)\mathbf{M} + 2b\mathbf{M}^3 + ... = 0 \tag{1.45}$$

And the magnetization is non zero as depicted in Fig 1.10 :

$$M_0 = |\mathbf{M}_0|^2 = \frac{\alpha_0}{b}(T_c - T) \tag{1.46}$$

The previous behavior is found in ferromagnets, a type of ferroics characterized by the parallel ordering of dipoles in the same direction. The result total magnetic moment gives rise to magnetization. Another type of ordering is antiferromagnetic ordering, where the net magnetization is null even for low temperatures due

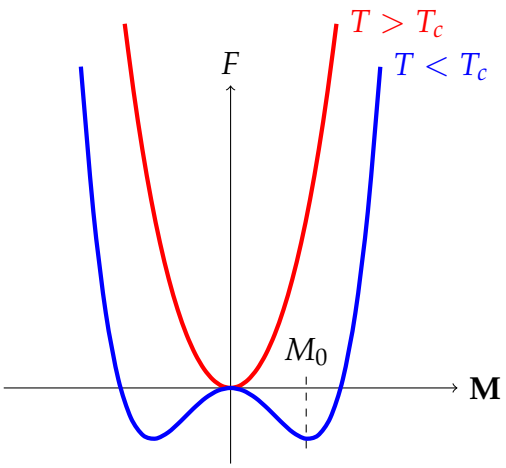

FIGURE 1.10: The Landau free energy as a function of the magnetization $\mathbf{M}$ at $T > T_c$ and $T < T_c$.

to the anti-parallel arrangement of dipoles. In some other materials, we also find noncollinear ordering, which depends on the nature of the exchange interactions between the magnetic dipoles.

1.3 Fundamental magnetic orderings in insulators

Expanding the spins $\mathbf{S}_i$ in terms of their Fourier components on the lattice yields:

$$\mathbf{S}_i = \frac{1}{\sqrt{N}} \sum_{\mathbf{q}} e^{i\mathbf{q}\cdot\mathbf{R}_i} \mathbf{S}_{\mathbf{q}} \qquad \mathbf{S}_{-\mathbf{q}} = \mathbf{S}_{\mathbf{q}}^* \tag{1.47}$$

This will lead us to define the spin structure factor to characterize different magnetic orders.

$$\mathcal{S}(\mathbf{Q}) = \frac{1}{N} \sum_{i,j} e^{-i\mathbf{Q}\cdot(\mathbf{R}_i - \mathbf{R}_j)} \langle \mathbf{S}_i \cdot \mathbf{S}_j \rangle \tag{1.48}$$

1.3.1 Ferromagnetic order

Before talking about ferromagnetism, there is the paramagnetic phase at high temperatures, in which the spins of the magnetic ions are disordered due to thermal fluctuations being stronger than the exchange interaction, this disordered state results in zero net magnetization. For ferromagnets, if we go from high to low temperatures, the material undergoes a phase transition to the ferromagnetic

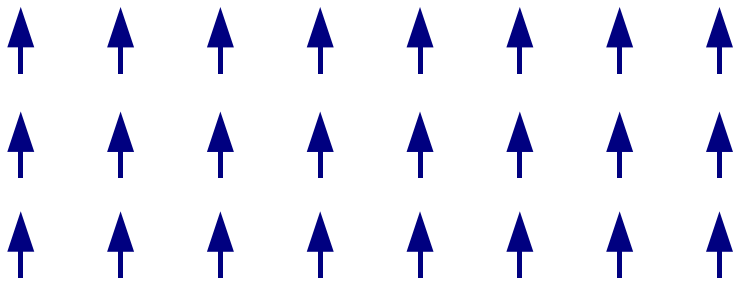

FIGURE 1.11: Spin alignment in ferromagnetic state

state, where we have spontaneous net magnetization below a transition temperature called the Curie temperature T_c. This macroscopic magnetization results from magnetic dipole moments (spins) lining up in the same direction due to Heisenberg interaction [23]. For the ferromagnetic state $|\mathcal{S}(\mathbf{Q})|^2$ have a single nonzero value and is attained at $\mathbf{Q} = 0$ corresponding to a uniform polarization of spins, thus being a signature for ferromagnetic phase.

1.3.2 Antiferromagnetic order

In the antiferromagnetic state, the spins on individual atoms are aligned in an antiparallel configuration. Each spin cancels its neighbor, so there is zero net magnetization even at low temperatures. The antiferromagnetic state is ordered in contrast to the paramagnetic phase, where the spins are disordered. There is a transition from a high-temperature paramagnetic state to a low-temperature antiferromagnetic phase by passing a critical temperature called Néel temperature T_N [23].

There are several types of antiferromagnetism [24], depending on the relationship between the propagation vector $\mathbf{Q}$ and reciprocal lattice vector $\mathbf{G}$. In the case of the cubic lattice with parameter a, we have A-type antiferromagnetism attained when $\mathbf{Q} = [\frac{\pi}{a}, 0, 0]$ this type is referred to as layer-area antiferromagnetism. The C-type antiferromagnetism or the chain-like antiferromagnetism is attained when $\mathbf{Q} = [\frac{\pi}{a}, \frac{\pi}{a}, 0]$, and all next neighbor antiferromagnetism or G-type ferromagnetism is attained for $\mathbf{Q} = [\frac{\pi}{a}, \frac{\pi}{a}, \frac{\pi}{a}]$. Other types are mixed types of the aforementioned types, such as the zigzag type E-type.

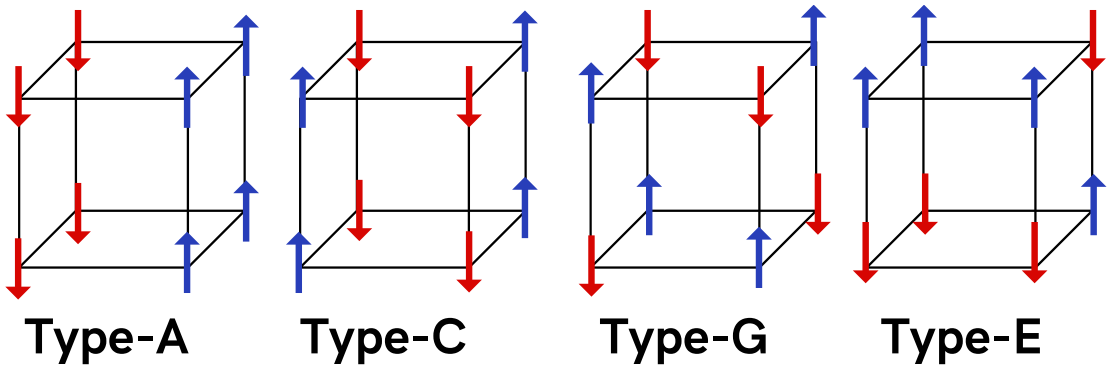

FIGURE 1.12: Spin alignment in different types of antiferromagnetic states

1.3.3 Ferrimagnetic order

In the ferrimagnetic state, we have the same order as in the antiferromagnetic state, where the spins are arranged in an antiparallel ordering. Nonetheless, a nonzero total magnetization is observed. The magnetization is due to the spin polarization having a smaller moment than the opposite polarization, or the population ratio of polarization is higher than the opposite one, even with equal moments. Therefore both states result in macroscopic spontaneous magnetization even with an antiferromagnetic ordering.

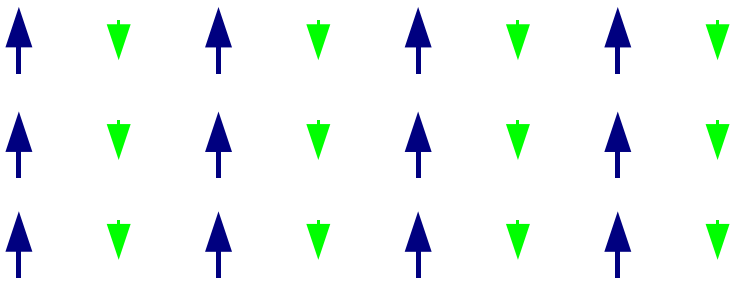

FIGURE 1.13: Spin alignment in a ferrimagnetic state

Chapter 2

Solitons in magnetic ferroics

2.1 Non-topological solitons in magnetic systems

Let us remind the readers of the formula of the spin structure factor that is used to characterize different magnetic solitons.

$$\mathcal{S}(\mathbf{Q}) = \frac{1}{N}\sum_{i,j} e^{-i\mathbf{Q}\cdot(\mathbf{R}_i-\mathbf{R}_j)}\langle \mathbf{S}_i \cdot \mathbf{S}_j\rangle \tag{2.1}$$

2.1.1 Helimagnetic order

Helimagnetism, or spin spiral state, is a form of noncollinear magnetic order where magnetic moments (spins) are arranged in a helical pattern and have either a left-handed spiral or a right-handed one, thus breaking the spatial inversion-symmetry. Helimagnetic order has no macroscopic spontaneous magnetization, there it may be qualified as a complex form of antiferromagnetic [25]. One must understand that adding a spontaneous permanent magnetization component to the spiral modulation creates a new particular helimagnetic order called the **conical order**. The essential feature of a spin spiral is the direction and periodicity of spatial modulation, which are defined by the propagation vector $\mathbf{q}_H$. In contrast to antiferromagnets, where there is a relationship between the reciprocal crystal lattice and propagation vector of the reciprocal magnetic lattice, the helimagnetic state is a more general state, defined by a nonzero propagation vector $\mathbf{q}_H$. However, adding to previous $\mathbf{q}_H$, the conical state also possesses a homogeneous net component with $\mathbf{q} = 0$. Modulated magnetic order parameter $\mathbf{M}(\mathbf{r})$ is written as :

$$\mathbf{M}(\mathbf{r}) = \mathbf{M}_\mathbf{q} e^{i\mathbf{q}\cdot\mathbf{r}} + \mathbf{M}^*_\mathbf{q} e^{-i\mathbf{q}\cdot\mathbf{r}} \tag{2.2}$$

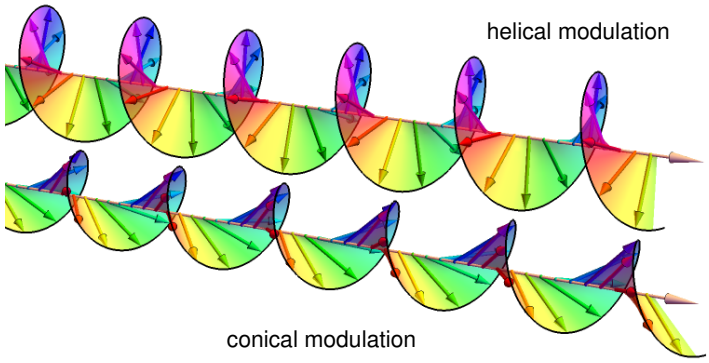

FIGURE 2.1: Spin alignment in a helical and conical states adapted from [26]

Where $\mathbf{r}$ is a real space variable, and $\mathbf{M_q}$ is a complex vector defining the spin spiral plane as :

$$\mathbf{M_q} = \frac{M_0}{2}(\mathbf{u} + i\eta\mathbf{v})e^{i\varphi} \tag{2.3}$$

M_0 is the amplitude of magnetic moments, $\mathbf{u}$ and $\mathbf{v}$ are unit vectors defining the spiral plane, $\eta = \pm 1$ is helicity of the spiral (left-handed or right-handed), and φ is the phase of modulation at $\mathbf{r} = 0$. There are different mechanisms for helical states in ferromagnetic or ferroic in general. For example, in centrosymmetric systems where the non-collinear exchange (DMI) vanishes for symmetry reasons, in metals, for instance, it can be related to RKKY interactions [27, 28, 29], or frustrated magnetism since we are dealing with ferroics. The main ingredient of spin spiral in centrosymmetric systems is magnetic frustration. The competition between a ferromagnetic nearest-neighbor J_{FM} interaction and antiferromagnetic next nearest-neighbor J_{AF} may lead in some conditions in creating a spin spiral with a spin modulation $q = \arccos(-J_{FM}/4J_{AF})/a$. This type of spiral state is found in various systems such as metallic iron phosphide FeP [30] and in triangular lattices such as $CuFeO_2$ [31]. On the other hand, in non-centrosymmetric systems, the existence of relevant DMI leads to a spin spiral with modulation $q = \arctan(-D/J)/a$ where a the lattice constant and D, J DMI and Heisenberg exchange respectively. This type of mechanism that creates the helical states is found to exist within B20 magnets such as manganese monosilicide MnSi [32], iron germanide FeGe [33], or in multiferroic Cu_2OSeO_3 [2] as well as other multiferroic materials such as perovskite structure $BiFeO_3$ [34, 35, 36].

2.1.2 Spirals spin liquids

Spin liquids are excellent illustrations of unusual phases of matter in which quantum phenomena and many-body effects interact to create new emergent properties. They emerge in systems with competing interactions leading to frustration. It has been previously studied in pyrochlore lattices and Kagome lattices. However, a less explored possibility of achieving a macroscopic classical ground state degeneracy is via spiral spin liquids.

Spiral spin liquids are correlated paramagnetic phase with degenerate propagation vectors that form a continuous ring in reciprocal magnetic space ($\mathbf{q}$-space) in case of 2D spiral spin liquids or a continuous 2D surface in $\mathbf{q}$-space for 3D spin liquids. In general, the spin liquids arise in frustrated magnetic systems [37] such as antiferromagnetic Kagome lattices like $Li_9Fe_3(P_2O_7)_3(PO_4)_2$ [38], the frustration in most systems is geometrical leading to interactions that cannot be simultaneously satisfied, this results in cooperative spin fluctuations [39, 40, 41]. The other types of systems are the ones where competition between interactions may give rise to new phases regardless of the geometry of lattice structure, like in bipartite magnets [42] and even in ferromagnets as long as the competition between interactions allows it [43].

This section will explore the possibility of having spiral spin liquids in chiral cubic magnets such as Cu_2OSeO_3. We first start from the Ginzburg-Landau functional of chiral magnets. As a starting point, the free energy is expanded in terms of a slow-varying spin density $\mathbf{S}(\mathbf{r})$ [44]

$$\mathcal{F}(\mathbf{r}) = \mathcal{J}((\nabla S_x)^2 + (\nabla S_y)^2 + (\nabla S_z)^2) + \mathcal{D}\mathbf{S} \cdot (\nabla \times \mathbf{S}) + F_{Ani} \tag{2.4}$$

Where the first term is the Heisenberg exchange and the second is the Dzyaloshinskii-Moriya interaction, for the rest, we will neglect the anisotropy terms of the free energy functional, this is the case of systems with small anisotropy like our system. We can develop a theory of the spin structure that minimizes the free energy $\mathcal{F} - F_{Ani}$. Let us consider the variational spin structure for a given $\mathbf{q}$

$$\mathbf{S}(\mathbf{r}) = \frac{1}{\sqrt{2}}(\mathbf{S}_\mathbf{q} e^{i\mathbf{q}\cdot\mathbf{r}} + \mathbf{S}_{-\mathbf{q}} e^{-i\mathbf{q}\cdot\mathbf{r}}) \qquad \mathbf{S}_{-\mathbf{q}} = \mathbf{S}_\mathbf{q}^* \tag{2.5}$$

Where $\mathbf{S_q}$ is the Fourier vector component of spin density, this changes the free energy functional (2.4) into

$$\mathcal{F}(\mathbf{r}) - F_{Ani} = \mathcal{J}|\mathbf{q}|^2\mathbf{S_q}\cdot\mathbf{S_{-q}} + i\mathcal{D}\mathbf{S_{-q}}\cdot(\mathbf{q}\times\mathbf{S_q}) \tag{2.6}$$

The ground state configuration minimizing the previous functional is to figure out once the complex vector $\mathbf{S_q}$ is decomposed into a pair of real vectors $\mathbf{a_q}$ and $\mathbf{b_q}$ where:

$$\mathbf{S_q} = \mathbf{a_q} + i\mathbf{b_q} \tag{2.7}$$

This transform the DMI part into

$$F_{DM} = 2\mathcal{D}\mathbf{q}\cdot(\mathbf{a_q}\times\mathbf{b_q}) \tag{2.8}$$

Given that the spin norm is fixed (normalized spin) we have $\mathbf{S_q^2} = \mathbf{a_q^2} + \mathbf{b_q^2}$ we can only manipulate the relative size and direction of $\mathbf{a_q}$ and $\mathbf{b_q}$ to one another in order the optimize the gain from DMI term. The most favorable configuration is obtained when they mutually orthogonal $\mathbf{a_q} \perp \mathbf{b_q}$ and $|\mathbf{a_q}|^2 = |\mathbf{b_q}|^2$ (circular helix). For a positive DMI term ($\mathcal{D} > 0$) the F_{DM} is negative if $\mathbf{q}\cdot(\mathbf{a_q}\times\mathbf{b_q}) < 0$. Thus the two terms of the free energy become

$$\mathcal{J}(|\mathbf{q}|^2 - 2\kappa|\mathbf{q}|) \qquad \kappa = \frac{\mathcal{D}}{\mathcal{J}} \tag{2.9}$$

Minimizing the previous energy term with respect to a non zero $|\mathbf{q}|$ yields the following equation

$$|\mathbf{q}_{min}| = |\mathbf{q_H}| = \frac{\mathcal{D}}{\mathcal{J}} \tag{2.10}$$

The spiral wavevector length is therefore fixed by the ratio of the DM energy and the exchange energy. However, the previous equation has no information about the preference for a direction for the spin spiral since all the other terms in the free energy are invariant under the simultaneous $O(3)$ rotation (rotations in three-dimensional space $\mathbb{R}^3$) of spin and space. Henceforth, we have a spiral manifold or the spiral surface, and in the case of 2D systems, we have a spiral ring that characterizes the spiral spin liquid phase where there are infinite degenerate spiral states with the same wavevector length. In conclusion, the spin structure minimizing the free energy of equation (2.6) (in presence of a small or a nil anisotropy) for positive values of the DM energy is the spin spiral structure

FIGURE 2.2: Spin Chain alignment with winding number $w = 1$

with a chirality (helicity) determined by the DMI, the period is defined as :

$$\lambda_H = 2\pi \frac{\mathcal{J}}{\mathcal{D}} \tag{2.11}$$

2.2 Topological defects - Topological solitons

2.2.1 Topology in spin textures

Prior to discussing the topological defects, we will discuss how a mathematical field intervenes in characterizing spin textures in magnetic systems. Let us consider a one-dimensional spin chain that rotates strictly into the easy plane, such that the tilt angle $\theta(x)$ describes the magnetization. The order-parameter space is the unit circle (the 1-sphere) $\mathbb{S}^1$. Suppose that $\theta(x \to \pm\infty) = 0°$ where the zero angle is perpendicular to the x-axis. In this configuration, the space $\mathbb{R}$ is topologically equivalent to the 1-sphere $\mathbb{S}^1$, and we have the continuous map $f : \mathbb{S}^1 \to \mathbb{S}^1$, the homotopy class may classify this homotopy denoted $\pi_1(\mathbb{S}^1) = \mathbb{Z}$. Therefore topologically distinct configurations are then classified by how many times the magnetization wraps around the 1-sphere (unit circle), which coincides with the degree of the map f, that is equal to the winding number w [45]. We depict a spin chain alignment with $w = 1$ in Fig.2.2. The winding number is defined as follow:

$$\deg f = w = \frac{1}{2\pi} \int_{-\infty}^{+\infty} \frac{\partial \theta}{\partial x} \mathrm{d}x \tag{2.12}$$

In real systems, the configuration space is not the 1-sphere. It is the 3D real space $\mathbb{R}^3$, which can be identified with stereographic projection with $\mathbb{S}^3$ in the same way 2D configuration space can be identified with the 2-sphere $\mathbb{S}^2$. In this case, there are no one-dimensional nontrivial configurations since $\pi_1(\mathbb{S}^2) = 0$, nonetheless, 2D solitons with nontrivial topology are possible since $\pi_2(\mathbb{S}^2) = \mathbb{Z}$ (the definition of $\pi_n(\mathbb{M})$ is in the appendix A).

2.2.2 Magnetic skyrmions

The concept of a skyrmion was first proposed by T. Skyrme in 1962 in the context of particle physics to describe a solution of the non-linear field in the context of dense nuclear matter [46]. Thereafter the idea of skyrmions has been found in various condensed matter systems, such as liquid crystals, quantum hall systems, and magnetic materials, which initiated a new wave in spintronics called the skyrmioncs. In 1989 Bogdanov's pioneering theoretical work [1, 47] showed the possibility of the existence of a stable "vortex" state in magnetic systems in materials with specific crystal structures, which reinitiated the quest for magnetic skyrmions. Further works showed that DMI might be the principal mechanism that stabilizes the magnetic skyrmions, which were theoretically predicted in 2006 [48] and eventually found in 2009 with small angle neutron scattering with the sixfold pattern signature of the skyrmion lattice phase in chiral helimagnet MnSi [49] and a year later using the Lorentz transmission electron microscopy [50]. The Lorentz transmission electron microscopy also leads to the observation of skyrmion in $Fe_{1-x}Co_xSi$ [51]. In the following few years, magnetic skyrmions were found in the B20 magnets family with the chiral noncentrosymmetric space group $P2_13$, and Cu_2OSeO_3 [2] where we find Bloch type skyrmions and also in other noncentrosymmetric materials where DMI exists and tends to stabilize skyrmions in the presence of thermal fluctuations as the lacunar spinel GaV_4S_8 [52] with Néel type skyrmions depicted in Fig.2.3. Since then, magnetic skyrmions were also found in centrosymmetric materials even with vanishing DMI, and magnetic frustration plays a significant role in the stability of skyrmions. Magnetic skyrmions were also found in thin films such as FeGe [53], in Co/Ru(001) monolayer as isolated skyrmions [54], in ultrathin Pt/Co/MgO nanostructures [55], and even at room-temperature in the ultrathin ferromagnetic Pt/Co/Ta [56]. In such systems, interfacial DMI is the origin of the stabilization of skyrmions in magnetic multilayers. Recent progress has also been made with room-temperature stabilized isolated antiferromagnetic skyrmions with radiuses smaller than 10 nm in synthetic antiferromagnets [57]. Information technology has become increasingly relevant in our everyday lives, leading to the demand for energy-efficient data storage and manipulation. New spintronic proposals, such as racetrack memory [59] and topological matter, have

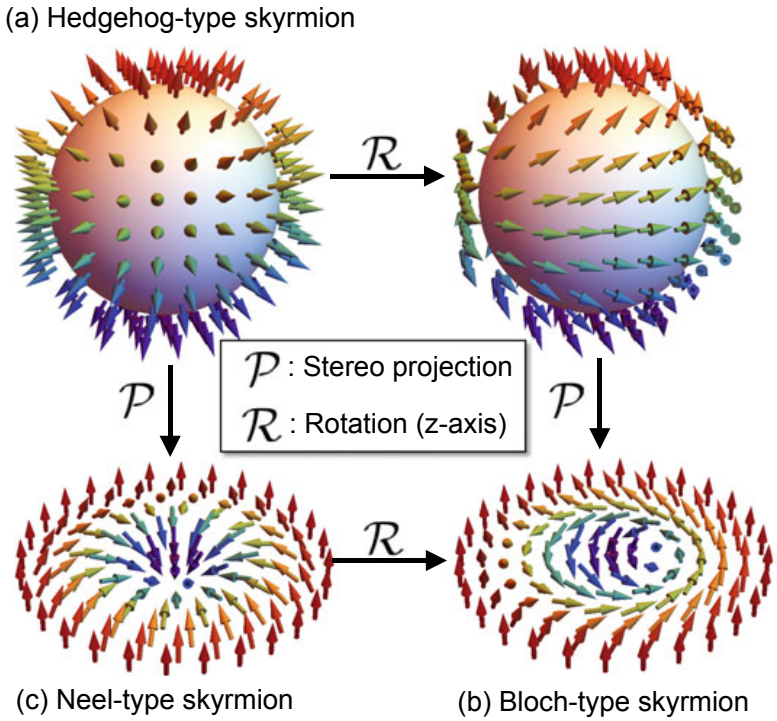

FIGURE 2.3: Spin alignment in a (b) Bloch type skyrmion and (c) Néel type skyrmion and (a) their stereographic projections adapted from [58]

been proposed and may become relevant shortly. Racetrack memory is a quasi-one-dimensional setup that is tackable, allowing for three-dimensional data storage with drastically increased bit densities. Topological defects are also an aspiring research field, with magnetic skyrmion being the most prominent example. Magnetic skyrmions were found to be a reliable building block for various devices such as low-power memory devices such as racetrack memory devices [60, 61], neuromorphic computing, and logic gates [62]. Its topological protection gives it enormous stability even at small sizes, which makes it a promising data storage device. Skyrmions are potential information carriers in future data storage devices, such as racetrack nanodevices. They can be easily manipulated with external stimuli such as electrical currents, including the writing, deleting, and moving of single skyrmions[63, 64]. Since skyrmions are topological entities, they come with their emergent electrodynamics, such as the topological Hall effect [65, 66] and the skyrmion Hall effect [67, 68], which is beneficial for detecting of skyrmions, may however also lead to pinning or data loss in the case of an applied current because of the drifting to the edge of the racetrack, thus the lack of prototype of a skyrmion-based spintronic device nowadays.

A magnetic skyrmion is a localized spin configuration where the spins or magnetic dipoles whirl to form a 2D non-trivial topology. The magnetic skyrmions are characterized by a topological charge (Pontryagin charge) or the winding number and are calculated as:

$$\mathcal{Q}_{sk} = \frac{1}{4\pi}\iint \mathbf{s}\cdot(\frac{\partial \mathbf{s}}{\partial x}\times\frac{\partial \mathbf{s}}{\partial y})dxdy \qquad \mathbf{s} = \frac{\mathbf{S}}{|\mathbf{S}|} \tag{2.13}$$

Geometrically, the integrand is the solid angle spanned by $\mathbf{s}$ when one moves all spins to the Bloch sphere center in the spin space. Thus, $\mathcal{Q}_{sk}$ measures how many times the vector $\mathbf{s}$ wraps the unit Bloch sphere, the topological charge defined in the previous integral expression corresponds to the number of times unit sphere $\mathbb{S}^2$. The prior definition of skyrmion number or winding number is applied for continuous models. In 1981 Berg and Lüscher developed a method to calculate the topological charge in lattice-based systems [69] (atomistic spin dynamics), such as the generalized Heisenberg model that we will explore in the next chapter. The topological charge is given by the sum over an ensemble of elementary signed triangles constituted of spins q_Δ where the sign is related to chosen orientation (we chose here anticlockwise) as seen in Fig.2.4, and the topological charge $\mathcal{Q}_{sk}$ is calculated with :

$$\mathcal{Q}_{sk} = \frac{1}{4\pi}\sum_{\Delta_{ijk}} q_\Delta \tag{2.14}$$

where

$$q_{\Delta_{ijk}} = 2\arctan\left(\frac{\mathbf{S_i}\cdot(\mathbf{S_j}\times\mathbf{S_k})}{1+\mathbf{S_i}\cdot\mathbf{S_j}+\mathbf{S_j}\cdot\mathbf{S_k}+\mathbf{S_k}\cdot\mathbf{S_i}}\right) \tag{2.15}$$

A topologically trivial configuration is characterized with $\mathcal{Q}_{sk} = 0$, and for example, in the case of Cu_2OSeO_3 (CSO), the field polarized phase, helical phase, and conical phase are all characterized with a zero skyrmion number. The transformation of one structure with a defined topological charge into another with the same topological charge can happen continuously. However, it is impossible to continuously pass between two states with different topological charges (with a homotopy). Therefore the robustness of skyrmions regarding mechanical deformations (continuous transformations). Hence, the only way to go from a trivial state with $\mathcal{Q}_{sk} = 0$ to a skyrmion state with $\mathcal{Q}_{sk} > 0$ is with a discontinuous transformation. One can think of a trivial state as a pot made of clay. Going from

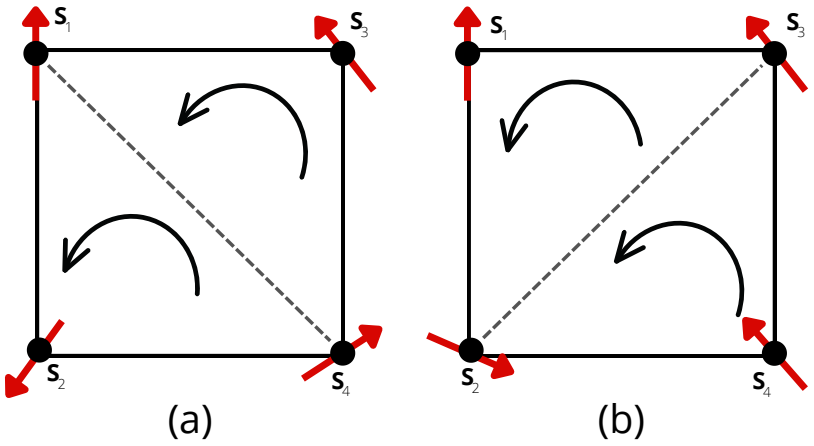

FIGURE 2.4: Lattice scheme for computing the topological charge. (a) Two signed triangles, q_{124} and q_{143} , make up the unit cell. (b) Alternative definition of the signed triangles

a bowl to a vase without a handle requires only molding the clay, which is a continuous transformation. However, making a mug with a handle requires adding more clay on top or poking a hole, which are not continuous transformations.

Isolated skyrmions are generally hard to stabilize, so in most bulk systems, skyrmions form a phase called the skyrmions lattice phase (SkL). Where they are arranged in a 2D hexagonal lattice, for example, in CSO, our target material, the phase diagram has a small pocket of temperature and magnetic field in which the SkL phase is stable. as depicted in Fig.2.5. This SkL is made from Bloch-type skyrmions due to chirality induced by DMI. However, in multilayer heterostructures, inversion symmetry can also be broken at interfaces of thin film ferromagnets and heavy metal bilayers, where strong spin-orbit coupling generates interfacial DMI. These stacks host Néel type skyrmions and are known to be stabilized even above room temperature with sizes that are bigger than in bulk (50-250 nm), but minimizing the size to only a few nanometers is also possible with the cost of reducing the temperature of stabilization to cryogenic levels.

In contrast to ferromagnetic skyrmions, skyrmions having mutually reversible spins can be combined to form antiferromagnetic skyrmions[57, 71]. They are distinguished by a vanishing topological charge as a result. However, in this instance, the sub-skyrmions are not spatially separated but somewhat entangled. This results in the local disappearance of the magnetization density, and the magnetization can be replaced by the Néel order parameter, which is the primary

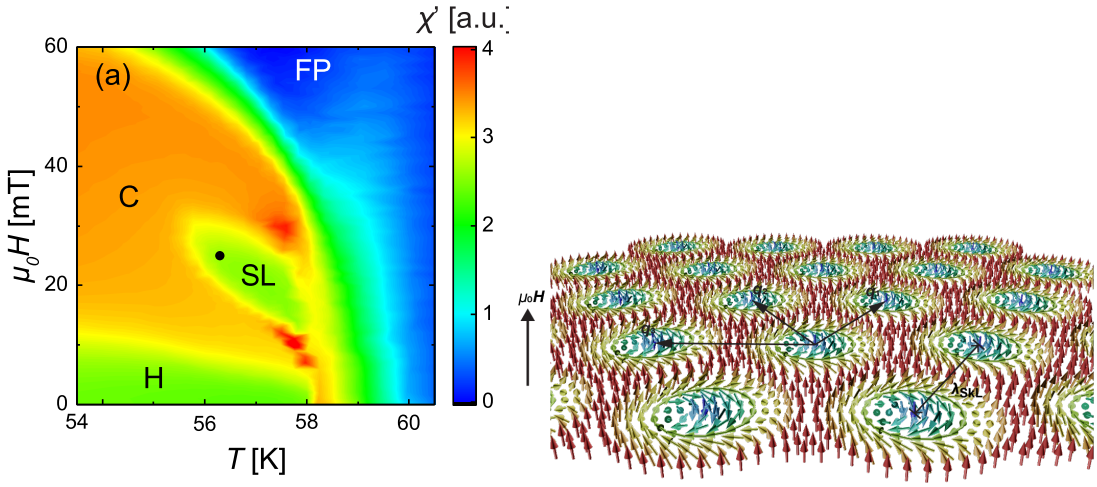

FIGURE 2.5: Schematic phase diagrams of chiral magnet CSO adapted from [70] Where C : Conical , H: Helical , SL : Skyrmion Lattice (SkL in the text) and FP: Field Polarized, and illustration of a Bloch type skyrmion lattice

order parameter for antiferromagnets [72]. From a topological perspective, antiferromagnetic skyrmions are still skyrmions, but their dynamics differ from those of their ferromagnetic counterparts. The skyrmion Hall effect does not exist for this type of skyrmions [73]. However, the two subsystem that makes the antiferromagnetic skyrmions are strongly coupled, which do not allow for deformation due to a pairwise opposing transverse motion by the other sub-skyrmion lattice. Nonetheless, antiferromagnetic skyrmions can be propelled much faster by currents compared to conventional skyrmions [74], which gives them the advantage of being the ideal carriers of information for data storage devices [75]. Furthermore, in contrast to the previously mentioned conventional skyrmions, AF skyrmions exhibit no stray field, which allows for higher stacking densities in stacking 1D racetracks upon building the three-dimensional storage devices. The same can also be said about ferrimagnetic skyrmions that inherit the favorable emergent electrodynamics of antiferromagnetic skyrmions. It consists of two coupled subskyrmions with mutually reversed spins with different magnitudes on the two sublattices leading to an uncompensated magnetization. The existence of a nonzero magnetization allows the detection by X-ray imaging of ferrimagnetic skyrmions in GdFeCo films [76].

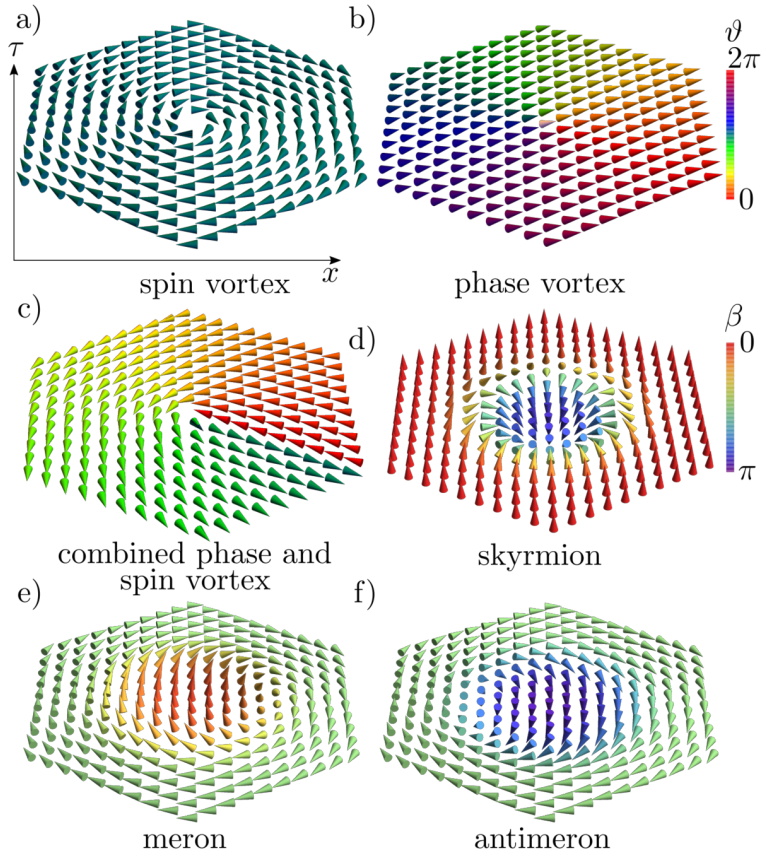

FIGURE 2.6: Some topologically nontrivial configurations where we can see difference between Néel skyrmion with $\mathcal{Q}_{sk} = 1$ and vortices , merons and antimerons with $\mathcal{Q}_{sk} = \pm\frac{1}{2}$ adapted from [77]

2.2.3 Vortices and merons

While there is ongoing research for improving the applicability of magnetic skyrmions in spintronic devices, several alternative topological nano-objects have been predicted and observed during the last few years [78]. Emergent stable topological structures are ubiquitous in condensed matter. The previously mentioned skyrmions are the most prominent example. However, if one splits a skyrmion into two halves, we obtain a meron and an antimeron. Similarly to skyrmions, meron crystals have been predicted to exist in quantum Hall ferromagnets [79], as well as in bilayer graphene [80]. Recently have been observed in planar α-Fe_2O_3/Co heterostructure [81] where they identified magnetic vortices as merons. In the bulk skyrmion host chiral magnet $Co_8Zn_9Mn_3$[82], they were observed as a distinct phase from the SkL, and also found as merons pairs created in continuous permalloy film by local vortex imprinting from a Co disk [83]. Vortexes were

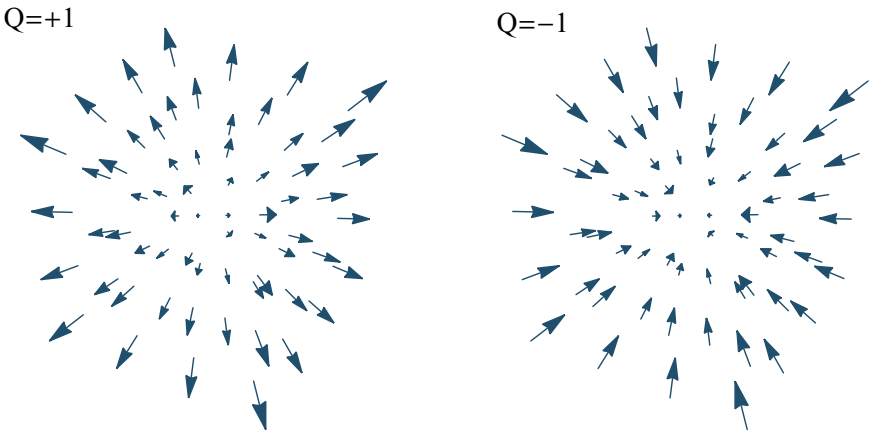

FIGURE 2.7: Schematic view of spin configurations showing ideal hedgehogs of charges $\mathcal{Q} = +1$ (source-like) and $\mathcal{Q} = -1$ (sink-like)

also have been proven to exist within 2D magnet $CrCl_3$ and other Cr-trihalides CrX_3. [84].

Vortices (or antivortices) and merons can be characterized using the same previous skyrmion number. The main difference is that vortices/merons have half-integer skyrmion numbers. The simplest vortex or meron have $\mathcal{Q}_{sk} = \pm\frac{1}{2}$ as seen in Fig.2.6.

Geometrically, this half-integer skyrmion number is because the spins can only map a hemisphere when making an inverse stereographic projection. We have different types of vortices depending on the charge. The type can be extracted from polar angle Θ and azimuthal angle Φ of the spins where r, ϕ radial and angular coordinates in $\mathbb{R}^2$ [77].

$$\Theta(r) = \frac{\pi}{2}(1 - pe^{-r/R}) \qquad \Phi(\phi) = c\phi + \Delta\Phi \tag{2.16}$$

c takes integer values, and measures how many turns the spin does around the vortex center (pole). It also measures the chirality of the vortex. $p = \pm 1$ denotes the polarity of the vortex or the spin direction at the pole $p = 1$ for a spin up and $p = -1$ for a spin down, and the charge is calculated as $\mathcal{Q}_{sk} = \frac{1}{2}cp$.

2.2.4 Hedgehogs/Antihedgehogs (Point defects)

In contrast to skyrmions and vortices, which are 2D defects, hedgehogs are topological point defects whose dimensionality depends on the system dimension.

The hedgehogs/antihedgehogs as as seen in Fig.2.7, are generated by strong directional fluctuations and thus positioned at the junctions of differently ordered regions, at isolated points, where the order changes discontinuously and is thus ill-defined. Hedgehogs can be seen as reminiscent of the disordered phase and were studied in many ferroic systems such as Heisenberg ferromagnets [85, 86], 2D Heisenberg antiferromagnets [87], relaxor ferroelectrics [88], and are found to be valuable in 2D systems that are approximated by XY model (same as Heisenberg model but the spins rotations are restricted to the 2D plane). Since the Berezinskii–Kosterlitz–Thouless transition(BKT)[1][89, 90] involve 2D Hedgehogs-antihedghog pairs (which coincide at this dimensionality with vortices and antivortices) at low temperatures to unpaired vortices and antivortices.

2.2.5 Hopfions

So far, we have seen point defects (0D solitons), vortices, and skyrmions (2D solitons). The question is whether there are 3D solitons. The existence of stable 3D topological defects is a complex problem. It is known that there are no stable 3D solitons in the Heisenberg model [91]. However, this is only valuable for infinite systems, and adding DMI to the picture makes stable 3D solitons possible. The existence of 3D topological solitons has been proposed by Fadeev [92] as the limit of the Skyrme model. These topological defects are known as Faddeev-Hopf knots [93], better known as Hopfions, and are characterized by topological invariant called Hopf charge $\mathbb{H}$, that classify those solitons with respect to the linking number of knots. Recently magnetic hopfions were predicted in a finite-size noncentrosymmetric magnetic system with DMI and perpendicular interfacial anisotropy or with relevant higher-order exchange interactions. The first statically stable magnetic hopfions have been reported by Bogolubsky [94] where an isotropic micromagnetic model possessing $O(3)$ symmetry with higher-order derivatives of the magnetization has been used. The hopfion solutions in this model are stable at zero applied fields when the system's ground state is a ferromagnetic state.

The hopfions are non-homeomorphic maps from $\mathbb{R}^3 \cup \{\infty\}$ to $\mathbb{S}^2$, the Hopf index differs from the skyrmion number, one can see hopfions as skyrmion tube twisted one complete revolution and where both ends are attached, we define the Hopf

[1] Work on the transition led to the 2016 Nobel Prize in physics

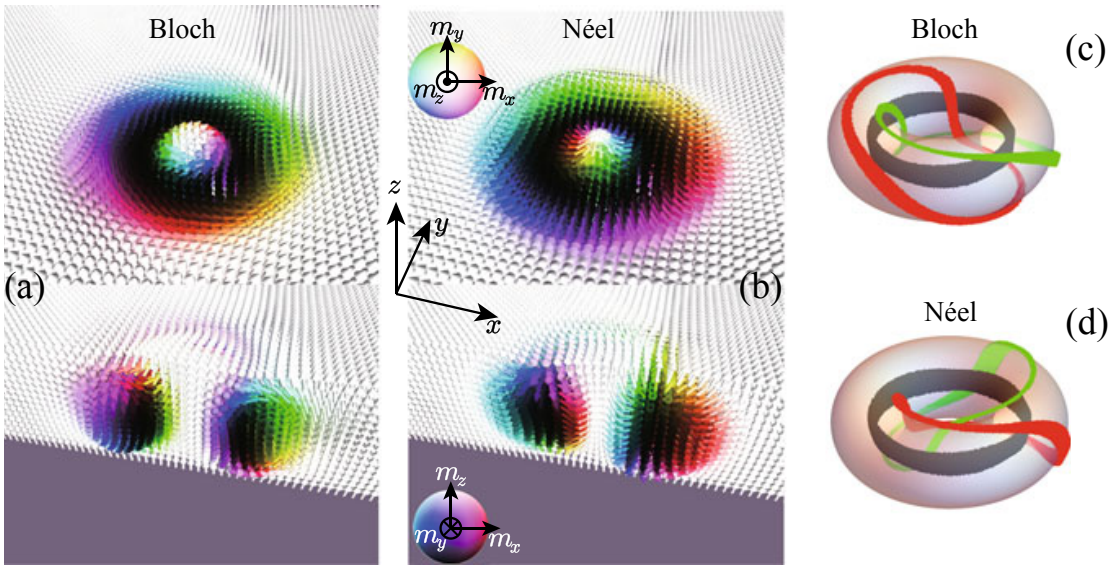

FIGURE 2.8: (a) and (b) Mid-plane cross-sections in the xy-plane (the upper panel) and the xz-plane (the lower panel) of (a) a Bloch-type hopfion and (b) a Néel-type hopfion. (c) and (d) The preimages of $\mathbf{s} = (0, 0, -1)$, $(1, 0, 0)$ and $(0, 1, 0)$ for (c) a Bloch-type Hopfion and (d) a Néel-type hopfion., The gray tori in (c) and (d) are isosurfaces with $s_z = 0$. Adapted from [95]

index as :

$$\mathbb{H} = \frac{1}{(4\pi)^2} \int \mathbf{F} \cdot \mathbf{A}\, d^3\mathbf{r} \tag{2.17}$$

where $F_i = \frac{1}{2}\varepsilon_{ijk}\mathbf{s} \cdot (\partial_j \mathbf{s} \times \partial_k \mathbf{s})$, and ε_{ijk} is the Levi-Civita antisymmetric tensor, and $\mathbf{A}$ is a vector potential which is defined as $\nabla \times \mathbf{A} = \mathbf{F}$. From the geometrical point of view Hopf index indicate how many times the close loop-preimages (inverse images where spins maintain same direction and norm) link with each other.

The hopfions profile is expressed in terms of $\Phi(r, \phi, z)$ and $\Theta(r, \phi, z)$ in cylindrical spatial coordinates, and Φ, Θ are respectively azimuthal and polar angles of magnetization. For system invariant by rotation, one must assume that magnetization profile along Θ is independent of ϕ and $\Phi(r, \phi, z) = \Delta\Phi(r, z) + n\phi$ (where

$n \in \mathbb{Z}$), when can write **F** as [96]:

$$F_r = -n\frac{\sin\Theta}{r}\frac{\partial\Theta}{\partial z} \tag{2.18}$$

$$F_\phi = \sin\Theta\left(\frac{\partial\Theta}{\partial z}\frac{\partial\Delta\Phi}{\partial r} - \frac{\partial\Theta}{\partial r}\frac{\partial\Delta\Phi}{\partial z}\right) \tag{2.19}$$

$$F_z = -n\frac{\sin\Theta}{r}\frac{\partial\Theta}{\partial r} \tag{2.20}$$

The vector potential **A** is :

$$A_r = -(1+\cos\Theta)\frac{\partial\Delta\Phi}{\partial r} \tag{2.21}$$

$$A_\phi = \frac{n}{r}(1-\cos\Theta) \tag{2.22}$$

$$F_z = -(1+\cos\Theta)\frac{\partial\Delta\Phi}{\partial z} \tag{2.23}$$

The Hopf index is :

$$\mathbb{H} = \frac{n}{4\pi}\int_{\mathbb{R}}\int_0^{+\infty}\sin\Theta\left(\frac{\partial\Theta}{\partial z}\frac{\partial\Delta\Phi}{\partial r} - \frac{\partial\Theta}{\partial r}\frac{\partial\Delta\Phi}{\partial z}\right)drdz \tag{2.24}$$

Thus Hopf index is the whirling number n (that characterizes the number of times we twisted the skyrmion tube) multiplied by the skyrmion number of the slice of the tube [97].

Hopfions have been observed and predicted in various systems, including ferroelectrics such as PbZr0.6Ti0.4O_3 [98], chiral liquid crystals where they form a crystal of hopfions (heliknotons) [99], and magnetic Ir/Co/Pt multilayers shaped into nanoscale disks system [100]. Unlike magnetic skyrmions that require strong spin–orbit coupling and a lattice lacking inversion symmetry to have a relevant DMI, magnetic hopfions are more achievable, as reported by F. N. Rybakov, N. S. Kiselev, A. B. Borisov, et al. [101]. Magnetic hopfions can arise in both centrosymmetric and non-centrosymmetric systems. The formation of hopfions requires the competition between multiple spin exchanges, such as ferromagnetic and multispin exchanges, including the bi-quadratic, three-spin four-site, four-spin, or chiral–chiral interactions [102]. The emergent electrodynamics of hopfions is promising due to the presence of a globally compensated, locally finite emergent field, resulting in the deflection of current electrons perpendicular to the hopfion plane. One half of the object displays a positive Hall resistance, while

the other half produces a negative signal. Local measurements of the topological Hall effect for hopfions in a racetrack device generate a unique signature [103]. In addition to the ordinary and anomalous Hall effects, this topological Hall effect is expected to occur and can be observed in the extra component of the resistivity tensor. As a result, it is directly accessible and highly relevant for spintronic applications. Hopfions provide an alternative to 2D magnetic skyrmions, which are not restricted by strong spin-orbit coupling conditions and are the smallest 3D information-carrying particles in spintronics. Like skyrmions, hopfions can be manipulated with spin-current, opening the door to true 3D memory devices and offering a new perspective for neuromorphic computing.

Chapter 3

Ab-initio Methods

3.1 Density Functional Theory (DFT)

3.1.1 Pre-DFT & fundamentals of DFT

The description of physical properties in solid state systems relies on the information inside the wave function of the nucleus and also of the electrons. In material science and solid-state physics, we deal with solids and systems that contain a large number of electrons. This situation is an N-body problem. Solving the many body problem analytically is only possible for a few electrons. However, the systems that are studied are larger. Thus such solving is not possible. In order to overcome this issue, some approximations must be used; since the mass of nuclei is way larger than the mass of the electrons, a first simplification of the problem consists of decoupling their dynamics. This is called the Born-Oppenheimer approximation [104], leading to the reduction of the many-body problem into studying the interactions between electrons in a frozen configuration of nuclei described by the Hamiltonian.

$$\mathcal{H}_e = \sum_{i=1}^{N} \frac{\mathbf{p}_i^2}{2m} + \sum_{i=1}^{N} V_{ext}(\mathbf{r}_i) + \frac{1}{2} \sum_{i \neq j} \frac{e^2}{4\pi\varepsilon_0 r_{ij}} \tag{3.1}$$

The first term is the kinetic energy of the electrons, the second term is the external potential that interacts with electrons, including the interaction between the nucleus and electrons, and the third is the electron-electron interaction. Unfortunately, the problem remains a complex one due to electron-electron interaction. Instead of solving the Schrodinger equation directly to find the wave function

of the N-body electron gas, we solve an optimization problem based on a variational approach, which is the main idea behind the Hartree and the Hartree-Fock methods [105, 106, 107, 108]. However, another paradigm shift in this variational approach led to the widely used method of calculations of electronic properties, the density functional theory (DFT).

3.1.2 Theorems of DFT : Hohenberg-Kohn Theorems

In 1964, Hohenberg and Kohn proved that the energy of the fundamental state is a functional of only the spatial distribution of the electrons, which is depicted as the electronic density of the system $n(\mathbf{r})$ [109]. The expectation value of the electronic Hamiltonian $\mathcal{H}_e$ can be written:

$$E = \langle \psi | \mathcal{H}_e | \psi \rangle = T + V_{ext} + V_{ee} \tag{3.2}$$

With T the kinetic energy, V_{ext} the external potential energy and V_{ee} the electron-electron interactions that represent the internal interactions energy, which are written respectively as :

$$T = \left\langle \sum_i \frac{\mathbf{p}_i^2}{2m} \right\rangle = \frac{\hbar^2}{2m} \int d^3\mathbf{r} \nabla\psi^*(\mathbf{r}) \nabla\psi(\mathbf{r}) \tag{3.3}$$

$$V_{ext} = \langle V_{ext} \rangle = \int d^3\mathbf{r} V_{ext}(\mathbf{r}) n(\mathbf{r}) \tag{3.4}$$

$$V_{ee} = \left\langle \frac{1}{2} \sum_{i \neq j} \frac{e^2}{4\pi\varepsilon_0 r_{ij}} \right\rangle = \frac{e^2}{4\pi\varepsilon_0} \iint d^3\mathbf{r} d^3\mathbf{r}' \frac{n(\mathbf{r}) n(\mathbf{r}')}{|\mathbf{r} - \mathbf{r}'|} + E_{xc}(\mathbf{r}) \tag{3.5}$$

We have $n(\mathbf{r}) = e|\psi|^2$; this means that all the operators mentioned above are either implicit or explicit functions of electronic density. Thus, we can define a universal functional $F_{HK}[n]$ independently of the considered system and include both kinetic and electron-electron energies.

$$F_{HK}[n] = T[n] + V_{ee}[n] \tag{3.6}$$

This lead to the expectation value E, which is a function of the universal functional F_{HK} and a functional of density that is specific to the studied material given

by the external potential energy V_{ext}:

$$E = F_{HK}[n] + \int d^3\mathbf{r} V_{ext}(\mathbf{r}) n(\mathbf{r}) \tag{3.7}$$

Now we set the framework for the density functional of energy of the system. We must establish a link between the ground state density of our system n_0 and the external potential V_{ext}, then find this ground state density. Fortunately, this is precisely the purpose of the Hohenberg-Kohn theorems. The first establishes a link between the density and the applied external potential, and the second gives us a way to find the ground state density. Thus all properties of the system, since those properties are determined by knowing this ground state density $n_0(\mathbf{r})$.

Theorem 3.1.1: Hohenberg-Kohn Theorem 1

The external potential $V_{ext}(\mathbf{r})$ in the electronic Hamiltonian $\mathcal{H}_e$ is, within a constant, a unique functional of the ground state density $n(\mathbf{r})$

Proof

Let $V_{ext}(\mathbf{r}), V'_{ext}(\mathbf{r})$ be two external potentials such that $V_{ext}(\mathbf{r}) \neq V'_{ext}(\mathbf{r})$, since the external potentials are different thus the expected value for the ground energy is respectively E, E' such that $E \neq E'$, where the corresponding ground state wave functions are ψ, ψ'. Let us assume that $\langle\psi| n(\mathbf{r}) |\psi\rangle = \langle\psi'| n'(\mathbf{r}) |\psi'\rangle$, then:

$$E' = \langle\psi'| (T + V_{ee} + V'_{ext}) |\psi'\rangle < \langle\psi| (T + V_{ee} + V'_{ext}) |\psi\rangle \tag{3.8}$$

$$< \langle\Psi| (T + V_{ee} + V_{ext}) |\psi\rangle + \langle\psi| (V'_{ext} - V_{ext}) |\psi\rangle \tag{3.9}$$

$$< E + \langle\psi| (V'_{ext} - V_{ext}) |\psi\rangle \tag{3.10}$$

The last inequality is due to the fact that ψ' is not the ground state of $(T + V_{ee} + V_{ext}$, interchanging primed and unprimed quantities leads to similar inequality

$$E < E' + \langle\psi'| (V_{ext} - V'_{ext}) |\psi'\rangle \tag{3.11}$$

Combining both inequalities leads to

$$E + E' < E' + E \tag{3.12}$$

Therefore the assumption $\langle\psi|\, n(\mathbf{r})\, |\psi\rangle = \langle\psi'|\, n'(\mathbf{r})\, |\psi'\rangle$ is false, and the ground state density is non-degenerate.

Theorem 3.1.2: Hohenberg-Kohn Theorem 2

The ground state energy is expressed as a functional of the density :

$$E[n] = F_{HK}[n] + \int d^3\mathbf{r} V_{ext}(\mathbf{r}) n(\mathbf{r}) \tag{3.13}$$

And the ground state density $n_0(\mathbf{r})$ is the one that minimizes this energy functional.

Proof

Let $n_0(\mathbf{r})$ be the true ground state for the external potential V_{ext}, and let $n'(\mathbf{r})$ be some other density and $|\psi[n']\rangle$ the corresponding ground state. Then :

$$E[n'] = \langle\psi[n']|\, T + V_{ee}\, |\psi[n']\rangle + \int d^3\mathbf{r} V_{ext}(\mathbf{r}) n'(\mathbf{r}) \tag{3.14}$$

$$= \langle\psi[n']|\, \mathcal{H}_e\, |\psi[n']\rangle > E[n_0] \tag{3.15}$$

The equation follows the variational theorem since $|\psi[n']\rangle$ is not the ground state of the electronic Hamiltonian $\mathcal{H}_e$. Therefore the energy functional $E[n]$ is minimized by the ground state density $n_0(\mathbf{r})$.

3.1.3 Kohn-Sham ansatz

Although Hohenberg-Kohn theorems state that minimizing the energy density functional gives us the electronic properties about the studied system, they only state the existence and uniqueness of the density and do not provide any instruction on how to find such functional. In 1965, Kohn and Sham provided a further step to make DFT practical [110]. The main assumption is that the Couloumb interaction between electrons can be substituted by the interaction between one electron and an effective potential called Kohn-Sham potential. The ansatz of Kohn-Sham considers the density as :

$$n(\mathbf{r}) = \sum_{\sigma,i} n_{i,\sigma} |\varphi_i(\mathbf{r})|^2 \tag{3.16}$$

With $n_{i,\sigma}$ the occupation number of orbital i and spin σ, and have either 0 or 1 and sum up to N. Kohn and Sham separated the energy functional for interacting electrons into pieces:

$$F_{HK}[n] = T_S[n] + E_H[n] + E_{xc}[n] \tag{3.17}$$

Where $T_S[n] = \langle \psi_S[n'] | \, T \, | \psi_S[n'] \rangle = \sum_{\sigma,i} n_{i,\sigma} \langle \varphi_i | \, \frac{\mathbf{p}^2}{2m} \, | \varphi_i \rangle$ is the kinetic energy of a fictional system of non-interacting electrons, the second one is the Hartree functional which is the Hartree contribution to Couloumb interaction and is written as:

$$E_H[n] = \frac{1}{2} \iint d^3\mathbf{r} d^3\mathbf{r}' n(\mathbf{r}) \frac{e^2}{|\mathbf{r} - \mathbf{r}'|} n(\mathbf{r}') \tag{3.18}$$

and the last part is the exchange-correlation energy functional. Minimizing the total energy with respect to density is equivalent to minimization with respect to single electron orbitals under the constraint of orthogonality, which gives rise to the Kohn-Sham single-particle equations:

$$[\frac{\mathbf{p}^2}{2m} + v_{ext}(\mathbf{r}) + v_H(\mathbf{r}) + v_{xc}(\mathbf{r})]\varphi_i(\mathbf{r}) = \epsilon_i \varphi_i(\mathbf{r}) \tag{3.19}$$

where the previously mentioned Kohn-Sham potential is $v_{KS} = v_{ext}(\mathbf{r}) + v_H(\mathbf{r}) + v_{xc}(\mathbf{r})$ and

$$v_H(\mathbf{r}) = e^2 \int d^3\mathbf{r}' \frac{n(\mathbf{r}')}{|\mathbf{r} - \mathbf{r}'|} \tag{3.20}$$

$$v_{xc}(\mathbf{r}) = \frac{\delta E_{xc}[n]}{\delta n(\mathbf{r})} \tag{3.21}$$

So far, the Kohn-Sham scheme starts with an initial guess of the input density leading to corresponding Kohn-Sham potential v_{KS}, which in turn gives rise to a set of orbitals that construct the new density, and the procedure is reiterated until we reach a convergence criterion that we have set at the start within this self-consistent cycle. Nonetheless, the scheme relies on knowing the form of the exchange-correlation functional $E_{xc}[n]$, which is *a priori* unknown and must be approximated. Furthermore, this description of DFT does not consider the spin of the electrons. Fortunately, Hohenberg-Kohn theorems still hold for this case, and we consider the minimization of the energy functional either by considering the density of each spin (up and down) $n^{\uparrow}, n^{\downarrow}$ or with respect to total density

$n = n^{\uparrow} + n^{\downarrow}$ and magnetization $m = n^{\uparrow} - n^{\downarrow}$.

3.1.4 The local density approximation (LDA)

As said in the previous subsection, the exchange-correlation functional has an unknown form. To counter this problem, Kohn and Sham considered the limit of slowly varying density. They approximated the functional with the most used exchange-correlation functional to this day. The approximation is treating the inhomogeneous problem as a local homogeneous electron gas. It assumes that the exchange-correlation energy per particle at a point $\mathbf{r}$ depends only on the density at this point, and it is equal to the exchange-correlation energy per particle of a homogeneous electron gas [110].

$$E_{xc}^{LDA}[n] = \int d\mathbf{r} n(\mathbf{r}) \epsilon_{xc}^{LDA}[n] = \int d\mathbf{r} n(\mathbf{r}) (\epsilon_x^{hom}[n] + \epsilon_c^{hom}[n]) \tag{3.22}$$

The exchange part can be found analytically by Bloch and Dirac method as

$$\epsilon_x^{hom}[n(\mathbf{r})] = -\frac{3}{4\pi} \left(\frac{3}{\pi} n(\mathbf{r})\right)^{1/3} \tag{3.23}$$

For the correlation part, the most common practice is using quantum Monte Carlo simulations to extract numerical and fitted data for $\epsilon_c^{hom}[n]$. Even if this approximation is hardly met in the real electronic system, LDA and its spin variant LSDA work exceptionally well, with results within 1% of experimental lattice constants and 5% of phonon frequencies. However, LDA/LSDA fails to reproduce well the physical properties of the system that are very sensitive to lattice parameters, underestimates gap energies, and poorly predicts other physical properties such as electronic susceptibility and cohesive energy [111]. The aforementioned Local Spin Density approximation (LSDA) treats magnetic systems by taking electronic spin into account, and the exchange-correlation energy functional in this case can be written as:

$$E_{xc}^{LSDA}[n^{\uparrow}, n^{\downarrow}] = \int d\mathbf{r} n(\mathbf{r}) \epsilon_{xc}^{LSDA}[n^{\uparrow}, n^{\downarrow}] \tag{3.24}$$

3.1.5 The generalized gradient approximation (GGA)

The step further of the local density approximation is to include the density gradient at the point where we want to evaluate the exchange-correlation functional. In this semi-local approximation, the exchange-correlation energy functional has

the form:

$$E_{xc}^{GGA}[n^{\uparrow}, n^{\downarrow}] = \int d\mathbf{r} n(\mathbf{r}) \epsilon_{xc}[n^{\uparrow}(\mathbf{r}), n^{\downarrow}(\mathbf{r}), \nabla n(\mathbf{r})] \tag{3.25}$$

The widely used GGA-type functional is the Perdew, Burke, Ernzerhof (PBE) functional [112, 113]. Which is usually more accurate at estimating the crystal bulk and lattice [114] due to a better description of total energies, cohesive energies, energy barriers, and structural properties by correcting bond strengths and lengths with respect to the basic local density functionals. However, cases in which GGAs and the PBE overcorrect LSD predictions, such as lattice constants, could occur. As for the previous case of LDA, such inaccuracy can affect properties susceptible to volume change, such as ferroelectric instabilities.

3.1.6 DFT+U

The Hubbard model inspires the U-correction, the method is formulated to account for the strong electron correlations, and it is added to treat d-orbitals and f-orbitals. The U-correction is added to treat localized electrons' strong on-site Coulomb interaction. This approach can be added to previous approximations resulting in LDA+U or GGA+U [115]. The method is described by two parameters U the Coulomb on-site term and J the site exchange term [116], which can be calculated either from *ab initio* calculation or semi-empirical approach, we will see later that the GGA+U within Dudarev formulation is the one used for our calculation [117].

3.1.7 Description of electronic wavefunctions

For the numerical representation of wavefunctions, two general kinds of bases can be used, the delocalized type basis and the localized type basis. From the name, one can guess the main difference between the basis. The localized one involves a function or a description attached to a specific localized atom as in Fig.3.1, an example of localized basis we can cite Gaussian basis or numerical orbitals [118] as in SIESTA code [119], or the Full-Potential Linearized Augmented Plane Waves (FLAPW) in the FLEUR code [120]. The use of such a basis gives, in general, highly accurate results. However, the better the results, the higher the costs, such localized basis calculations demand heavy computational time. The other type of basis is the delocalized one. For instance, the most famous example is plane-wave basis, which is used in our DFT calculation with VASP code [121]

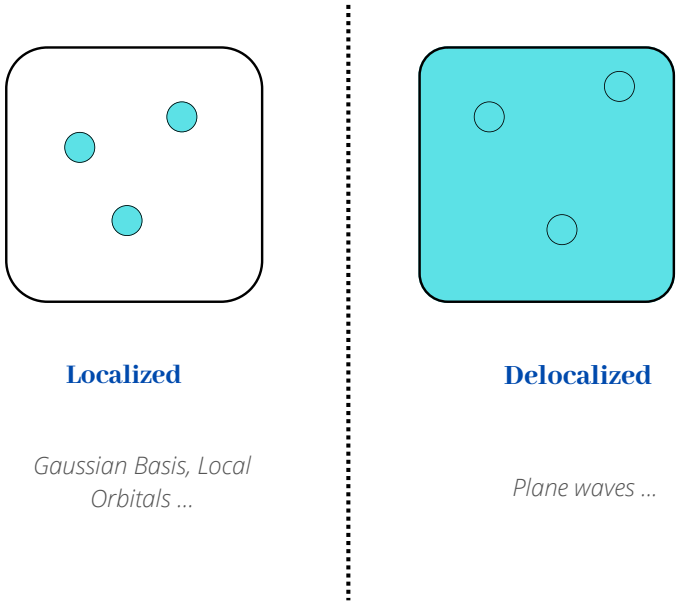

FIGURE 3.1: Types of basis used to describe electronic wavefunctions.

or ABINIT code [122]. Plane-wave DFT uses the Bloch theorem and decomposes each one-electron wave function into the sum of plane waves to solve Kohn-Sham single-particle equations. In theory, the sum should be an infinite one, but in practice, we sum to a specific cut, called the cut-off energy, which is related to a plane wave with a vector $\mathbf{k}$ such that $\frac{\hbar^2\mathbf{k}^2}{2m} < E_{cut}$, and the more significant E_{cut} is, the higher the numerical accuracy, since the set of plane-wave basis is bigger. However, there is a flaw in plane-wave-based DFT, and it shows in its failure to treat strong and fast oscillations close to atomic nuclei. This behavior implies that we must choose a finer grid to treat them numerically. However, it is shown that core states do not influence the properties as much as the valence electrons. Hence, the frozen-core electron hypothesis, where core states can be determined for every atom type and do not change if atoms are combined to form crystals. The frozen-core hypothesis leaves us with the idea that only the tail outside a radius r_c plays a significant role in electronic and chemical properties. Therefore, we replace the real wavefunction ψ with a pseudo-wavefunction $\tilde{\psi}$, which is smoother (but wrong) and equals the real wavefunction outside the radius r_c. These transformations lead to a change in the Kohn-Sham potential, represented by the pseudopotential V_{PS}. Dealing with pseudized wavefunction enables decomposing them in plane-wave basis with fewer elements and retrieving the long-range electrostatic

behavior; one must impose the constraint of norm-conserving inside the sphere of radius r_c.

$$\int_{r<r_c} d\mathbf{r}|\psi(\mathbf{r})|^2 = \int_{r<r_c} d\mathbf{r}|\tilde{\psi}(\mathbf{r})|^2 \tag{3.26}$$

The simplest pseudopotential is having a local multiplicative function. However, this method is still insufficient, and a generalization comes with adding projector functions to the previous local potential, and projector functions are chosen to make valence state and core state orthogonal:

$$V_{PS} = V_{local} + \sum_c \alpha_c \left|\psi_c\right\rangle \left\langle\psi_c\right| \tag{3.27}$$

Many popular generations of pseudopotentials are included in the norm-conserving pseudopotentials, such as Troullier-Martins pseudopotential [123]. However, other types, such as Vanderbilt's ultrasoft pseudopotentials [124] or Blochl's Projector Augmented Wave (PAW) [125] method, do not inherit such constraints.

The PAW method does not rely on the all-electron wave function. Instead, it uses smooth functions obtained from the all-electron wavefunction ψ by PAW linear transformation:

$$\left|\psi_n\right\rangle = \left|\tilde{\psi}_n\right\rangle + \sum_{i,R} \left|\phi_i^R\right\rangle \left\langle \tilde{p}_i{}^R \middle| \tilde{\psi}_n \right\rangle - \sum_{i,R} \left|\tilde{\phi}_i{}^R\right\rangle \left\langle \tilde{p}_i{}^R \middle| \tilde{\psi}_n \right\rangle \tag{3.28}$$

Where $\left|\phi_i^R\right\rangle$ are the partial wave basis inside the sphere with radius r_c and $\left|\tilde{\phi}_i{}^R\right\rangle$ its related soft pseudo partial wave basis and $\left|\tilde{p}_i{}^R\right\rangle$ its dual defined as

$$\left\langle \tilde{p}_i{}^R \middle| \tilde{\phi}_j{}^{R'} \right\rangle = \delta_{RR'}\delta_{ij} \tag{3.29}$$

In other words, the wave function is split into three components. The first one is a smooth wavefunction described by plane-wave basis and equals the wavefunction outside the sphere of radius r_c, the second term is the decomposition of wavefunction inside the core into a basis of atomic orbitals, and the third term is the correction to the last term as depicted in Fig.3.2.

Throughout this thesis, we will use the pseudopotential that employs the PAW method for calculation.

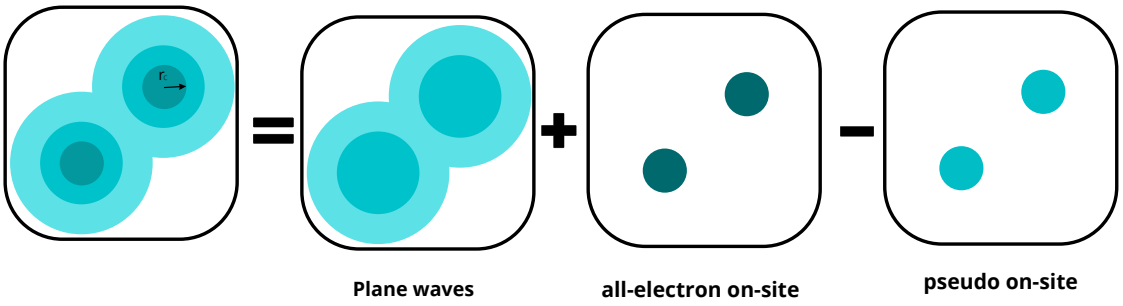

FIGURE 3.2: The PAW linear transformation illustrated

3.1.8 Sampling of the first Brillouin zone

The wave-function depends on the **k** wave-vector, which lies within the boundary of the first Brillouin zone due to Periodic Boundary Conditions (PBC). The properties are determined by averaging over the Brillouin zone. The k-mesh is the discrete sampling of the first Brillouin zone to calculate those averaged properties, and k-mesh have a physical meaning due to PBC and simulating $5 \times 5 \times 5$ k-mesh is equivalent to $5 \times 5 \times 5$ units cells, and the larger the "k-mesh", the closer we are to an infinite system. There are some techniques to reduce the number of k-points in the irreducible Brillouin zone and thus speed up calculations. The most famous is the Monkhorst-Pack scheme which is used in our calculations [126].

3.1.9 Optimization of lattice structure

Before calculating all the physical properties with an assumed constant lattice structure (atomic positions and lattice parameters), one should determine the lowest energy configuration for a given system. This relies on the relaxation of ionic positions and the lattice's volume and shape. We start the initial configuration from experimental data (X-Ray diffraction). This initial configuration is the starting guess to find the minimum energy as a function of atomic positions $\mathbf{R}_I$, and/or lattice parameters. The equilibrium geometry is given by the condition of the vanishing of forces acting on ions I, which can be written as :

$$\mathbf{F}_I = -\frac{\partial E(\mathbf{R}_I)}{\partial \mathbf{R}_I} = 0 \tag{3.30}$$

In practice, the calculation relies on computing the first derivative of the Born-Oppenheimer energy surface by applying the Hellmann-Feynman theorem [127], which states that the derivative of total energy with respect to a parameter λ is equal to the expectation value of the derivative of the Hamiltonian with respect to the same parameter λ.

$$\langle \psi_\lambda | \frac{\partial \mathcal{H}}{\partial \lambda} | \psi_\lambda \rangle = \frac{\partial E_\lambda}{\partial \lambda} \tag{3.31}$$

In the case the parameters are either the atomic position $\mathbf{R}_I$, or lattice parameters a (related to volume), thus for the positions $\mathbf{R}_I$, it reduces to the derivation of the electrons-nuclei interaction potential and Coulomb nuclei-nuclei repulsion energy. Therefore, the force acting on a given ion I depends on the negative gradient of the electrostatic potential energy originating from all the other nuclei and the unperturbed electronic charge density. Consequently, we calculate the forces only if the electronic configuration is close to its ground state. For every change in the geometric configuration, we have to bring the electronic density close to the ground state to calculate forces and stress (derivative with respect to volume change). In practice, for each iteration of the relaxation of the ionic structure, an electronic relaxation must also be done to calculate the forces $\mathbf{F}_I$ [128].

3.2 Second-principles approach : Effective Hamiltonian

In order to explore finite temperature properties, one must be able to model entropy and the random thermal vibrations in which DFT fails. The DFT method is restricted to 0K calculations. The effective Hamiltonian approach is one remedy to this issue if one desires to study dynamical properties and treat finite temperature effects, which include studying various phases at different temperatures and the phase transitions. In 1995, K. Rabe, Z. Zhong, and D. Vanderbilt used DFT to calculate the effective Hamiltonian parameters for ferroelectric perovskite $BaTiO_3$ [129, 130]. The main idea is to reduce the problem to only the degrees of freedom of the system that governs the targeted dynamical properties. In their case, they constructed a Hamiltonian in terms of soft mode ionic degrees of freedom and strains, where the total energy of this Hamiltonian is used in Monte Carlo simulations.

In our case, the material is a multiferroic compound without any structural phase transition, Cu_2OSeO_3 is a type II multiferroic, in which the polarization is spin-induced the interaction can be modeled by the magnetoelectric coupling and is a host of various non-collinear magnetic phases. Therefore, to study these phases, the degrees of freedom in our effective Hamiltonian are the spins of copper ion $\mathbf{S}$, the strain η, and the effective Hamiltonian can be written as :

$$\mathcal{H}_{eff} = \underbrace{\mathcal{H}_{mag}}_{\text{Magnetic}} + \underbrace{\mathcal{H}_{el}}_{\text{Elastic}} + \underbrace{\mathcal{H}_{me}}_{\text{Magnetoelastic}} + \underbrace{\mathcal{H}_{ME}}_{\text{Magnetoelectric}} \tag{3.32}$$

This effective Hamiltonian correspond to an energy which can be written as :

$$\begin{aligned} E^{eff}(\{\mathbf{S}\},\{\eta_k\}) = E^{H}(\{\mathbf{S}\}) + E^{DMI}(\{\mathbf{S}\}) + E^{ani}(\{\mathbf{S}\}) \\ + \sum_i g_{\mathbf{S}} \frac{\mu_B}{\hbar} \mathbf{S}_i \cdot \mathbf{H}_{ext} + E^{me}(\{\mathbf{S}\},\{\eta_k\}) + E^{el}(\{\eta_k\}) \end{aligned} \tag{3.33}$$

The first term corresponds to the Heisenberg exchange interaction, the second to the Dzyaloshinskii-Moriya interaction (DMI), the third to cubic anisotropy contribution to energy, the fourth to Zeeman interaction, the fifth one to the magnetoelastic interaction and the last one to the elastic couplings. In our case, we will only focus on the magnetic part because we are going to study the magnetic non-colinear phases in the absence of mechanical constraints and electric field. For the Cu_2OSeO_3 we have the Heisenberg part of the form:

$$E^{H}(\{\mathbf{S}\}) = \sum_{i<j} [J_w^{FM} \mathbf{S}_i^{II} \cdot \mathbf{S}_j^{II} + J_s^{AF} \mathbf{S}_i^{I} \cdot \mathbf{S}_j^{II} + J_s^{FM} \mathbf{S}_i^{II} \cdot \mathbf{S}_j^{II} + J_w^{AF} \mathbf{S}_i^{I} \cdot \mathbf{S}_j^{II} + J_O^{AF} \mathbf{S}_i^{I} \cdot \mathbf{S}_j^{II}] \tag{3.34}$$

Where the five type of interactions as we will show in the next chapter. In the same spirit we define the DMI as follow:

$$\begin{aligned} E^{DMI}(\{\mathbf{S}\}) = \sum_{i<j} [\mathbf{D}_w^{FM} \cdot \mathbf{S}_i^{II} \times \mathbf{S}_j^{II} + \mathbf{D}_s^{AF} \cdot \mathbf{S}_i^{I} \times \mathbf{S}_j^{II} \\ + \mathbf{D}_s^{FM} \cdot \mathbf{S}_i^{II} \times \mathbf{S}_j^{II} + \mathbf{D}_w^{AF} \cdot \mathbf{S}_i^{I} \times \mathbf{S}_j^{II} + \mathbf{D}_O^{AF} \cdot \mathbf{S}_i^{I} \times \mathbf{S}_j^{II}] \end{aligned} \tag{3.35}$$

Since the crystal has cubic symmetry, the first non-zero term of the magnetocrystalline anisotropic energy (MAE) is of fourth order in spin and is written :

$$E^{ani}(\{\mathbf{S}\}) = \sum_i \mathcal{K}((S_i^x)^4 + (S_i^y)^4 + (S_i^z)^4) \tag{3.36}$$

Where S_i^x, S_i^y and S_i^z are x, y and z components of the spin $\mathbf{S}_i$ and $\mathcal{K}$ is the cubic magnetocrystalline anisotropy coefficient. And what remains now is the to compute the finite temperature properties with Monte Carlo simulations, but before that one must calculate the parameters of the previous Hamiltonian from DFT.

3.3 Monte Carlo simulations

3.3.1 The Monte Carlo method

The Monte Carlo simulation [131] is a widely used method to evaluate the dynamical properties of many systems. In physics, it is used to explore the finite temperature behavior of materials. In statistical physics we define the partition function $\mathcal{Z}$ as:

$$\mathcal{Z} = \int e^{-\beta \mathcal{H}_{eff}(\mathcal{S})} d\mathcal{S} \tag{3.37}$$

Where $\mathcal{S}$ denotes the degrees of freedom in our Hamiltonian, those degrees of freedom are the dynamical variables of our system, and in our case, they correspond to the N $\frac{1}{2}$-spins in copper atoms $\mathbf{S}$ and the homogeneous strain η which lead to rewriting the partition function as :

$$\mathcal{Z} = \int e^{-\beta E^{eff}(\{\mathbf{S}\}_i, \{\eta\})} d\mathbf{S}_i d\eta \tag{3.38}$$

Note that $\beta = 1/k_B T$, and $\mathbf{S}_i$, $d\eta$ denotes integration over magnetic and elastic degrees of freedom. For the rest, we will assume that the strain is constant and the partition function will have the form :

$$\mathcal{Z} = \int \prod_i d\mathbf{S}_i e^{-\beta E^{eff}(\{\mathbf{S}\}_i)} \tag{3.39}$$

The meaningful quantities in physical systems are the observables $\mathcal{O}$, which can be extracted from its thermal expectation value that involves the previous partition function and the system's configuration $\{\mathbf{S}\}_i$

$$\langle \mathcal{O} \rangle = \frac{1}{\mathcal{Z}} \int \prod_i d\mathbf{S}_i \mathcal{O}(\{\mathbf{S}\}_i) e^{-\beta E^{eff}(\{\mathbf{S}\}_i)} \tag{3.40}$$

Unfortunately, this method of extracting physical quantities, even if analytically correct, is useless in computing averages. One can see that evaluating integral on a mesh of point made by the N-spins while assuming that we take p points equidistant along each axis (in our case, 3D space) need a colossal time, which is proportional to p^{3N} (as an example take N=100 spins and $p = 5$ the integral must be evaluated on $\sim 10^{210}$ points !!)[132]. Therefore, a better numerical technique to estimate averages is needed, achieved by so-called importance sampling.

3.3.2 Importance Sampling

The main idea behind importance sampling is to approach integral with sums. Let us look at the simplest Monte Carlo technique: random sampling. Let $f(x)$ be a one-dimensional function, and we want to evaluate the integral:

$$I = \int_a^b f(x)\, dx \tag{3.41}$$

Instead of using the conventional way where we evaluate the integral at predetermined values of abscissa, we used a method based on the average of the function

$$I = (b - a)\langle f(x) \rangle \tag{3.42}$$

The average is an unweighted average of $f(x)$ over the interval. Using Monte Carlo, the average is obtained by evaluating the function at L randomly distributed values x on the interval. One can see that as $L \to \infty$, the procedure gives the correct value. However, this sampling is inefficient since we still spent computing time on points where the probability density is negligible, which in the physical system is the Boltzmann factor.

$$\rho(\{\mathbf{X}_i\}) = \frac{\exp\big(-\beta E_{eff}(\mathbf{X}_i)\big)}{\mathcal{Z}} \tag{3.43}$$

Thus it is important to consider configurations $\mathbf{X}_i$ with a larger Boltzmann ratio than one with a negligible ratio, and the same as we can evaluate the integral with some non-zero probability density over L weighted distributions of point x as

$$I \simeq \frac{1}{L} \sum_{i=1}^{L} \frac{f(x(u_i))}{w(x(u_i))} \tag{3.44}$$

One can do the same of any observable where the central idea is to approximate the large sum by a subset of configurations $\{\mathbf{X}_i\}$ of finite number L_c, sampled according to Boltzmann factor, and the average of an observable over the L_c configurations is :

$$\langle \mathcal{O} \rangle = \lim_{L_c \to +\infty} \frac{1}{L_c} \sum_{i=1}^{L_c} \mathcal{O}(\mathbf{X}_i) \tag{3.45}$$

It is shown that the statistical error is proportional to $1/\sqrt{L_c}$, and the exact value is attained when $L_c \to +\infty$.

3.3.3 The Metropolis-Hasting algorithm

The purpose, as said previously, is to compute the equilibrium properties of many-body systems at finite temperatures. The Metropolis method is a Markov process in which the random walk is constructed such that the probability of visiting a particular configuration is related to its Boltzmann ratio [133].

$$\mathbf{X}_1 \to \mathbf{X}_2 \to \mathbf{X}_3 \to ... \tag{3.46}$$

There are many ways to construct such a Markov process. In the Metropolis-Hasting Method, the configurations $\mathbf{X}_i$ are generated for each iteration called the Monte Carlo step, such that the configuration $\mathbf{X}_{i+1}$ depends only on the previous configuration $\mathbf{X}_i$, this process is made such that the configurations with a larger probability (Boltzmann ratio) are visited more often. The algorithm goes as follow:

- Propose a change of the system state $\mathbf{X} \to \mathbf{X}'$.
- Evaluate the energy change $\Delta E = E^{eff}\{\mathbf{X}'\} - E^{eff}\{\mathbf{X}\}$
- if $\Delta E < 0$ the proposed changed is accepted
- if $\Delta E > 0$ the proposed changed is accepted with a probability $\exp(-\beta \Delta E)$

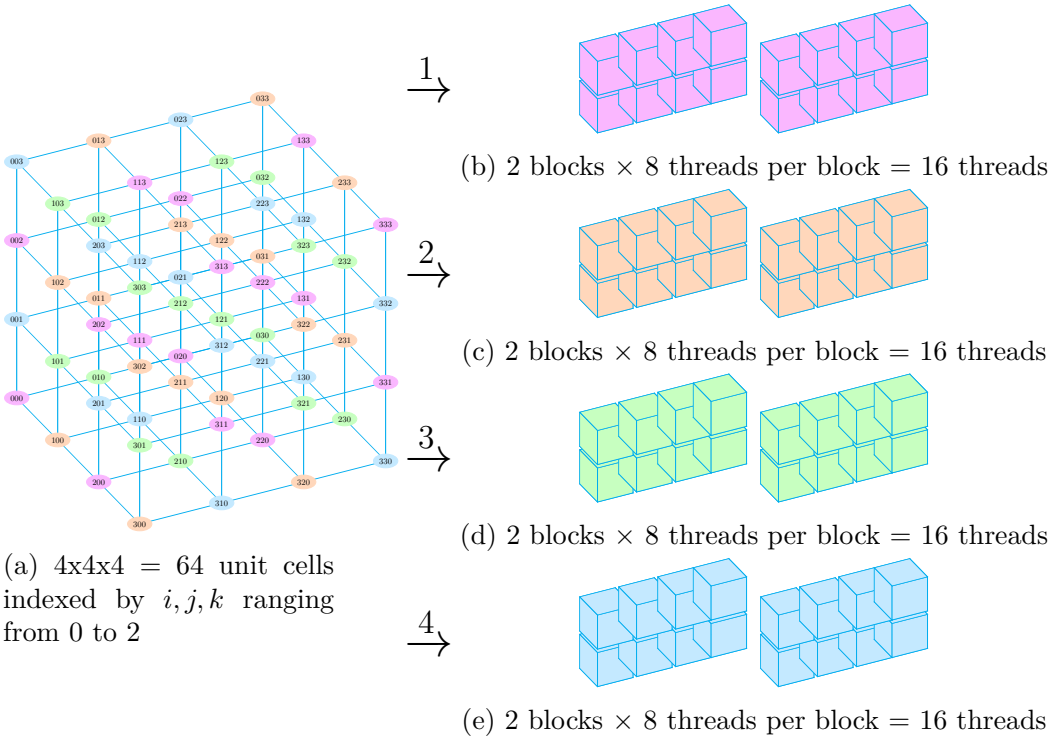

(a) 4x4x4 = 64 unit cells indexed by i, j, k ranging from 0 to 2

(b) 2 blocks × 8 threads per block = 16 threads

(c) 2 blocks × 8 threads per block = 16 threads

(d) 2 blocks × 8 threads per block = 16 threads

(e) 2 blocks × 8 threads per block = 16 threads

FIGURE 3.3: 3-D Checkerboard Algorithm for Cu_2OSeO_3.

- Repeat the procedure

After a fixed number of MCS have been made, the observables $\mathcal{O}_i$ are calculated, added to the statistical average, and kept. The average over the states becomes an arithmetic average over the entire kept-state sample. A finite sample estimate of an order parameter is

$$\langle \mathcal{O} \rangle = \frac{1}{N_S} \sum_{i=1}^{N_S} \mathcal{O}_i \tag{3.47}$$

And by employing fluctuation-dissipation theorems, we can similarly estimate specific heat and order parameter susceptibility from the energy and order parameter variances. In these studies, the Monte Carlo based on the Metropolis-Hasting algorithm, we start by generating an arbitrary norm-conserving configuration of spin 1/2. The initial state of total magnetization is zero at high temperatures. Then we proceed site by site to propose a random change to each of the spins that are not interacting with each other and then apply the acceptance

or rejection procedure. After this, we calculate the dynamical variables (susceptibility, energy ...). The Monte Carlo sweep (MCS) is completed, and we repeat the procedure for the intended number of MCS. We use $84 \times 84 \times 84$ superlattice with periodic boundary conditions for the main calculation. We use a GPU checkerboard algorithm to accelerate the computations as depicted in Fig.3.3 [134] with the non-interacting spins updated in parallel, each colored unit cell contains 16 Cu atoms with spin $1/2$ each. Unit cells and spins in the lattice are colored. The energy difference for updating a spin of one color is entirely described by (i) other 15 spins of the same color in that unit cell and (ii) its neighbors of a different color. Thus, the spins of the same color in different unit cells have no interactions with each other and can be updated independently using the Metropolis algorithm.

Part II

Computational Results and Analysis

Chapter 4

Thermodynamical properties of Cu_2OSeO_3

4.1 Copper Oxide Selenite Cu_2OSeO_3

Among the non-centrosymmetric bulk skyrmions lattice phase hosts, the only non-metallic material is Cu_2OSeO_3 (CSO). This multiferroic of type II crystallizes in the cubic chiral $P2_13$ space group, and the atomic coordinates of CSO contain two nonequivalent Cu^{2+} sites, one at the center of a trigonal bi-pyramid of oxygen ligands and the other at the center of the square based pyramid of oxygen atoms. The crystal structure of copper oxide selenite Cu_2OSeO_3 is depicted in Fig.4.1. The underlying copper ions structure controls the magnetism in the materials. The magnetic structure consists of tetrahedrons formed by three copper ions of type 2 with spin 1/2 and one copper ion of type one with spin 1/2 in the opposite direction, resulting in ferrimagnetic ordering. As we have seen in previous chapters, CSO is multiferroic material, a chiral magnet, and a skyrmion lattice host. Thus the primary goal of our study is to reveal the thermodynamical properties of CSO, which include calculating the strength of different interactions (Heisenberg, DMI, cubic anisotropy), the different phases at various temperatures and magnetic fields, and also the mechanisms governing phase transitions in CSO phase diagram.

The DFT geometry-optimization calculation yields fractional atomic coordinates of the Cu atoms $\rho_i = (x_i/a_0, y_i/a_0, z_i/a_0)$ presented in Table 4.1, where the optimized cubic lattice constant is $a_0 = 8.975$ Å.

ρ_1	(0.879	0.374	0.361)
ρ_2	(0.874	0.138	0.120)
ρ_3	(0.125	0.638	0.379)
ρ_4	(0.138	0.120	0.874)
ρ_5	(0.620	0.625	0.861)
ρ_6	(0.638	0.379	0.125)
ρ_7	(0.625	0.861	0.620)
ρ_8	(0.861	0.620	0.625)
ρ_9	(0.886	0.886	0.886)
ρ_{10}	(0.374	0.361	0.879)
ρ_{11}	(0.361	0.879	0.374)
ρ_{12}	(0.386	0.613	0.113)
ρ_{13}	(0.120,	0.874	0.138)
ρ_{14}	(0.113	0.386	0.613)
ρ_{15}	(0.379	0.125	0.638)
ρ_{16}	(0.613	0.113	0.386)

TABLE 4.1: DFT geometry-optimized fractional atomic coordinates of the Cu atoms where Cu^I atoms are in red

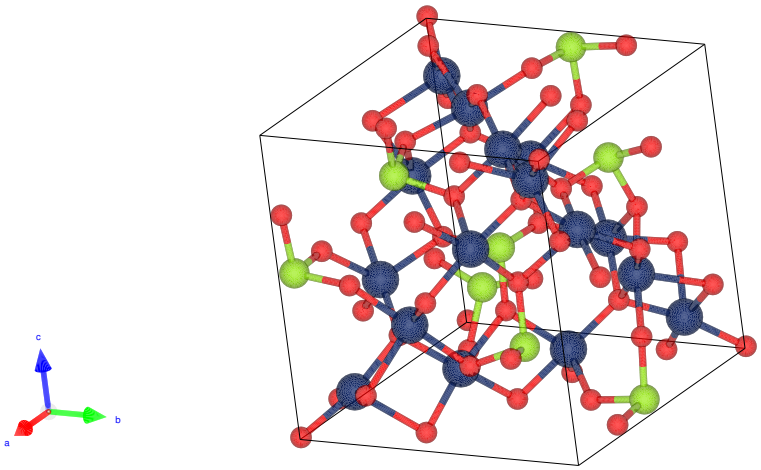

FIGURE 4.1: Crystal structure of copper oxide selenite Cu_2OSeO_3 , Dark Blue : Copper, Red : Oxygen and Green : Selenium

Atoms 9, 12, 14, and 16 are type I copper ions; the rest are type II copper ions. In the next paragraph, we will discuss the strength of various magnetic interactions using DFT calculations and explore the different energy scales and their consequences on thermodynamical properties of Cu_2OSeO_3. We have compared our results with Janson et al.[135]; their calculations adopt the experimental structural data without performing additional relaxations of unit cell parameters and atomic coordinates, resulting in a difference of -0.72% in lattice parameter when compared with our results. It is worth mentioning that both structures have the same $P2_13$ space group symmetry, with Wyckoff positions 4a in red in the table and Wyckoff positions 12b in black with a difference in fractional atomic coordinates around 0.1%. The difference between our calculation and the Janson et al. calculations [135] is more apparent when comparing the electronic structures. Their electronic structure shows a tiny energy gap ($\sim$ 0.2 eV), whereas, in our calculations, we find a value of $E_g = 1.96$ eV as shown in Fig.4.2, which is slightly smaller than the observed experimental gap $E_g \sim 2 - 2.5$ eV [136]. It is due to the fact that the used GGA functional in our calculations underestimates the band gap.

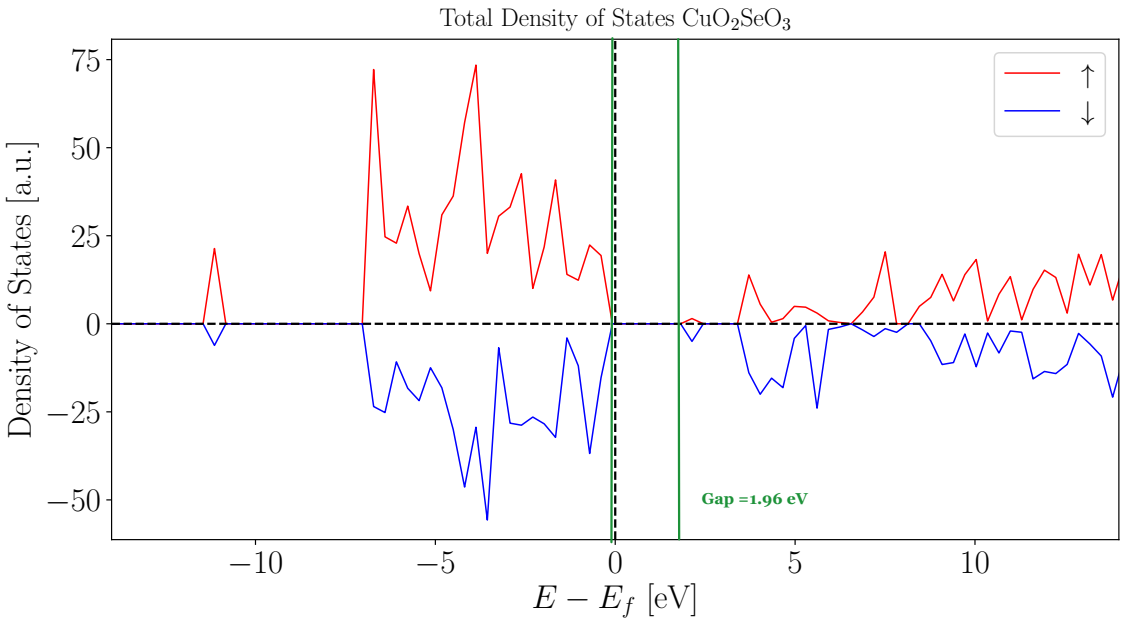

FIGURE 4.2: Total density of states (TDOS) of Cu_2OSeO_3 showing a bandgap of $E_g = 1.96$ eV

4.2 Effective Hamiltonian parameters

4.2.1 Energy scales

In Cu_2OSeO_3, as seen in the previous section, there are two types of copper ions as depicted in Fig.(4.3), arranged in small and large tetrahedron constituted of 3 copper ions of type II (dark blue) and one copper ion of type I (light blue). The two types of tetrahedrons create two energy scales, which will be labeled (strong (s) and weak (w)). Each tetrahedron has two types of interactions based on the link between the types of copper ion, thus resulting in ferromagnetic interaction (FM) and antiferromagnetic interaction (AF), which lead us to four types of interactions $J_W^{FM}, J_S^{AF}, J_S^{FM}, J_W^{AF}$ depicted in Fig.4.4. Moreover, a relevant superexchange interaction mediated by oxygen ligands results in superexchange antiferromagnetic interactions J_{O-O}^{AF}. For every Heisenberg interaction mentioned, there is an equivalent DMI vector (for example $\mathbf{D}_W^{FM}$), adding to previous interactions, the single ion anisotropy, which is going to be of fourth order in term of spin components since the material structure is cubic.

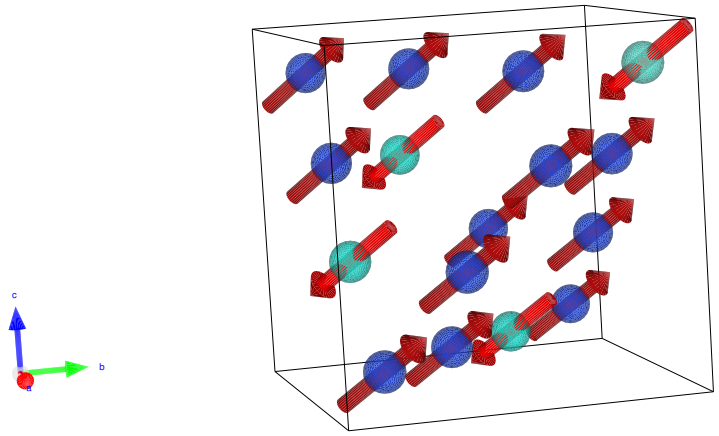

FIGURE 4.3: Magnetic atoms in the system : Light Blue : Copper atoms I (Cu^{I}) And Dark Blue for Copper atoms II(Cu^{II})

4.2.2 Energy-mapping method

To calculate the strength of magnetic interactions, many methods exist such as the energy mapping four-state method[137, 138], the Green's function approach employing infinitesimal rotations [139, 140], and The FLAPW method employing spin-spiral states [141, 142]. The simplest one is the four-states energy-mapping method. The method consists of performing multiple DFT+U energy calculations for four different states. For example, for a dimer composed of two spins i and j, the idea is to calculate the energy of states 1 to 4 depicted in Fig.4.5.

The spin Hamiltonian then can be written as

$$E_{spin} = E_{other} + J_{ij}\mathbf{S}_i \cdot \mathbf{S}_j + \mathbf{D}_{ij} \cdot \mathbf{S}_i \times \mathbf{S}_j + \mathbf{K}_i \cdot \mathbf{S}_i + \mathbf{K}_j \cdot \mathbf{S}_j \tag{4.1}$$

Where $\mathbf{K}_j = \sum_{k \neq j,i} J_{jk}\mathbf{S}_k$ and $\mathbf{K}_i = \sum_{k \neq j,i} J_{ik}\mathbf{S}_k$, and E_{other} does not depend on spin alignment of sites i and j. For the collinear case, we perform calculations without spin-orbit coupling. Thus DMI is zero, leaving us only with E_{other} and

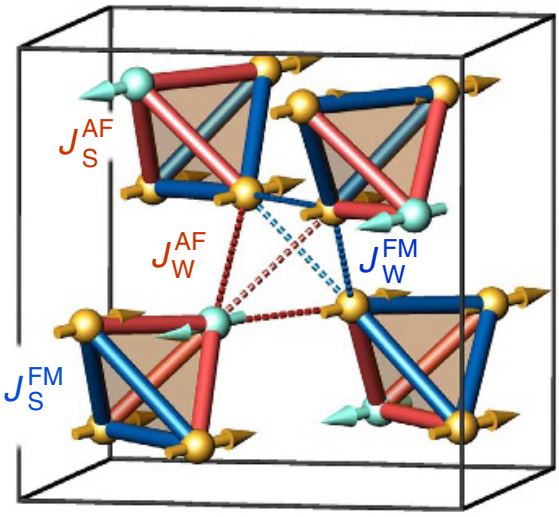

FIGURE 4.4: Interaction inside Cu_2OSeO_3 between type I copper ion (blue) and type II copper ion (gold), adapted from [135]

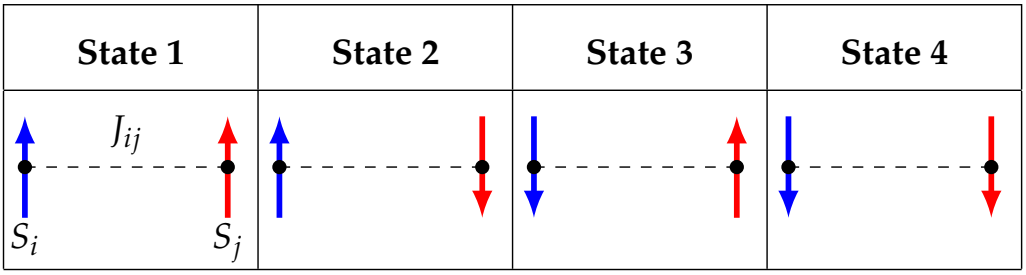

FIGURE 4.5: Four-state energy-mapping method for collinear configurations

the Heisenberg part. The spin energy for the four states is then written as :

$$E_1 = E_0 + E_{other} + J_{ij}\mathbf{S}_i \cdot \mathbf{S}_j + \mathbf{K}_i \cdot \mathbf{S}_i + \mathbf{K}_j \cdot \mathbf{S}_j \tag{4.2}$$

$$E_2 = E_0 + E_{other} - J_{ij}\mathbf{S}_i \cdot \mathbf{S}_j + \mathbf{K}_i \cdot \mathbf{S}_i - \mathbf{K}_j \cdot \mathbf{S}_j \tag{4.3}$$

$$E_3 = E_0 + E_{other} - J_{ij}\mathbf{S}_i \cdot \mathbf{S}_j - \mathbf{K}_i \cdot \mathbf{S}_i + \mathbf{K}_j \cdot \mathbf{S}_j \tag{4.4}$$

$$E_4 = E_0 + E_{other} + J_{ij}\mathbf{S}_i \cdot \mathbf{S}_j - \mathbf{K}_i \cdot \mathbf{S}_i - \mathbf{K}_j \cdot \mathbf{S}_j \tag{4.5}$$

Where E_0 is the DFT energy unrelated to spin alignment, these four energies yield the formula to extract the Heisenberg exchange between sites i and j by the following formula.

$$J_{ij} = \frac{E_1 + E_4 - E_3 - E_2}{4|S_i S_j|} \tag{4.6}$$

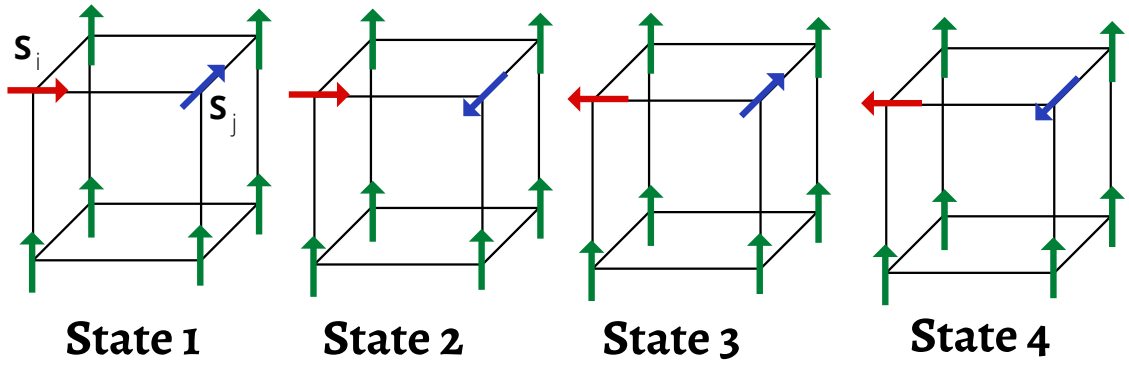

FIGURE 4.6: Four-state energy-mapping method for non-collinear configurations

The same strategy is for the case of DMI, except the DFT+U calculations are done with spin-orbit coupling, and the four states are noncollinear in contrast to the previous case. For example, if one wants to calculate the z-component of $\mathbf{D}_{ij}$ the spins i and j are going to be in x and y directions, respectively, while the rest of spins will be in the z direction as depicted in Fig.4.6. The four states remain the same while respecting the previous directions for spins, and we get:

$$D_{ij}^{z} = \frac{E_1 + E_4 - E_3 - E_2}{4|S_i S_j|} \tag{4.7}$$

4.2.3 DFT Calculations

All the first-principles density functional theory calculations were performed using the Vienna Ab initio Simulation Package (VASP) [121] for both geometrical structure optimization and to calculate the Heisenberg exchange, DMI constants with the four energies states method [137, 138].

The electronic wavefunction adopts a plane-wave basis, and the pseudo-potentials adopt the projector augmented-wave method (PAW), with Generalized Gradient Approximation of Perdew, Burke, and Ernzernhof (GGA-PBE) [112] used as exchange-correlation functional. For 3d orbitals of Cu atoms, a GGA+U correction is used within Dudarev's formulation [117] to treat the strong correlation properties of 3d electrons with U (on-site Coulomb repulsion energy) and J (Hund

exchange parameter) are set, respectively, to 7.5 eV and 0.98 eV [143], the spin-orbit coupling parameter was turned on for the case of DMI. The plane-wave cutoff energy is set to 520 eV. The sampling of the Brillouin zone is done using a $4 \times 4 \times 4$ Γ-centred k-mesh with the Monkhorst-Pack scheme.

4.2.4 The strength of interactions

Magnetic interactions are crucial in forming magnetic textures, such as the helical structure and magnetic skyrmions in Cu_2OSeO_3. We evaluate the Heisenberg interaction and DMI using the four-state energy-mapping method [137, 138]. The results reveal two energy scales for exchange constants. There is weak and strong interaction for both ferromagnetic and antiferromagnetic exchanges, and an important superexchange (long-range) antiferromagnetic compared to weak interactions. Table 4.2 presents all the values for the five exchanges and their corresponding DMI vectors. We observe that the ratio of DMI over Heisenberg constant δ, which is usually smaller than 0.05 [19], is between 0.11 and 0.20 and an enormous ratio of 0.84 in the case of the weak antiferromagnetic exchange $J_w^{AF}, \mathbf{D}_w^{AF}$. The immense ratio reveals the existence of a very strong DMI in our system, which is a necessary condition in creating magnetic textures, particularly magnetic skyrmions. We have compared our results with O.Janson et al.[135] starting with the exchange constants; we report a difference between the Heisenberg exchange in our work and their results. The ratios between the DMI and Heisenberg interaction were smaller than 0.10, except for the weak antiferromagnetic exchange, which is at the order of 0.58. The small ratios could be the origin of the absence of non-collinear spin textures when using their results as input parameters of our effective Hamiltonian. We have also compared our results with a previous study by Yang et al. [144] and find them to be consistent.

4.2.5 Elastic and magnetoelastic coupling

We computed the magnetoelastic interaction, more precisely the microscopic one, due to the effect of homogeneous strain $\eta_{\alpha\beta}$ on Heisenberg exchange constants.

$$\mathcal{H}_{me} = E^{me}(\{\mathbf{S}\}, \{\eta_{\alpha\beta}\}) = \sum_{\alpha,\beta}\sum_{i<j} \frac{\partial J_{ij}}{\partial \eta_{\alpha\beta}} \mathbf{S}_i \cdot \mathbf{S}_j \cdot \eta_{\alpha\beta} = \sum_{\alpha,\beta}\sum_{i<j} \Lambda^{ij}_{\alpha\beta} \mathbf{S}_i \cdot \mathbf{S}_j \cdot \eta_{\alpha\beta} \quad (4.8)$$

J and $\mathbf{D}$	(ρ_i, ρ_j)	d_{ij}(Å)	J_{ij} (K)	$\mathbf{D}_{ij}$ (K)	$\delta = \frac{\lvert\mathbf{D}_{ij}\rvert}{\lvert J_{ij}\rvert}$
$J_W^{FM}, \mathbf{D}_W^{FM}$	(ρ_8, ρ_7)	3.011	-27.57	(-2.53, -3.85, 0.20)	0.167
$J_S^{AF}, \mathbf{D}_S^{AF}$	(ρ_{12}, ρ_6)	3.067	146.76	(-3.60, 13.88, 9.75)	0.118
$J_S^{FM}, \mathbf{D}_S^{FM}$	(ρ_1, ρ_8)	3.226	-60.00	(4.57, 8.15, 4.47)	0.173
$J_W^{AF}, \mathbf{D}_W^{AF}$	(ρ_{12}, ρ_{13})	3.336	16.84	(-9.53, 8.06, 6.84)	0.845
$J_{O-O}^{AF}, \mathbf{D}_{O-O}^{AF}$	(ρ_{16}, ρ_3)	6.396	30.57	(-0.55, 4.26, -3.88)	0.189
Cubic magnetocrystalline anisotropy constant $\mathcal{K}$ (K) : 3.435					

TABLE 4.2: Microscopic magnetic model parameters from DFT four states energy-mapping calculations : the column respectively designate the interaction type, the involved atoms (ρ_i, ρ_j), distance between atoms, the Heisenberg exchange, DMI vector and the ratio between DMI and Heisenberg exchange. The last line is Cubic magnetocrystalline anisotropy constant.

The microscopic magnetoelastic tensor $\Lambda_{\alpha\beta}^{ij}$ is a second-order symmetric tensor; its symmetric property is derived from the symmetry of strain tensor $\eta_{\alpha\beta}$ and since we have five different Heisenberg constants, the same goes for the magnetoelastic tensor, with each having six different components. Using Voigt's notation, we have the energy contribution of magnetoelastic interaction.[145]

$$E^{me}(\{\mathbf{S}\}, \{\eta_k\}) = \sum_{k=1}^{6} \sum_{i<j} [\Lambda_k^1 \mathbf{S}_i^{II} \cdot \mathbf{S}_j^{II} \eta_k + \Lambda_k^2 \mathbf{S}_i^{I} \cdot \mathbf{S}_j^{II} \eta_k + \Lambda_k^3 \mathbf{S}_i^{II} \cdot \mathbf{S}_j^{II} \eta_k + \Lambda_k^4 \mathbf{S}_i^{I} \cdot \mathbf{S}_j^{II} \eta_k + \Lambda_k^5 \mathbf{S}_i^{I} \cdot \mathbf{S}_j^{II} \eta_k] \quad (4.9)$$

In our case, we have 30 microscopic magnetoelastic coefficients to calculate related to the effect of strain (traction-compression and shear) on Heisenberg exchange constants. The results are presented in Table.4.3

$$\Lambda^n = \begin{pmatrix} \Lambda_{xx}^n & \Lambda_{xy}^n & \Lambda_{zx}^n \\ & \Lambda_{yy}^n & \Lambda_{yz}^n \\ sym & & \Lambda_{zz}^n \end{pmatrix} \qquad n \in \{1, 5\} \quad (4.10)$$

The interaction	Λ^n_{xx} (meV)	Λ^n_{yy} (meV)	Λ^n_{zz} (meV)	Λ^n_{yz} (meV)	Λ^n_{zx} (meV)	Λ^n_{xy} (meV)
Λ^{FM}_W	15.96	6.60	-0.16	-4.77	1.00	-14.79
Λ^{AF}_S	-2.27	2.35	2.15	11.00	33.74	-80.46
Λ^{FM}_S	2.44	13.75	8.75	31.63	-13.31	-15.50
Λ^{AF}_W	2.33	-13.25	-0.65	57.00	-18.00	-14.99
Λ^{AF}_{O-O}	-10.50	-2.60	-1.85	7.23	19.00	-2.74

TABLE 4.3: magnetoelastic model parameters from DFT finite difference calculations

Although it was not implemented in the Monte Carlo simulation since we explore the properties in the absence of mechanical constraints, the parameters of the elastic energy have been calculated from DFT using the finite difference method.

$$\mathcal{H}_{el} = E^{el}(\{\eta_{ik}\}) = \sum_{ijkl} C_{ijkl}\eta_{ij}\eta_{kl} \tag{4.11}$$

Our material has a B20 crystal structure, which is a non-centrosymmetric cubic structure. With this consideration and using the Voigt notation, the previous Hamiltonian reduces to three parts with three different coefficients C_{11}, C_{44} and C_{12} related respectively to traction-compression strain, shear strain and transverse traction-compression strain of the cubic crystal lattice.

$$\begin{aligned} E^{el}(\{\eta_{ik}\}) = &\frac{1}{2}C_{11}(\eta^2_{xx} + \eta^2_{yy} + \eta^2_{zz}) \\ &+ \frac{1}{2}C_{44}(\eta^2_{xy} + \eta^2_{yz} + \eta^2_{zx}) + C_{12}(\eta_{xx}\eta_{zz} + \eta_{xx}\eta_{yy} + \eta_{yy}\eta_{zz}) \end{aligned} \tag{4.12}$$

Since the crystal has cubic symmetry, we have only three independent coefficients for the elastic stiffness. The results are in the table 4.4.

C_{11}	C_{12}	C_{44}	Young Modulus E	Shear Modulus G	Poisson ratio ν
244.57 GPa	75.62 GPa	120.51 GPa	251.02 GPa	106.10 GPa	0.18

TABLE 4.4: Elastic model parameters from DFT finite difference calculations

4.3 Finite size scaling

It is impossible to perform numerical simulations on systems as big as the experimental, at least if one desires to include all the degrees of freedom of interest. The sizes reachable by current effective Hamiltonian schemes are way smaller, leading to emulating infinite systems with finite-size systems with special boundary conditions. The boundary conditions, in our case, are periodic boundary conditions (PBC), which induce errors and mismatches between the actual phase transition temperature T_c and temperatures T_c^L that depend on the characteristic length of the system L. However, the T_c^L deviates from the real T_c in infinite systems in a controllable way, studying the trend of T_c^L as a function of L leads to the prediction of the infinite size $T_c^\infty = T_c$. This theory and set of methods in which we treat the effect of size on thermodynamical properties of finite lattices are called *Finite Size Scaling* [146].

4.3.1 Second-order phase transition

A crucial quantity in scaling the statistical properties of thermodynamical observables is the correlation length, which diverges at the vicinity of critical temperature in the case of a second-order phase transition $\xi \sim \tau^{-\nu}$ where $\tau = |T - T_c|/T_c$ is the reduced temperature. However, in a finite system, it cannot be larger than the size of the system L. The pseudocritical temperature $T_c^L > T_c$ and depends on L and using the scaling ansatz for the free energy $\mathcal{F}$ and the idea that the only way $\mathcal{F}$ can depend on L is via the dimensionless parameter $L/\xi \sim L\tau^\nu$, we obtain the method for finite-size analysis.

Since the magnetization, the magnetic susceptibility and specific heat all scale with L as (for $\tau = 0$) :

$$M^c(L) \sim L^{\frac{-\beta}{\nu}} \qquad C_v^c(L) \sim L^{\frac{\alpha}{\nu}} \qquad \chi^c(L) \sim L^{\frac{\gamma}{\nu}} \tag{4.13}$$

It is better to use the Binder cumulant of the order parameter, or energy [147], since the prefactor depends on size gets canceled, and the ratio becomes size independent. Kurt Binder proposed this approach, and the correspondent quantity is called Binder cumulant, defined as the kurtosis of the statistical parameter s

(energy, magnetization ...), and is expressed as :

$$U_B^L = 1 - \frac{\langle s^4 \rangle_L}{\langle s^2 \rangle_L^2} \tag{4.14}$$

Thus we obtain a way to extract the transition temperature value by abscissa of the common intersection of the set of U_B^L plots, and then the critical exponents can be extracted by using the estimate of T_c.

4.3.2 First-order phase transition

The behavior of the observables in the first-order transition is very different from the continuous second-order transition considered before. The correlation length ξ does not diverge. Nonetheless, the system's energy exhibits a discontinuous finite jump, and the critical exponents are meaningless. The main scaling parameter in case of first-order phase transition in the volume V, which in our case $V = L^3$ and the position of T_c^L scales with $1/V$, Therefore, to obtain the estimate of the infinite system transition temperature one can plot T_c^L against $1/V$ [148].

$$U_B^L|_E = 1 - \frac{\langle E^4 \rangle_L}{\langle E^2 \rangle_L^2} \tag{4.15}$$

4.3.3 Finite size scaling of Cu_2OSeO_3

To characterize the effect of size on phase transitions in CSO, we performed a series of Monte Carlo simulations at different sizes ranging from $L = 24$ to $L = 96$, where L denotes the number of unit cells per direction. Thus we have a volume L^3 representing the total number of unit cells in the superlattice, and $N_a = 16L^3$ is the number of spins in the superlattice. To explore the finite size scaling of Cu_2OSeO_3, we calculated the Binder cumulant of energy for various sizes.

Fig.4.7 shows that the Binder energy cumulant exhibit a minimum at T_c^L for the second phase transition. As expected, the pseudocritical temperature T_c^L depends on superlattice size L such that T_c^L decreases as L increases, an extrapolation of T_c^L as a function of $1/L$ yields the value $T_c^\infty = 42.08$ K.

We observe a second minimum starting from $L = 72$ in a lower temperature, which designates a phase transition. From previous results, it corresponds to

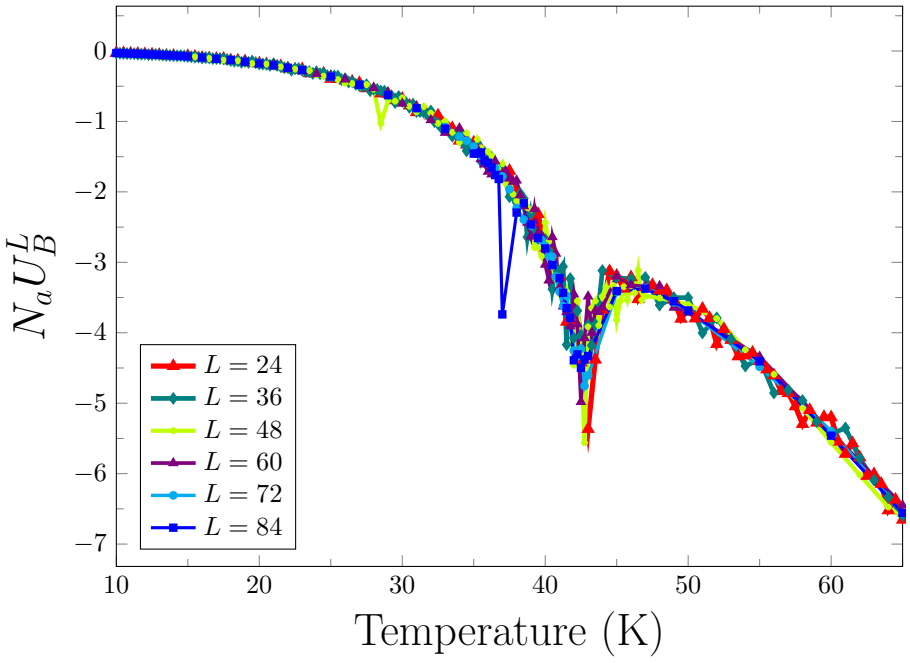

FIGURE 4.7: Temperature evolution of the Binder cumulant of energy multiplied by N_a for $\mathbf{B}_{ext} = 0$ mT

the first-order phase transition driven by critical fluctuation from the fluctuation-disordered phase.

We performed the same analysis for an applied field of 15 mT, where we calculated the energy Binder cumulant $U_B^L|_E$. We find the same behavior, with double minima for $L = 84$, where the minimum toward lower temperature determines the first-order phase transition to the fluctuation-disordered phase.

4.3.4 Second moment correlation length

The second moment correlation length is a measure of the width of the distribution of the distance between pairs of correlated points in the system. It is related to the fluctuations in the system and can provide information about critical phenomena, phase transitions, and other physical properties of the system. To compute the second-moment correlation length in our case, one may measure the Fourier amplitudes of the spin-spin correlation function $G(x, y) = \langle \mathbf{S}(x) \cdot \mathbf{S}(y) \rangle - \langle \mathbf{S}(x) \rangle \cdot \langle \mathbf{S}(y) \rangle$.

$$\tilde{G}(\mathbf{k}) = \sum_{\mathbf{r}} G(\mathbf{r}) e^{-i\mathbf{k}\cdot\mathbf{r}} \tag{4.16}$$

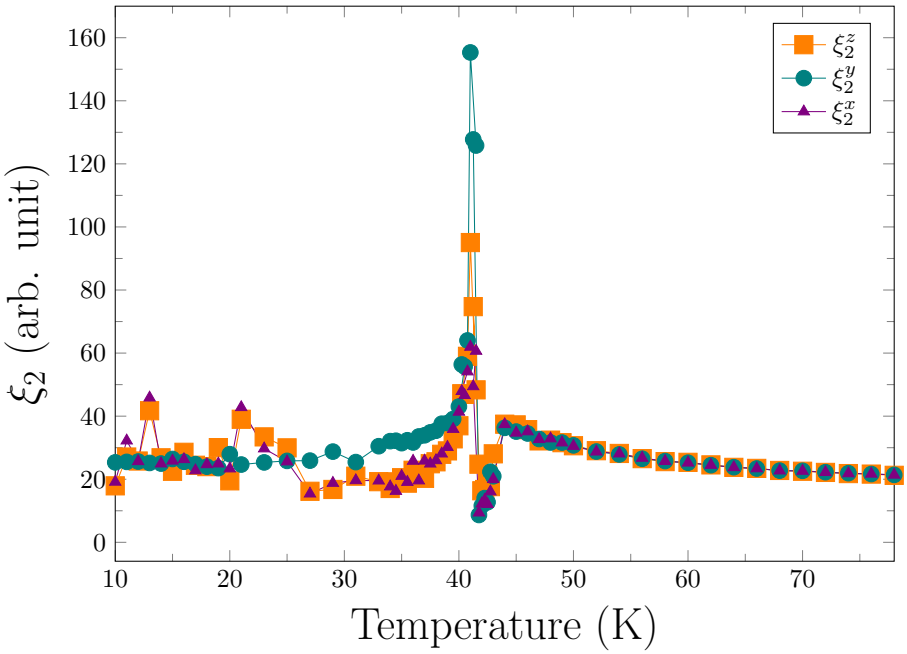

FIGURE 4.8: The second moment correlation length as a function of temperature where we observe a divergence near the second order phase transition, the finite peak of first is eclipsed by the divergence of the second order phase transition

the squared correlation length can be extracted from a linear fit of $G(\mathbf{k})^{-1}$ as a function of $\mathbf{k}^2$. However, one can extract the second-moment correlation length without needing a fit. the simplest expression, using only $\mathbf{k} = 0$ and $\mathbf{k} = 1 = (2\pi/L)(1,0,0)$.

$$\xi_2 = \frac{1}{2\sin(\pi/L)}\sqrt{\frac{\tilde{G}(\mathbf{0})}{\tilde{G}(\mathbf{1})} - 1} \tag{4.17}$$

This quantity, which is comparatively easy to measure in a Monte Carlo simulation, is usually referred to as second-moment correlation length, which is very similar to the (actual) correlation length [149].

Fig.4.8 shows the thermal behavior of the second moment correlation length for zero fields, where we have the divergence at the second order phase transition, with a correlation length double the characteristic size of the supercell. This high value eclipses the finite peak of the first-order phase transition to the helical state. At high temperatures, ξ_2 typically tends to zero, indicating that the field is totally "randomized" at high temperatures, even for very nearby points. Conversely, for very low temperatures, the correlation length is fixed by the characteristic length of the magnetic order (the helical state in our case) [150].

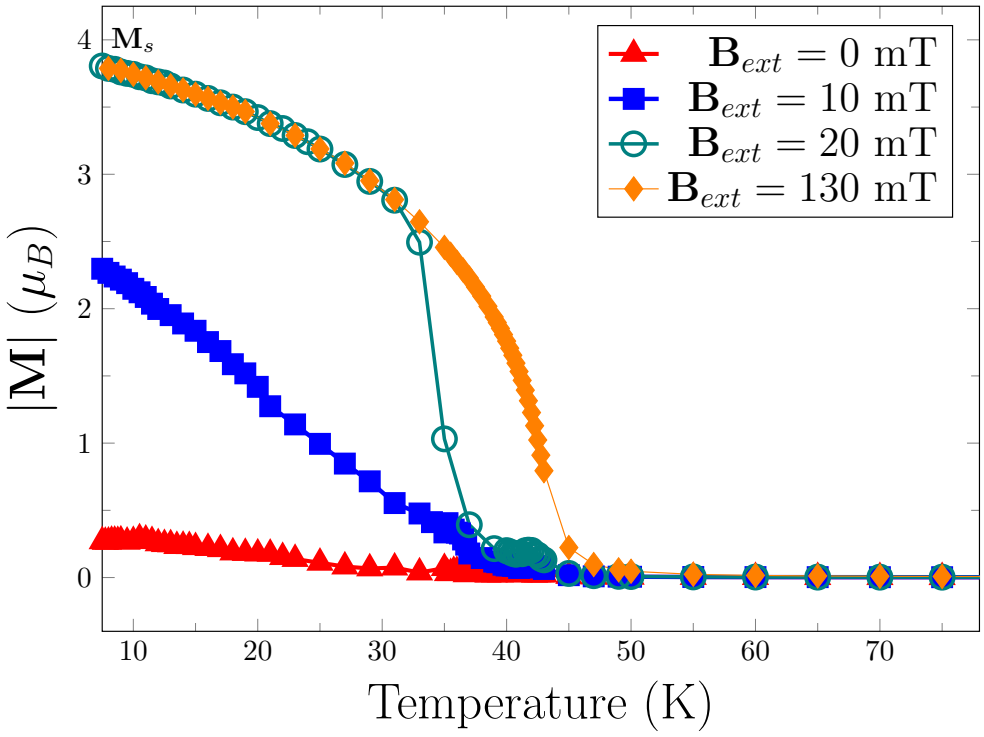

FIGURE 4.9: Temperature evolution of the magnetization, for various field, where we find the zero magnetization (red line) for helical state, the expected saturation value for high fields $|\mathbf{M}_s| = 4\ \mu_B$

4.4 Characterization of magnetic phases

4.4.1 The helical state

In order to probe the characteristics of our system, the expectation value of thermodynamical observables is estimated within the Monte Carlo simulations as simple arithmetic means over the Markov chain or the number of sweeps. In our case, the order parameter is the total magnetization $|\mathbf{M}|$. To compute this quantity, one takes the sum of all the spins in the supercell, divided by the number of units cells, and averages over the sweeps.

$$\langle |\mathbf{M}| \rangle = \frac{1}{L^3} \langle \sum_i \mathbf{S}_i \rangle \tag{4.18}$$

Fig.4.9 shows the evolution of the magnetization as a function of temperature for various magnetic fields. We performed a series of Monte Carlo simulations to study different phases of CSO as a function of temperature and magnetic field. We managed to get other statistical observables, such as the specific heat C_v and

magnetic susceptibility χ_M as a function of temperature for various magnetic fields. Previous experimental results show that the ground state of copper oxide selenite at zero field and low temperature is a spin spiral (helical state).

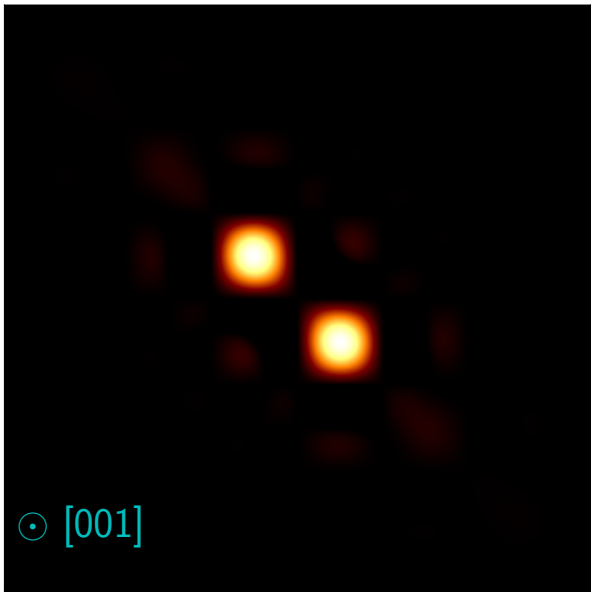

FIGURE 4.10: Logarithm of the square of spin structure factor ($(\log_{10}(|\mathbf{F}|^2)$), where $|\mathbf{F}|^2$ is summed along the [001] direction at 35 K and and zero magnetic field

We calculate the spin structure factor as :

$$\mathcal{S}(\mathbf{Q}) = \frac{1}{N}\sum_{i,j} e^{-i\mathbf{Q}\cdot(\mathbf{R}_i-\mathbf{R}_j)}\langle \mathbf{S}_i \cdot \mathbf{S}_j\rangle \tag{4.19}$$

and we show, using the DFT calculated parameters of the effective Hamiltonian, the existence of a helical state at zero fields characterized with a propagation vector $||\mathbf{q_H}|| = 0.008$ (Å^{-1}) as seen in Fig.4.10, the helical state has a periodicity along $[1\bar{1}0]$ direction [2] with a wavelength $\lambda_H \simeq 78.4$ nm, and is shown to exist in all the temperature range below $T_H \simeq 37.5$ K which delimits the helical phase from fluctuations disordered phase. This value is lower than the critical temperature $T_c \simeq 42.5$ K of the ordered phase to the paramagnetic phase where its experimental value is $T_c^{exp} \simeq 58$ K [151]. The discrepancy between the reported critical temperature and the experimental one is due to the use of the lattice constant of the paramagnetic phase as a lattice parameter in the range of temperatures of the

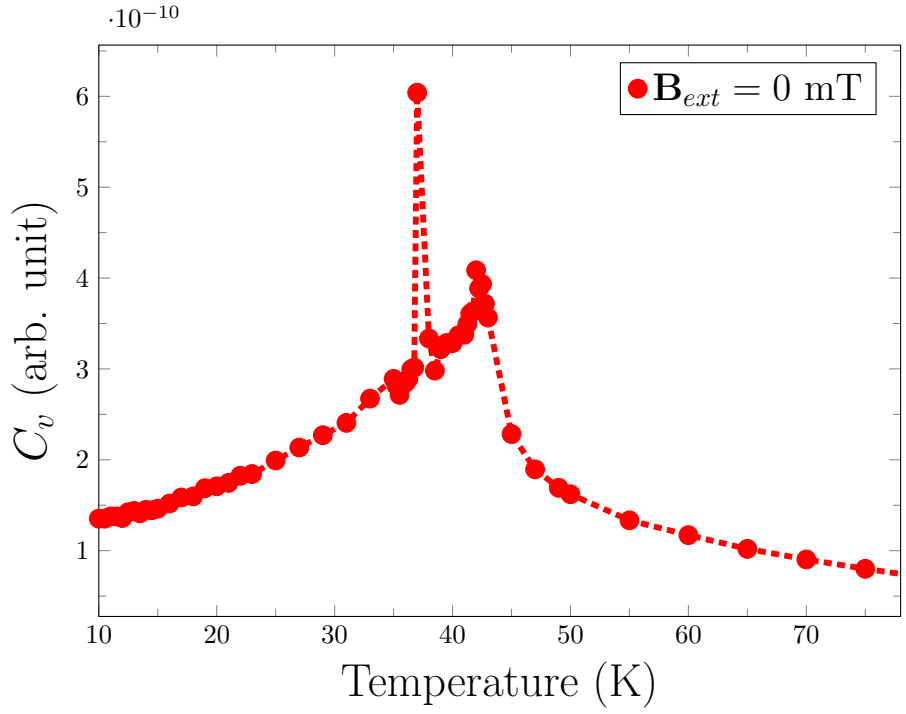

FIGURE 4.11: Heat capacity for zero field, with the head (lower temperature peak) and shoulder (higher temperature peak) characteristic of B20 magnets, with second order phase transition toward high temperature and the low temperature peak is first-order phase transition.

field polarized phase (helical and SkL) which correspond to a 2 GPa applied hydrostatic pressure P on the crystal which affects the magnetic exchange constant and thus T_c according to [152] where P_c is material dependent critical pressure :

$$T_c(P) = T_c(0)(1 - \frac{P}{P_c}) \tag{4.20}$$

We also report that for the heat capacity, we have the same peak and shoulder feature near T_c found in experimental results in MnSi and Cu_2OSeO_3 [153]. Figure 4.11 shows this feature where the shoulder is toward high temperatures. This study is the first one with the *ab-initio* inputs that reproduce this behavior. Belemuk et al. [154] show the same features with Monte Carlo simulation but with artificial inputs for Heisenberg exchange and DMI in the effective magnetic Hamiltonian. The first peak (which is field dependent) around $T_H \simeq 37$ K for zero fields is a characteristic of a first-order phase transition between the fluctuation-disordered regime (FD) and helical state, as was discovered experimentally by

H.C. Chauhan et al. [155]. The second peak (the shoulder) at $T \simeq T_c \sim 42.5$ K delimits the FD region from the uncorrelated paramagnetic region.

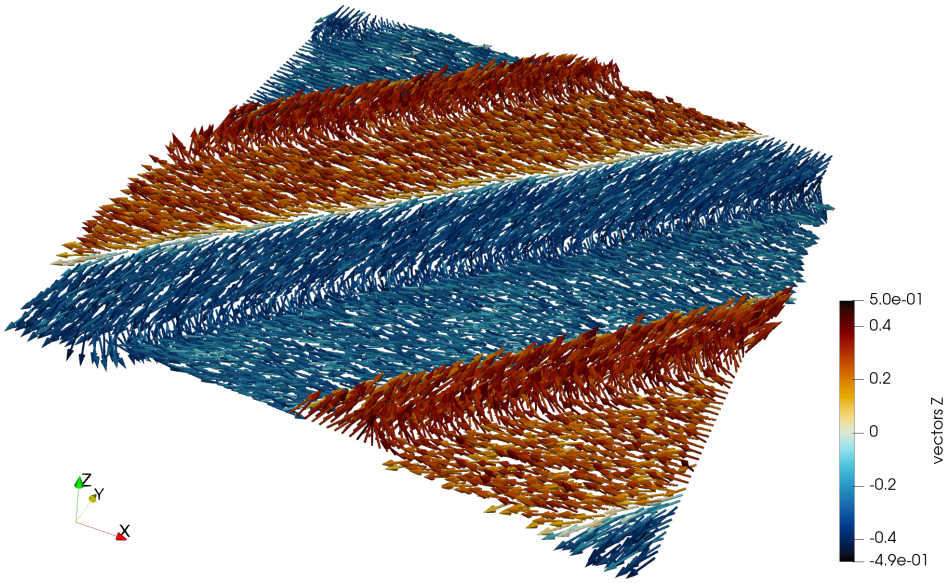

FIGURE 4.12: Real space spin configuration in Cu_2OSeO_3 (001) slice in the helical phase. The z-component and the in-plane orientations of the spins are illustrated by the colorbar and colored arrows

The helical state persists in low magnetic fields and low temperatures. We observe the spin spiral along the (111) direction up to 10 mT, and for all the temperatures under the T_H that delimits the ordered phases from the fluctuations disordered phase, we depict the spatial configuration of the spin spiral in our system as in Fig.4.12.

4.4.2 The skyrmion lattice phase (SkL)

When we apply higher intensity magnetic fields, the helical state develops a $\mathbf{q} = 0$ component and thus changes to the conical state. However, when we get close to the T_H at the border of the fluctuation-disordered regime, magnetization adopts an exotic behavior and shows a peak near T_H as seen in Fig.4.13. In this region, topological defects start to emerge as the skyrmion lattice phase

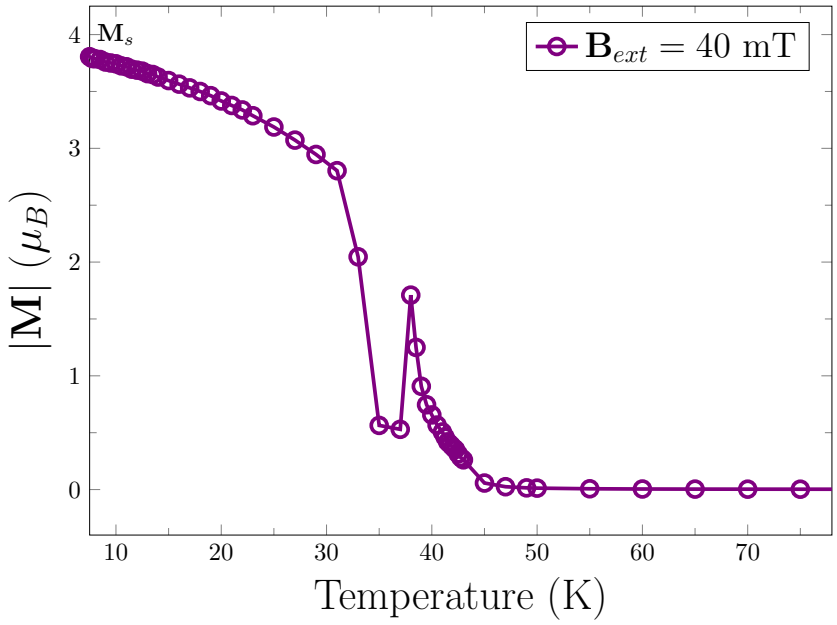

FIGURE 4.13: Temperature evolution of the magnetization, for $\mathbf{B}_{ext} = 40$ mT where we observe an anomaly indicating the existence of an exotic behavior of magnetization around T_H.

is observed for $\mathbf{B}_{ext} = 40$ mT characterized by a six-fold propagation vector pattern depicted in the Fig.4.14. This skyrmion lattice phase exists in a small pocket of magnetic field and temperature, and in our case, the pocket ranges between 25 mT to 40 mT in magnetic fields and temperatures between 34-42 K (where it overlaps with the fluctuation-disordered regime).

The noncollinear sixfold pattern shows the projection of the spin structure factor in this case on the (111) plane, which shows, the six spots corresponding to $\mathbf{q}^{\mathbf{i}}_{\mathbf{SkL}}$ and $-\mathbf{q}^{\mathbf{i}}_{\mathbf{SkL}}$ with $i \in \{1,2,3\}$. These three noncollinear vectors are coplanar since $\det(\mathbf{q}^{\mathbf{1}}_{\mathbf{SkL}}, \mathbf{q}^{\mathbf{2}}_{\mathbf{SkL}}, \mathbf{q}^{\mathbf{3}}_{\mathbf{SkL}}) = 0$, which is a necessary condition for having a skyrmion lattice. This six-fold pattern is the main definition of a skyrmion lattice phase first used by S. Muhlbauer et al. [49] to characterize skyrmion lattice in MnSi. If the three vectors are not coplanar, they will describe a hedgehog lattice phase [156]. Fig.4.15 shows the skyrmions lattice in real space.

It is worth mentioning that the transition from a topologically trivial state, such as the spin spiral phase, is done by surpassing an energy barrier between the two topologically nonequivalent states. In our case, the magnetic field along (111) is the driving power for this transition in the presence of thermal fluctuations.

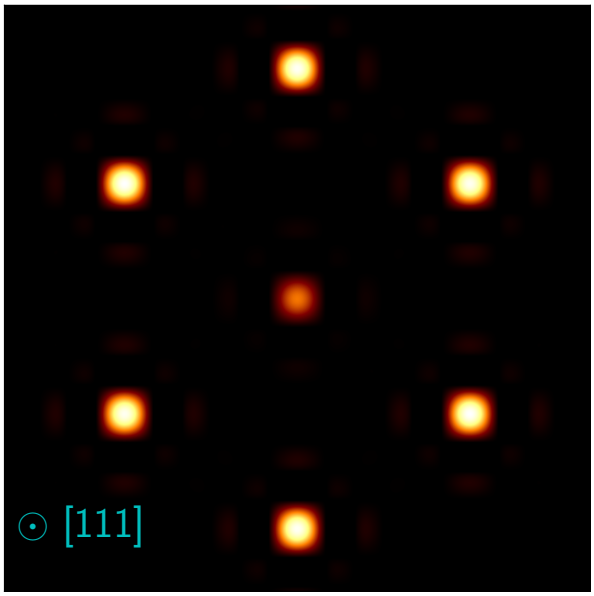

FIGURE 4.14: Logarithm of the square of spin structure factor ($(\log_{10}(|\mathbf{F}|^2)$), where $|\mathbf{F}|^2$ is summed along the [111] direction at 35 K and and 40 mT magnetic field

However, an intermediate state emerges in an even smaller pocket of magnetic field and temperature. A vortex lattice phase appears when we apply an intensity of $\sim$ 15 mT near the fluctuation-disordered regime. This state is characterized by the four-fold pattern of the spin structure factor depicted in Fig.4.16.

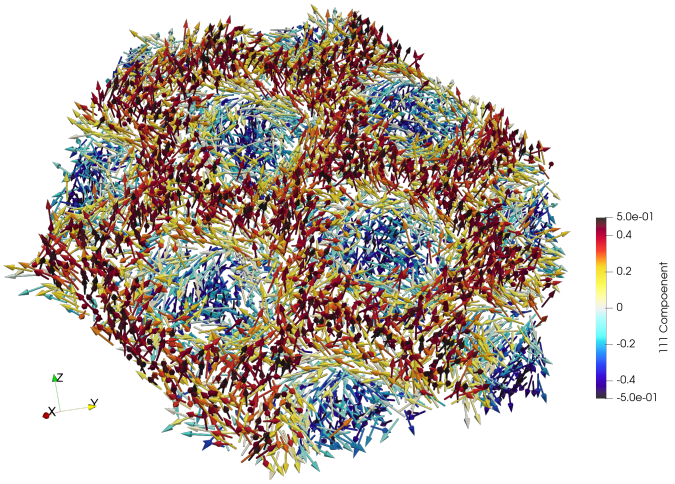

FIGURE 4.15: Real space spin configuration in Cu_2OSeO_3 (111) slice at the 35 K and 40 mT [111] magnetic field, which shows the Skyrmion lattice. The z-component and the in-plane orientations of the spins are illustrated by the colorbar and colored arrows, respectively.

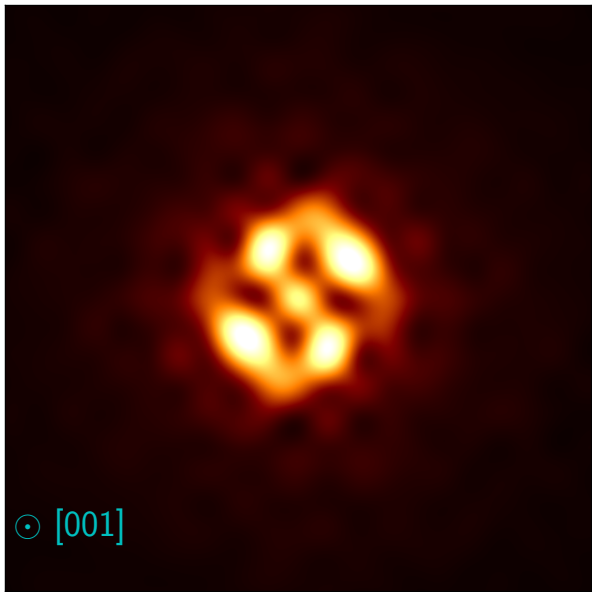

FIGURE 4.16: Logarithm of the square of spin structure factor ($(\log_{10}(|\mathbf{F}|^2)$), where $|\mathbf{F}|^2$ is summed along the [001] direction at 37.5 K and and 15 mT magnetic field showing a four-fold pattern characteristic of a vortex lattice.

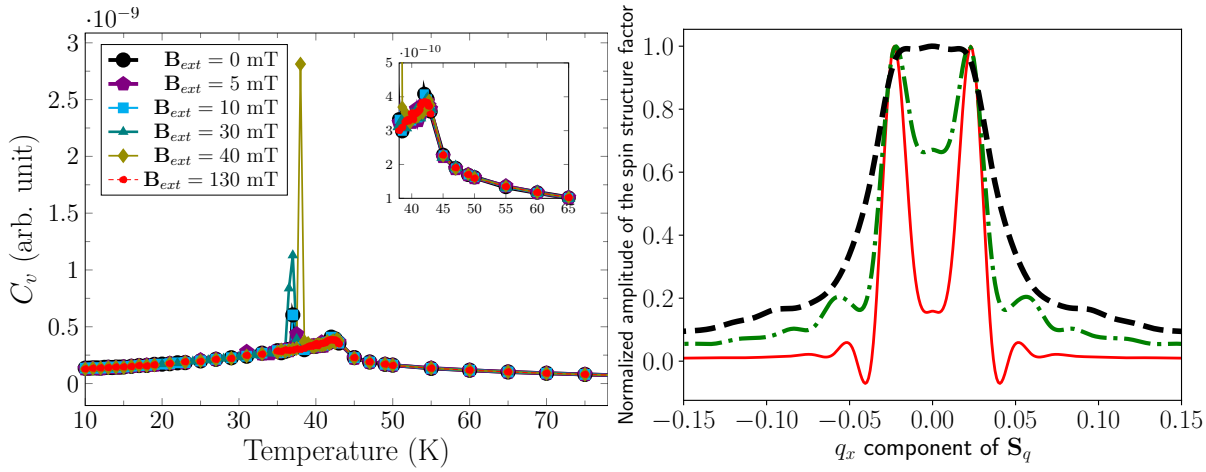

(A) (B)

FIGURE 4.17: (A) : Heat capacity for multiple value of magnetic fields, the second-order phase transition is independent of magnetic whereas the first-order phase transition is field dependent, the window at left corner is a zoom of the second peak (toward higher temperatures). (B) : The distribution of spin Fourier component along $(1\bar{1}0)$ direction across the transition T_H, solid line is $T_H - 0.25$ K, dashed-dotted line is $T_H + 0.25$ K and dashed line is $T_H + 2$ K. The transition from double peak distribution into single peak is a signature of first-order phase transition.

4.5 Phase transition mechanisms

In order to understand the origin of the head and shoulder peaks signature of chiral magnets as depicted in Fig.4.11, we analyze the heat capacity for several applied fields. As mentioned before, the first peak is facing low temperatures and is found around $T_H \simeq 37$ K for zero fields, which is also a characteristic of a first-order phase transition between the fluctuation-disordered regime (FD) and helical state, as was discovered experimentally by H.C. Chauhan et al. [155]. We also observe that this peak is field-dependent. In Fig.4.17.(A), we see a non-linear dependency of T_H on the applied field as the peak changes its temperature depending on the applied magnetic field. The second peak (the shoulder) at $T \simeq T_c \sim 42.5$ K delimits the FD region from the uncorrelated paramagnetic region. Janoscheck et al. [157] showed that the phase transition in a helimagnet

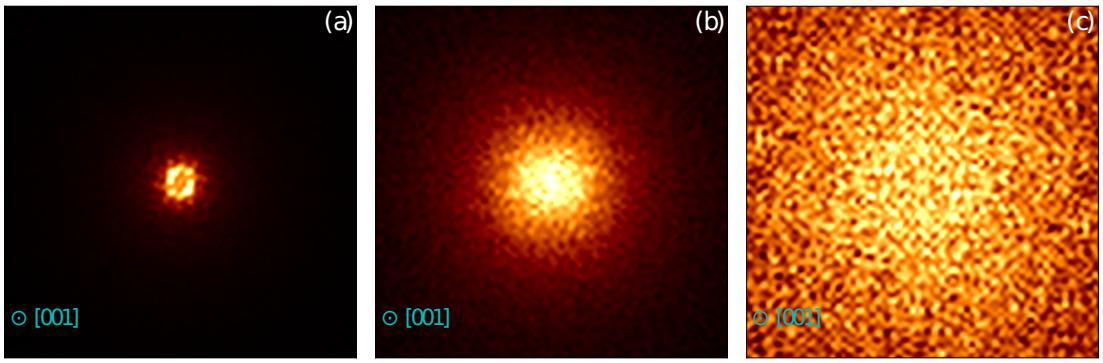

FIGURE 4.18: Evolution of the spin structure factor in the first Brillouin zone (BZ) above T_c at zero field: (a) at T_c+0.5 K. It shows isotropic chiral strongly interacting fluctuations; (b) the spreading of propagation vector on a sphere at T_c+3 K, indicating strongly interacting fluctuations, (c) at $T \gg T_c$ exhibiting ferromagnetic fluctuation behavior where the fluctuations spectrum spreads over the whole BZ

of the B20 family (MnSi) displays a fluctuation-induced first-order phase transition that follows a Brazovskii mechanism[1] [158]. To explore the induced first-order phase transition mechanism, we calculated the inverse of correlation length $\kappa = \frac{2\pi}{\xi}$ for temperatures above T_H. There are several scenarios if the inverse Ginzburg length of the system κ_G satisfies the condition $\kappa_G < \kappa_{DM}$ for $T > T_H$, where $\kappa_{DM} = ||\mathbf{q}_H||$, the system undergoes a first-order transition that follows a Brazovskii mechanism. In this mechanism, the strongly interacting fluctuations suppress the mean-field transition temperature T_{MF}. On the other hand, if $\kappa_G > \kappa_{DM}$, the mechanism governing the induced phase transition can be described within the Wilson-Fisher renormalization group [159]. The latter mechanism is what governs the induced transition in Cu_2OSeO_3, as previously confirmed by Živković et al. [160]. The fit of the magnetic susceptibility with the Brazovskii Eq. (4.21) [157], where $\eta = \frac{\kappa_{Gi}}{\kappa_{DM}}$ give a value of $\eta > 1$ which means that in our system $\kappa_G > \kappa_{DM}$.

$$\chi_{|T>T_c} = \frac{\chi_0}{1+\eta^2\mathcal{Z}(T)} \qquad \mathcal{Z}(T) = \frac{[\tau + (1-\tau^3+\sqrt{1-2\tau^3})^{1/3}]^2}{2^{1/3}[1-\tau^3+\sqrt{1-2\tau^3}]^{1/3}} \qquad \tau = \frac{T-T_{MF}}{T_0} \tag{4.21}$$

Far from the transition, $T \gg T_c$, the fluctuations have a mean-field ferromagnet-

[1] When the fluctuations in the order parameter have a particular spatial frequency, then they can become amplified and grow to form a periodic pattern. This happens because the fluctuations can interact with each other in a way that reinforces the periodicity.

like behavior as seen in Fig. (4.18c). As the temperature approaches T_c from high temperatures, $\kappa < \kappa_G$, we enter the strongly-interacting fluctuations regime that suppresses the transition temperature before the fluctuations interactions acquire an isotropic chiral behavior. This behavior can be seen from spreading propagation vectors in **q**-space on a sphere as seen in Figs. (4.18a), (4.18b). In this region, the inverse correlation length satisfies $\kappa \lesssim \kappa_{DM}$. However, these results remain indecisive since it relies on fitting the magnetic susceptibility with the Brazovskii equation to get the parameter η. Further study is required to directly extract the Ginzburg and correlation lengths to understand the mechanism that induces the first-order phase transition fully.

The region between the helimagnetic and paramagnetic transitions (between the first-order and second-order transition, $T_H < T < T_c$) is denoted as the fluctuation-disordered phase. To explore the nature of this phase, we study the evolution of the norm of the propagation vector as a function of temperature in the region $T_H < T < T_c$. We observe that the propagation vector related to the helical state is increasing in the norm, which indicates that the helical state periodicity is getting smaller to adapt to the supercell size, which in turn shows that the FD is an incommensurate phase. As the temperature increases, we observe a spread over the Brillouin zone until we get a sphere-like shape as in Fig. (4.18a). The existence of an incommensurate phase along the FD phase, encapsulated by the commensurate phase (ferrimagnetic phase) and paramagnetic phase, indicates the presence of a Lifshitz point (LP)[2] [161] at the border of these three phases.

4.6 The spiral spin liquid phase

The spiral spin liquid (SSL) phase is a type of classical spin liquids realized in many systems, in honeycomb lattices as in $FeCl_3$ [42], in systems where spins form a diamond lattice as in $MnSc_2S_4$ [162], $CoAl_2O_4$ [163], and other systems as the frustrated antiferromagnetic pyrochlore $MgCr_2O_4$ [164]. The spiral spin liquid is a state where spin fluctuates as a spiral, resulting from the infinite degeneracy of spin spirals that manifest as the continuous ring or 2D surface (sphere) of propagation vectors. Each vector on the ring or the sphere has the same energy;

[2] A tricritical point at which the free energy of the commensurate phase, the disordered phase, and the free energy of the modulated (incommensurate) phase are equal. At this point, the system undergoes a second-order phase transition from the disordered phase to the ordered phase, with the modulated phase acting as an intermediate state.

in general, magnetic field or anisotropy lifts this degeneracy by selecting a certain $\mathbf{q}$ on this ring as the propagation vector of the helical state or as the sixfold pattern of skyrmion lattice state as seen in Cu_2OSeO_3 [2]. In the case of very small or no anisotropy, all the helical states on the sphere or ring are degenerate and thermal fluctuations cause the spins to fluctuate from one spin spiral state to another, creating the SSL state. Another type of classical spin liquids is skyrmion liquids, which correspond to the continuous ring in reciprocal space that emerges from the six-fold pattern signature of skyrmion lattice phase as found in Cu_2OSeO_3 under varying applied magnetic field [165].

A significant quantity is the spin structure factor (magnetic structure factor), which can be detected experimentally with neutron diffraction. The spin structure factor provides an essential characterization of the physical properties of the classical ground-state degenerate manifold (spiral ring). We show that the ground state for Cu_2OSeO_3 is compatible with previous experimental studies [151] where we find a helical state characterized by a two-fold pattern with propagation vector $(\mathbf{q}_h, -\mathbf{q}_h)$, henceforth making the spin spiral along $(1\bar{1}0)$ the configuration that minimizes the total energy. However, as we get close to the transition from the helical state to the fluctuation-disordered regime, thermal spin fluctuations have strong interaction, changing the state from a two-fold pattern into a ring-like pattern called the spiral ring, which characterizes the spin liquid phase. We emphasize that this spiral spin liquid phase exists in the FD region. Fig.(4.19) shows the spin structure factor of Cu_2OSeO_3 for a magnetic field of 5 mT and temperature of 42 K, which reside inside the fluctuation-disordered regime. Another signature of the spin spiral phase is the unusual double peak feature in specific heat C_v. This double peak feature is found in other spin liquid candidates α-$RuCl_3$ [166]. Fig.(4.17.A) shows the double peak feature of the specific heat in Cu_2OSeO_3, where we have a sharp peak at low temperature representing the transition from the magnetically ordered state (helical) to FD, and then a broad peak facing higher temperature, which in case of Kitaev model spin liquid, is related to spin fractionalization. Nonetheless, our generalized Heisenberg model treats spin in a classical manner, and the spiral spin liquid, in our case, is just a subcategory of classical spin liquids. The SSL phase arises from the strong interacting thermal spin fluctuations between the double peaks. The energy scale of DMI, which lifts the degeneracy between all the helical states on the spiral ring,

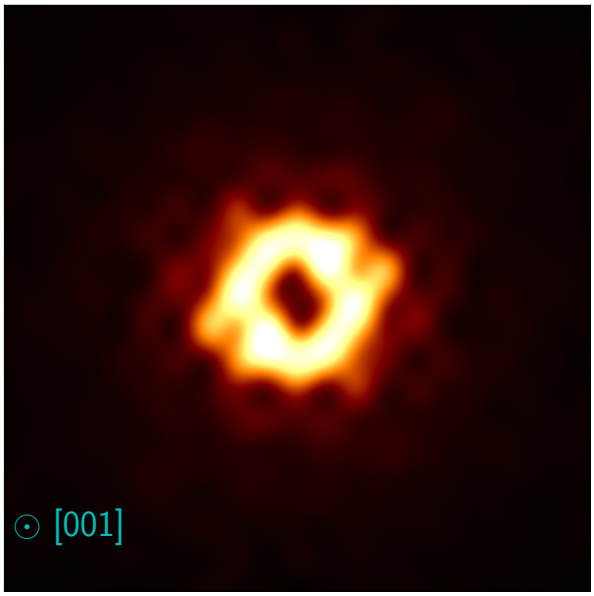

FIGURE 4.19: Spin structure factor of Cu_2OSeO_3 summed along (001) direction over all Brillouin zone at 42 K slightly under T_c and 5 mT showing ring like shape characteristic of spiral spin liquids

is not enough in this region to maintain the spiral in the direction the DM vector imposes. However, the thermal fluctuations are not strong enough to create an uncorrelated paramagnetic state, thus making the correlated spiral spin liquid. We emphasize that in contrast to the spiral spin liquids and quantum spin liquids found in other materials where the origin is the geometric frustration or the competition between ferromagnetic and antiferromagnetic Heisenberg exchange, the origin of the spiral spin liquid in Cu_2OSeO_3 might be related to the existence of competition between the ferromagnetic and antiferromagnetic interactions, and the presence of a strong DMI.

4.7 Phase diagram

To understand the mechanism of creating the SkL, we performed a series of low magnetic field calculations, leading to the magnetic field-temperature phase diagram shown in Fig. 4.20. As predicted by the present scheme, seven phases exist within this range; five are well known, namely the helical, conical, SkL, paramagnetic, and ferrimagnetic (field polarized) phases. Moreover, we have two other phases. The first of them is between the helical phase and the SkL (at 15 mT), where a double non-collinear **q** pattern is created, indicating the existence of an

intermediate vortex lattice (half-skyrmions or merons). This prediction is yet to be confirmed experimentally. The last phase previously mentioned, where there is a dominance of fluctuations, is the fluctuation-disordered regime. The phase diagram shows a tricritical point at the crossing between the conical, FD phase, and ferrimagnetic phase, as previously shown experimentally [155].

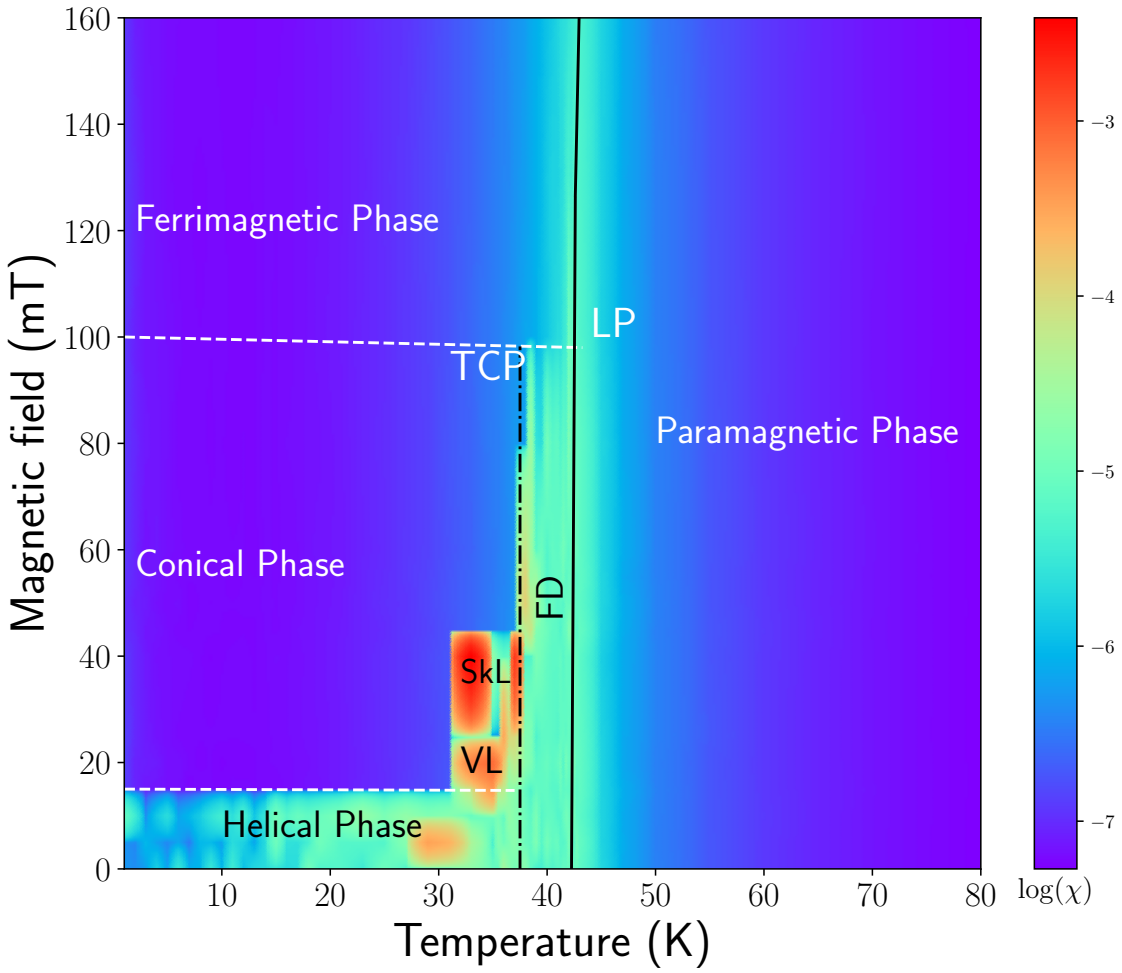

FIGURE 4.20: Phase diagram of various magnetic orders in Cu_2OSeO_3 : SkL : Skyrmion lattice , VL : vortex lattice, FD : Fluctuation disordered , TCP : Tricritical point , LP : Lifshitz point, solid line is the second-order phase transition, the dashed-dotted black line refers to the field dependent first-order phase transition with T_H varying non-linearly between (37K to 38 K) and white dashed lines are continuous transitions

The vortex lattice phase exists in a tiny pocket near T_H and between $\mathbf{B}_{ext}$ of stable helical phase and stable SkL and has never been suggested as a possible ground

state of Cu_2OSeO_3. The existence of the vortex lattice phase implies that the transition from helical state to SkL undergoes a step-by-step transition in terms of the topological invariant by passing from the topologically trivial single **q** state to double **q** state characterized with a half-integer invariant to triple **q** state with an integer invariant [167].

Chapter 5

Topological properties of spin textures

Topological defects are localized excitations that overcome their finite creation energy associated with the large configurational entropy they carry. They induce phase transitions in two-dimensional systems, including the superfluid transition in thin ^{4}He films, the superconducting transition in thin metallic films, and the melting transition in two dimensions. Depending on the models and dimensionality, they appear as points, lines, surfaces, etc...

5.1 2D solitons in Cu_2OSeO_3 : Skyrmions and Vortices

Following the approach by Berg and Luscher [69, 168], we define the skyrmion number in the case of lattice systems. For a plane of four spins, the topological charge is given by the sum over the ensemble of oriented triangles Δ_{ijk}. We calculate first the local charge q_Δ of the triangle Δ_{ijk} with respect the orientation chosen as :

$$q_\Delta = 2 \arctan \left(\frac{\mathbf{s_i} \cdot (\mathbf{s_j} \times \mathbf{s_k})}{1 + \mathbf{s_i} \cdot \mathbf{s_j} + \mathbf{s_j} \cdot \mathbf{s_k} + \mathbf{s_k} \cdot \mathbf{s_i}} \right) \tag{5.1}$$

The local charge is invariant under cyclic permutation of the indices ijk. The skyrmion number can be extracted from the local charge by summing on the whole space (in the case of 2D solitons as skyrmions (depicted in Fig.5.1) and vortices, we sum over the 2D surface), and the lattice-based formula for the skyrmion

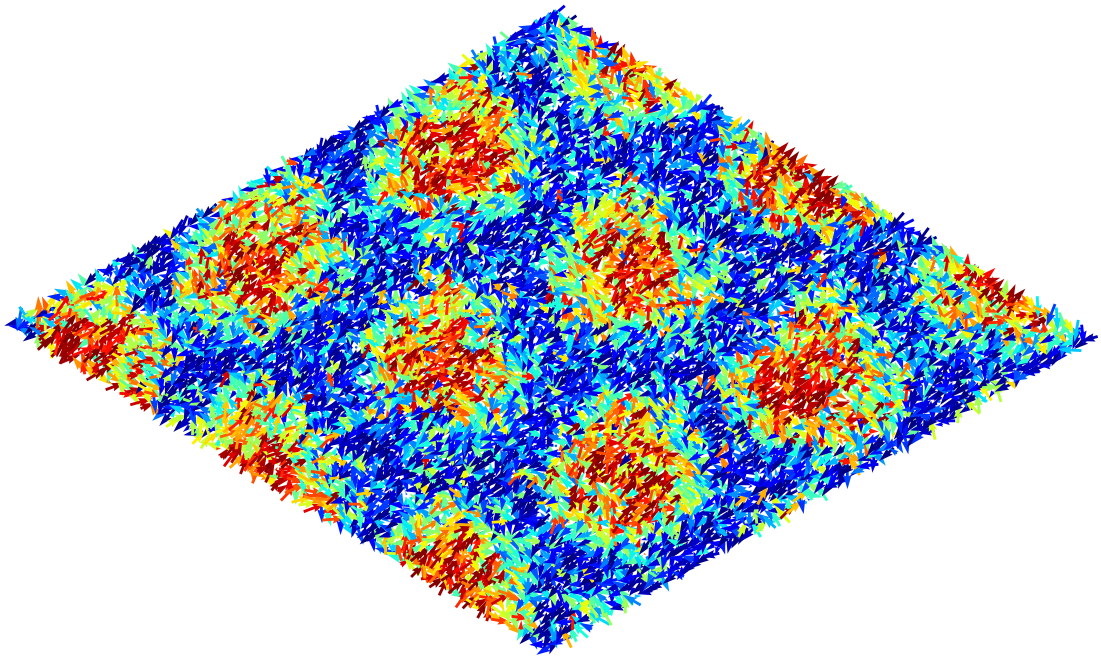

FIGURE 5.1: Skyrmion lattice phase on the (111) plane where the skyrmions are arranged in a hexagonal lattice. Spin up in blue, spin down in red, and the in-plane spin in green.

number is:

$$\mathcal{Q}_{sk} = \frac{1}{4\pi} \sum_{\Delta=\langle ijk \rangle} q_{\Delta} \tag{5.2}$$

We start by analyzing the topological skyrmion number for the zero-field case, where we have a helical state at lower temperatures and then a transition to the FD phase. As expected, the spiral state is a trivial one characterized by $\langle \mathcal{Q}_{sk} \rangle = 0$. As we enter the fluctuation-disordered regime, the strong fluctuations of spins make the skyrmion number fluctuate around the trivial state. This means the DMI itself does not create the net topological charge, and it needs the magnetic field to break the symmetry, in agreement with the work of Hou et al. [169]. Fig.5.2 shows the temperature evolution of the skyrmion number for the helical ground state where it remains zero. However, as for the skyrmion lattice phase, when we apply a 40 mT magnetic field, the topological charge increases steeply at a specific temperature and then decreases smoothly again. This behavior is previously found in ultra-thin films of Pd/Fe/Ir(111) [170].

Fig.5.1 shows the spatial arrangement, where the skyrmion lattice has a hexagonal structure. To understand why in Cu_2OSeO_3 the skyrmion are arranged in

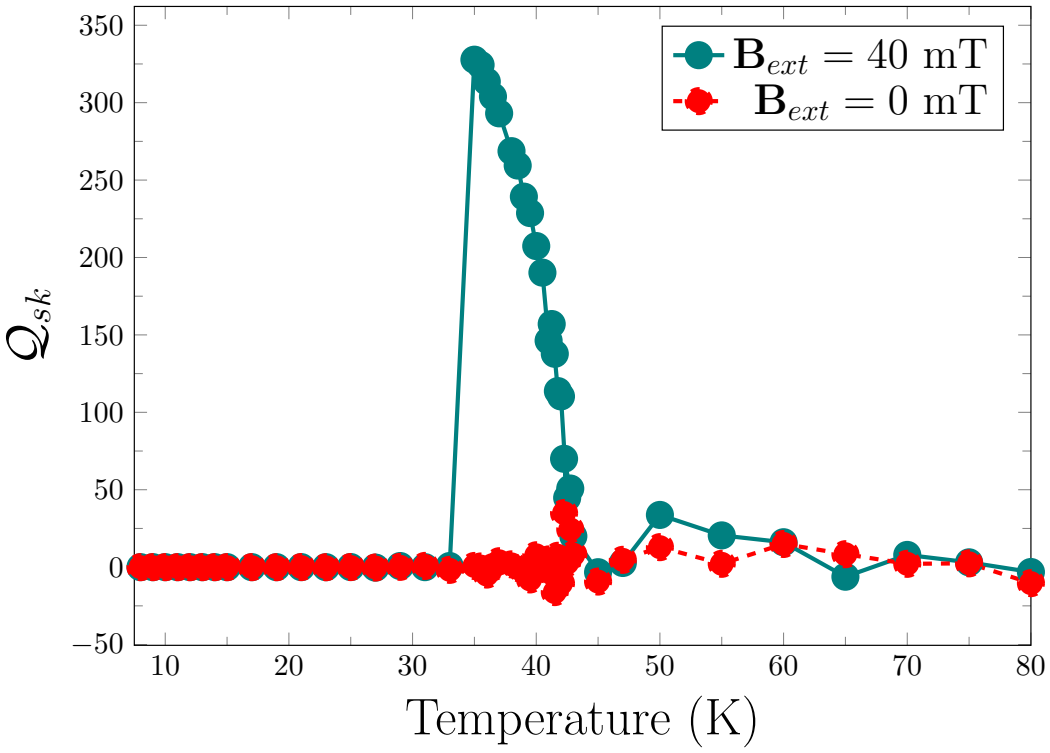

FIGURE 5.2: Temperature evolution of the skyrmion number of the helical state ($\mathbf{B}_{ext} = 0$) and skyrmion lattice phase ($\mathbf{B}_{ext} = 40$ mT) .

such a way, we studied the behavior of another topological defect, the hedgehogs/antihedgehogs pairs. We study the interaction between those defects in a two-types particles gas model that we will show in the next section.

5.2 3D point defects in Cu_2OSeO_3 : hedgehogs and antihedgehogs

5.2.1 Topological characterization of point defects

Topological defects carry an integer topological charge which indicates how often one meets all possible orientations of the vector field while moving along an oriented closed surface enclosing the defect core [171]. We use the same previous Berg and Luscher procedure to extract the topological charge, with a slight modification. We use the method of Motrunich and Vishwanath [172], where we define the monopole number (hedgehog or antihedgehog) in each unit cell inside the supercell by defining a gauge potential $\mathcal{A}_{ij}$ between any pair of neighboring

spins with orientations $\mathbf{s}_i, \mathbf{s}_j$. This gauge potential is defined by introducing an arbitrary reference vector $\mathbf{s}_\star$ forming the spherical triangle $(\mathbf{s}_i, \mathbf{s}_j, \mathbf{s}_\star)$. The edges of this spherical triangle are segments of circles[1], and we denote the solid angle subtended by this spherical triangle by $\Omega[\mathbf{s}_i, \mathbf{s}_j, \mathbf{s}_\star]$ then the formula for $\mathcal{A}_{ij}$ is written as :

$$e^{\frac{i\Omega}{2}} = e^{i\mathcal{A}_{ij}} = \frac{1 + \mathbf{s_i} \cdot \mathbf{s_j} + \mathbf{s_j} \cdot \mathbf{s}_\star + \mathbf{s}_\star \cdot \mathbf{s_i} + i\mathbf{s_i} \cdot (\mathbf{s_j} \times \mathbf{s}_\star)}{\sqrt{2(1 + \mathbf{s_i} \cdot \mathbf{s_j} + \mathbf{s_j} \cdot \mathbf{s}_\star + \mathbf{s}_\star \cdot \mathbf{s_i})}} \tag{5.3}$$

The choice of the $\mathbf{s}_\star$ is arbitrary, and any choice $\mathbf{s}_\spadesuit$ with respect to $\mathbf{s}_\star$ accounts for a gauge transformation. If $\mathcal{A}_{ij} = \mathcal{A}_{ij} + \theta_i - \theta_j$ where $\theta_i = \Omega[\mathbf{s}_i, \mathbf{s}_\spadesuit, \mathbf{s}_\star]/2$, thus gauge invariant quantities are independent of the choice of the reference vector. We define then a flux $\mathsf{F}_\square$ on every face bounded by the sites (i, j, k, l)

$$\mathsf{F}_\square = (\mathcal{A}_{ij} + \mathcal{A}_{jk} + \mathcal{A}_{kl} + \mathcal{A}_{li}) \qquad \mathsf{F}_\square \in (-\pi, \pi] \tag{5.4}$$

The flux $\mathsf{F}_\square$ is gauge invariant, and henceforth it is independent of the choice of the reference unit vector $\mathbf{s}_\star$. The hedgehog/antihedgehog topological charge $\mathcal{Q}_\pm$ enclosed by the unit cube (i, j, k, l, m, n, o, p) containing six square corresponds to the flux out of the volume made by the six squares.(i, j, k, l) (l, m, n, o) (i, j, m, n) ... which can be written as follow:

$$\mathcal{Q}_\pm = \frac{1}{2\pi} \sum_{\square=1}^{6} \mathsf{F}_\square \tag{5.5}$$

This charge is guaranteed to be an integer from the previous definitions. Moreover, this definition ensures that the net topological charge (the supercell sum of topological charges associated with unit cells) always equals zero in the considered system with periodic boundary conditions. The flux over a triangular face is related to spin chirality (or helicity) mentioned in the previous section, where $\sin(\mathsf{F}_\Delta) \sim \mathbf{s_i} \cdot (\mathbf{s_j} \times \mathbf{s_k})$.

5.2.2 Density of hedgehogs

Let us now define the density $\mathsf{n}_\pm$ of topological point defects as the ratio of cells containing hedgehogs or antihedgehog to the supercell volume L^3 with $L = 84$.

[1] Any line on the 2-sphere is a segment of a certain circle

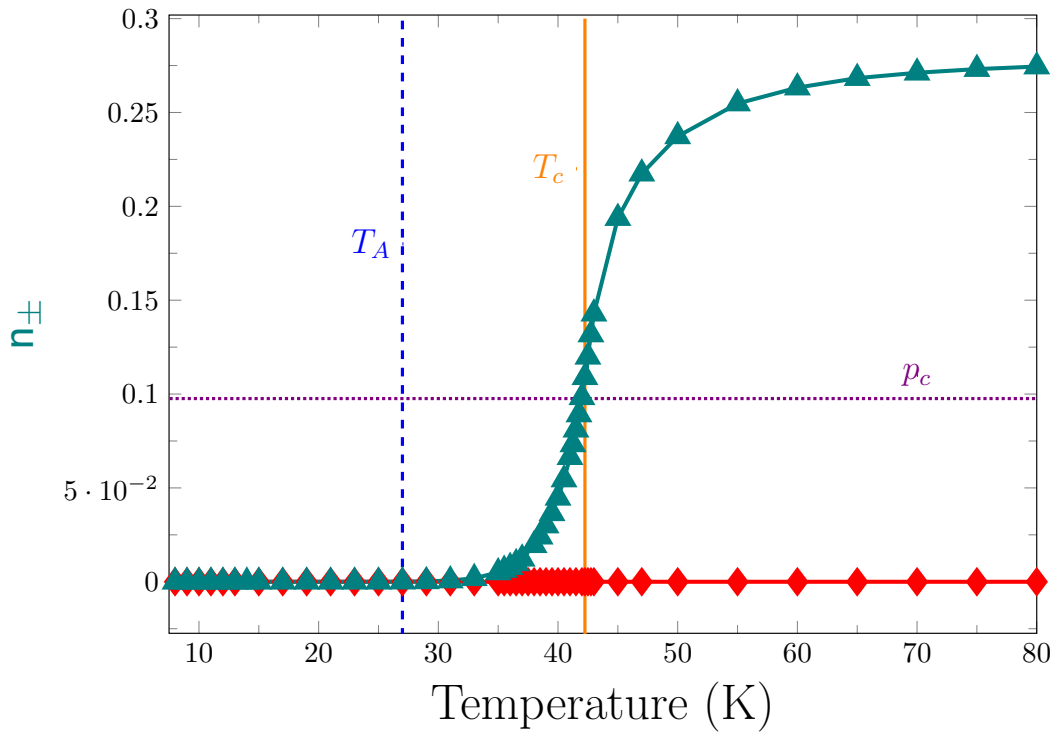

FIGURE 5.3: Temperature evolution of topological point defects density at zero field. The red line is the total charge density .

Fig.5.3 shows the thermal evolution of the density of hedgehog/antihedgehog pairs. We observe that the pairs of hedgehogs-antihedgehogs have a plateau at high temperatures where we have the maximum density. As the temperature is decreased, $n_\pm$ is reduced, and once we get near T_c, we observe a rapid decrease. However, the density of pairs remains positive even below T_c till a specific temperature $T_A < T_c$, where the density of pairs gets canceled. It is striking to realize that this critical temperature is exactly the inflection temperature of hedgehogs' density, which coincides with the site-percolation threshold of a Rubik's cube neighborhood[2] p_c at the same inflection point. This behavior is previously found in relaxor ferroelectric PSN and PZT systems [88] and Heisenberg ferromagnets [85, 86]. The nonvanishing value of hedgehogs density under T_c indicates the coexistence of hedgehogs/antihedgehogs pair alongside the skyrmion lattice phase in the case of an applied 40 mT magnetic field. The site percolation threshold $p_c = 0.0976$ is the one of a regular lattice with a neighborhood extending to the third-nearest neighbors (Rubik cube-like) [173], this threshold can be seen as the critical probability above which we have the appearance of a single cluster of

[2]Cubic configuration with 26 neighbors (shared face, edge and corner)

topological defects spanning through the whole supercell "infinite cluster"[3]. This means that if the density of hedgehog/antihedgehog pairs $n_{\pm} > p_c$, the appearance of long-range spin configuration is hindered by the "infinite cluster" of topological defects.

Interestingly, since the total topological charge is constrained to be zero in systems with periodic boundaries conditions, the decrease of $n_{\pm}$ upon cooling can only happen by annihilation among defects of opposite topological charge, i.e., between hedgehogs with charge $\mathcal{Q}_+$ and antihedgehogs with charge $\mathcal{Q}_-$. Thus, it is interesting to inquire into the dynamical nature of topological singularities and their annihilation. For the temperature dependence of $n_{\pm}$ in Fig.5.3, we find that for $T > T_A$, the density can be very well approximated by:

$$n_{\pm} = n_{\pm}^0 + (n_{\pm}^{\infty} - n_{\pm}^0) \exp\left(-\frac{A}{T - T_A}\right) \tag{5.6}$$

This lead to the Vogel-Fulcher-Tammann law-like equation for relaxation time τ associated with the annihilation process between hedgehogs and antihedgehogs $\tau \sim \tau_0 \exp\left(\frac{A}{T-T_A}\right)$ [174]. In this context, the relaxation time becomes very large as the temperature is lowered, indicating that the dynamics of the annihilation process between hedgehogs and antihedgehogs become extremely slow.

5.2.3 Binding-Unbinding mechanism

An important question pertaining to the role of topological defects is whether the observed proliferation of defects as T increases is accompanied by the unbinding of defect pairs. For that, we calculated the number of total bonds as a function of temperature and the bond at the minimal distance as a function of temperature. It is thus essential to develop criteria by which one may determine whether a given system is in a bound or unbound hedgehog state. The ratio of bonds at the minimum distance over the total bounds will explain the biding-unbinding mechanism of hedgehogs/antihedgehogs pairs occurring in Cu_2OSeO_3. A decreasing ratio as increasing temperatures means the pairs tend to unbind, tending to a plasma-like state of hedgehogs and antihedgehogs.

Fig.5.4 shows the evolution of the ratio of the bounds at a minimum distance, revealing the proportion of bounded pairs. The sudden decrease is the signature

[3] A connected cluster of point defects that extends from one end of the supercell to the other.

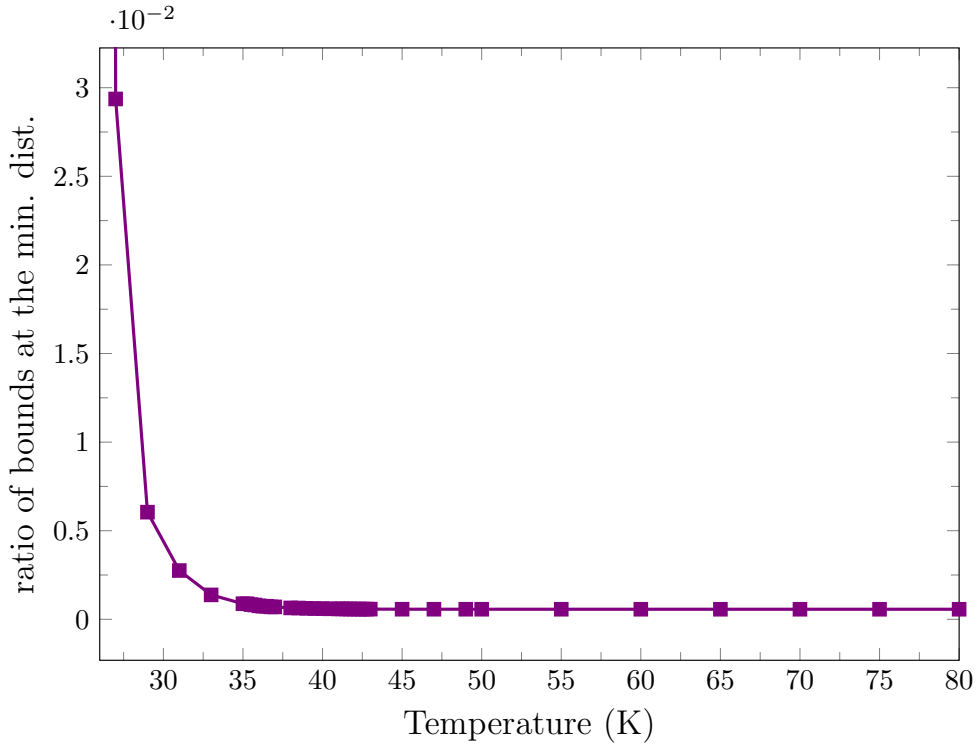

FIGURE 5.4: Temperature evolution of ratio of bound at minimum distance with respect to total number of bounds

of unbinding of the hedgehog/antihedgehog pairs. This dissociation of pairs of oppositely charged topological defects, depicted in Fig.5.5 and seen in the profile of pairwise potential (mean-force potential between defects) in Fig.5.6 with a changing nature from attractive to repulsive, induces empowered distortions in the spin field, progressively destroying the helical ground-state order before T_c, and creates the fluctuation disordered state previously mentioned in the last chapter.

5.2.4 Hedgehogs clusters and fractal dimension

As the temperature is lowered, the mobility of hedgehogs is associated with a decrease in their density. Hedgehogs hence evolve in a smooth background, whose volume can be obtained from the ratio of topologically free cells (with vanishing charge) over the total number of cells 84^3. This background is denominated by free volume, and since it is defined as complementary to the density of topological defects, it is merely indicative of the maximal potentially ordered volume. We

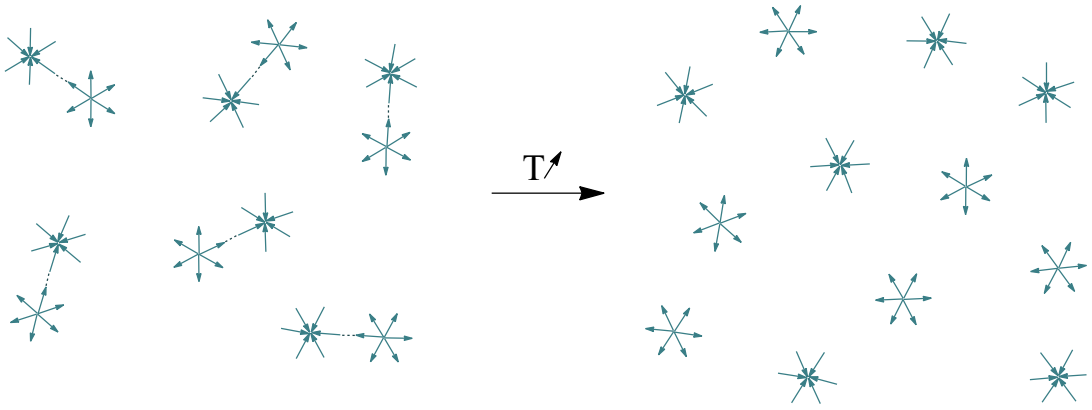

FIGURE 5.5: Two-dimensional schematic representation of the unbinding mechanism of hedgehog/antihedgehog pairs with increasing temperature. While at low temperatures, pairs of oppositely charged defects are bound yielding a phase akin to a gas of (hedgehog/antihedgehog) dipoles, the higher temperature phase constitutes a plasma of unbound hedgehogs. Adapted from [175]

also used clustering algorithms to study the number of clusters of hedgehogs/antihedgehogs as a function of temperature. Using the K-means clustering method, we explore the evolution of point defect clusters. We also compute the radial distribution function $g(r)$, and from it, we extract the mean-force potential between defects $W(r) = -k_B T \ln(g(r))$, thus for high temperatures hedgehogs repel each other, they tend to stay away from each other, so their excluded volumes do not overlap. Hedgehogs cannot easily be close to each other lest they overlap the nearest hedgehogs already present there. As the temperature decreases, the pairwise potential W becomes slightly attractive. This is the short-range and rather weak entropic depletion attraction. Clusters start to form. The radial distribution function obtained at these temperatures significantly differs from that obtained at $T \geq 60$ K, implying that hedgehogs' behavior (as individual particles) is also very different. At this density of hedgehogs, the depletion forces can be described by the depletion model of Asakura and Oosawa [176, 177], which predicts a monotonically attractive potential. As we get close to T_c from high temperatures, hedgehogs become more structured and form multiscale complexes of various degrees of connectivity. As we enter the temperature range below T_c, we enter the sub-percolation regime, and hedgehogs form separated structured clusters that look like a diffusion-limited aggregation. The pairwise potential becomes even more attractive as we lower temperatures and get closer to activation

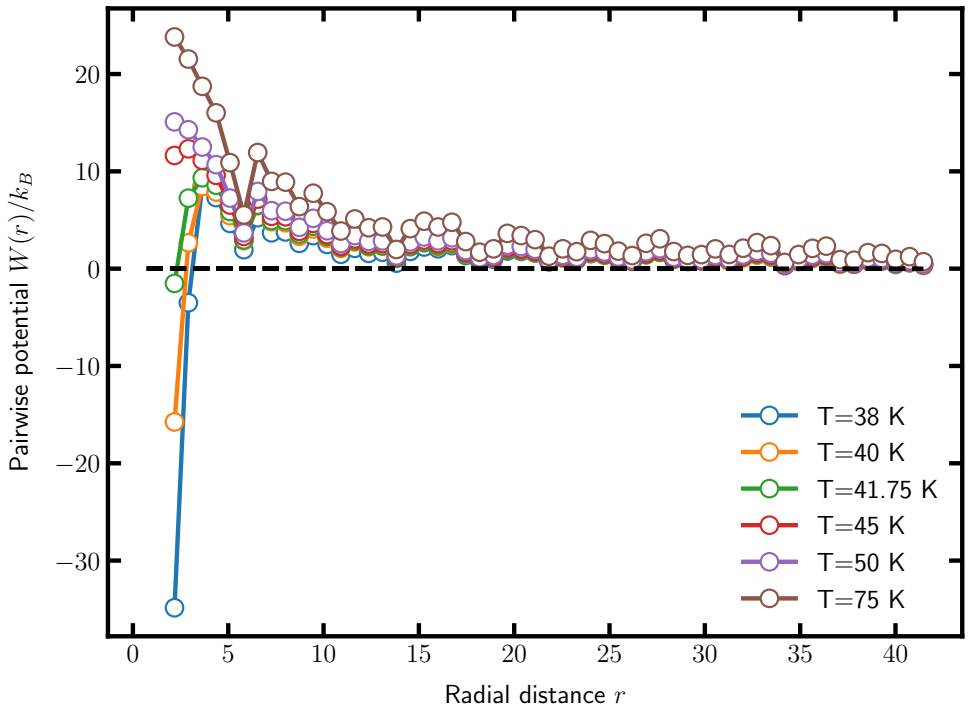

FIGURE 5.6: Defects pairwise potential interaction $W(r)/k_B$ at different temperatures .

temperature T_A. Hedgehogs form smaller, separated clusters. In other words, hedgehogs become trapped in a cage formed by their neighbors. This behavior is seen in a glassy state of particles [87].

Moreover, a study of the fractal dimension d_H was carried out based on the box-counting method [178, 179], that defines the Minkowski-Bouligand dimension as a limit [180] :

$$\mathrm{d}_H = \lim_{\varepsilon \to \infty} \frac{\ln(N_\varepsilon)}{\ln(1/\varepsilon)} \tag{5.7}$$

Where N_ε is the number of boxes needed to cover the free volume and ε is the side length of one box used in the covering of the box. In our case, the fractal dimension depicts the fractal nature of the hedgehogs' clusters, Fig.5.7 shows the evolution of the fractal dimension of hedgehogs/antihedgehogs cluster, and one must note that for lower temperatures, there are at least two separate clusters with different dimensions and two different separate scales.

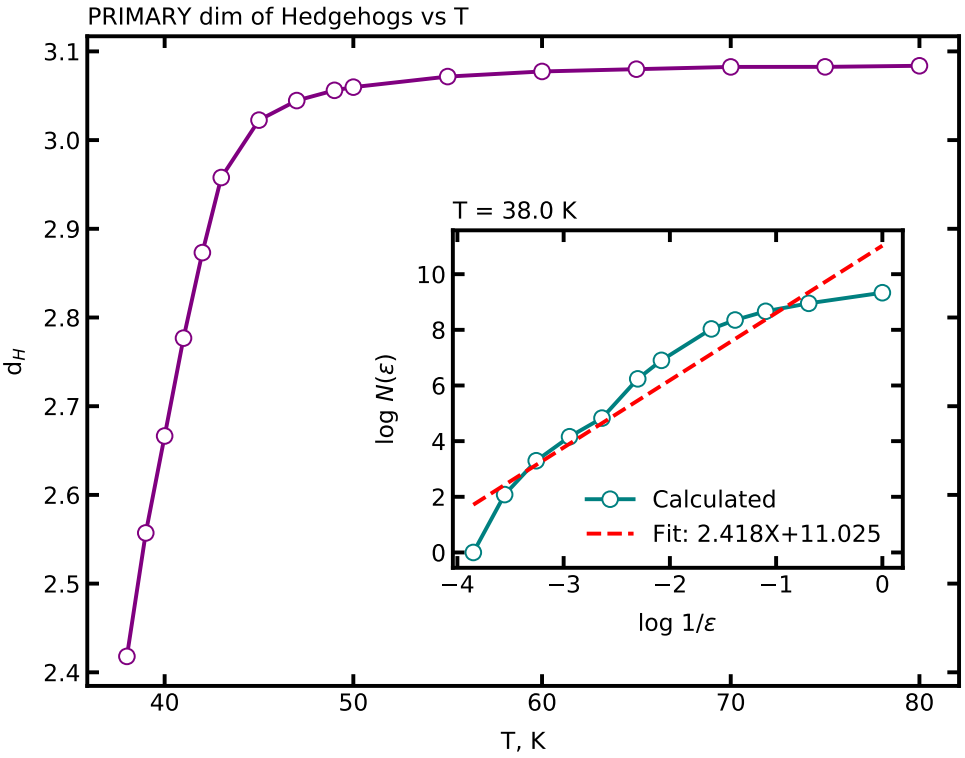

FIGURE 5.7: Temperature evolution of the fractal dimension with the box counting method d_H .

5.2.5 Point defects clusters and interaction with the skyrmion lattice phase

To understand the effect of point defect clusters on the skyrmion lattice, we analyzed how the point defects are scattered on the (111) plan in the presence of skyrmions. As seen previously, in a magnetic field of 40 mT applied along (111) direction, a skyrmion lattice phase emerges near T_c. In the presence of skyrmions, the point defects are arranged in clusters in the space between skyrmions as seen in Fig.5.8, leading to applied pressure on them. As the temperature increases, the point defect's density increases, as seen in Fig.5.3. To elucidate the nature of the point defect gas, we calculate the second virial coefficient B_2 as a function of temperature. The Virial expansion expresses the pressure of the point defect gas as:

$$\beta P_{\pm} = n_{\pm} + B_2 n_{\pm}^2 \qquad B_2 > 0 \tag{5.8}$$

The point defects exert increasing pressure as the temperature rises, leading to

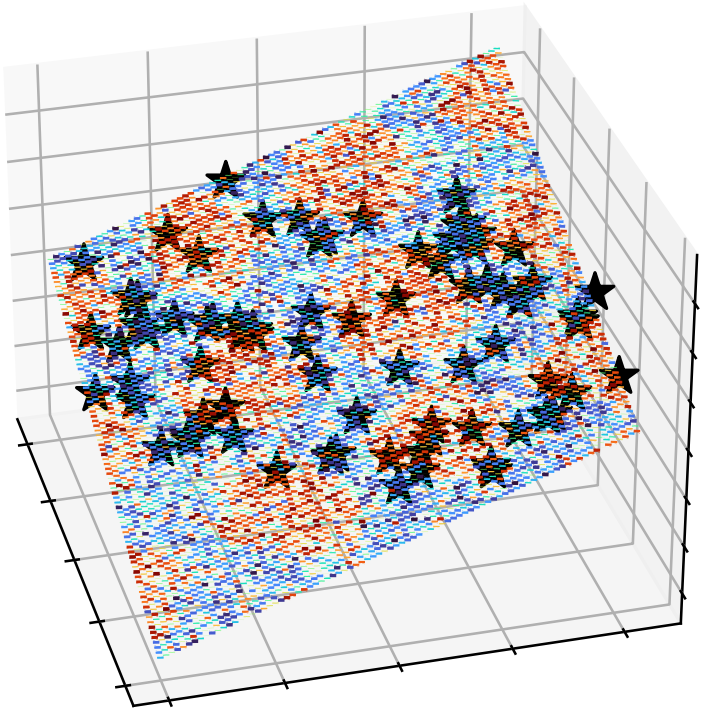

FIGURE 5.8: Point defect distribution in a (111) plane in presence of skyrmion lattice phase ($\mathbf{B}_{ex}$=40 mT and T =37 K) .

the annihilation of the skyrmion lattice phase. The process of the skyrmion annihilation by the point defects is depicted in Fig.5.9. We observe that the applied pressure gradually reduces the topological charge. However, the radius does not change except for 37.5 K, which suddenly decreases as we enter the FD phase. The radius increases until a maximum at 40 K and decreases again until the complete annihilation of the skyrmion phase, hence the gradual decrease in the skyrmion number $\mathcal{Q}_{sk}$ as temperatures increase toward T_c.

5.3 3D solitons : Hopfions and Hopfion-like solitons

A well-known type of 3D soliton is the Hopfion [181], which is a topological soliton characterized by a nontrivial topological structure. This soliton can be visualized as a knot or twisted loop in space, with its unique properties arising

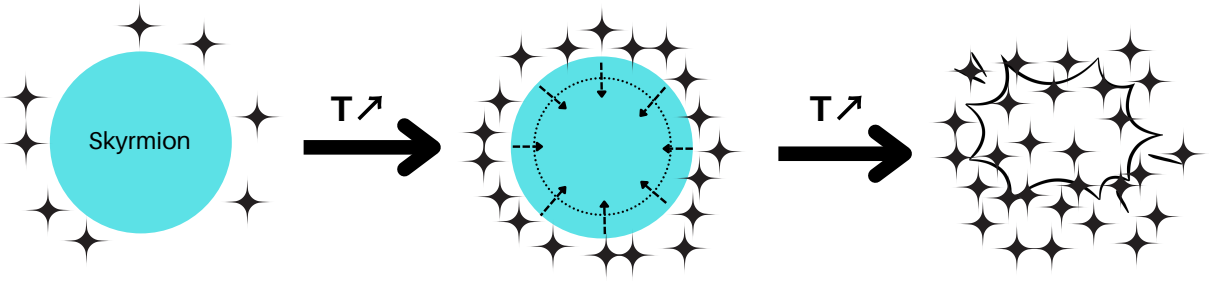

FIGURE 5.9: Schematic representation of the skyrmion lattice phase annihilation by point defects .

from the Hopf invariant. The Hopf invariant is calculated as the degree of a map called the Hopf fibration, which links a circle on a 3-sphere $\mathbb{S}^3$ to a point on a 2-sphere $\mathbb{S}^2$. By examining the linking number of two such circles, one can extract the degree of the Hopf map, or Hopf invariant.

On the other hand, performing simulation on a 3D cubic lattice with periodic boundary conditions (PBC) is equivalent to having a 3D space similar to a 3-Torus $\mathbb{T}^3$. In this case, a Hopf invariant is not the correct description for 3D solitons in 3-Torus $\mathbb{T}^3$ since it is a characterization if the degree of the Hopf map $h : \mathbb{S}^3 \to \mathbb{S}^2$. The proper description would be the Pontraygin invariant of the map $g_L : \mathbb{T}^3 \to \mathbb{S}^2$, DeTurck et al. proved the following theorems [182] :

Theorem 5.3.1: Theorem A

Let L be a 3-component link in $\mathbb{S}^3$. Then the pairwise linking numbers p, q and r of L are equal to the degrees of its characteristic map $g_L : \mathbb{T}^3 \to \mathbb{S}^2$ on the two-dimensional coordinate subtori of $\mathbb{T}^3$, while twice Milnor's μ_M-invariant for L is equal to Pontryagin's ν-invariant for g_L modulo $2\gcd(p,q,r)$

$$\nu(g_L) = 2\mu_M(L) \mod \gcd(p,q,r) \tag{5.9}$$

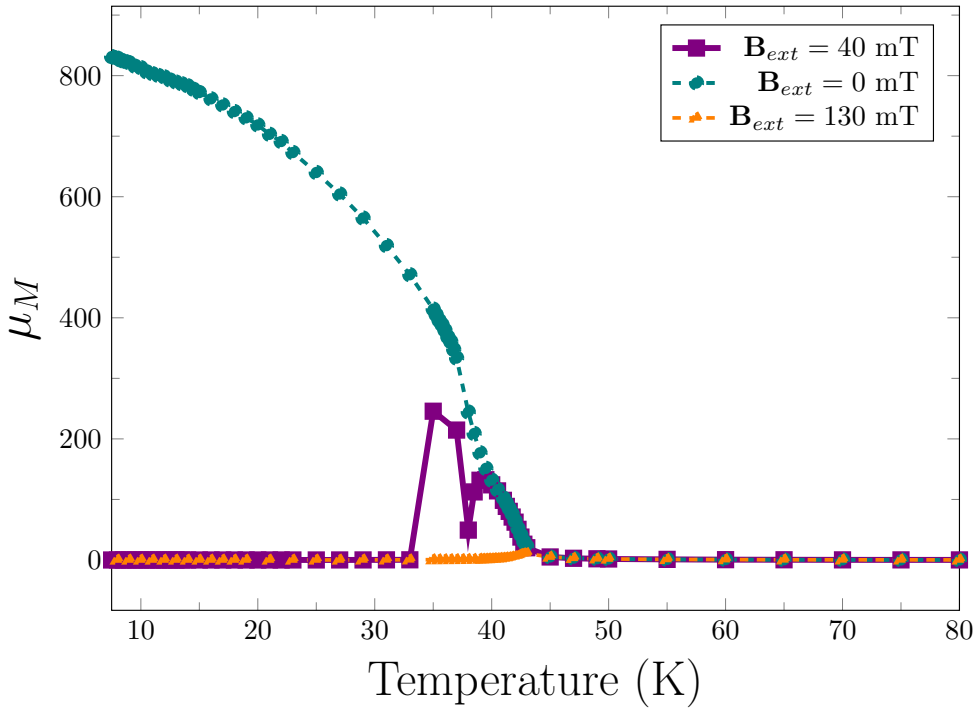

FIGURE 5.10: Temperature evolution of the milnor μ_M invariant under different magnetic fields .

Theorem 5.3.2: Theorem B

If the pairwise linking numbers of a three-component link L in $\mathbb{S}^3$ are all zero $p = 0, q = 0$ and $r = 0$, then Milnor's μ_M-invariant of L is given by :

$$\mu_M(L) = 8\pi^3 \sum_{\mathbf{n}\neq 0} \mathbf{a_n} \times \mathbf{b_n} \cdot \frac{\mathbf{n}}{|\mathbf{n}|^2} \tag{5.10}$$

With $\mathbf{c_n} = \mathbf{a_n} + i\mathbf{b_n}$ are the Fourier components of spin field in $\mathbb{T}^3$.

In the following, we will quantify the Milnor μ_M invariant as a function of temperature in our system to analyze the possibility of the existence of 3D solitons in CuO_2SeO_3 with PBC. The PBC impose a 3-torus topology on our superlattice. Thus the characterization of 3D solitons is obtained via the Milnor triple linking number, which is related to the degree of the map $\mathbb{T}^3 \to \mathbb{S}^2$. Fig.5.10 shows the evolution of the Milnor triple linking number in our system for various fields as a function of temperature. It is worth mentioning that at high fields, where we have a field-polarized phase, the linking number is zero, with small fluctuations near the phase transition. This behavior is expected since the uniform field on $\mathbb{T}^3$

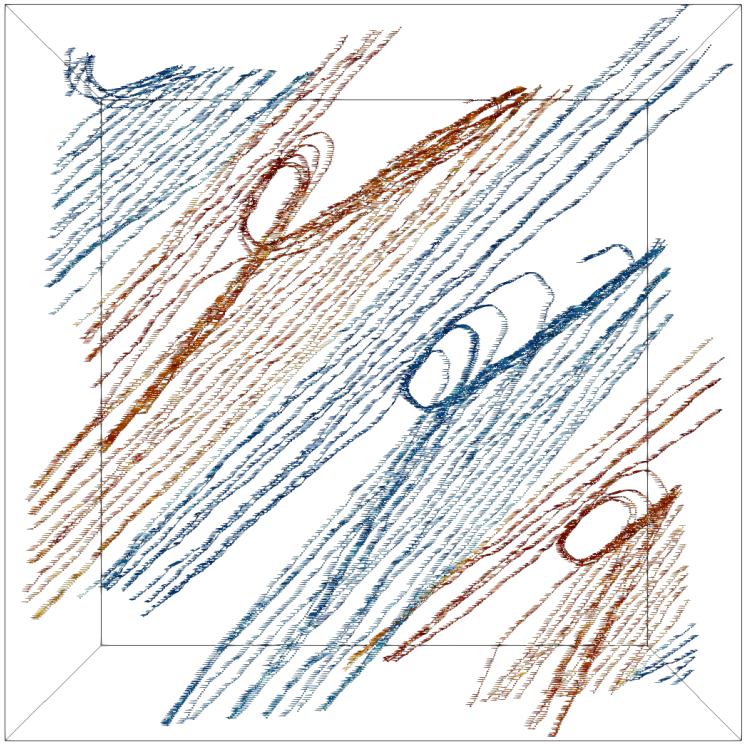

FIGURE 5.11: Closed loops of spin component streamline in $\mathbb{T}^3$ for a helical state .

is equivalent to having a trivial link, i.e., closed loops of the same spin component that does not link. However, we observe a high linking number for zero field and low temperatures, where the helical state is stable. This high linking number is due to the fact that the spiral state on the 3-Torus (3D cube with PBC) entangles the closed loops of the same spin component, thus revealing a nonvanishing Pontryaging invariant. For the skyrmion lattice phase at 40 mT, we expect to have the same behavior as the helical state, adding to that the skyrmions tubes along (111) direction form a closed loop, any twist of the skyrmion tube would lead to the creation of Hopfions-like defects. These phases are not expected in the real system since the PBC create this artifact. Nonetheless, one expects to find Hopfion-like solitons in nanodisk chiral magnets [183]. The existence of a nonvanishing value of Milnor's triple linking number in the helical state can be explained by the presence of linked closed loops in the 3-torus as shown in Fig.5.11. The helical state is characterized by a propagation vector $\mathbf{q}$ since in the helical state, the magnetic

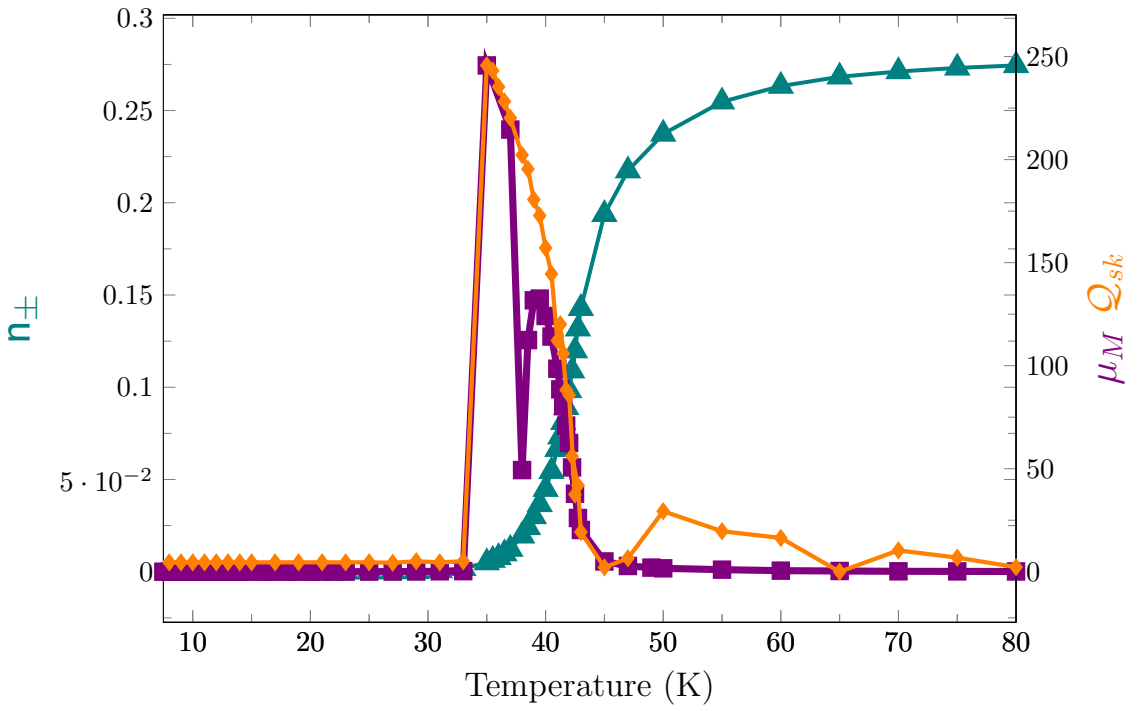

FIGURE 5.12: Temperature evolution of various topological entities at 40 mT, where we observe the coexistence of skyrmions (orange line), hedgehogs/antihedgehogs (teal), and 3D solitons (violet) in the region 35 K to 42 K .

moments rotate in a plane $(\tilde{u}, \tilde{v})$ and the Fourier component can be written as :

$$\mathbf{S_q} = [\frac{\mu_1 \tilde{\mathbf{u}} + i\mu_2 \tilde{\mathbf{v}}}{2}] \tag{5.11}$$

In the case of $\mu_1 = \mu_2$ we have a circular helix, thus the equation 5.10 has a non-zero value in the case of a helical state as depicted in Fig.5.10. The real and imaginary parts of the Fourier component are always non-collinear and perpendicular to the non-zero component (propagation vector). In the case of the skyrmion lattice phase, the Milnor triple linking number has a nonvanishing value only in the range where skyrmions are stable. We notice a sudden drop precisely at the temperature where there is a sudden decrease in skyrmion radius, and this can be explained again by the increase of the area of the ferromagnetic background leading to a smaller Milnor invariant. The decrease of the skyrmion radius is related to the sudden increase of pressure applied by point defect, which on the other hand, can be linked with the sudden jump in the second Virial coefficient B_2 and the growing rate of point defect density at this temperature as seen in Fig.5.12.

Thus this invariant is also sensitive to the skyrmion radius.

We have shown that multitudes of different topological defects can coexist in Cu_2OSeO_3. In the case of applied 40 mT magnetic fields along (111), we show that skyrmions, hedgehogs/antihedgehogs pairs, and 3D solitons coexist in the same range of temperatures. Fig.5.12 shows the topological charge of skyrmions, the density of hedgehogs/antihedgehogs, and the Milnor triple linking number as a function of temperature. We observe overlapping non-zero charges and density in the region between 35 K to 42 K. This confirms the possibility of the coexistence of multiple types of topological defects in the same part of the magnetic field-temperature phase diagram.

Conclusion

To summarize the results, we can say that several new developments have been added to the existing atomistic approaches to handle the complexity of ferroic systems such as Cu_2OSeO_3. These developments have enabled the study of properties of topological defects present in ferroic compounds and can be encompassed as follow :

- Monte Carlo simulations based on a first-principles-derived Hamiltonian are conducted to study the finite-temperature properties of chiral-lattice multiferroic insulator Cu_2OSeO_3. The use of this numerical technique (i) reveals basic features of the phase diagram as a function of temperature and external magnetic field, including the long-range helical phase at low temperature and zero magnetic fields and the skyrmion lattice phase, in which skyrmions are arranged in a two-dimensional hexagonal lattice, and (ii) leads to the discovery of an overlooked vortex lattice phase in a narrow pocket of the phase diagram near the fluctuations disordered-helical phase transition. The scheme also provides strong numerical evidence that the transition to a helical state in Cu_2OSeO_3 is first-order driven by critical fluctuations. We have developed a first-principle approach to study the magnetic phases and finite-temperature properties of multiferroic chiral magnet copper oxide selenite Cu_2OSeO_3. In detail, we constructed an effective Hamiltonian with all the magnetic interactions (in absence of mechanical constraints), the parameters of this Hamiltonian were determined via density functional theory calculations with U-correction (DFT+U). The Monte Carlo simulation gives us insight into the finite-temperature properties of Cu_2OSeO_3. We have obtained the same experimental head and shoulder peak signature of heat capacity found in Cu_2OSeO_3 and B20 Magnets. We have found a very narrow pocket of temperature and magnetic field where the magnetic skyrmion lattice phase is stabilized in agreement with experimental observations and a stabilized magnetic helical phase at zero or small

field under the critical temperature T_c. Our calculation also predicts the existence of a vortex lattice phase at a tiny region near T_H between the helical phase to the SkL phase.

- After studying the thermodynamical properties, we investigated the topological properties of the various topological entities, from the skyrmion number to hedgehog density. We found the previous quantities acting in accordance with the expected behavior of skyrmions and hedgehogs found in previous studies. Moreover, we introduced a new way to quantify 3D solitons in the case of the PBC system, with the Milnor triple linking invariant that characterizes topological defects inside a 3-Torus-like space.
- We predict using first-principles-based calculations, combined with Monte Carlo studies, that the distorted pyrochlore B20 Magnet Copper oxide selenite Cu_2OSeO_3 exhibits signatures of a classical spiral spin liquid phase in the region of the fluctuation-disordered phase.
- We also explored the effect of point defect on the annihilation of the skyrmion lattice phase. The applied pressure of hedgehogs and antihedgehogs destabilizes the skyrmion and leads to their destruction.
- We also showed the signature of the binding-unbinding mechanism in which we have a transition where point defects go from bounded hedgehogs-antihedgehogs pairs at low temperatures to unpaired point defects above T_c.

In conclusion, we have developed an effective Hamiltonian approach that reproduced well the experimental signatures and phase diagram of Cu_2OSeO_3, leading us to explore and quantify the topological properties of different solitons in this multiferroic magnet, as well as predicting potential novel phases (Vortex lattice and spiral spin liquid).

Appendix A

Some topology concepts

A.1 Basic concepts and definitions

Defintion A.1.1: Topological space

A topological space is a pair $(X, \mathcal{T})$ where X is an non-empty set and $\mathcal{T}$ is a collection of subsets of X that satisfies :

- $\emptyset, X \in \mathcal{T}$
- for a collection of arbitray open set $G_\alpha \in \mathcal{T}$ then $\bigcup_\alpha G_\alpha \in \mathcal{T}$
- let $G_i \in \mathcal{T}$ be a collection of finite number of open set then $\bigcap_i G_{i=1}^n \in \mathcal{T}$

From now on, we will denote the topological space X.

Defintion A.1.2: Homeomorphism

A map (function) $f : X \to Y$ between two topological spaces X and Y is called a homeomorphism (topological isomorphism) if :

- f is a bijection
- f is continuous
- the inverse map f^{-1} is continuous

Defintion A.1.3: Neighborhood of a point

If X is a topological space and x is a point in X, then a neighborhood of x is a subset $\mathcal{U}$ that includes an open set $\mathcal{V}$ containing x $\quad x \in \mathcal{U} \subseteq \mathcal{V} \subseteq X$

Defintion A.1.4: Hausdorff space

Let X be a topological space, X is a Hausdorff space if $\exists \mathcal{U}, \mathcal{V}$ neighborhood of $x, y \in X$ respectively such that $\mathcal{U} \cap \mathcal{V} = \emptyset$

Defintion A.1.5: Locally Euclidean

Let X be a topological space, X is called locally Euclidean if $\exists n \in \mathbb{N}^*$ such $\forall x \in X$ x has a neighborhood which is homeomorphic to $\mathbb{R}^n$

Defintion A.1.6: Topological Manifold

A topological manifold is a locally Euclidean Hausdorff space.

A.2 Homotopy groups

Defintion A.2.1: Homotopy class

let $f, g : X \to Y$ be two continuous maps. f, g are said to be in the same homotopy class if f can be continuously deformed into g i.e f is homotopic to g if $h : X \times [0,1] \to Y$ a continuous map such that : $h(x,0) = f(x)$ and $h(x,1) = g(x)$

We can extend this analysis by considering the homotopy classes of continuous maps from the n-sphere $\mathbb{S}^n$. Recall that the unit n-sphere is the set of points in $\mathbb{R}^{n+1}$ at the unit distance from the origin. For example, the 1-sphere is the unit circle. The homotopy classes of continuous maps from the n-sphere are special because one can define the composition of any two classes and show that the usual group axioms of closure, associativity, identity, and inversion are satisfied. Hence, from these homotopy classes, one can construct homotopy groups $\pi_n(X)$

Defintion A.2.2: Homotopy group

The set of homotopy classes of the continuous map $f : \mathbb{S}^n \to Y$ with $n \geq 1$ is known as the n^{th} homotopy group of Y $\quad \pi_n(Y)$

Clearly, sorting homotopy classes into homotopy groups will be useful in categorizing topologies. In order to make use of the n-sphere map in our analysis, we

show that the X manifold is isomorphic to an n-sphere. By considering stereographic projection, it is easy to confirm that this requirement is satisfied.

Defintion A.2.3: Sterographic projection

Let $\mathbb{E}^{n+1}$ a $n+1$-Euclidean space, let $Q \in \mathbb{S}^n$ then the stereographic projection of a point $P \in \mathbb{S}^n - \{Q\}$ is the point P' of intersection of the line QP with E a hyperplane in $\mathbb{E}^{n+1}$.

One of the simplest ways to get a feel for how these groups behave is to examine the homotopy groups of the m-sphere, which basically is exploring the homotopy group of $f : \mathbb{S}^n \to \mathbb{S}^m$.

- $\pi_0(\mathbb{S}^1) = 0$ This corresponds to mapping antipodal points onto a circle, and since any two points on the circle are connected, there can be only one topologically distinct way of putting antipodal points on a circle.
- $\pi_1(\mathbb{S}^1) \cong \mathbb{Z}$ This corresponds to mapping a circle onto a closed loop, remembering that we can wrap loops around the circle clockwise and anticlockwise implies that this homotopy group is isomorphic to the set of integers.
- $\pi_0(\mathbb{S}^2) = 0$ the same argument of $\mathbb{S}^1$ can be applied for the sphere. There can be only one topologically distinct way of putting antipodal points on a sphere.
- $\pi_1(\mathbb{S}^2) = 0$ any closed loop on the 2-sphere can be contracted into a point. Therefore, on its surface, a circle and a point are topologically indistinguishable, and as before, there is only one topologically distinct way of mapping a point onto a sphere.
- $\pi_2(\mathbb{S}^2) \cong \mathbb{Z}$ This corresponds to mapping a 2-sphere onto another 2-sphere, the same argument of $\pi_1(\mathbb{S}^1)$ can be brought here, even if it is difficult to visualize it.
- $\pi_1(\mathbb{T}^2) \cong \mathbb{Z} \times \mathbb{Z}$ the fundamental group of a 2-Torus can be seen as the Cartesian product of two circles. Thus one needs a pair of integers to characterize the map.($\mathbb{T}^2 = \mathbb{S}^1 \times \mathbb{S}^1$)

Appendix B

Primer on statistical physics

B.1 Partition function

Let us consider a system with energy levels ϵ_i the probability of a j-state existing is

$$\mathcal{P}_j = \frac{e^{-\beta\epsilon_j}}{\sum_i e^{-\beta\epsilon_i}} \tag{B.1}$$

where $\beta = 1/k_B T$. The denominator is what we call the partition function

$$\mathcal{Z} = \sum_i e^{-\beta\epsilon_i} \tag{B.2}$$

The use of the partition function can be seen in this example, where we calculate the internal energy U of the system.

$$U = \langle E \rangle = \frac{\sum_i \epsilon_i e^{-\beta\epsilon_i}}{\sum_i e^{-\beta\epsilon_i}} = -\frac{1}{\mathcal{Z}}\frac{\partial \mathcal{Z}}{\partial \beta} = -\frac{\partial \ln(\mathcal{Z})}{\partial \beta} \tag{B.3}$$

B.2 The free energy

The free energy $\mathcal{F}$ can be obtained from the partition function as

$$\mathcal{F} = -\frac{1}{\beta}\ln(\mathcal{Z}) \tag{B.4}$$

We justify this since the free energy can be calculated from internal energy.

$$\mathcal{F} = U - TS = U - \frac{1}{k_B \beta} S \tag{B.5}$$

The entropy is then obtained from the free energy by

$$S = -\frac{\partial \mathcal{F}}{\partial T} = k_B \ln(\mathcal{Z}) - \frac{k_b \beta}{\mathcal{F}} \frac{\partial \mathcal{Z}}{\partial \beta} \tag{B.6}$$

Combining with internal energy leads to the equation B.5

B.3 Thermodynamical quantities

B.3.1 Heat Capacity

The heat capacity is given by

$$C_v = \frac{\partial U}{\partial T} = -k_B \beta^2 \frac{\partial U}{\partial \beta} = -\frac{k_B \beta^2}{\mathcal{Z}^2} (\frac{\partial \mathcal{Z}}{\partial \beta})^2 + \frac{k_B \beta^2}{\mathcal{Z}} (\frac{\partial^2 \mathcal{Z}}{\partial \beta^2}) \tag{B.7}$$

The first term is the mean-energy squared, while the second is the mean of square of energy, therefore:

$$C_v = k_B \beta^2 (\langle E^2 \rangle - \langle E \rangle^2) \tag{B.8}$$

B.3.2 Susceptibility

If a system is subjected to an excitation (external field, a flux of particles...), there will be a response. In the case of magnetic systems, we have the magnetic field as the excitation and the magnetization as the response. We define susceptibility as

$$\chi = \frac{\partial Q}{\partial H} \tag{B.9}$$

the field will change the energy of the system as $-HQ_j$ Thus an additional term will be added to the partition function

$$\mathcal{Z} = \sum_i e^{-\beta \epsilon_i - HQ_j} \tag{B.10}$$

It follows that

$$\langle Q \rangle = \frac{1}{\beta \mathcal{Z}} \frac{\partial \mathcal{Z}}{\partial H} \tag{B.11}$$

and

$$\langle Q^2 \rangle = \frac{1}{\beta^2 \mathcal{Z}} \frac{\partial^2 \mathcal{Z}}{\partial H^2} \tag{B.12}$$

Henceforth

$$\chi = \frac{\partial Q}{\partial H} = \beta(\langle Q^2 \rangle - \langle Q \rangle^2) \tag{B.13}$$

Appendix C

On Ginzburg-Landau Functional for chiral magnets

This appendix provides a straightforward derivation of the Ginzburg-Landau functional for Cu_2OSeO_3. Although elementary, to our knowledge, it has not been presented previously and is distinct from other functionals used for Cu_2OSeO_3. The derivation is not mathematically rigorous – in fact, we are not specifying the precise conditions for some assumptions to hold or making precise statements about the convergence of perturbation series. The Ginzburg-Landau functional of free energy density f, where $\mathcal{F} = \int_{\mathbb{R}^3} f d\mathbf{r}$, is given as :

$$f = \frac{1}{2}\varphi(r - \mathcal{J}\nabla^2)\varphi + \mathcal{D}\varphi \cdot (\nabla \times \varphi) + \frac{u}{4!}\varphi^4 + \mu\mu_0\phi \cdot \mathbf{H} + f_{ani} \tag{C.1}$$

We choose dimensionless units for the three component order parameter field φ..

C.1 The model : Matrix form

The model is defined in terms of the following classical Hamiltonian,

$$-\beta\mathcal{H} = \frac{1}{2}\sum_{i,j}\mathbf{J}_{ij}\vec{S}_i \cdot \vec{S}_j + \mathbf{D}_{ij} \cdot \vec{S}_i \times \vec{S}_j \; + \sum_i \vec{h} \cdot \vec{S}_i, \tag{C.2}$$

where S_i^α are the components of the classical vectors $\vec{S}_i = \{S_i^\alpha, \alpha = 1, 2, 3\}$ at site i. These vectors can change their direction but their magnitudes $|\vec{S}_i|$ obey the condition

$$\vec{S}_i^2 = \sum_{\alpha=1}^{3=:n} (S_i^\alpha)^2 = u.$$

To derive the effective order-parameter field theory for the model, let us write the Hamiltonian in Eq.(C.2) in compact matrix form,

$$-\beta\mathcal{H} = \frac{1}{2}\mathbf{S}^T\mathbb{K}\mathbf{S} + \mathbf{h}^T\mathbf{S}, \tag{C.3}$$

where $\mathbf{S}$ and $\mathbf{h}$ are N-dimensional column vectors and $\mathbb{K}$ is an $3N\times3N$-matrix with matrix elements $J_{ij}^{\alpha\beta}$ and $D_{ij}^{\alpha\beta}$.

Let us take for example two spins with one J and D_z then we have $\mathbf{S} = (S_1^x, S_1^y, S_1^z, S_2^x, S_2^y, S_2^z)^T$ and

$$\mathbb{K} = \begin{pmatrix} 0 & 0 & 0 & J & D_z & 0 \\ 0 & 0 & 0 & -D_z & J & 0 \\ 0 & 0 & 0 & 0 & 0 & J \\ J & -D_z & 0 & 0 & 0 & 0 \\ D_z & J & 0 & 0 & 0 & 0 \\ 0 & 0 & J & 0 & 0 & 0 \end{pmatrix} = \begin{pmatrix} \mathbf{0_{3\times3}} & \mathbf{J_{1,2}} + \mathbf{D_{1,2}} \\ \mathbf{J_{2,1}} + \mathbf{D_{2,1}} & \mathbf{0_{3\times3}} \end{pmatrix} \tag{C.4}$$

The matrix $\mathbb{K}$ is symmetric ($\mathbb{K} = \mathbb{K}^T$) and not positive definite ($\mathbb{K} \not\geq 0$). Since the matrix $\mathbb{K}$ is real-symmetric, an orthogonal transformation can reduce it to a diagonal form. Note that for some $\mu > 0$, $\mathbb{K} + \mu\mathbb{I}_{6\times6}$ is positive definite, where $\mathbb{I}_{6\times6}$ is the 6×6 identity matrix. On the minimum value of μ: since $\mathbb{K}$ is symmetric (with real eigenvalues), one can choose μ to be the absolute value of the smallest eigenvalue of $\mathbb{K}$.

The partition function [1] can now be written as [184, Chapter 3] [2]

$$\mathcal{Z} = \frac{\int \mathcal{D}[S] \prod_{j=1}^{N} \delta(\mathbf{S}_j^2 - u) e^{-\beta \mathcal{H}}}{\underbrace{\int \mathcal{D}[S] \prod_{j=1}^{N} \delta(\mathbf{S}_j^2 - u)}_{(\text{without } \prod_{j=1}^{N}) = \frac{\pi^{\frac{n}{2}}}{\Gamma\left(\frac{n}{2}\right)} u^{\frac{n}{2}-1} =: \mathcal{N}.}} \tag{C.5}$$

where we have introduced the notation

$$\int \mathcal{D}[S] = \int_{-\infty}^{\infty} \prod_{j=1}^{N} \prod_{\alpha=1}^{3} dS_j^{\alpha} \tag{C.6}$$

$$\begin{aligned} I &:= \int_{\mathbb{R}^n} \mathrm{d}^n x \, \delta \underbrace{\left(\frac{x^2}{b} - a \right)}_{=f(r)} \\ &\overset{\text{Spher. coord.}}{=} Vol(\mathbb{S}^{n-1}) \int_{\mathbb{R}_+} \mathrm{d}r \, r^{n-1} \, \delta(f(r)) \\ &= Vol(\mathbb{S}^{n-1}) \int_{\mathbb{R}_+} \mathrm{d}r \, r^{n-1} \sum_{r_0>0}^{f(r_0)=0} \frac{1}{|f'(r)|} \delta(r - r_0) \\ &\overset{r_0=\sqrt{ab}}{=} Vol(\mathbb{S}^{n-1}) \int_{\mathbb{R}_+} \mathrm{d}r \, r^{n-1} \, \frac{b}{2r} \delta(r - r_0) \\ &= Vol(\mathbb{S}^{n-1}) \frac{r_0^{n-2} b}{2} = \frac{\pi^{\frac{n}{2}}}{\Gamma\left(\frac{n}{2}\right)} a^{\frac{n}{2}-1} b^{\frac{n}{2}}, \end{aligned}$$

C.2 Positive definiteness of the matrix

C.2.1 Constraint method

There are at least a couple of ways to transform the matrix $\mathbb{K}$ into a positive definite matrix. The first one uses the constraint introduced in the previous section.

[1] In Eq.(C.5) and later in the text, there must be δ, not δ^3. Note: $\delta^3(\mathbf{x}_1 - \mathbf{x}_0) = \delta(x_1 - x_0)\delta(y_1 - y_0)\delta(z_1 - z_0)$

[2] Eq.(11.7) in [184, Chapter 3] seems to be incomplete.

Because of the constraint $\mathbf{S}_j^2 = u$, we can add a term $\lambda_j(\mathbf{S}_j^2 - u)$ to the Hamiltonian, such that λ_j is greater than the absolute value of the smallest eigenvalue of $\vec{K}$. Thus, we redefine $\mathbb{K}$ as

$$\mathbb{K} \to \mathbb{K} + \mathrm{diag}(\lambda) \tag{C.7}$$

where

$$\mathrm{diag}(\lambda) = \begin{pmatrix} \lambda_1 & & & & \\ & \lambda_2 & & & \\ & & \lambda_3 & & \\ & & & \ddots & \\ & & & & \lambda_N \end{pmatrix}$$

In other words, choose the arbitrary constants λ_j sufficiently large to ensure that all the eigenvalues of $\mathbb{K}$ have a positive real part. In this way, the matrix $\mathbb{K}$ becomes positive definite.

The expression for $\mathcal{Z}$ is utilized to get the free energy, f, for the system. The parameters $\{\lambda_i\}$ are determined or eliminated (as desired) from the equations obtained from the equilibrium conditions

$$\frac{\partial f}{\partial \lambda_i} = 0, \; \frac{\partial f}{\partial y} = 0,$$

where y stands for the ordering parameters of the system.

C.2.2 Dirac delta method

The constraint in Eq. (C.5) is most conveniently imposed using an integral representation of the Dirac delta function. In turn, we can exponentiate the constraint on the length of the vector $\mathbf{S}_j$ in different ways. For example :

$$\delta(t_j) = \frac{1}{2\pi i} \int_{a-i\infty}^{a+i\infty} \mathrm{d}z_j e^{-z_j t_j}, \; t_j = (\mathbf{S}_j^2 - u). \tag{C.8}$$

$$\Longrightarrow \prod_{j=1}^{N} \delta(\mathbf{S}_j \cdot \mathbf{S}_j - u) = \int \mathcal{D}[z] \exp\left\{ \left[\sum_j z_j (u - \mathbf{S}_j^2) \right] \right\} \tag{C.9}$$

By analogy to the Gaussian integration over S and x above, the product measure $\mathcal{D}[z]$ is normalized so that $\int D[z] \exp(-\frac{1}{2}\, zAz) = 1/\sqrt{\det A}$ for any symmetric bilinear form (symmetric kernel) A. Thus, we redefine $\mathbb{K}$ in Eq. (C.3) as

$$\mathbb{B}_{ij} = -\mathbb{K}_{ij} + \mathbf{z}\delta_{ij} \tag{C.10}$$

The interchange of limits $\mathcal{D}[S]$ and $\mathcal{D}[z]$ is allowed provided that all eigenvalues of $\mathbb{B}$ are positive when $z_j = a$; clearly, a real a can be chosen such that this is true. [3]

C.3 Hubbard-Stratonovich transformation

We next use the following mathematical identity for N-dimensional Gaussian integrals [185], valid for any positive symmetric matrix $\mathbb{A}$ (see, for example, Ref. [186, Sec. 6.6]),

$$\left(\prod_{j=1}^{N} \int_{-\infty}^{\infty} \frac{dx_j}{\sqrt{2\pi}} \right) \exp\left\{ -\frac{1}{2}\mathbf{x}^T \mathbb{A}\mathbf{x} + \mathbf{x}^T \mathbf{y} \right\} = [\det \mathbb{A}]^{-1/2} \exp\left\{ \frac{1}{2}\mathbf{y}^T \mathbb{A}^{-1}\mathbf{y} \right\} \tag{C.11}$$

$$\Longrightarrow \exp\left\{ \frac{1}{2}\mathbf{S}^T \mathbb{K}\mathbf{S} \right\} = \frac{\int \mathcal{D}[x] \exp\left[-\frac{1}{2}\mathbf{x}^T \mathbb{K}^{-1}\mathbf{x} + \mathbf{x}^T \mathbf{S} \right]}{\underbrace{\int \mathcal{D}[x] \exp\left[-\frac{1}{2}\mathbf{x}^T \mathbb{K}^{-1}\mathbf{x} \right]}_{=(2\pi)^{N/2}\left[\det \mathbb{K}^{-1}\right]^{-1/2}}} \tag{C.12}$$

where we have introduced the notation

$$\int \mathcal{D}[x] = \prod_{j=1}^{N} \int_{-\infty}^{\infty} \frac{dx_j}{\sqrt{2\pi}}$$

[3] for mean field solution, one uses the following decoupling of the product

$$AB = A\langle B\rangle + B\langle A\rangle - \langle A\rangle\langle B\rangle,$$

where the fluctuations $A - \langle A\rangle$ and $B - \langle B\rangle$ are ignored. In this way the original Hamiltonian is replaced by a mean-field Hamiltonian $\mathcal{H}_{MF}$.

Thus an interacting spin system has been converted into a non-interacting system living in fluctuating external auxiliary fields $\mathbf{x}$, and the summation (integration) over all such auxiliary-field configurations recovers the many-body interactions.

C.4 The Partition function

C.4.1 The constraint method

Using constraint method above and Eq. (C.12), the partition function can now be written as

$$\mathcal{Z} = \frac{\left(\prod_{j=1}^{N}\int_{-\infty}^{\infty} d\mathbf{S}_j \delta^3(\mathbf{S}_j^2 - u)\right)\int \mathcal{D}[x]\exp\left[\overbrace{-\frac{1}{2}\mathbf{x}^T\mathbb{K}^{-1}\mathbf{x} + (\mathbf{h}+\mathbf{x})^T\mathbf{S} - u\sum_{j=1}^{N}\lambda_j}^{=-\tilde{S}[\mathbf{x}]}\right]}{\mathcal{N}\int \mathcal{D}[x]\exp\left[-\frac{1}{2}\mathbf{x}^T\mathbb{K}^{-1}\mathbf{x}\right]}, \tag{C.13}$$

where $\mathbb{K}$ is given by Eq. (C.7) and $\mathcal{N}$ is defined in Eq. (C.5). The order of the x and S integration can be interchanged if $\mathbb{K}$ has a positive real part.

For a given configuration of the Hubbard—Stratonovich field $\mathbf{x}$, the spin integration in the numerator factorizes in a product of independent terms, each describing the partition function of a single spin in a site-dependent magnetic field $h + x_i$. Therefore, this spin integration can easily be carried out,

$$\begin{aligned}\left(\prod_{j=1}^{N}\int_{-\infty}^{\infty} d\mathbf{S}_j \delta(\mathbf{S}_j^2 - u)\right) e^{(\mathbf{h}+\mathbf{x})^T\mathbf{S}} &= \int \mathcal{D}[S]\prod_{j=1}^{N}\delta(\mathbf{S}_j^2 - u)e^{(\mathbf{h}+\mathbf{x})_j^T\mathbf{S}_j} \\ \text{Using Eq. C.6} &= \prod_{j=1}^{N}\left[\int_{-\infty}^{\infty} d\mathbf{S}_j\delta(\mathbf{S}_j^2 - u)e^{(\mathbf{h}+\mathbf{x})_j^T\mathbf{S}_j}\right] \\ &= \prod_{j=1}^{N} I_j(\mathbf{x}_j).\end{aligned} \tag{C.14}$$

Now our task is to calculate the integral [186, Sec. 6.6])

$$I_j(\mathbf{x}_j)^4 = \int_{-\infty}^{\infty} d\mathbf{S}_j \delta(\mathbf{S}_j^2 - u) e^{(\mathbf{h}+\mathbf{x})_j^T \mathbf{S}_j} \qquad \tilde{\mathbf{x}} = \mathbf{h} + \mathbf{x} \tag{C.15}$$

This can be calculated and we have :

$$I_j(\mathbf{x}_j) = \pi^{n/2} u^{n/2-1} \sum_{p=0}^{\infty} \frac{1}{p!} \left(\frac{u|\tilde{\mathbf{x}}_j|^2}{4} \right)^p \frac{1}{\Gamma(p+n/2)} \tag{C.16}$$

The resulting partition function is given by the path integral

$$\mathcal{Z} = \frac{\left[\det \mathbb{K}^{-1}\right]^{1/2}}{(2\pi)^{N/2}} \int_{-\infty}^{\infty} \left(\prod_{j=1}^{N} \mathrm{d}x_j \right) e^{-\mathcal{H}_{eff}[\mathbf{x}]}, \tag{C.17}$$

Where

$$\beta \mathcal{H}_{eff}[\mathbf{x}] = \frac{1}{2} \mathbf{x}^T \mathbb{K}^{-1} \mathbf{x} + u \sum_{j=1}^{N} \lambda_j - \sum_{j=1}^{N} \underbrace{\ln \left(\sum_{p=0}^{\infty} \frac{1}{p!} \left(\frac{u|\tilde{\mathbf{x}}_j|^2}{4} \right)^p \frac{\Gamma(n/2)}{\Gamma(p+n/2)} \right)}_{\ln(\cdots) = \sum_{s=0}^{\infty} c_{2s} \left(|\tilde{\mathbf{x}}_j|^2 \right)^s} \tag{C.18}$$

Or, if we use the shift transformation $\mathbf{h} + \mathbf{x} \to \mathbf{x}$ (see the footnote Eq. (C.15))

$$\beta \mathcal{H}_{eff}[\mathbf{x}] = \frac{1}{2} \left(\mathbf{x}^T \mathbb{K}^{-1} \mathbf{x} + \mathbf{h}^T \mathbb{K}^{-1} \mathbf{h} - 2\mathbf{h}^T \mathbb{K}^{-1} \mathbf{x} \right) + u \sum_{j=1}^{N} \lambda_j \tag{C.19}$$

$$- \sum_{j=1}^{N} \ln \left(\sum_{p=0}^{\infty} \frac{1}{p!} \left(\frac{u|\mathbf{x}_j|^2}{4} \right)^p \frac{\Gamma(n/2)}{\Gamma(p+n/2)} \right) \tag{C.20}$$

Next, c_{2s} are given in Ref. ([187]). Until now, no approximations have been made, so the name "effective Hamiltonian" points out the coming approximations.

[4] Probably, it would be useful to perform the shift transformation $h \vec{+} x \to \vec{x}$. Thus, instead of $\tilde{\vec{x}}$ in Eq. (C.15) and Eq. (C.16) below we got just $\vec{x}$. Additionally, the term $\frac{1}{2}\vec{x}^T \vec{K}^{-1} \vec{x}$ in Eq. (C.13) has to be replaced with $\frac{1}{2}(\vec{x}^T \vec{K}^{-1} \vec{x} + \vec{h}^T \vec{K}^{-1} \vec{h} - 2\vec{h}^T \vec{K}^{-1} \vec{x})$.

C.4.2 Physics behind x

To understand the physical meaning of the variables $\mathbf{x}$, we calculate the expectation value of its i-th component (see, for example, Ref. [188]). Introducing an auxiliary N-component column vector $\mathbf{y} = (y_1, \ldots, y_N^T)$ and the term $+\mathbf{x}^T\mathbf{y}$ in $\tilde{S}[\mathbf{x}]$ of Eq. (C.13), we get

$$\langle \mathbf{x}_j \rangle = \lim_{\mathbf{y}\to 0} \frac{\partial}{\partial \mathbf{y}_j} \frac{\int \mathcal{D}[S] \prod_{j=1}^{N} \delta(\mathbf{S}_j^2 - u) \int \mathcal{D}[x] e^{-\tilde{S}[\mathbf{x}] + \mathbf{x}^T\mathbf{y}}}{\int \mathcal{D}[S] \prod_{j=1}^{N} \delta(\mathbf{S}_j^2 - u) \int \mathcal{D}[x] e^{-\tilde{S}[\mathbf{x}]}}$$

$$\text{Eq. C.12 from } x \to S = \lim_{\mathbf{y}\to 0} \frac{\partial}{\partial \mathbf{y}_j} \frac{\int \mathcal{D}[S] \prod_{j=1}^{N} \delta(\mathbf{S}_j^2 - u) e^{\frac{1}{2}(\mathbf{S}+\mathbf{y})^T \mathbb{K} (\mathbf{S}+\mathbf{y}) + \mathbf{h}^T\mathbf{S}}}{\int \mathcal{D}[S] \prod_{j=1}^{N} \delta(\mathbf{S}_j^2 - u) e^{\frac{1}{2}\mathbf{S}^T\mathbb{K}\mathbf{S} + \mathbf{h}^T\mathbf{S}}}$$

$$= \langle [\mathbb{K}\mathbf{S}]_j \rangle$$

In order to introduce variables ϕ_j whose expectation value can be identified with the average magnetization $\mathbf{m} = \langle \mathbf{S}_j \rangle$, we simply define $\phi = \mathbb{K}^{-1}\mathbf{x}$. That is, use a transformation of $\mathbf{x}$ to represent the term $\mathbf{x}^T\mathbb{K}^{-1}\mathbf{x}$ in the Heisenberg-like form [186, Sec. 6.6]) $\phi^T\mathbb{K}\phi$:

$$\mathbf{x}_i = \sum_j \mathbb{K}_{ij}\boldsymbol{\phi}_j \tag{C.21}$$

Substituting $\phi = \mathbb{K}^{-1}\mathbf{x}$ in Eq.(C.17), we can finally obtain the exact representation of the partition function. Substituting Eq. (C.21) into Eq. (C.20), we get

$$\begin{aligned}\beta\mathcal{H}_{eff}[\mathbf{x}] &= \frac{1}{2}\left(\phi^T\mathbb{K}\phi + \mathbf{h}^T\mathbb{K}^{-1}\mathbf{h} - 2\mathbf{h}^T\mathbf{x}\right) + u\sum_{j=1}^{N}\lambda_j \\ &\quad - \sum_{j=1}^{N}\ln\left(\sum_{p=0}^{\infty}\frac{1}{p!}\left(\frac{u|\mathbf{x}_j|^2}{4}\right)^p\frac{\Gamma(n/2)}{\Gamma(p+n/2)}\right) \qquad \text{(C.22)} \\ &\overset{\text{up to } 4^{th}}{=} \frac{1}{2}\left(\phi^T\mathbb{K}\phi + \mathbf{h}^T\mathbb{K}^{-1}\mathbf{h} - 2\mathbf{h}^T\mathbf{x}\right) + u\sum_{j=1}^{N}\lambda_j \\ &\quad - \frac{1}{2}\sum_{j=1}^{N}\left[\sum_{m_1,m_2;\alpha}\mathbb{K}_{jm_1}\mathbb{K}_{jm_2}\phi^{\alpha}_{m_1}\phi^{\alpha}_{m_2}\right. \\ &\qquad \left. - \frac{1}{2(n+2)}\sum_{\alpha\beta}\sum_{m_1\ldots m_4}\mathbb{K}_{jm_1}\cdots\mathbb{K}_{jm_4}\phi^{\alpha}_{m_1}\phi^{\alpha}_{m_2}\phi^{\beta}_{m_3}\phi^{\beta}_{m_4}\right] \qquad \text{(C.23)}\end{aligned}$$

Note that $\mathbb{K} = \beta(\mathbb{J} + \mathbb{D})$ and $\mathbf{h} = \beta\mathbf{H}$.

For the continuum limit we either

1. Perform the continuum limit and then use the Fourier transformation (see, for example, Ref. [186, Sec. 6.6] and, as a help, [189])
2. we may simplify $\mathcal{H}_{eff}$ by Fourier transforming the variables ϕ since our lattice model has discrete translational invariance.

C.4.3 The dirac delta method

The partition function can now be written as

$$\begin{aligned}\mathcal{Z} &= C\int\mathcal{D}[S]\mathcal{D}[z]\exp\left\{\left[\frac{1}{2}\mathbf{S}^T\mathbb{K}\mathbf{S} + \mathbf{h}^T\mathbf{S}\right]\right\}\exp\left\{\left[\sum_j z_j(u - \mathbf{S}_j^2)\right]\right\} \\ \mathbb{B}\text{ is positive definite} &= C\int\mathcal{D}[z]\mathcal{D}[S]\exp\left\{\left[-\frac{1}{2}\mathbf{S}^T\mathbb{B}(z)\mathbf{S} + \mathbf{h}^T\mathbf{S} + u\sum_j z_j\right]\right\} \qquad \text{(C.24)}\end{aligned}$$

where $\mathbb{B}$ is given by Eq. (C.10).

The path integral over the field $\mathbf{S}$ is Gaussian (see Eq. (C.11)), and is given by N-copies of the real scalar field partition function.

We can follow Ref. ([190, Ch. 5]).

$$\mathcal{Z} = \int \mathcal{D}[z] \left(\frac{2\pi^N}{\det \mathbb{B}(z)} \right)^{1/2} \exp \left[\frac{1}{2} \mathbf{h}^T \mathbb{B}(z)^{-1} + u \sum_j z_j \right] \tag{C.25}$$

The matrix $\mathbb{B}$ depends on $\mathbf{z}$ and the structure of the lattice. If we impose periodic boundary conditions, then $\mathbb{B}$ is cyclic and from Eq. (C.10) its eigenvalues can be found by the Gaussian expansion of the determinant discussed in the following :

Let $\boldsymbol{M}$ be a diagonalizable matrix $\boldsymbol{M} = \boldsymbol{X}\boldsymbol{\Lambda}\boldsymbol{X}^{-1}$, where $\boldsymbol{\Lambda}$ is a diagonal $N \times N$ matrix with the eigenvalues of $\boldsymbol{M}$ as its entries and $\boldsymbol{X}$ is a non-singular $N \times N$ matrix consisting of the eigenvectors corresponding to the eigenvalues in $\boldsymbol{M}$. The identity $\det(\exp(\mathbb{B})) = \exp(\mathrm{Tr}(\mathbb{B}))$:

$$\det\{\boldsymbol{M}\} = \prod_i \lambda_i \tag{C.26}$$

$$\exp(\mathrm{Tr}(\log(\boldsymbol{M}))) = \exp\Big(\mathrm{Tr}\Big(\boldsymbol{X} \log \boldsymbol{\Lambda} \boldsymbol{X}^{-1}\Big)\Big) = \exp\left(\sum_i \log(\lambda_i)\right) = \prod_i \lambda_i \tag{C.27}$$

We need to approximate

$$\begin{aligned}
\mathrm{Tr} \ln \boldsymbol{M} &:= \mathrm{Tr} \ln(\boldsymbol{M}_0 + \boldsymbol{M}_1) \\
&= \mathrm{Tr} \ln[\boldsymbol{M}_0(1 + \boldsymbol{M}_0^{-1}\boldsymbol{M}_1)] \\
&= \mathrm{Tr} \ln \boldsymbol{M}_0 + \mathrm{Tr} \ln\Big(1 + \boldsymbol{M}_0^{-1}\boldsymbol{M}_1\Big) \\
&= \mathrm{Tr} \ln\Big(-\boldsymbol{G}_0^{-1}\Big) - \sum_{m=1}^{\infty} \frac{1}{m} \mathrm{Tr}(\boldsymbol{G}_0\boldsymbol{M}_1)^m
\end{aligned}$$

where $\boldsymbol{M} := \mathbb{B}_{ij} = -\mathbb{K}_{ij} + \mathbf{z}\delta_{ij}$ and $\boldsymbol{M}_0 := -\mathbb{K}_{ij}$; and we defined the unperturbed Green function $\boldsymbol{G}_0 := -\boldsymbol{M}_0^{-1}$, where the sign is convention.

Appendix D

Multiferroics

Ferromagnetic order is one of the types of ferroic order. The other ferroic states can be classified as ferroelectricity, related to the emergence of spontaneous electric polarization and its switchability by the external electric field. The other two are ferroelasticity, in which material exhibits spontaneous strain that can be switched with applied stress σ, and ferrotoroidicity, where we have a spontaneous vortex-like spin alignment with a toroidization $\mathbf{T}$ that can be switched by a toroidal field with the form $\mathbf{E} \times \mathbf{B}$.

A multiferroic is a material that can unite two or more of those ferroic orders. A subset of multiferroics are the magnetoelectric materials, which are defined as the ones that display a coupling between the electric and magnetic properties (polarization and magnetization). This includes all couplings phenomena that occur between charge and spin, and these materials are called magnetoelectric multiferroics [191].

D.1 A brief history of multiferroics

The term multiferroics appeared in literature only in the early 2000s [192, 193, 194, 195, 196], the quest for materials in which the magnetic order can be controlled with an electric field, or ferroelectric order that a magnetic field can control, started a long time before that. The search for new types of electric and magnetic order peaked in the first third of the 20th century, especially after the discovery of antiferromagnetism by L. Néel [15] and the discovery of ferroelectricity earlier by J. Valasek [197]. The first attempt at combining both orders came

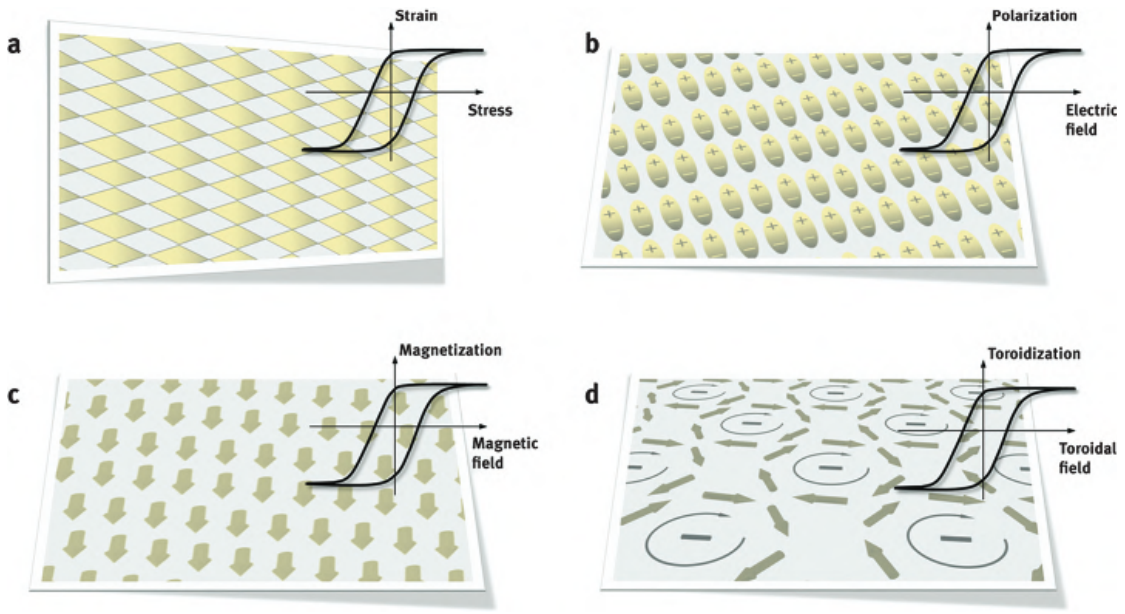

FIGURE D.1: Four types of ferroic order are classified as primary ferroic properties, namely ferroelasticity (a), ferroelectricity (b), ferromagnetism (c), and ferrotoroidicity (d) . Adapted from [191]

with the soviets in the 50s. Smolenskii and Ioffe [198] have introduced magnetic ions in ferroelectric perovskites to create long-range magnetic order along with the original ferroelectric state. This was successful and led to the synthesis of $Pb(Fe_{0.5}Nb_{0.5})O_3$ single crystal and poly-crystalline solid-solutions such as $(1-x)Pb(Fe_{2/3}W_{1/3})O_3 - xPb(Mg_{0.5}W_{0.5})O_3$ [199] which represent the first multiferroic that was designed on purpose and were called ferroelectromagnets. The most studied multiferroic compounds now are bismuth ferrite $BiFeO_3$ [200] and hexagonal manganites ($RMnO_3$, R = Sc, Y, In ...)[201, 202], and they were identified in the early 60s. However, the most famous multiferroics of that era were the boracites, due to the enormous linear magnetoelectric effect found in $Ni_3B_7O_{13}I$ [203], allowing switching of multiferroic state (ferromagnetic and ferroelectric) with magnetic and also electric fields. These experimental findings were complemented in 1970 with the development of the classification of ferroics [204]. Even though the 1970s knew a dip in interest in multiferroics, Newnham et al. in 1978 [205] reported a spin spiral order in Cr_2BeO_4 which broke spatial inversion symmetry and thus induced a spontaneous polarization, thus foreshadowing the physics of improper ferroelectricity (magnetically driven) which will be a path for

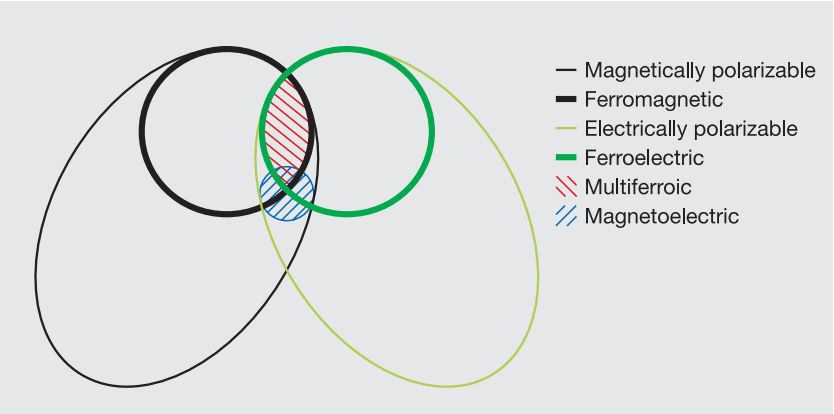

FIGURE D.2: Relationship between multiferroics and magnetoelectrics. Adapted from [207]

physicists to explore multiferroics with strong magnetoelectric coupling. This behavior was phenomenologically explained five years later with Bar'yakhtar and coworkers elucidating how a magnetic order can break spatial inversion symmetry and induce a spontaneous polarization [206]. In the 90s the new elaboration techniques, especially for thin films and the possibility to work at very low temperatures, refreshed the quest for multiferroics. In 2000 Spaldin (then Hill) explained why multiferroics are rare in nature by revisiting the idea of Ioffe and Smolenskii. Spaldin showed that displacive ferroelectricity and magnetic order are working against each other [208]. This work made the researchers restart the hunt for new multiferroics after understanding why they stagnates, leading to a new era of multiferroics whose main achievement is understanding the types of multiferroic materials and the mechanism behind magnetoelectric couplings.

D.2 Types of multiferroics

Multiferroics can be described as the coexistence of two ferroic orders as seen in Fig.D.2; more precisely, it now refers to a material that exhibit a ferroelectric order and magnetic order (ferro, antiferro, ferri, or helimagnetic order). We can distinguish two main types of multiferroic materials when discussing the coexistence of ferroelectric and ferromagnetic order. Type I are the materials where both orders can emerge independently, thus the existence of two phase transitions, one for the magnetic order and the second for the ferroelectric order. Below the smallest of them, we have the coexistence of both orders. On the other hand, type II

refers to the multiferroics where both orders emerge jointly, thus sharing a transition temperature, and one is inducing the other via magnetoelectric coupling [209].

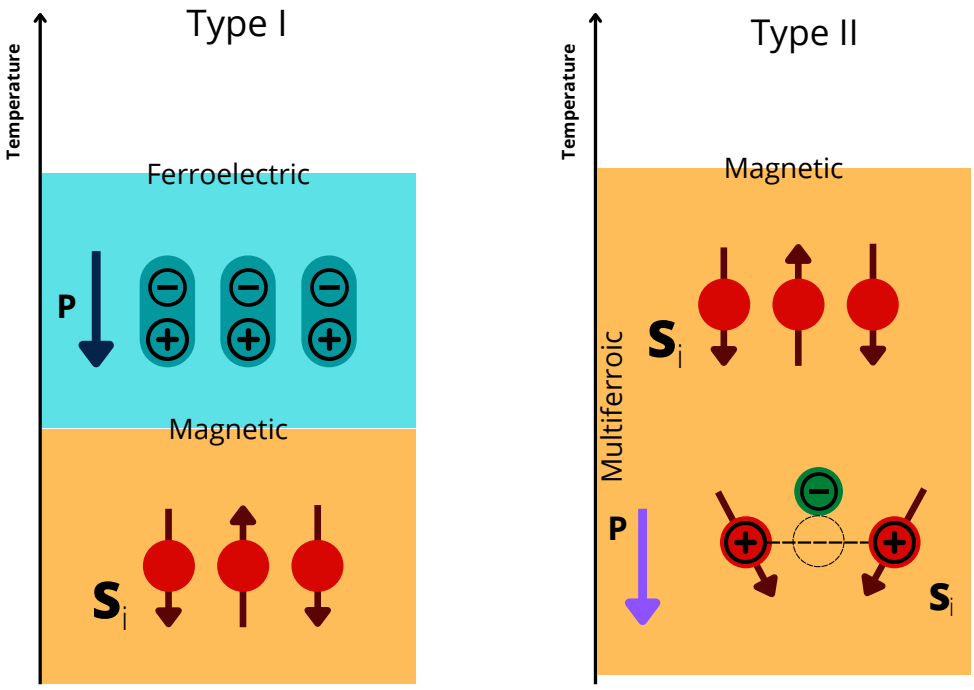

FIGURE D.3: Types of multiferroicity

D.3 Mechanisms of multiferroicity

The new era of multiferroics managed to understand the mechanisms behind the emerging ferroelectric and magnetic orders. We can distinguish four main classes of multiferroics according to the mechanism behind multiferroicity [210, 211]. In the case of the first three classes, we find that orders emerge independently, thus qualifying them as type I multiferroics, and the last classes can be subdivided into three different spin-driven mechanisms which qualify such materials as type II multiferroics.

D.3.1 Lone-pair mechanism

TThe anisotropic distribution of unbounded valence electrons around the ion creates a spatial asymmetry, thus inducing polarization. This mechanism is responsible for ferroelectric behavior at room temperature of $BiFeO_3$, in which pair of Bi^{3+} $6s$ valence electrons that shift away from the Bi^{3+} ion and towards the FeO_6 octahedra, giving rise to a spontaneous polarization along [111] direction [212] as seen in Fig.D.4.a. This behavior happens below $T_C = 1103$ K [213]. Moreover, a long-range periodic antiferromagnetic structure emerges below $T_N = 643$ K [214].

D.3.2 Geometric ferroelectricity

Another mechanism for type I multiferroics is the geometric ferroelectricity, where geometric constraints and space-packing effects cause structural instabilities and lead to ionic shifts, which result in polar states. An example of this is hexagonal manganites, h-$R$$MnO_3$ (R = Sc, Y, Dy-Lu ...) where unit cell tripling drives the emergence of ferroelectric state for $T_C \simeq 1200$ K [215], along with a magnetic ordering below $T_N = 120$ K [202, 216]. In h-$R$$MnO_3$, the polarization emerges from a tilt and deformation of MnO_5 bipyramids, which displace the rare-earth ions R leading to a spontaneous polarization along the [001], the Fig.D.4.b illustrate this mechanism

D.3.3 Charge ordering

TThe non-uniform distribution of valence electrons around the host ions in a crystal lattice can form a periodic superstructure. For example, in $LuFe_2O_3$ [217], the charge ordering creates an alternating sequence of Fe^{3+} and Fe^{2+} ions, which creates a spontaneous polarization between the two alternating layers [218] as depicted in Fig.D.4.c

D.3.4 Spin-driven mechanisms

Ferroelectricity arises from breaking in spatial symmetry and magnetic orders can sometimes break inversion symmetry. The spin-charge interaction may transfer the non-centrosymmetry from the magnetic ordering to the electric lattice, inducing the formation of a polar states. This so-called improper ferroelectricity,

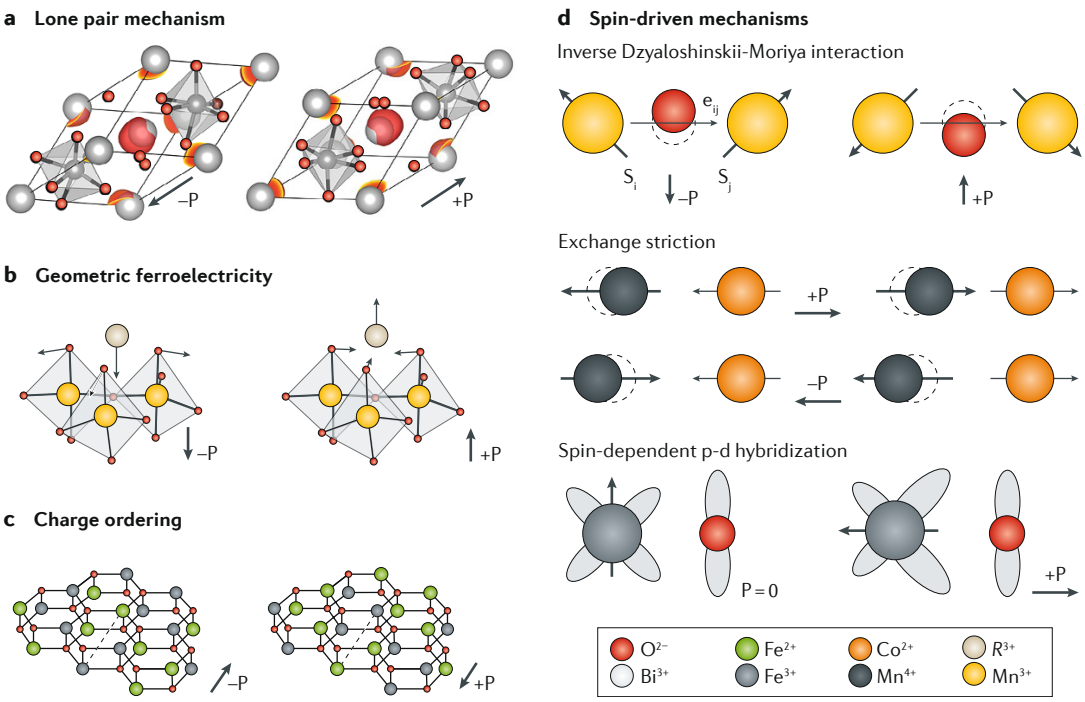

FIGURE D.4: Mechanisms of multiferroicity. Adapted from [209]

which is magnetically driven, is different from regular displacive ferroelectricity that inhibits magnetic ordering. There are three different spin-driven mechanisms for ferroelectricity. The first is inverse Dzyaloshinskii-Moriya interaction (DMI), where the polar displacement is induced by antisymmetric spin exchange and yields a one-to-one correlation between the electric polarization and antiferromagnetic order and was first found in Cr_2BeO_4 [205] and $CaMn_7O_{12}$ [219]. In contrast to DMI, the second type is related to Heisenberg-like interaction and is called exchange striction, which describes the acentric shift of charges due to Heisenberg interaction. The polarization that emerges from this type is usually of higher orders than inverse DMI and was first observed in $TbMn_2O_5$ [220].

The last spin-driven mechanism is the spin-dependent *p-d* hybridization where modulations of magnetic $3d$ and ligand $2p$ orbitals (grey clouds in Fig.D.4.d) yield a spontaneous polarization along the bond direction in delafossite such as $CuFeO_2$ [221].

Bibliography

[1] A. N. Bogdanov and U. K. Rößler. "Chiral Symmetry Breaking in Magnetic Thin Films and Multilayers". In: *Phys. Rev. Lett.* 87 (3 2001), p. 037203. DOI: 10.1103/PhysRevLett.87.037203. URL: https://link.aps.org/doi/10.1103/PhysRevLett.87.037203.

[2] S. Seki et al. "Observation of Skyrmions in a Multiferroic Material". In: *Science* 336.6078 (2012), pp. 198–201. DOI: 10.1126/science.1214143. eprint: https://www.science.org/doi/pdf/10.1126/science.1214143. URL: https://www.science.org/doi/abs/10.1126/science.1214143.

[3] Jan-Willem G. Bos, Claire V. Colin, and Thomas T. M. Palstra. "Magnetoelectric coupling in the cubic ferrimagnet Cu_2OSeO_3". In: *Phys. Rev. B* 78 (9 2008), p. 094416. DOI: 10.1103/PhysRevB.78.094416. URL: https://link.aps.org/doi/10.1103/PhysRevB.78.094416.

[4] E. Ruff et al. "Magnetoelectric effects in the skyrmion host material Cu 2 OSeO 3". In: *Scientific Reports* 5 (2015), pp. 1–9. ISSN: 20452322. DOI: 10.1038/srep15025.

[5] J. S. White et al. "Electric field control of the skyrmion lattice in Cu 2OSeO 3". In: *Journal of Physics Condensed Matter* 24.43 (2012).

[6] Lev D. Landau. "On the Theory of Phase Transitions". In: *Zh. Eksp. Teor. Fiz* 7 (1937), pp. 19–32.

[7] H. N. Russell and F. A. Saunders. "New Regularities in the Spectra of the Alkaline Earths". In: 61 (Jan. 1925), p. 38. DOI: 10.1086/142872.

[8] R.M. White. *Quantum Theory of Magnetism: Magnetic Properties of Materials*. Springer Series in Solid-State Sciences. Springer Berlin Heidelberg, 2007. ISBN: 9783540690252. URL: https://books.google.fr/books?id=LQBHAAAAQBAJ.

[9] L.P. Lévy. *Magnétisme et supraconductivité*. SAVOIRS ACTUELS. EDP Sciences, 2012. ISBN: 9782759802791. URL: https://books.google.fr/books?id=yIoo4vE_5KIC.

[10] Stephen Blundell. *Magnetism in condensed matter*. Includes bibliographical references and index. Oxford ; New York : Oxford University Press, 2001., 2001. URL: https://search.library.wisc.edu/catalog/999921680802121.

[11] J. Hubbard and Brian Hilton Flowers. "Electron correlations in narrow energy bands". In: *Proceedings of the Royal Society of London. Series A. Mathematical and Physical Sciences* 276.1365 (1963), pp. 238–257. DOI: 10.1098/rspa.1963.0204. eprint: https://royalsocietypublishing.org/doi/pdf/10.1098/rspa.1963.0204. URL: https://royalsocietypublishing.org/doi/abs/10.1098/rspa.1963.0204.

[12] Edmund Clifton Stoner. "Collective electron ferromagnetism". In: *Proceedings of the Royal Society of London. Series A. Mathematical and Physical Sciences* 165.922 (1938), pp. 372–414. DOI: 10.1098/rspa.1938.0066. eprint: https://royalsocietypublishing.org/doi/pdf/10.1098/rspa.1938.0066. URL: https://royalsocietypublishing.org/doi/abs/10.1098/rspa.1938.0066.

[13] W. Heisenberg. "Zur Theorie des Ferromagnetismus". In: *Zeitschrift für Physik* 49 (1928), pp. 619–636. URL: https://doi.org/10.1007/BF01328601.

[14] Paul Adrien Maurice Dirac and Ralph Howard Fowler. "The quantum theory of the electron". In: *Proceedings of the Royal Society of London. Series A, Containing Papers of a Mathematical and Physical Character* 117.778 (1928), pp. 610–624. DOI: 10.1098/rspa.1928.0023.

[15] Néel, Louis. "Propriétés magnétiques de l'état métallique et énergie d'interaction entre atomes magnétiques". In: *Ann. Phys.* 11.5 (1936), pp. 232–279. DOI: 10.1051/anphys/193611050232. URL: https://doi.org/10.1051/anphys/193611050232.

[16] Michael El-Batanouny. "Advanced Quantum Condensed Matter Physics: One-Body, Many-Body, and Topological Perspectives". In: Cambridge University Press, 2020, 712–738.

[17] J. H. van Vleck. "On the Anisotropy of Cubic Ferromagnetic Crystals". In: *Phys. Rev.* 52 (11 1937), pp. 1178–1198. DOI: 10.1103/PhysRev.52.1178. URL: https://link.aps.org/doi/10.1103/PhysRev.52.1178.

[18] I. Dzyaloshinskii. "A thermodynamic theory of "weak" ferromagnetism of antiferromagnetics". In: *Journal of Physics and Chemistry of Solids* 4.4 (1958), pp. 241–255. ISSN: 00223697. DOI: 10.1016/0022-3697(58)90076-3. URL: https://linkinghub.elsevier.com/retrieve/pii/0022369758900763.

[19] Tôru Moriya. "Anisotropic superexchange interaction and weak ferromagnetism". In: *Physical Review* 120.1 (1960), pp. 91–98. ISSN: 0031899X. DOI: 10.1103/PhysRev.120.91.

[20] A. Fert and Peter M. Levy. "Role of Anisotropic Exchange Interactions in Determining the Properties of Spin-Glasses". In: *Phys. Rev. Lett.* 44 (23 1980), pp. 1538–1541. DOI: 10.1103/PhysRevLett.44.1538. URL: https://link.aps.org/doi/10.1103/PhysRevLett.44.1538.

[21] H.A Kramers. "L'interaction Entre les Atomes Magnétogènes dans un Cristal Paramagnétique". In: *Physica* 1.1 (1934), pp. 182–192. ISSN: 0031-8914. DOI: https://doi.org/10.1016/S0031-8914(34)90023-9. URL: https://www.sciencedirect.com/science/article/pii/S0031891434900239.

[22] P. W. Anderson. "New Approach to the Theory of Superexchange Interactions". In: *Phys. Rev.* 115 (1 1959), pp. 2–13. DOI: 10.1103/PhysRev.115.2. URL: https://link.aps.org/doi/10.1103/PhysRev.115.2.

[23] Charles Kittel. *Solid state physics*. Vol. 3. Shell Development Company, 1955.

[24] Nicola A. Spaldin. *Magnetic materials : fundamentals and device applications*. Cambridge univ. press, 2003.

[25] Akio Yoshimori. "A New Type of Antiferromagnetic Structure in the Rutile Type Crystal". In: *Journal of the Physical Society of Japan* 14.6 (1959), pp. 807–821. DOI: 10.1143/JPSJ.14.807. URL: https://doi.org/10.1143/JPSJ.14.807.

[26] Jan Masell et al. "Combing the helical phase of chiral magnets with electric currents". In: *Phys. Rev. B* 102 (18 2020), p. 180402. DOI: 10.1103/PhysRevB.102.180402. URL: https://link.aps.org/doi/10.1103/PhysRevB.102.180402.

[27] M. A. Ruderman and C. Kittel. "Indirect Exchange Coupling of Nuclear Magnetic Moments by Conduction Electrons". In: *Phys. Rev.* 96 (1 1954), pp. 99–102. DOI: 10.1103/PhysRev.96.99. URL: https://link.aps.org/doi/10.1103/PhysRev.96.99.

[28] Tadao Kasuya. "A Theory of Metallic Ferro- and Antiferromagnetism on Zener's Model". In: *Progress of Theoretical Physics* 16.1 (July 1956), pp. 45–57. ISSN: 0033-068X. DOI: 10.1143/PTP.16.45. eprint: https://academic.oup.com/ptp/article-pdf/16/1/45/5266722/16-1-45.pdf. URL: https://doi.org/10.1143/PTP.16.45.

[29] Kei Yosida. "Magnetic Properties of Cu-Mn Alloys". In: *Phys. Rev.* 106 (5 1957), pp. 893–898. DOI: 10.1103/PhysRev.106.893. URL: https://link.aps.org/doi/10.1103/PhysRev.106.893.

[30] A. S. Sukhanov et al. "Frustration model and spin excitations in the helimagnet FeP". In: *Phys. Rev. B* 105 (13 2022), p. 134424. DOI: 10.1103/PhysRevB.105.134424. URL: https://link.aps.org/doi/10.1103/PhysRevB.105.134424.

[31] T. Kimura, J. C. Lashley, and A. P. Ramirez. "Inversion-symmetry breaking in the noncollinear magnetic phase of the triangular-lattice antiferromagnet $CuFeO_2$". In: *Phys. Rev. B* 73 (22 2006), p. 220401. DOI: 10.1103/PhysRevB.73.220401. URL: https://link.aps.org/doi/10.1103/PhysRevB.73.220401.

[32] O. Nakanishi et al. "The origin of the helical spin density wave in MnSi". In: *Solid State Communications* 35.12 (1980), pp. 995–998. ISSN: 0038-1098. DOI: https://doi.org/10.1016/0038-1098(80)91004-2. URL: https://www.sciencedirect.com/science/article/pii/0038109880910042.

[33] M. T. Birch et al. "Real-space imaging of confined magnetic skyrmion tubes". In: *Nature Communications* 11.1 (2020), p. 1726. ISSN: 2041-1723. DOI: 10.1038/s41467-020-15474-8. arXiv: 1909.04528. URL: http://dx.doi.org/10.1038/s41467-020-15474-8http://www.nature.com/articles/s41467-020-15474-8.

[34] I Sosnowska, T P Neumaier, and E Steichele. "Spiral magnetic ordering in bismuth ferrite". In: *Journal of Physics C: Solid State Physics* 15.23 (1982), p. 4835. DOI: 10.1088/0022-3719/15/23/020. URL: https://dx.doi.org/10.1088/0022-3719/15/23/020.

[35] A. Haykal et al. "Antiferromagnetic textures in BiFeO3 controlled by strain and electric field". In: *Nature Communications* 11.1 (2020), p. 1704. ISSN: 2041-1723. DOI: 10.1038/s41467-020-15501-8. URL: https://doi.org/10.1038/s41467-020-15501-8.

[36] Bin Xu et al. "First-principles study of spin spirals in the multiferroic $BiFeO_3$". In: *Phys. Rev. B* 103 (21 2021), p. 214423. DOI: 10.1103/PhysRevB.103.214423. URL: https://link.aps.org/doi/10.1103/PhysRevB.103.214423.

[37] Leon Balents. "Spin liquids in frustrated magnets". In: *Nature* 464 (2010), pp. 199–208.

[38] E. Kermarrec et al. "Classical Spin Liquid State in the $S = \frac{5}{2}$ Heisenberg Kagome Antiferromagnet $Li_9Fe_3(P_2O_7)_3(PO_4)_2$". In: *Phys. Rev. Lett.* 127 (15 2021), p. 157202. DOI: 10.1103/PhysRevLett.127.157202. URL: https://link.aps.org/doi/10.1103/PhysRevLett.127.157202.

[39] Steven T. Bramwell and Michel J. P. Gingras. "Spin Ice State in Frustrated Magnetic Pyrochlore Materials". In: *Science* 294.5546 (2001), pp. 1495–1501.

[40] Christopher L. Henley. "The "Coulomb Phase" in Frustrated Systems". In: *Annual Review of Condensed Matter Physics* 1.1 (2010), pp. 179–210.

[41] J. Knolle and R. Moessner. "A Field Guide to Spin Liquids". In: *Annual Review of Condensed Matter Physics* 10.1 (2019), pp. 451–472. DOI: 10.1146/annurev-conmatphys-031218-013401. eprint: https://doi.org/10.1146/annurev-conmatphys-031218-013401. URL: https://doi.org/10.1146/annurev-conmatphys-031218-013401.

[42] Shang Gao et al. "Spiral Spin Liquid on a Honeycomb Lattice". In: *Phys. Rev. Lett.* 128 (22 2022), p. 227201. DOI: 10.1103/PhysRevLett.128.227201. URL: https://link.aps.org/doi/10.1103/PhysRevLett.128.227201.

[43] Doron Bergman et al. "Order-by-disorder and spiral spin-liquid in frustrated diamond-lattice antiferromagnets". In: *Nature Physics* 3.7 (2007), pp. 487–491. ISSN: 1745-2473. DOI: 10.1038/nphys622. arXiv: 0612001 [cond-mat]. URL: http://www.nature.com/articles/nphys622.

[44] P Bak and M H Jensen. "Theory of helical magnetic structures and phase transitions in MnSi and FeGe". In: *Journal of Physics C: Solid State Physics* 13.31 (1980), p. L881. DOI: 10.1088/0022-3719/13/31/002. URL: https://dx.doi.org/10.1088/0022-3719/13/31/002.

[45] Jiadong. editor Zang, Vincent. editor. Cros, and Axel. editor. Hoffmann. *Topology in Magnetism*. 1st ed. 2018. 2018. ISBN: 9783319973340. URL: http://lib.ugent.be/catalog/ebk01:4100000006675108.

[46] T. H.R. Skyrme. "A unified field theory of mesons and baryons". In: *Nuclear Physics* 31.C (1962), pp. 556–569. ISSN: 00295582. DOI: 10.1016/0029-5582(62)90775-7.

[47] A. Bogdanov and A. Hubert. "Thermodynamically stable magnetic vortex states in magnetic crystals". In: *Journal of Magnetism and Magnetic Materials* 138.3 (1994), pp. 255–269. ISSN: 0304-8853. DOI: https://doi.org/10.1016/0304-8853(94)90046-9. URL: https://www.sciencedirect.com/science/article/pii/0304885394900469.

[48] U. K. Rößler, A. N. Bogdanov, and C. Pfleiderer. "Spontaneous skyrmion ground states in magnetic metals". In: *Nature* 442.7104 (2006), pp. 797–801. ISSN: 1476-4687. DOI: 10.1038/nature05056. URL: https://doi.org/10.1038/nature05056.

[49] S. Muhlbauer et al. "Skyrmion Lattice in a Chiral Magnet". In: *Science* 323.5916 (2009), pp. 915–919. ISSN: 0036-8075. DOI: 10.1126/science.1166767. arXiv: science.1166767 [10.1126]. URL: https://www.sciencemag.org/lookup/doi/10.1126/science.1166767.

[50] X. Z. Yu et al. "Real-space observation of a two-dimensional skyrmion crystal". In: *Nature* 465.7300 (2010), pp. 901–904. ISSN: 0028-0836. DOI: 10.1038/nature09124. URL: http://www.nature.com/articles/nature09124.

[51] W. Münzer et al. "Skyrmion lattice in the doped semiconductor <math display="inline"> <mrow> <msub> <mrow> <mtext>Fe</mtext> </mrow> <mrow> <mn>1</mn> <mo></mo> <mi>x</mi> </mrow> </msub> <msub> <mrow> <mtext>Co</mtext> </mrow> <mi>x</mi> </msub> <mtext>Si</mtext> </mrow>". In: *Physical Review B* 81.4 (2010), p. 041203. ISSN: 1098-0121. DOI: 10.1103/PhysRevB.81.041203. URL: https://link.aps.org/doi/10.1103/PhysRevB.81.041203.

[52] I. Kézsmárki et al. "Néel-type skyrmion lattice with confined orientation in the polar magnetic semiconductor GaV4S8". In: *Nature Materials* 14.11 (2015), pp. 1116–1122. ISSN: 1476-4660. DOI: 10.1038/nmat4402. URL: https://doi.org/10.1038/nmat4402.

[53] X. Z. Yu et al. "Near room-temperature formation of a skyrmion crystal in thin-films of the helimagnet FeGe". In: *Nature Materials* 10.2 (2011), pp. 106–109. ISSN: 1476-1122. DOI: 10.1038/nmat2916. URL: http://www.nature.com/articles/nmat2916.

[54] Marie Hervé et al. "Stabilizing spin spirals and isolated skyrmions at low magnetic field exploiting vanishing magnetic anisotropy". In: *Nature Communications* 9.1 (2018), p. 1015. ISSN: 2041-1723. DOI: 10.1038/s41467-018-03240-w. URL: https://doi.org/10.1038/s41467-018-03240-w.

[55] Olivier Boulle et al. "Room-temperature chiral magnetic skyrmions in ultrathin magnetic nanostructures". In: *Nature Nanotechnology* 11.5 (2016), pp. 449–454. ISSN: 1748-3395. DOI: 10.1038/nnano.2015.315. URL: https://doi.org/10.1038/nnano.2015.315.

[56] Seonghoon Woo et al. "Observation of room-temperature magnetic skyrmions and their current-driven dynamics in ultrathin metallic ferromagnets". In:

Nature Materials 15.5 (2016), pp. 501–506. ISSN: 1476-4660. DOI: 10.1038/nmat4593. URL: https://doi.org/10.1038/nmat4593.

[57] William Legrand et al. "Room-temperature stabilization of antiferromagnetic skyrmions in synthetic antiferromagnets". In: *Nature Materials* 19.1 (2020), pp. 34–42. ISSN: 1476-4660. DOI: 10.1038/s41563-019-0468-3. URL: https://doi.org/10.1038/s41563-019-0468-3.

[58] Masahito Mochizuki. "Microwave-Driven Dynamics of Magnetic Skyrmions Under a Tilted Magnetic Field: Magnetic Resonances, Translational Motions, and Spin-Motive Forces", bookTitle="Chirality, Magnetism and Magnetoelectricity: Separate Phenomena and Joint Effects in Metamaterial Structures". In: Springer International Publishing, 2021, pp. 183–206. DOI: 10.1007/978-3-030-62844-4_8. URL: https://doi.org/10.1007/978-3-030-62844-4_8.

[59] Stuart S. P. Parkin, Masamitsu Hayashi, and Luc Thomas. "Magnetic Domain-Wall Racetrack Memory". In: *Science* 320.5873 (2008), pp. 190–194. DOI: 10.1126/science.1145799. eprint: https://www.science.org/doi/pdf/10.1126/science.1145799. URL: https://www.science.org/doi/abs/10.1126/science.1145799.

[60] Yan Zhou and Motohiko Ezawa. "A reversible conversion between a skyrmion and a domain-wall pair in a junction geometry". In: *Nature Communications* 5.1 (2014), p. 4652. ISSN: 2041-1723. DOI: 10.1038/ncomms5652. URL: https://doi.org/10.1038/ncomms5652.

[61] Wang Kang et al. "Voltage controlled magnetic skyrmion motion for racetrack memory". In: *Scientific Reports* 6.February (2016), pp. 1–11. ISSN: 20452322. DOI: 10.1038/srep23164. URL: http://dx.doi.org/10.1038/srep23164.

[62] Albert Fert, Vincent Cros, and João Sampaio. "Skyrmions on the track". In: *Nature Nanotechnology* 8.3 (2013), pp. 152–156. DOI: 10.1038/nnano.2013.29. URL: http://www.nature.com/articles/nnano.2013.29.

[63] Junichi Iwasaki, Masahito Mochizuki, and Naoto Nagaosa. "Current-induced skyrmion dynamics in constricted geometries". In: *Nature Nanotechnology* 8.10 (2013), pp. 742–747. ISSN: 1748-3395. DOI: 10.1038/nnano.2013.176. URL: https://doi.org/10.1038/nnano.2013.176.

[64] Niklas Romming et al. "Writing and Deleting Single Magnetic Skyrmions". In: *Science* 341.6146 (2013), pp. 636–639. DOI: 10.1126/science.1240573. eprint: https://www.science.org/doi/pdf/10.1126/science.1240573. URL: https://www.science.org/doi/abs/10.1126/science.1240573.

[65] P. Bruno, V. K. Dugaev, and M. Taillefumier. "Topological Hall Effect and Berry Phase in Magnetic Nanostructures". In: *Phys. Rev. Lett.* 93 (9 2004), p. 096806. DOI: 10.1103/PhysRevLett.93.096806. URL: https://link.aps.org/doi/10.1103/PhysRevLett.93.096806.

[66] A. Neubauer et al. "Topological Hall Effect in the *A* Phase of MnSi". In: *Phys. Rev. Lett.* 102 (18 2009), p. 186602. DOI: 10.1103/PhysRevLett.102.186602. URL: https://link.aps.org/doi/10.1103/PhysRevLett.102.186602.

[67] Wanjun Jiang et al. "Direct observation of the skyrmion Hall effect". In: *Nature Physics* 13.2 (2017), pp. 162–169. ISSN: 1745-2481. DOI: 10.1038/nphys3883. URL: https://doi.org/10.1038/nphys3883.

[68] Kai Litzius et al. "Skyrmion Hall effect revealed by direct time-resolved X-ray microscopy". In: *Nature Physics* 13.2 (2017), pp. 170–175. ISSN: 1745-2481. DOI: 10.1038/nphys4000. URL: https://doi.org/10.1038/nphys4000.

[69] B. Berg and M. Lüscher. "Definition and statistical distributions of a topological number in the lattice O(3) -model". In: *Nuclear Physics B* 190.2 (1981), pp. 412–424. ISSN: 0550-3213. DOI: https://doi.org/10.1016/0550-3213(81)90568-X. URL: https://www.sciencedirect.com/science/article/pii/055032138190568X.

[70] K. J. A. Franke et al. "Investigating the magnetic ground state of the skyrmion host material Cu2OSeO3 using long-wavelength neutron diffraction". In: *AIP Advances* 9.12 (2019), p. 125228. DOI: 10.1063/1.5129400. URL: https://doi.org/10.1063/1.5129400.

[71] Takaaki Dohi et al. "Formation and current-induced motion of synthetic antiferromagnetic skyrmion bubbles". In: *Nature Communications* 10.1 (2019), p. 5153. ISSN: 2041-1723. DOI: 10.1038/s41467-019-13182-6. URL: https://doi.org/10.1038/s41467-019-13182-6.

[72] Erlend G. Tveten et al. "Staggered Dynamics in Antiferromagnets by Collective Coordinates". In: *Phys. Rev. Lett.* 110 (12 2013), p. 127208. DOI: 10.1103/PhysRevLett.110.127208. URL: https://link.aps.org/doi/10.1103/PhysRevLett.110.127208.

[73] Joseph Barker and Oleg A. Tretiakov. "Static and Dynamical Properties of Antiferromagnetic Skyrmions in the Presence of Applied Current and Temperature". In: *Phys. Rev. Lett.* 116 (14 2016), p. 147203. DOI: 10.1103/

PhysRevLett.116.147203. URL: https://link.aps.org/doi/10.1103/PhysRevLett.116.147203.

[74] Chendong Jin et al. "Dynamics of antiferromagnetic skyrmion driven by the spin Hall effect". In: *Applied Physics Letters* 109.18 (2016), p. 182404. DOI: 10.1063/1.4967006. eprint: https://doi.org/10.1063/1.4967006. URL: https://doi.org/10.1063/1.4967006.

[75] Xue Liang et al. "Antiferromagnetic skyrmion-based logic gates controlled by electric currents and fields". In: *Applied Physics Letters* 119.6 (2021), p. 062403. DOI: 10.1063/5.0056259. eprint: https://doi.org/10.1063/5.0056259. URL: https://doi.org/10.1063/5.0056259.

[76] Seonghoon Woo et al. "Current-driven dynamics and inhibition of the skyrmion Hall effect of ferrimagnetic skyrmions in GdFeCo films". In: *Nature Communications* 9.1 (2018), p. 959. ISSN: 2041-1723. DOI: 10.1038/s41467-018-03378-7. URL: https://doi.org/10.1038/s41467-018-03378-7.

[77] Michael A. Rampp, Elio J. König, and Jörg Schmalian. "Topologically Enabled Superconductivity". In: *Phys. Rev. Lett.* 129 (7 2022), p. 077001. DOI: 10.1103/PhysRevLett.129.077001. URL: https://link.aps.org/doi/10.1103/PhysRevLett.129.077001.

[78] Börge Göbel, Ingrid Mertig, and Oleg A. Tretiakov. "Beyond skyrmions: Review and perspectives of alternative magnetic quasiparticles". In: *Physics Reports* 895 (2021). Beyond skyrmions: Review and perspectives of alternative magnetic quasiparticles, pp. 1–28. ISSN: 0370-1573. DOI: https://doi.org/10.1016/j.physrep.2020.10.001. URL: https://www.sciencedirect.com/science/article/pii/S0370157320303525.

[79] L Brey et al. "Skyrme and meron crystals in quantum Hall ferromagnets". In: *Physica Scripta* 1996.T66 (1996), p. 154. DOI: 10.1088/0031-8949/1996/T66/027. URL: https://dx.doi.org/10.1088/0031-8949/1996/T66/027.

[80] R. Côté et al. "Orbital and interlayer skyrmion crystals in bilayer graphene". In: *Phys. Rev. B* 82 (24 2010), p. 245307. DOI: 10.1103/PhysRevB.82.245307. URL: https://link.aps.org/doi/10.1103/PhysRevB.82.245307.

[81] F. P. Chmiel et al. "Observation of magnetic vortex pairs at room temperature in a planar α-Fe2O3/Co heterostructure". In: *Nature Materials* 17.7 (2018), pp. 581–585. ISSN: 1476-4660. DOI: 10.1038/s41563-018-0101-x. URL: https://doi.org/10.1038/s41563-018-0101-x.

[82] X. Z. Yu et al. "Transformation between meron and skyrmion topological spin textures in a chiral magnet". In: *Nature* 564.7734 (2018), pp. 95–98. ISSN: 1476-4687. DOI: 10.1038/s41586-018-0745-3. URL: https://doi.org/10.1038/s41586-018-0745-3.

[83] N. Gao et al. "Creation and annihilation of topological meron pairs in in-plane magnetized films". In: *Nature Communications* 10.1 (2019), p. 5603. ISSN: 2041-1723. DOI: 10.1038/s41467-019-13642-z. URL: https://doi.org/10.1038/s41467-019-13642-z.

[84] Mathias Augustin et al. "Properties and dynamics of meron topological spin textures in the two-dimensional magnet CrCl3". In: *Nature Communications* 12.1 (2021), p. 185. ISSN: 2041-1723. DOI: 10.1038/s41467-020-20497-2. URL: https://doi.org/10.1038/s41467-020-20497-2.

[85] S. Ostlund. "Interactions between topological point singularities". In: *Phys. Rev. B* 24 (1 1981), pp. 485–488. DOI: 10.1103/PhysRevB.24.485. URL: https://link.aps.org/doi/10.1103/PhysRevB.24.485.

[86] Man-hot Lau and Chandan Dasgupta. "Numerical investigation of the role of topological defects in the three-dimensional Heisenberg transition". In: *Phys. Rev. B* 39 (10 1989), pp. 7212–7222. DOI: 10.1103/PhysRevB.39.7212. URL: https://link.aps.org/doi/10.1103/PhysRevB.39.7212.

[87] D. P. Landau and K. Binder. "Phase diagrams and critical behavior of a two-dimensional anisotropic Heisenberg antiferromagnet". In: *Phys. Rev. B* 24 (3 1981), pp. 1391–1403. DOI: 10.1103/PhysRevB.24.1391. URL: https://link.aps.org/doi/10.1103/PhysRevB.24.1391.

[88] Y. Nahas et al. "Topological Point Defects in Relaxor Ferroelectrics". In: *Phys. Rev. Lett.* 116 (12 2016), p. 127601. DOI: 10.1103/PhysRevLett.116.127601. URL: https://link.aps.org/doi/10.1103/PhysRevLett.116.127601.

[89] V. L. Berezinskiĭ. "Destruction of Long-range Order in One-dimensional and Two-dimensional Systems having a Continuous Symmetry Group I. Classical Systems". In: *Soviet Journal of Experimental and Theoretical Physics* 32 (Jan. 1971), p. 493.

[90] J M Kosterlitz and D J Thouless. "Ordering, metastability and phase transitions in two-dimensional systems". In: *Journal of Physics C: Solid State Physics* 6.7 (1973), p. 1181. DOI: 10.1088/0022-3719/6/7/010. URL: https://dx.doi.org/10.1088/0022-3719/6/7/010.

[91] G. H. Derrick. "Comments on Nonlinear Wave Equations as Models for Elementary Particles". In: *Journal of Mathematical Physics* 5.9 (Dec. 2004), pp. 1252–1254. ISSN: 0022-2488. DOI: 10.1063/1.1704233. URL: https://doi.org/10.1063/1.1704233.

[92] L. D. Faddeev. "Some comments on the many-dimensional solitons". In: *Letters in Mathematical Physics* 1.4 (1976), pp. 289–293. ISSN: 1573-0530. DOI: 10.1007/BF00398483. URL: https://doi.org/10.1007/BF00398483.

[93] Jarmo Hietarinta and Petri Salo. "Faddeev-Hopf knots: dynamics of linked un-knots". In: *Physics Letters B* 451.1 (1999), pp. 60–67. ISSN: 0370-2693. DOI: https://doi.org/10.1016/S0370-2693(99)00054-4. URL: https://www.sciencedirect.com/science/article/pii/S0370269399000544.

[94] I.L. Bogolubsky. "Three-dimensional topological solitons in the lattice model of a magnet with competing interactions". In: *Physics Letters A* 126.8 (1988), pp. 511–514. ISSN: 0375-9601. DOI: https://doi.org/10.1016/0375-9601(88)90049-7. URL: https://www.sciencedirect.com/science/article/pii/0375960188900497.

[95] X. S. Wang, A. Qaiumzadeh, and A. Brataas. "Current-Driven Dynamics of Magnetic Hopfions". In: *Phys. Rev. Lett.* 123 (14 2019), p. 147203. DOI: 10.1103/PhysRevLett.123.147203. URL: https://link.aps.org/doi/10.1103/PhysRevLett.123.147203.

[96] J. H. C. Whitehead. "An Expression of Hopf's Invariant as an Integral*". In: *Proceedings of the National Academy of Sciences* 33.5 (1947), pp. 117–123. DOI: 10.1073/pnas.33.5.117. eprint: https://www.pnas.org/doi/pdf/10.1073/pnas.33.5.117. URL: https://www.pnas.org/doi/abs/10.1073/pnas.33.5.117.

[97] Jens Gladikowski and Meik Hellmund. "Static solitons with nonzero Hopf number". In: *Phys. Rev. D* 56 (8 1997), pp. 5194–5199. DOI: 10.1103/PhysRevD.56.5194. URL: https://link.aps.org/doi/10.1103/PhysRevD.56.5194.

[98] I. Luk'yanchuk et al. "Hopfions emerge in ferroelectrics". In: *Nature Communications* 11.1 (2020), p. 2433. ISSN: 2041-1723. DOI: 10.1038/s41467-020-16258-w. URL: https://doi.org/10.1038/s41467-020-16258-w.

[99] Jung-Shen B. Tai and Ivan I. Smalyukh. "Three-dimensional crystals of adaptive knots". In: *Science* 365.6460 (2019), pp. 1449–1453. DOI: 10.1126/science.aay1638. eprint: https://www.science.org/doi/pdf/10.1126/science.aay1638. URL: https://www.science.org/doi/abs/10.1126/science.aay1638.

[100] Noah Kent et al. "Creation and observation of Hopfions in magnetic multilayer systems". In: *Nature Communications* 12.1 (2021), p. 1562. ISSN: 2041-1723. DOI: 10.1038/s41467-021-21846-5. URL: https://doi.org/10.1038/s41467-021-21846-5.

[101] Filipp N. Rybakov et al. "Magnetic hopfions in solids". In: *APL Materials* 10.11 (2022), p. 111113. DOI: 10.1063/5.0099942. eprint: https://doi.org/10.1063/5.0099942. URL: https://doi.org/10.1063/5.0099942.

[102] S. Grytsiuk et al. "Topological–chiral magnetic interactions driven by emergent orbital magnetism". In: *Nature Communications* 11.1 (2020), p. 511. ISSN: 2041-1723. DOI: 10.1038/s41467-019-14030-3. URL: https://doi.org/10.1038/s41467-019-14030-3.

[103] Börge Göbel et al. "Topological Hall signatures of magnetic hopfions". In: *Phys. Rev. Res.* 2 (1 2020), p. 013315. DOI: 10.1103/PhysRevResearch.2.013315. URL: https://link.aps.org/doi/10.1103/PhysRevResearch.2.013315.

[104] M. Born and R. Oppenheimer. "Zur Quantentheorie der Molekeln". In: *Annalen der Physik* 389.20 (1927), pp. 457–484. DOI: https://doi.org/10.1002/andp.19273892002. eprint: https://onlinelibrary.wiley.com/doi/pdf/10.1002/andp.19273892002. URL: https://onlinelibrary.wiley.com/doi/abs/10.1002/andp.19273892002.

[105] V. Fock. "Näherungsmethode zur Lösung des quantenmechanischen Mehrkörperproblems". In: *Zeitschrift für Physik* 61.1-2 (1930), pp. 126–148. ISSN: 1434-6001. DOI: 10.1007/BF01340294. URL: http://link.springer.com/10.1007/BF01340294.

[106] D. R. Hartree. "The Wave Mechanics of an Atom with a Non-Coulomb Central Field. Part I. Theory and Methods". In: *Mathematical Proceedings of the Cambridge Philosophical Society* 24.1 (1928), 89–110. DOI: 10.1017/S0305004100011919.

[107] J. C. Slater. "Note on Hartree's Method". In: *Phys. Rev.* 35 (2 1930), pp. 210–211. DOI: 10.1103/PhysRev.35.210.2. URL: https://link.aps.org/doi/10.1103/PhysRev.35.210.2.

[108] J. C. Slater. "A Simplification of the Hartree-Fock Method". In: *Phys. Rev.* 81 (3 1951), pp. 385–390. DOI: 10.1103/PhysRev.81.385. URL: https://link.aps.org/doi/10.1103/PhysRev.81.385.

[109] P. Hohenberg and W. Kohn. "Inhomogeneous Electron Gas". In: *Phys. Rev.* 136 (3B 1964), B864–B871. DOI: 10.1103/PhysRev.136.B864. URL: https://link.aps.org/doi/10.1103/PhysRev.136.B864.

[110] W. Kohn and L. J. Sham. "Self-Consistent Equations Including Exchange and Correlation Effects". In: *Phys. Rev.* 140 (4A 1965), A1133–A1138. DOI: 10.1103/PhysRev.140.A1133. URL: https://link.aps.org/doi/10.1103/PhysRev.140.A1133.

[111] I. N. YAKOVKIN and P. A. DOWBEN. "THE PROBLEM OF THE BAND GAP IN LDA CALCULATIONS". In: *Surface Review and Letters* 14.03 (2007), pp. 481–487. DOI: 10.1142/S0218625X07009499. eprint: https://doi.org/10.1142/S0218625X07009499. URL: https://doi.org/10.1142/S0218625X07009499.

[112] John P. Perdew, Kieron Burke, and Matthias Ernzerhof. "Generalized gradient approximation made simple". In: *Physical Review Letters* 77.18 (1996), pp. 3865–3868. ISSN: 10797114. DOI: 10.1103/PhysRevLett.77.3865.

[113] John P. Perdew, Kieron Burke, and Matthias Ernzerhof. "Generalized Gradient Approximation Made Simple [Phys. Rev. Lett. 77, 3865 (1996)]". In: *Phys. Rev. Lett.* 78 (7 1997), pp. 1396–1396. DOI: 10.1103/PhysRevLett.78.1396. URL: https://link.aps.org/doi/10.1103/PhysRevLett.78.1396.

[114] John P. Perdew et al. "Atoms, molecules, solids, and surfaces: Applications of the generalized gradient approximation for exchange and correlation". In: *Phys. Rev. B* 46 (11 1992), pp. 6671–6687. DOI: 10.1103/PhysRevB.46.6671. URL: https://link.aps.org/doi/10.1103/PhysRevB.46.6671.

[115] Burak Himmetoglu et al. "Hubbard-corrected DFT energy functionals: The LDA+U description of correlated systems". In: *International Journal of Quantum Chemistry* 114.1 (2014), pp. 14–49. DOI: https://doi.org/10.1002/qua.24521. eprint: https://onlinelibrary.wiley.com/doi/pdf/10.1002/qua.24521. URL: https://onlinelibrary.wiley.com/doi/abs/10.1002/qua.24521.

[116] M Cococcioni. "Correlated Electrons: From Models to Materials Modeling and Simulation". In: *Correlated Electrons: From Models to Materials Modeling and Simulation* 2 (2012).

[117] S. L. Dudarev et al. "Electron-energy-loss spectra and the structural stability of nickel oxide: An LSDA+U study". In: *Phys. Rev. B* 57 (3 1998), pp. 1505–1509. DOI: 10.1103/PhysRevB.57.1505. URL: https://link.aps.org/doi/10.1103/PhysRevB.57.1505.

[118] Javier Junquera et al. "Numerical atomic orbitals for linear-scaling calculations". In: *Phys. Rev. B* 64 (23 2001), p. 235111. DOI: 10.1103/PhysRevB.64.235111. URL: https://link.aps.org/doi/10.1103/PhysRevB.64.235111.

[119] José M Soler et al. "The SIESTA method foriab initio/iorder-iN/imaterials simulation". In: *Journal of Physics: Condensed Matter* 14.11 (2002), pp. 2745–2779. DOI: 10.1088/0953-8984/14/11/302. URL: https://doi.org/10.1088/0953-8984/14/11/302.

[120] *FLEUR: the Jülich FLAPW code family*. URL: http://www.flapw.de.

[121] G. Kresse and J. Furthmüller. "Efficient iterative schemes for ab initio total-energy calculations using a plane-wave basis set". In: *Phys. Rev. B* 54 (16 1996), pp. 11169–11186. DOI: 10.1103/PhysRevB.54.11169. URL: https://link.aps.org/doi/10.1103/PhysRevB.54.11169.

[122] X. Gonze et al. "First-principles computation of material properties: the ABINIT software project". In: *Computational Materials Science* 25.3 (2002), pp. 478–492. ISSN: 0927-0256. DOI: https://doi.org/10.1016/S0927-0256(02)00325-7. URL: https://www.sciencedirect.com/science/article/pii/S0927025602003257.

[123] N. Troullier and José Luís Martins. "Efficient pseudopotentials for plane-wave calculations". In: *Phys. Rev. B* 43 (3 1991), pp. 1993–2006. DOI: 10.1103/PhysRevB.43.1993. URL: https://link.aps.org/doi/10.1103/PhysRevB.43.1993.

[124] David Vanderbilt. "Soft self-consistent pseudopotentials in a generalized eigenvalue formalism". In: *Phys. Rev. B* 41 (11 1990), pp. 7892–7895. DOI: 10.1103/PhysRevB.41.7892. URL: https://link.aps.org/doi/10.1103/PhysRevB.41.7892.

[125] P. E. Blöchl. "Projector augmented-wave method". In: *Phys. Rev. B* 50 (24 1994), pp. 17953–17979. DOI: 10.1103/PhysRevB.50.17953. URL: https://link.aps.org/doi/10.1103/PhysRevB.50.17953.

[126] Hendrik J. Monkhorst and James D. Pack. "Special points for Brillouin-zone integrations". In: *Phys. Rev. B* 13 (12 1976), pp. 5188–5192. DOI: 10.1103/PhysRevB.13.5188. URL: https://link.aps.org/doi/10.1103/PhysRevB.13.5188.

[127] R. P. Feynman. "Forces in Molecules". In: *Phys. Rev.* 56 (4 1939), pp. 340–343. DOI: 10.1103/PhysRev.56.340. URL: https://link.aps.org/doi/10.1103/PhysRev.56.340.

[128] M. C. Payne et al. "Iterative minimization techniques for ab initio total-energy calculations: molecular dynamics and conjugate gradients". In: *Rev. Mod. Phys.* 64 (4 1992), pp. 1045–1097. DOI: 10.1103/RevModPhys.64.1045. URL: https://link.aps.org/doi/10.1103/RevModPhys.64.1045.

[129] W. Zhong, David Vanderbilt, and K. M. Rabe. "Phase Transitions in $BaTiO_3$ from First Principles". In: *Phys. Rev. Lett.* 73 (13 1994), pp. 1861–1864. DOI: 10.1103/PhysRevLett.73.1861. URL: https://link.aps.org/doi/10.1103/PhysRevLett.73.1861.

[130] W. Zhong, David Vanderbilt, and K. M. Rabe. "First-principles theory of ferroelectric phase transitions for perovskites: The case of $BaTiO_3$". In: *Phys. Rev. B* 52 (9 1995), pp. 6301–6312. DOI: 10.1103/PhysRevB.52.6301. URL: https://link.aps.org/doi/10.1103/PhysRevB.52.6301.

[131] Nicholas Metropolis and S. Ulam. "The Monte Carlo Method". In: *Journal of the American Statistical Association* 44.247 (1949). PMID: 18139350, pp. 335–341. DOI: 10.1080/01621459.1949.10483310.

[132] David Landau and Kurt Binder. *A guide to Monte Carlo simulations in statistical physics*. Cambridge university press, 2021.

[133] W. K. Hastings. "Monte Carlo sampling methods using Markov chains and their applications". In: *Biometrika* 57.1 (Apr. 1970), pp. 97–109. ISSN: 0006-3444. DOI: 10.1093/biomet/57.1.97. URL: https://doi.org/10.1093/biomet/57.1.97.

[134] Tobias Preis et al. "GPU accelerated Monte Carlo simulation of the 2D and 3D Ising model". In: *Journal of Computational Physics* 228.12 (2009), pp. 4468–4477. ISSN: 0021-9991. DOI: https://doi.org/10.1016/j.jcp.2009.03.018. URL: https://www.sciencedirect.com/science/article/pii/S0021999109001387.

[135] Oleg Janson et al. "The quantum nature of skyrmions and half-skyrmions in Cu2OSeO3". In: *Nature Communications* 5.1 (2014), p. 5376. ISSN: 2041-1723. DOI: 10.1038/ncomms6376. URL: http://www.nature.com/articles/ncomms6376.

[136] R. B. Versteeg et al. "Optically probed symmetry breaking in the chiral magnet Cu_2OSeO_3". In: *Phys. Rev. B* 94 (9 2016), p. 094409. DOI: 10.1103/PhysRevB.94.094409. URL: https://link.aps.org/doi/10.1103/PhysRevB.94.094409.

[137] H J Xiang et al. "Predicting the spin-lattice order of frustrated systems from first principles". In: *Physical Review B* 84.22 (2011), p. 224429. ISSN:

1098-0121. DOI: 10.1103/PhysRevB.84.224429. URL: https://link.aps.org/doi/10.1103/PhysRevB.84.224429.

[138] D. Šabani, C. Bacaksiz, and M. V. Milošević. "Ab initio methodology for magnetic exchange parameters: Generic four-state energy mapping onto a Heisenberg spin Hamiltonian". In: *Physical Review B* 102.1 (2020).

[139] A.I. Liechtenstein et al. "Local spin density functional approach to the theory of exchange interactions in ferromagnetic metals and alloys". In: *Journal of Magnetism and Magnetic Materials* 67.1 (1987), pp. 65–74. ISSN: 0304-8853. DOI: https://doi.org/10.1016/0304-8853(87)90721-9. URL: https://www.sciencedirect.com/science/article/pii/0304885387907219.

[140] Dm M. Korotin et al. "Calculation of exchange constants of the Heisenberg model in plane-wave-based methods using the Green's function approach". In: *Physical Review B - Condensed Matter and Materials Physics* 91.22 (2015), pp. 1–7. ISSN: 1550235X. DOI: 10.1103/PhysRevB.91.224405. arXiv: 1411.4169.

[141] Ph. Kurz et al. "Ab initio treatment of noncollinear magnets with the full-potential linearized augmented plane wave method". In: *Phys. Rev. B* 69 (2 2004), p. 024415. DOI: 10.1103/PhysRevB.69.024415. URL: https://link.aps.org/doi/10.1103/PhysRevB.69.024415.

[142] Bernd Zimmermann et al. "Comparison of first-principles methods to extract magnetic parameters in ultrathin films: Co/Pt(111)". In: *Phys. Rev. B* 99 (21 2019), p. 214426. DOI: 10.1103/PhysRevB.99.214426. URL: https://link.aps.org/doi/10.1103/PhysRevB.99.214426.

[143] Vladimir I Anisimov, Jan Zaanen, and Ole K Andersen. "Band theory and Mott insulators: Hubbard U instead of Stoner I". In: *Physical Review B* 44.3 (1991), pp. 943–954. ISSN: 0163-1829. DOI: 10.1103/PhysRevB.44.943. URL: https://link.aps.org/doi/10.1103/PhysRevB.44.943.

[144] J H Yang et al. "Strong Dzyaloshinskii-Moriya Interaction and Origin of Ferroelectricity in <math display="inline"> <msub> <mi>Cu</mi> <mn>2</mn> </msub> <msub> <mi>OSeO</mi> <mn>3</mn> </msub> </math>". In: *Physical Review Letters* 109.10 (2012), p. 107203. ISSN: 0031-9007. DOI: 10.1103/PhysRevLett.109.107203. URL: https://link.aps.org/doi/10.1103/PhysRevLett.109.107203.

[145] X. Z. Lu, Xifan Wu, and H. J. Xiang. "General microscopic model of magnetoelastic coupling from first principles". In: *Physical Review B - Condensed*

Matter and Materials Physics 91.10 (2015), pp. 1–5. ISSN: 1550235X. DOI: 10.1103/PhysRevB.91.100405.

[146] K. Binder. "Finite size effects at phase transitions". In: *Computational Methods in Field Theory*. Ed. by H. Gausterer and C. B. Lang. Berlin, Heidelberg: Springer Berlin Heidelberg, 1992, pp. 59–125. ISBN: 978-3-540-47338-1.

[147] K. Binder. "Critical Properties from Monte Carlo Coarse Graining and Renormalization". In: *Phys. Rev. Lett.* 47 (9 1981), pp. 693–696. DOI: 10.1103/PhysRevLett.47.693. URL: https://link.aps.org/doi/10.1103/PhysRevLett.47.693.

[148] K. Binder and D. P. Landau. "Finite-size scaling at first-order phase transitions". In: *Phys. Rev. B* 30 (3 1984), pp. 1477–1485. DOI: 10.1103/PhysRevB.30.1477. URL: https://link.aps.org/doi/10.1103/PhysRevB.30.1477.

[149] Martin Hasenbusch. "The two-dimensional XY model at the transition temperature: a high-precision Monte Carlo study". In: *Journal of Physics A: Mathematical and General* 38.26 (2005), p. 5869. DOI: 10.1088/0305-4470/38/26/003. URL: https://dx.doi.org/10.1088/0305-4470/38/26/003.

[150] Wolfgang Bietenholz, Urs Gerber, and Fernando G Rejón-Barrera. "Berezinskii–Kosterlitz–Thouless transition with a constraint lattice action". In: *Journal of Statistical Mechanics: Theory and Experiment* 2013.12 (2013), P12009. DOI: 10.1088/1742-5468/2013/12/P12009. URL: https://dx.doi.org/10.1088/1742-5468/2013/12/P12009.

[151] T. Adams et al. "Long-wavelength helimagnetic order and skyrmion lattice phase in Cu 2OSeO 3". In: *Physical Review Letters* 108.23 (2012), pp. 1–5. ISSN: 00319007. DOI: 10.1103/PhysRevLett.108.237204. arXiv: 1204.3597.

[152] Peter Mohn. *Magnetism in the Solid State*. Solid-State Sciences. Springer-Verlag, 2003. DOI: https://doi.org/10.1007/3-540-30981-0.

[153] V. A. Sidorov et al. "Comparative study of helimagnets MnSi and Cu 2 O Se O 3 at high pressures". In: *Physical Review B - Condensed Matter and Materials Physics* 89.10 (2014), pp. 2–7. ISSN: 1550235X. DOI: 10.1103/PhysRevB.89.100403. arXiv: 1310.3988.

[154] A.M. Belemuk and S.M. Stishov. "Monte Carlo modeling the phase diagram of magnets with the Dzyaloshinskii - Moriya interaction". In: *Solid State Communications* 267 (2017), pp. 6–9. ISSN: 0038-1098. DOI: https://doi.org/10.1016/j.ssc.2017.08.022. URL: https://www.sciencedirect.com/science/article/pii/S0038109817302831.

[155] Harish Chandr Chauhan et al. "Multiple phases with a tricritical point and a Lifshitz point in the skyrmion host Cu_2OSeO_3". In: *Phys. Rev. B* 100 (16 2019), p. 165143. DOI: 10.1103/PhysRevB.100.165143. URL: https://link.aps.org/doi/10.1103/PhysRevB.100.165143.

[156] Naoya Kanazawa, Shinichiro Seki, and Yoshinori Tokura. "Noncentrosymmetric Magnets Hosting Magnetic Skyrmions". In: *Advanced Materials* 29.25 (2017). ISSN: 15214095.

[157] M. Janoschek et al. "Fluctuation-induced first-order phase transition in Dzyaloshinskii-Moriya helimagnets". In: *Phys. Rev. B* 87 (13 2013), p. 134407. DOI: 10.1103/PhysRevB.87.134407. URL: https://link.aps.org/doi/10.1103/PhysRevB.87.134407.

[158] S. A. Brazovskiĭ. "Phase transition of an isotropic system to a nonuniform state". In: *Soviet Journal of Experimental and Theoretical Physics* 41 (Jan. 1975), p. 85.

[159] Kenneth G. Wilson. "The renormalization group and critical phenomena". In: *Rev. Mod. Phys.* 55 (3 1983), pp. 583–600. DOI: 10.1103/RevModPhys.55.583. URL: https://link.aps.org/doi/10.1103/RevModPhys.55.583.

[160] , familyi=c., given=I., giveni=I., „ et al. "Critical scaling in the cubic helimagnet Cu_2OSeO_3". In: *Phys. Rev. B* 89 (6 2014), p. 060401. DOI: 10.1103/PhysRevB.89.060401. URL: https://link.aps.org/doi/10.1103/PhysRevB.89.060401.

[161] R. M. Hornreich, Marshall Luban, and S. Shtrikman. "Critical Behavior at the Onset of $\vec{k}$-Space Instability on the λ Line". In: *Phys. Rev. Lett.* 35 (25 1975), pp. 1678–1681. DOI: 10.1103/PhysRevLett.35.1678. URL: https://link.aps.org/doi/10.1103/PhysRevLett.35.1678.

[162] Shang Gao et al. "Spiral spin-liquid and the emergence of a vortex-like state in MnSc2S4". In: *Nature Physics* 13.2 (2017), pp. 157–161. ISSN: 1745-2473. DOI: 10.1038/nphys3914. eprint: 1605.04199. URL: http://www.nature.com/articles/nphys3914.

[163] O. Zaharko et al. "Spin liquid in a single crystal of the frustrated diamond lattice antiferromagnet $CoAl_2O_4$". In: *Phys. Rev. B* 84 (9 2011), p. 094403. DOI: 10.1103/PhysRevB.84.094403. URL: https://link.aps.org/doi/10.1103/PhysRevB.84.094403.

[164] X. Bai et al. "Magnetic Excitations of the Classical Spin Liquid $MgCr_2O_4$". In: *Phys. Rev. Lett.* 122 (9 2019), p. 097201. DOI: 10.1103/PhysRevLett.122.

097201. URL: https://link.aps.org/doi/10.1103/PhysRevLett.122.097201.

[165] Ping Huang et al. "Melting of a skyrmion lattice to a skyrmion liquid via a hexatic phase". In: *Nature Nanotechnology* 15.9 (2020), pp. 761–767. ISSN: 1748-3387. DOI: 10.1038/s41565-020-0716-3. URL: http://www.nature.com/articles/s41565-020-0716-3.

[166] Pontus Laurell and Satoshi Okamoto. "Dynamical and thermal magnetic properties of the Kitaev spin liquid candidate α-RuCl3". In: *npj Quantum Materials* 5.1 (2020), pp. 1–10. ISSN: 23974648. DOI: 10.1038/s41535-019-0203-y. arXiv: 1906.07579. URL: http://dx.doi.org/10.1038/s41535-019-0203-y.

[167] Houssam Sabri and Igor Kornev. "Monte Carlo studies of noncollinear magnetic phases in multiferroic Cu_2OSeO_3". In: *Phys. Rev. B* 107 (2 2023), p. 024417. DOI: 10.1103/PhysRevB.107.024417. URL: https://link.aps.org/doi/10.1103/PhysRevB.107.024417.

[168] Joo-Von Kim and Jeroen Mulkers. "On quantifying the topological charge in micromagnetics using a lattice-based approach". In: *IOP SciNotes* 1.2 (2020), p. 025211. DOI: 10.1088/2633-1357/abad0c. URL: https://dx.doi.org/10.1088/2633-1357/abad0c.

[169] Wen-Tao Hou et al. "Thermally driven topology in chiral magnets". In: *Phys. Rev. B* 96 (14 2017), p. 140403. DOI: 10.1103/PhysRevB.96.140403. URL: https://link.aps.org/doi/10.1103/PhysRevB.96.140403.

[170] M Böttcher et al. "B–T phase diagram of Pd/Fe/Ir(111) computed with parallel tempering Monte Carlo". In: *New Journal of Physics* 20.10 (2018), p. 103014. DOI: 10.1088/1367-2630/aae282. URL: https://dx.doi.org/10.1088/1367-2630/aae282.

[171] N. D. Mermin. "The topological theory of defects in ordered media". In: *Rev. Mod. Phys.* 51 (3 1979), pp. 591–648. DOI: 10.1103/RevModPhys.51.591. URL: https://link.aps.org/doi/10.1103/RevModPhys.51.591.

[172] Olexei I. Motrunich and Ashvin Vishwanath. "Emergent photons and transitions in the O(3) sigma model with hedgehog suppression". In: *Phys. Rev. B* 70 (7 2004), p. 075104. DOI: 10.1103/PhysRevB.70.075104. URL: https://link.aps.org/doi/10.1103/PhysRevB.70.075104.

[173] Łukasz Kurzawski and Krzysztof Malarz. "Simple Cubic Random-Site Percolation Thresholds for Complex Neighbourhoods". In: *Reports on Mathematical Physics* 70.2 (2012), pp. 163–169. ISSN: 0034-4877. DOI: https://

doi.org/10.1016/S0034-4877(12)60036-6. URL: https://www.sciencedirect.com/science/article/pii/S0034487712600366.

[174] L. S. Garca-Coln, L. F. del Castillo, and Patricia Goldstein. "Theoretical basis for the Vogel-Fulcher-Tammann equation". In: *Phys. Rev. B* 40 (10 1989), pp. 7040–7044. DOI: 10.1103/PhysRevB.40.7040. URL: https://link.aps.org/doi/10.1103/PhysRevB.40.7040.

[175] Yousra Nahas. "Gauge theory for relaxor ferroelectrics". PhD thesis. Ecole Centrale Paris, 2013.

[176] Sho Asakura and Fumio Oosawa. "On Interaction between Two Bodies Immersed in a Solution of Macromolecules". In: *The Journal of Chemical Physics* 22.7 (1954), pp. 1255–1256. DOI: 10.1063/1.1740347. eprint: https://doi.org/10.1063/1.1740347. URL: https://doi.org/10.1063/1.1740347.

[177] C. Bechinger et al. "Understanding Depletion Forces beyond Entropy". In: *Phys. Rev. Lett.* 83 (19 1999), pp. 3960–3963. DOI: 10.1103/PhysRevLett.83.3960. URL: https://link.aps.org/doi/10.1103/PhysRevLett.83.3960.

[178] Benoit B. Mandelbrot. *The fractal geometry of nature*. Vol. 1. WH freeman New York, 1982.

[179] AI Olemskoi and A Ya Flat. "Use of the concept of fractal in the physics of a condensed medium". In: *Usp. Fiz. Nauk* 163.12 (1993), pp. 1–50.

[180] Ralph H. Abraham. "Fractals, chaos, power laws: Minutes from an infinite paradise: Manfred Schroeder, (W.H. Freeman, New York, NY, 1991) 32.95, 429*pp*.". In: *Journal of Economic Dynamics and Control* 18.5 (1994), pp. 1041–1043. ISSN: 0165-1889. DOI: https://doi.org/10.1016/0165-1889(94)90045-0. URL: https://www.sciencedirect.com/science/article/pii/0165188994900450.

[181] Paul Sutcliffe. "Hopfions in chiral magnets". In: *Journal of Physics A: Mathematical and Theoretical* 51.37 (2018), p. 375401. DOI: 10.1088/1751-8121/aad521. URL: https://dx.doi.org/10.1088/1751-8121/aad521.

[182] Dennis DeTurck et al. "Generalized Gauss maps and integrals for three-component links: Toward higher helicities for magnetic fields and fluid flows". In: *Journal of Mathematical Physics* 54.1 (2013), p. 013515. DOI: 10.1063/1.4774172. eprint: https://doi.org/10.1063/1.477417. URL: https://doi.org/10.1063/1.4774172.

[183] Yizhou Liu, Roger K. Lake, and Jiadong Zang. "Binding a hopfion in a chiral magnet nanodisk". In: *Phys. Rev. B* 98 (17 2018), p. 174437. DOI: 10.1103/PhysRevB.98.174437. URL: https://link.aps.org/doi/10.1103/PhysRevB.98.174437.

[184] Yu. A. Izyumov and Yu.N. Skryabin. *Statistical Mechanics of Magnetically Ordered Systems*. Springer, 1988. URL: https://link.springer.com/book/9780306110153.

[185] URL: https://www.youtube.com/watch?v=5Om2fY3YoX8.

[186] D. I. Uzunov. *Introduction to the Theory of Critical Phenomena*. 2nd. WORLD SCIENTIFIC, 2010. DOI: 10.1142/7682. eprint: www.worldscientific.com/doi/pdf/10.1142/7682. URL: www.worldscientific.com/doi/abs/10.1142/7682.

[187] G. Grinstein and A. Luther. "Application of the renormalization group to phase transitions in disordered systems". In: *Phys. Rev. B* 13 (3 1976), pp. 1329–1343. DOI: 10.1103/PhysRevB.13.1329. URL: https://link.aps.org/doi/10.1103/PhysRevB.13.1329.

[188] Peter Kopietz, Lorenz Bartosch, and Florian Schütz. "Mean-Field Theory and the Gaussian Approximation". In: *Introduction to the Functional Renormalization Group*. Springer Berlin Heidelberg, 2010, pp. 23–52. DOI: 10.1007/978-3-642-05094-7_2. URL: https://doi.org/10.1007/978-3-642-05094-7_2.

[189] Sahand Tabatabaei (https://physics.stackexchange.com/users/116526/sahand tabatabaei). *Continuum Field Theory for the Ising Model*. Physics Stack Exchange. URL:https://physics.stackexchange.com/q/392265 (version: 2018-03-15). eprint: https://physics.stackexchange.com/q/392265. URL: https://physics.stackexchange.com/q/392265.

[190] R. J. Baxter. "Exactly Solved Models in Statistical Mechanics". In: *Integrable Systems in Statistical Mechanics*, pp. 5–63. DOI: 10.1142/9789814415255_0002. eprint: https://www.worldscientific.com/doi/pdf/10.1142/9789814415255_0002. URL: https://www.worldscientific.com/doi/abs/10.1142/9789814415255_0002.

[191] Andres Cano, Dennis Meier, and Morgan Trassin, eds. *Multiferroics : Fundamentals and Applications*. Berlin, Boston: De Gruyter, 2021. ISBN: 9783110582130. DOI: doi:10.1515/9783110582130. URL: https://doi.org/10.1515/9783110582130.

[192] Hans Schmid. "Multi-ferroic magnetoelectrics". In: *Ferroelectrics* 162.1 (1994), pp. 317–338. DOI: 10.1080/00150199408245120. eprint: https://doi.org/10.1080/00150199408245120. URL: https://doi.org/10.1080/00150199408245120.

[193] Hans Schmid. "On ferrotoroidics and electrotoroidic, magnetotoroidic and piezotoroidic effects*". In: *Ferroelectrics* 252.1 (2001), pp. 41–50. DOI: 10.1080/00150190108016239. eprint: https://doi.org/10.1080/00150190108016239. URL: https://doi.org/10.1080/00150190108016239.

[194] Manfred Fiebig. "Revival of the magnetoelectric effect". In: *Journal of Physics D: Applied Physics* 38.8 (2005), R123–R152. DOI: 10.1088/0022-3727/38/8/r01. URL: https://doi.org/10.1088/0022-3727/38/8/r01.

[195] R. Ramesh and Nicola A. Spaldin. "Multiferroics: progress and prospects in thin films". In: *Nature Materials* 6.1 (2007), pp. 21–29. ISSN: 1476-1122. DOI: 10.1038/nmat1805. URL: https://www.nature.com/articles/nmat1805.

[196] M. Fiebig et al. "Second Harmonic Generation and Magnetic-Dipole-Electric-Dipole Interference in Antiferromagnetic Cr_2O_3". In: *Phys. Rev. Lett.* 73 (15 1994), pp. 2127–2130. DOI: 10.1103/PhysRevLett.73.2127. URL: https://link.aps.org/doi/10.1103/PhysRevLett.73.2127.

[197] J. Valasek. "Piezo-Electric and Allied Phenomena in Rochelle Salt". In: *Phys. Rev.* 17 (4 1921), pp. 475–481. DOI: 10.1103/PhysRev.17.475. URL: https://link.aps.org/doi/10.1103/PhysRev.17.475.

[198] GA Smolenskii and VA Ioffe. *Communications Nr. 71 du Colloque International de Magnétisme*. 1958.

[199] VA Bokov, IE Mylnikova, and GA Smolenskii. "Ferroelectric antiferromagnetics". In: *Soviet Physics Jetp-Ussr* 15.2 (1962), pp. 447–449.

[200] SV Kiselev. "Detection of magnetic order in ferroelectric BiFeO_3 by neutron diffraction". In: *Sov. Phys.* 7 (1963), p. 742.

[201] Felix Bertaut, P Fang, and F Forrat. "PHYSIQUE DES SOLIDES-LES MANGANITES DE TERRES RARES ET DYTTRIUM-UNE NOUVELLE CLASSE DE FERROELECTRIQUES". In: *Comptes Rendus Hebdomadaires Des Seances De L Academie Des Sciences* 256.9 (1963), p. 1958.

[202] Philippe Coeuré et al. "Ferroelectric properties of hexagonal orthomanganites of yttrium and rare earths". In: *Proceedings of the International Meeting on Ferroelectricity*. Vol. 1. Institute of Physics of the Czechoslovak Academy of Sciences, Prague. 1966, p. 332.

[203] Eo Asher et al. "Some properties of ferromagnetoelectric nickel-iodine boracite Ni 3 B 7 O 13 I". In: *J. Appl. Phys.* 37.3 (1966), pp. 1404–1405. DOI: 10.1063/1.1708493.

[204] Kêitsiro Aizu. "Possible Species of Ferromagnetic, Ferroelectric, and Ferroelastic Crystals". In: *Phys. Rev. B* 2 (3 1970), pp. 754–772. DOI: 10.1103/PhysRevB.2.754. URL: https://link.aps.org/doi/10.1103/PhysRevB.2.754.

[205] Robert E Newnham et al. "Magnetoferroelectricity in Cr2BeO4". In: *Journal of Applied Physics* 49.12 (1978), pp. 6088–6091. DOI: 10.1063/1.324527.

[206] VG Bar'Yakhtar, VA L'vov, and DA Yablonskiĭ. "Inhomogeneous magnetoelectric effect". In: *ZhETF Pisma Redaktsiiu* 37 (1983), p. 565.

[207] W. Eerenstein, N. D. Mathur, and J. F. Scott. "Multiferroic and magnetoelectric materials". In: *Nature* 442.7104 (2006), pp. 759–765. ISSN: 0028-0836. DOI: 10.1038/nature05023. URL: http://www.nature.com/articles/nature05023.

[208] Nicola A. Hill. "Why Are There so Few Magnetic Ferroelectrics?" In: *The Journal of Physical Chemistry B* 104.29 (2000), pp. 6694–6709. ISSN: 1520-6106. DOI: 10.1021/jp000114x. URL: https://pubs.acs.org/doi/10.1021/jp000114x.

[209] Manfred Fiebig et al. "The evolution of multiferroics". In: *Nature Reviews Materials* 1.8 (2016), pp. 1–14. DOI: https://doi.org/10.1038/natrevmats.2016.46.

[210] Eric Bousquet and Andrés Cano. "Non-collinear magnetism in multiferroic perovskites". In: *Journal of Physics: Condensed Matter* 28.12 (2016), p. 123001. DOI: 10.1088/0953-8984/28/12/123001. URL: https://doi.org/10.1088/0953-8984/28/12/123001.

[211] Paolo Barone and Silvia Picozzi. "Mechanisms and origin of multiferroicity". In: *Comptes Rendus Physique* 16.2 (2015). Multiferroic materials and heterostructures / Matériaux et hétérostructures multiferroïques, pp. 143–152. ISSN: 1631-0705. DOI: https://doi.org/10.1016/j.crhy.2015.01.009. URL: https://www.sciencedirect.com/science/article/pii/S1631070515000109.

[212] J. Wang et al. "Epitaxial BiFeO₃ Multiferroic Thin Film Heterostructures". In: *Science* 299.5613 (2003), pp. 1719–1722. DOI: 10.1126/science.1080615. eprint: https://www.science.org/doi/pdf/10.1126/

science.1080615. URL: https://www.science.org/doi/abs/10.1126/science.1080615.

[213] S. A. Fedulov. "Determination of Curie temperature for BiFeO3". In: *Dokl. Akad. Nauk SSSR* 139.1345 (1961).

[214] R. P. Zhdanov G. S. Kiselev S. V. Ozerov. "Detection of magnetic order in ferroelectric BiFeO3 by neutron diffraction". In: *Dokl. Akad. Nauk SSSR* 145.1255 (1962).

[215] Bas B. Van Aken et al. "The origin of ferroelectricity in magnetoelectric YMnO3". In: *Nature Materials* 3.3 (2004), pp. 164–170. ISSN: 1476-1122. DOI: 10.1038/nmat1080. URL: https://www.nature.com/articles/nmat1080.

[216] M. Fiebig et al. "Determination of the Magnetic Symmetry of Hexagonal Manganites by Second Harmonic Generation". In: *Phys. Rev. Lett.* 84 (24 2000), pp. 5620–5623. DOI: 10.1103/PhysRevLett.84.5620. URL: https://link.aps.org/doi/10.1103/PhysRevLett.84.5620.

[217] Naoshi Ikeda et al. "Ferroelectricity from iron valence ordering in the charge-frustrated system LuFe2O4". In: *Nature* 436.7054 (2005), pp. 1136–1138. ISSN: 0028-0836. DOI: 10.1038/nature04039. URL: http://www.nature.com/articles/nature04039.

[218] Jeroen van den Brink and Daniel I Khomskii. "Multiferroicity due to charge ordering". In: *Journal of Physics: Condensed Matter* 20.43 (2008), p. 434217. DOI: 10.1088/0953-8984/20/43/434217. URL: https://doi.org/10.1088/0953-8984/20/43/434217.

[219] Noriki Terada, Yana S. Glazkova, and Alexei A. Belik. "Differentiation between ferroelectricity and thermally stimulated current in pyrocurrent measurements of multiferroic MMn$_7$O$_{12}$ (M = Ca, Sr, Cd, Pb)". In: *Phys. Rev. B* 93 (15 2016), p. 155127. DOI: 10.1103/PhysRevB.93.155127. URL: https://link.aps.org/doi/10.1103/PhysRevB.93.155127.

[220] N. Hur et al. "Electric polarization reversal and memory in a multiferroic material induced by magnetic fields". In: *Nature* 429.6990 (2004), pp. 392–395. ISSN: 0028-0836. DOI: 10.1038/nature02572. URL: http://www.nature.com/articles/nature02572.

[221] Yoshinori Tokura, Shinichiro Seki, and Naoto Nagaosa. "Multiferroics of spin origin". In: *Reports on Progress in Physics* 77.7 (2014), p. 076501. DOI: 10.1088/0034-4885/77/7/076501. URL: https://doi.org/10.1088/0034-4885/77/7/076501.

Publications

Monte Carlo studies of noncollinear magnetic phases in multiferroic Cu_2OSeO_3

Houssam Sabri* and Igor Kornev
Université Paris-Saclay, CentraleSupélec, CNRS, Laboratoire SPMS UMR 8580, 91190 Gif-sur-Yvette, France

(Received 30 September 2022; revised 6 November 2022; accepted 9 January 2023; published 17 January 2023)

Monte Carlo simulations based on a first-principles-derived Hamiltonian are conducted to study the finite-temperature properties of chiral-lattice multiferroic insulator Cu_2OSeO_3. The use of this numerical technique (i) reveals basic features of the phase diagram as a function of temperature and external magnetic field, including the long-range helical phase at low temperature and zero magnetic field and the skyrmion lattice phase, in which skyrmions are arranged in a two-dimensional hexagonal lattice, and (ii) leads to the discovery of an overlooked vortex lattice phase in a narrow pocket of the phase diagram near the fluctuations' disordered-helical phase transition. The scheme also provides strong numerical evidence that the transition to a helical state in Cu_2OSeO_3 is of first order driven by critical fluctuations.

DOI: 10.1103/PhysRevB.107.024417

I. INTRODUCTION

In recent years, there has been a surge in interest in topological spin textures due to their potential role as a building block in new spintronic devices [1]. A direct result of their topological stability is their robustness against continuous mechanical deformations and defects. An example of topological spin textures is skyrmions, which first emerged as a solution of the nonlinear field in the context of dense nuclear matter [2]. They are characterized by a topological invariant, which describes the local configuration of how the vector field whirls in the plan. This topological invariant categorizes the equivalent spin configurations in the case of magnetic systems [3]. The magnetic skyrmions were predicted to exist within magnets with relevant Dzyalonshinskii-Moriya interaction (DMI) [4,5]. They were first discovered in the noncentrosymmetric cubic B20 metallic chiral magnet MnSi [6], in other B20 crystals as FeGe [7], $Fe_{1-x}Co_xSi$ [8] both in bulk material and thin films [9], and also in other material with noncentrosymmetric crystal structures like β-Mn type Co-Zn-Mn alloys [10]. These topologically nontrivial spin configurations called skyrmions can be described as circular spin textures with spin up on the edge of the circle and spin down in the center. There is in between a smooth transition with topological features. Others such as copper oxide selenite Cu_2OSeO_3 that crystallize in the cubic space group $P2_13$ exhibit the same features of the B20 magnets [11]. However, this crystal is the only insulator in this family of chiral magnets that displays a multiferroic behavior with a magnetoelectric coupling [12,13]; this may give rise to the ferroelectric counterpart topological solitons and also the manipulation of skyrmions with an electric field [14].

The skyrmion lattice phase (SkL), in which the skyrmions are arranged in a two-dimensional hexagonal lattice, exists in a narrow pocket of magnetic field and temperature phase diagram near the paramagnetic-helical state phase transition temperature T_c. The helical state phase in Cu_2OSeO_3 is known to exist in a more extensive range of temperature-field (T-B) phase diagram [15]. The helical phase corresponds to a noncollinear magnetization pattern, in which spins are arranged in a periodic spiral. The helical phase arises from the competition between the collinear Heisenberg interaction and the noncollinear DMI. In the presence of Zeeman interaction, this competition may create in some conditions multiple helimagnetic states that overlap and create other spin textures like vortex lattices found recently in a centrosymmetric magnet $GdRu_2Si_2$ [16], hedgehog lattices, or skyrmion lattices [17]. The SkL is considered as the overlapping of three different helices with noncollinear and coplanar directions. The further contributions of thermal fluctuations stabilize the SkL and the ratio of Heisenberg exchange and DMI can determine the lattice constant of SkL and the size of skyrmions. The strength of both interactions does not depend on temperature; thus skyrmions' size and lattice constant are uniform on the whole lattice.

In the past years, there have been few attempts to model the behavior of Cu_2OSeO_3 with atomistic approaches. Janson *et al.* [18] attempted to reproduce the phase diagram with micromagnetic simulations which are fundamentally constrained by the continuum formulation [19,20]. Belemuk *et al.* [21] used artificial effective Hamiltonian parameters to model the high-pressure behavior of the phase transition in helical magnets. In this work, we investigate the helical phase and the SkL using the effective Hamiltonian method, which is parametrized using *ab initio* density functional theory (DFT) calculations. The resulting effective Hamiltonian is solved with Monte Carlo simulations. This approach is a purely atomistic attempt to reproduce the experimental phase diagram and gives us insight into the microscopic mechanism of creation and stability of the different magnetic phases and spin textures in multiferroic Cu_2OSeO_3.

II. EFFECTIVE HAMILTONIAN

The system's equilibrium properties at finite temperatures can be determined from the total energy, which is a function

*houssam.sabri@centralesupelec.fr

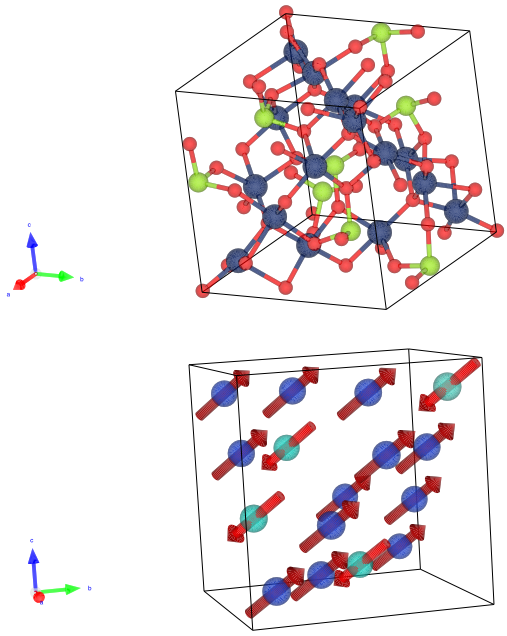

FIG. 1. Crystal structure of copper oxide selenite Cu_2OSeO_3: dark blue for copper, red for oxygen, and green for selenium. Magnetic atoms in the system: light blue for copper atoms I (Cu^I) and dark blue for copper atoms II (Cu^{II}).

of the atomic spins. The aim here is to build a parametrized Hamiltonian, which is totally *ab initio* with no experimental or empirical inputs.

The first term in our magnetic effective Hamiltonian is the Heisenberg interaction

$$E^H(\{\mathbf{S}\}) = \sum_{i<j} J_{ij}\mathbf{S}_i \cdot \mathbf{S}_j. \tag{1}$$

$E^H(\{\mathbf{S}\})$ is the energy contribution of collinear magnetic interaction at the atomic level. This interaction, in general, tends to make the spins align in the same direction [either ferromagnetic (FM) or antiferromagnetic (AF)]; in the case of the multiferroic Cu_2OSeO_3, the localized spin $S = \frac{1}{2}$ originates from the unpaired electron in the $3d$ shell and the copper ions Cu^{2+} make a network of tetrahedra made of four ions at each corner with two sites Cu^I and Cu^{II} with a ratio of 1 : 3, as shown in Fig. 1. This network of copper ions and tetrahedra gives rise to five types of Heisenberg exchanges, each related to a type of interaction:

$$E^H(\{\mathbf{S}\}) = \sum_{i<j} \big[J_w^{FM}\mathbf{S}_i^{II} \cdot \mathbf{S}_j^{II} + J_s^{AF}\mathbf{S}_i^{I} \cdot \mathbf{S}_j^{II} + J_s^{FM}\mathbf{S}_i^{II} \cdot \mathbf{S}_j^{II} + J_w^{AF}\mathbf{S}_i^{I} \cdot \mathbf{S}_j^{II} + J_O^{AF}\mathbf{S}_i^{I} \cdot \mathbf{S}_j^{II}\big]. \tag{2}$$

J_w^{FM} (J_s^{FM}) is the weak (strong) ferromagnetic interaction between copper (Cu^{II}) atoms, J_s^{AF} (J_w^{AF}) is the strong antiferromagnetic interaction (weak) between copper (Cu^{II} and Cu^I) atoms, and J_O^{AF} is the only superexchange interaction (long-range coupling mediated by the bridging oxo ligand) that is comparable to previous ones.

The second term, which is a crucial ingredient in observing the noncollinear spin textures in magnetic materials, is the DMI, which is the antisymmetric exchange that prevents the spins from aligning in the same direction; this interaction arises from spin-orbit coupling and is written as

$$E^{DMI}(\{\mathbf{S}\}) = \sum_{i<j} \mathbf{D}_{ij} \cdot \mathbf{S}_i \times \mathbf{S}_j. \tag{3}$$

The same analysis goes for DMI, where we have five different vectors related to the Heisenberg exchange constant. These vectors give rise to the noncollinear magnetic textures (such as helical, conical, and skyrmion lattice states):

$$E^{DMI}(\{\mathbf{S}\}) = \sum_{i<j} \big[\mathbf{D}_w^{FM} \cdot \mathbf{S}_i^{II} \times \mathbf{S}_j^{II} + \mathbf{D}_s^{AF} \cdot \mathbf{S}_i^{I} \times \mathbf{S}_j^{II} + \mathbf{D}_s^{FM} \cdot \mathbf{S}_i^{II} \times \mathbf{S}_j^{II} + \mathbf{D}_w^{AF} \cdot \mathbf{S}_i^{I} \times \mathbf{S}_j^{II} + \mathbf{D}_O^{AF} \cdot \mathbf{S}_i^{I} \times \mathbf{S}_j^{II}\big]. \tag{4}$$

The last term is the Zeeman energy that describes the potential energy of the interaction between the spins and the applied external magnetic field $\mathbf{B}_{\text{ext}}$,

$$E^{\text{Zeeman}}(\{\mathbf{S}\}) = \sum_i g_S \frac{\mu_B}{\hbar}\mathbf{S}_i \cdot \mathbf{B}_{\text{ext}}, \tag{5}$$

where g_S is the Landé g factor ($g_S = 2$) and μ_B is the Bohr magneton.

The total energy based on this Hamiltonian which includes all previous interactions is used as the energy to minimize in Monte Carlo simulations, in order to compute the finite temperature properties.

III. COMPUTATIONAL DETAILS

A. DFT calculations

The first-principles density functional theory calculations were performed using the Vienna Ab initio Simulation Package (VASP) [22] for geometrical structure optimization and to calculate the Heisenberg exchange, DMI constants with the four energies states method [23,24].

The electronic wave function adopts a plane-wave basis and the pseudopotentials adopt the projector augmented-wave method (PAW), with generalized gradient approximation of Perdew, Burke, and Ernzernhof (GGA-PBE) [25] used as the exchange-correlation functional. For $3d$ orbitals of Cu atoms, a GGA + U correction is used within Dudarev's formulation [26] to treat the strong correlation properties of $3d$ electrons with U (on-site Coulomb repulsion energy) and J (Hund exchange parameter) set, respectively, to 7.5 eV and 0.98 eV [27]; the spin-orbit coupling parameter was turned on for the case of DMI. The plane-wave cutoff energy is set to 520 eV. The sampling of the Brillouin zone is done using a $4 \times 4 \times 4$ Γ-centered k mesh with the Monkhorst-Pack scheme.

B. Monte Carlo simulations

For our system's study at finite temperatures, we have performed Monte Carlo simulations that compute the change in total energy as the configuration of spins' changes. We solve the effective Hamiltonian using the Monte Carlo simulations, which rely on the Metropolis-Hastings algorithm [28,29] inside an $L \times L \times L = N_L$ cubic supercell with periodic boundary conditions, where N_L designate the total

TABLE I. Microscopic magnetic model parameters from DFT four states energy-mapping calculations: the columns respectively designate the interaction type, the type of atoms involved, the involved atoms (ρ_i, ρ_j), distance between atoms, the Heisenberg exchange, DMI vector, and the ratio between DMI and Heisenberg exchange. The atomic positions for all involved atoms are listed in the Supplemental Material. J and $\mathbf{D}$ parameters are normalized with respect to the DFT obtained value $S = 0.73$.

Interactions	Atoms	(ρ_i, ρ_j)	$d_{ij} = \lvert r_i - r_j \rvert$ (Å)	J_{ij} (K)	$\mathbf{D}_{ij}$ (K)	$\delta = \frac{\lvert \mathbf{D}_{ij} \rvert}{\lvert J_{ij} \rvert}$
J_w^{FM}, $\mathbf{D}_w^{FM}$	Cu^{II}-Cu^{II}	(ρ_8, ρ_7)	3.011	−27.57	(−2.53, −3.85, 0.201)	0.167
J_s^{AF}, $\mathbf{D}_s^{AF}$	Cu^{I}-Cu^{II}	(ρ_{12}, ρ_6)	3.067	146.76	(−3.596, 13.88, 9.75)	0.118
J_s^{FM}, $\mathbf{D}_s^{FM}$	Cu^{II}-Cu^{II}	(ρ_1, ρ_8)	3.226	−60.00	(4.573, 8.15,4.473)	0.173
J_w^{AF}, $\mathbf{D}_w^{AF}$	Cu^{I}-Cu^{II}	(ρ_{12}, ρ_{13})	3.336	16.84	(−9.53, 8.06, 6.84)	0.845
J_O^{AF}, $\mathbf{D}_O^{AF}$	Cu^{I}-Cu^{II}	(ρ_{16}, ρ_3)	6.396	30.57	(−0.55, 4.26, −3.88)	0.189

number of magnetic unit cells and each magnetic unit cell contains 16 spins. In order to decrease computation time, GPU parallel programing is employed. The magnetic Hamiltonian includes only short-range interactions, so a parallel checkerboard type algorithm is used [30] (see the Supplemental Material [31]).

The trial moves in our case consist of updating the spin vector direction (constant norm), which changes the total energy. For $L = 84$, which corresponds to $N_a \sim 10^7$ atoms, each Monte Carlo sweep (MCS) takes about 0.93 s on our cluster workstation. The total number of MCS is chosen to be 5×10^7 for every temperature step, with half of these sweeps used for thermalization and the other half for extracting equilibrium properties. This process is done by decreasing the temperature in small steps (annealing) to get well-converged results.

IV. RESULTS AND DISCUSSION

The crucial parameters in forming magnetic textures such as helical structure and magnetic skyrmions in Cu_2OSeO_3 are the magnetic interactions. We evaluate the Heisenberg interaction and DMI using the four-state energy-mapping method [23,24]. The results reveal two energy scales for exchange constants; for both ferromagnetic and antiferromagnetic exchanges, there is weak and strong interaction and an important superexchange (long-range) antiferromagnetic compared to weak interactions. Table I presents all the values for the five different exchanges and the corresponding DMI vectors. We observe that the ratio of DMI over Heisenberg constant δ, which is usually smaller than 0.05 [5], is between 0.11 and 0.20 and an enormous ratio of 0.84 in the case of the weak antiferromagnetic exchange J_w^{AF}, $\mathbf{D}_w^{AF}$. The immense ratio reveals the existence of a very strong DMI in our system, which is a necessary condition in the creation of magnetic textures and, in particular, magnetic skyrmions. We have compared our results with Janson *et al.* [18] starting with the exchange constants; we report a difference between the Heisenberg exchange in this paper and their results. The ratios between the DMI and Heisenberg interaction were smaller than 0.10, except for the weak antiferromagnetic exchange, where it is at the order of 0.58. The small ratios could be the origin of the absence of noncollinear spin textures when using their results as input parameters of our effective Hamiltonian. We have also compared our results with a previous study by Yang *et al.* [32] and find them to be consistent.

We also show that, using Monte Carlo simulations and the previous constants as parameters of effective Hamiltonian, the existence of a helical state at zero field characterized with a propagation vector $||\mathbf{q_H}|| = 0.008$ (Å^{-1}), the helical state has a periodicity along $[1\bar{1}0]$ direction [11] with a wavelength $\lambda_H \simeq 78.4$ nm, and is shown to exist in all of the temperature range below $T_H \simeq 37.5$ K, which delimits the helical phase from the fluctuations disordered phase. This value is lower than the critical temperature $T_c \simeq 42.5$ of the ordered phase to the paramagnetic phase where its experimental value is $T_c^{\text{expt}} \simeq 58$ K [15]. The discrepancy between the reported critical temperature and experimental one is due to the use of lattice constant of paramagnetic phase as lattice parameter in the range of temperatures of the field polarized phase (helical and SkL), which correspond to a 2 GPa applied hydrostatic pressure on the crystal which affects the magnetic exchange constant $T_c(P) = T_c(0)(1 - P/P_c)$ [33]. To explore those noncollinear phases we calculated the spin structure factor $\mathbf{F}(\mathbf{q})$, which is defined as the Fourier transform of the spin distribution. Figure 2(a) shows the logarithm of spin structure factor for our system at 35 K, where we find two spots corresponding to $\mathbf{q_H}$ and $-\mathbf{q_H}$, while Fig. 2(b) shows the spatial distribution of the spins in helical phase in a (001) layer; this feature has been proven experimentally with the exception in the reported wavelength $\lambda_H^{\text{expt}} \simeq 61.6 \pm 4.5$ nm [15], which is due to the same argument as T_c.

We also report that, for the heat capacity, we have the same peak and shoulder feature near T_c found in experimental results in MnSi and Cu_2OSeO_3 [34]. Figure 3 shows the feature where the shoulder is toward high temperatures. We emphasize that this is the first atomistic study with the *ab initio* inputs that reproduce this behavior. Belemuk *et al.* [21] show the same features with Monte Carlo simulation but with artificial inputs for Heisenberg exchange and DMI in the effective magnetic Hamiltonian. The first peak (which is field dependent) around $T_H \simeq 37$ K for zero field is a characteristic of a first-order phase transition between the fluctuation-disordered regime (FD) and helical state, as was discovered experimentally by Chauhan *et al.* [35]. The second peak (the shoulder) at $T \simeq T_c \sim 42.5$ K delimits the FD region from the uncorrelated paramagnetic region. Janoscheck *et al.* [36] showed that the phase transition in a helimagnet of the B20 family (MnSi) displays a fluctuation-induced first-order phase transition that follows a Brazovskii mechanism [37]. To explore the induced first-order phase transition mechanism, we

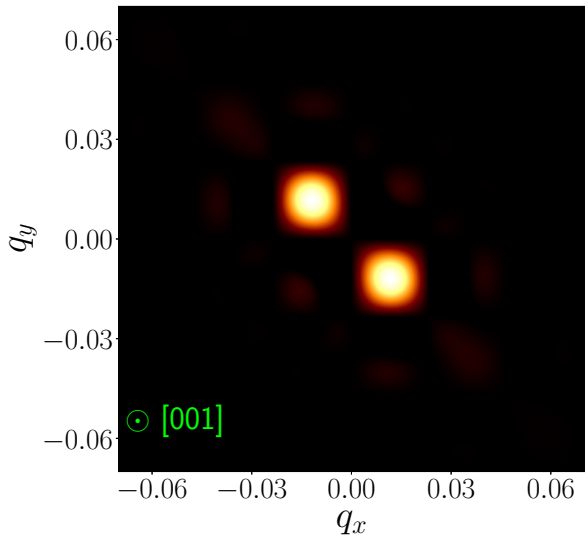

(a)

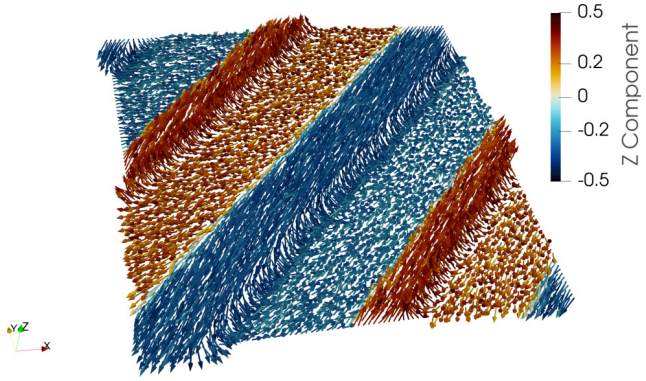

(b)

FIG. 2. (a) Logarithm of the square of spin structure factor $[\log_{10}(|\mathbf{F}|^2)]$, where $|\mathbf{F}|^2$ is summed along the [001] direction at 35 K and zero magnetic field, and (b) real space spin configuration in Cu_2OSeO_3 (001) slice in the helical phase. The z component and the in-plane orientations of the spins are illustrated by the color bar and colored arrows, respectively.

calculated the inverse of correlation length $\kappa = \frac{2\pi}{\xi}$ for temperature above T_H. There are several scenarios if the inverse Ginzburg length of the system κ_G satisfies the condition $\kappa_G < \kappa_{DM}$ for $T > T_H$, where $\kappa_{DM} = ||\mathbf{q}_H||$; the system undergoes a first-order transition that follows a Brazovskii mechanism. In this mechanism, the strongly interacting fluctuations suppress the mean-field transition temperature T_{MF}. On the other hand, if $\kappa_G > \kappa_{DM}$ the mechanism governing the induced phase transition can be described within the Wilson-Fisher renormalization group [38]. The latter mechanism is what governs the induced transition in Cu_2OSeO_3, as previously confirmed by Živković *et al.* [39]. The fit of the magnetic susceptibility with the Brazovskii Eq. (8) [36], where $\eta = \frac{\kappa_{Gi}}{\kappa_{DM}}$, gives a value of $\eta > 1$, which means that in our system $\kappa_G > \kappa_{DM}$,

$$\chi_{|T>T_c} = \frac{\chi_0}{1 + \eta^2 \mathcal{Z}(T)}, \tag{6}$$

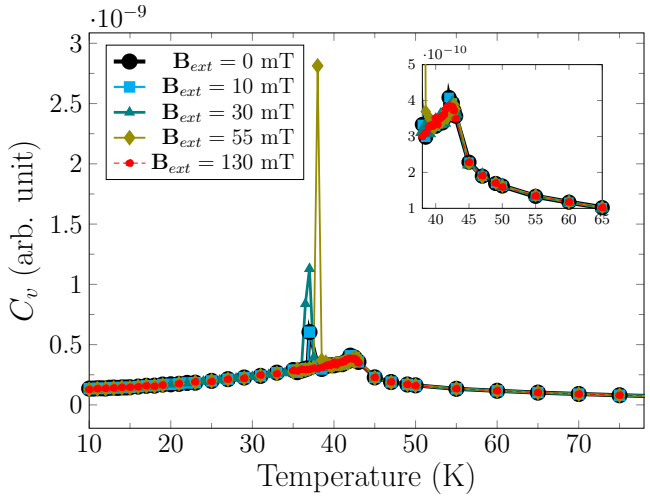

(a)

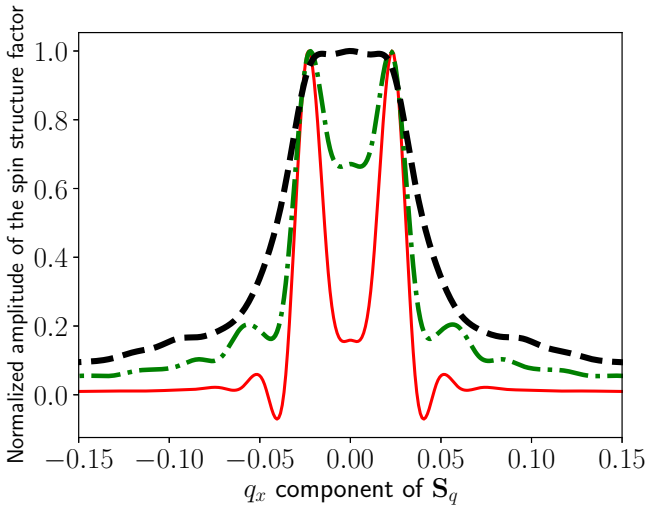

(b)

FIG. 3. (a) Heat capacity for multiple values of magnetic fields; the second-order phase transition is independent of magnetic fields, whereas the first-order phase transition is field dependent, where lines are guides to the eye. (b) The distribution of the spin Fourier component along $(1\bar{1}0)$ direction across the transition T_H: solid line is $T_H - 0.25$ K, dashed-dotted line is $T_H + 0.25$ K, and dashed line is $T_H + 2$ K. The transition from double peak distribution into single peak is a signature of first-order phase transition.

$$\mathcal{Z}(T) = \frac{[\tau + (1 - \tau^3 + \sqrt{1 - 2\tau^3})^{1/3}]^2}{2^{1/3}[1 - \tau^3 + \sqrt{1 - 2\tau^3}]^{1/3}}, \tag{7}$$

$$\tau = \frac{T - T_{MF}}{T_0}. \tag{8}$$

Far from the transition, $T \gg T_c$, the fluctuations have a mean-field ferromagnetlike behavior as seen in Fig. 4(c). In our case, as the temperature approaches T_c from high temperatures, $\kappa < \kappa_G$, we enter the strongly interacting fluctuations regime that suppresses the transition temperature before the fluctuations' interactions acquire an isotropic chiral behavior. This can be seen from the spreading of propagation vectors in $\mathbf{q}$ space

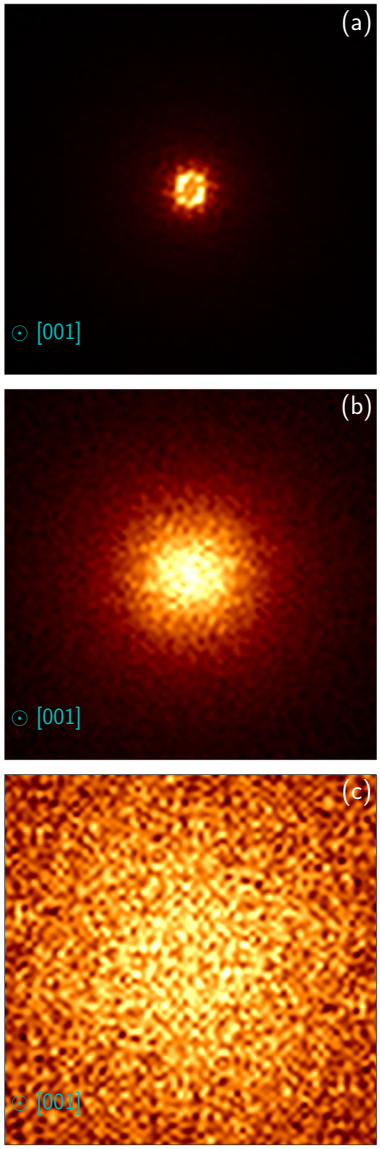

FIG. 4. Evolution of the spin structure factor in the first Brillouin zone (BZ) above T_c: (a) at $T_c + 0.5$ K, it shows isotropic chiral strongly interacting fluctuations, (b) the spreading of propagation vector on a sphere at $T_c + 3$ K, indicating strongly interacting fluctuations, and (c) at $T \gg T_c$ exhibiting ferromagnetic fluctuation behavior where the fluctuation spectrum spreads over the whole BZ.

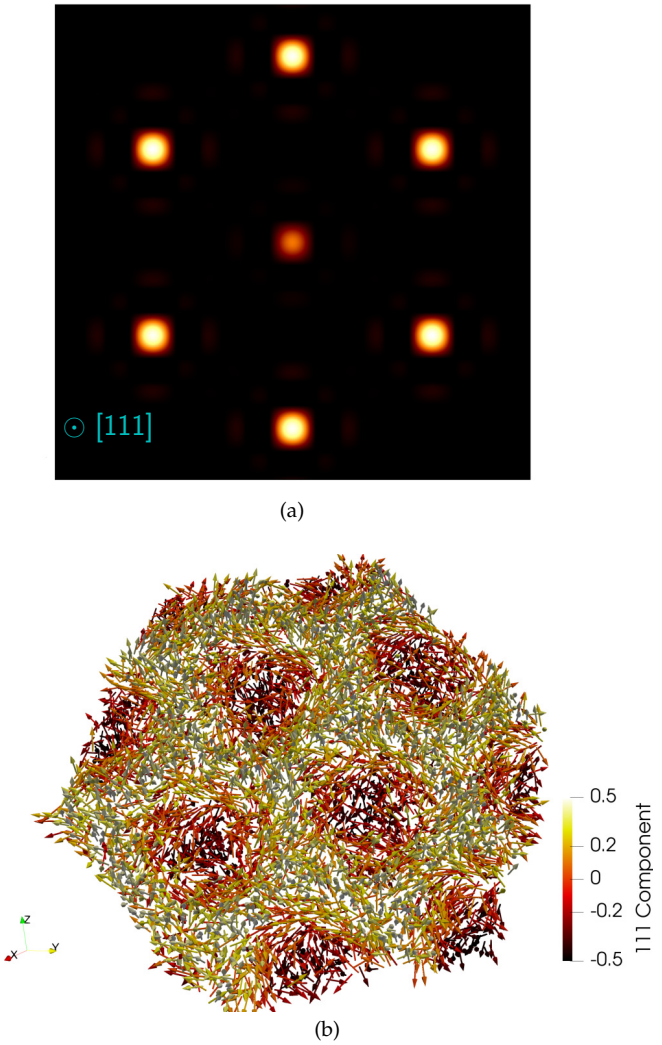

FIG. 5. (a) Logarithm of the square of the spin structure factor $[\log_{10}(|\mathbf{F}|^2)]$, where $|\mathbf{F}|^2$ is summed along the [111] direction at 35 K and 40 mT [111] magnetic field. Pixels on the corners of the image correspond to $|\mathbf{q}| \simeq 0.1$. (b) Real space spin configuration in Cu_2OSeO_3 (111) slice at the 35 K and 40 mT [111] magnetic field, which shows the skyrmion lattice. The z component and the in-plane orientations of the spins are illustrated by the color bar and colored arrows, respectively.

on a sphere as seen in Figs. 4(a) and 4(b). In this region, the inverse correlation length satisfies $\kappa \lesssim \kappa_{DM}$. However, these results remain indecisive since they rely on fitting the magnetic susceptibility with the Brazovskii equation to get the parameter η. Further study is required to directly extract the Ginzburg length and correlation length to fully understand the mechanism that induces the first-order phase transition.

The region between the helimagnetic transition and paramagnetic transition (between the first order and second order transition, $T_H < T < T_c$) is denoted as the fluctuation-disordered phase. In order to explore the nature of this phase, we study the evolution of the norm of the propagation vector as a function of temperature in the region $T_H < T < T_c$. We observe that the propagation vector related to the helical state is increasing in the norm, which indicates that the helical state periodicity is getting smaller to adapt to the supercell size, which in turn shows that the FD is an incommensurate phase. As the temperature increases, we observe spread over the Brillouin zone until we get a spherelike shape as in Fig. 4(a). The existence of an incommensurate phase along the FD phase, encapsulated by the commensurate phase (ferrimagnetic phase) and paramagnetic phase, indicates the existence of a Lifshitz point (LP) [40] at the border of these three phases.

Furthermore, in the case of an applied 40 mT magnetic field along (111) direction, we observe a skyrmion lattice phase in a range of temperature between 42.25 K and 34 K, which is characterized by three noncollinear propagation vectors: $\mathbf{q}^{\mathbf{1}}_{\mathbf{SkL}} = \frac{1}{84}[\bar{2}11]$, $\mathbf{q}^{\mathbf{2}}_{\mathbf{SkL}} = \frac{1}{84}[1\bar{2}1]$, and $\mathbf{q}^{\mathbf{3}}_{\mathbf{SkL}} = \frac{1}{84}[11\bar{2}]$. Figure 5(a) shows the projection of the spin structure factor

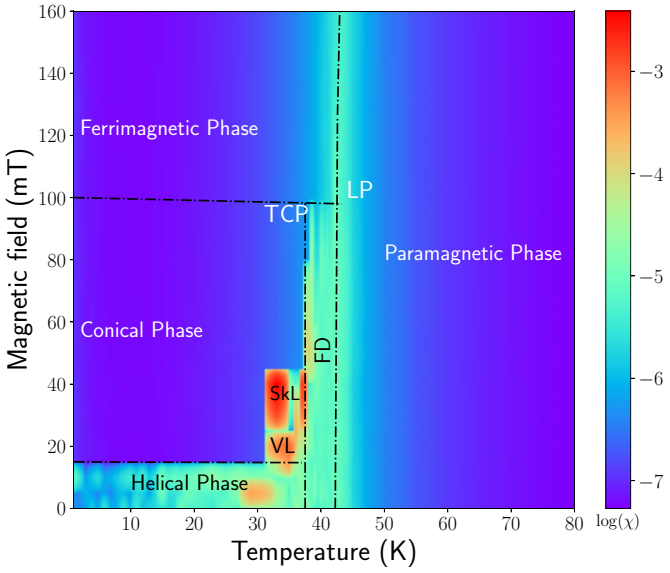

FIG. 6. Phase diagram of various magnetic orders in Cu_2OSeO_3: SkL, skyrmion lattice; VL, vortex lattice; FD, fluctuation disordered; TCP, tricritical point; LP, Lifshitz point. The logarithm of the magnetic susceptibility, the specific heat, and spin structure factor patterns at different temperatures and magnetic fields are used to calculate the borders of the phases.

in this case on the (111) plan, which shows a sixfold pattern, the six spots corresponding to $\mathbf{q}^{\mathbf{i}}_{\mathbf{SkL}}$ and $-\mathbf{q}^{\mathbf{i}}_{\mathbf{SkL}}$ with $i \in \{1, 2, 3\}$; these three noncollinear vectors are coplanar since $\det(\mathbf{q}^{\mathbf{1}}_{\mathbf{SkL}}, \mathbf{q}^{\mathbf{2}}_{\mathbf{SkL}}, \mathbf{q}^{\mathbf{3}}_{\mathbf{SkL}}) = 0$, which is a necessary condition for having a skyrmion lattice; otherwise, the three vectors would characterize a hedgehog lattice phase [41]. Figure 5(b) shows the skyrmions' lattice in real space.

To understand the mechanism of the creation of SkL, we performed a series of low magnetic field calculations, leading to the magnetic field-temperature phase diagram shown in Fig. 6 and, as predicted by the present scheme, seven phases exist within this range; five are well known, namely the helical, conical, SkL, paramagnetic, and ferrimagnetic (field polarised) phases. Moreover, we have two other phases; the first of them is between the helical phase and the SkL (at 15 mT), where a double noncollinear $\mathbf{q}$ pattern is created, indicating the existence of an intermediate vortex lattice (half skyrmions or merons). This prediction is yet to be confirmed experimentally. The last phase is previously mentioned where there is a dominance of fluctuation in the fluctuation-disordered regime. The phase diagram shows a tricritical point at the crossing between the conical, FD phase, and ferrimagnetic phase, as previously shown experimentally [35].

The vortex lattice phase is found to exist in a very tiny pocket near T_H, and between $\mathbf{B}_{\text{ext}}$ of stable helical phase and stable SkL, and has never been suggested as a possible ground state of Cu_2OSeO_3. The existence of the vortex lattice phase implies that the transition from helical state to SkL undergoes a step-by-step transition in terms of the topological invariant by passing from the topologically trivial single $\mathbf{q}$ state to a double $\mathbf{q}$ state characterized with a half-integer invariant to a triple $\mathbf{q}$ state with an integer invariant.

V. CONCLUSION

We have developed a first-principle approach to study the magnetic phases and finite-temperature properties of multiferroic chiral magnet copper oxide selenite Cu_2OSeO_3. We constructed an effective Hamiltonian with all the magnetic interactions; the parameters of this Hamiltonian were determined via density functional theory calculations with U correction (DFT + U). The Monte Carlo simulation gives us insight into the finite-temperature properties of Cu_2OSeO_3. We have obtained the same experimental head and shoulder peak signature of heat capacity found in Cu_2OSeO_3 and B20 magnets in general. We have found a very narrow pocket of temperature and magnetic field where the magnetic skyrmion lattice phase is stabilized in agreement with experimental observations and a stabilized magnetic helical phase at zero or small field under the critical temperature T_c. Our calculation also predicts the existence of a vortex lattice phase at a tiny region near T_H, between the helical phase and the SkL phase. This approach may be further enriched with the same ferroelectric Hamiltonian approach by Zhong, Vanderbilt, and Rabe [42] to study the multiferroic behavior of Cu_2OSeO_3, to understand the origin of magnetoelectric coupling, and also to study the topological defects in ferroic materials.

ACKNOWLEDGMENTS

The authors are grateful for support provided by NVIDIA via the NVIDIA GPU Grant. This work was performed using HPC resources from the Mésocentre" computing center of CentraleSupélec and École Normale Supérieure Paris-Saclay supported by CNRS and Région Île-de-France [43]. This project has received funding from the European Union's Horizon 2020 research and innovation programme under Grant Agreement No. 964931 (TSAR).

[1] W. Kang, Y. Huang, C. Zheng, W. Lv, N. Lei, Y. Zhang, X. Zhang, Y. Zhou, and W. Zhao, Voltage controlled magnetic skyrmion motion for racetrack memory, Sci. Rep. **6**, 23164 (2016).

[2] T. Skyrme, A unified field theory of mesons and baryons, Nucl. Phys. **31**, 556 (1962).

[3] S. Heinze, K. Von Bergmann, M. Menzel, J. Brede, A. Kubetzka, R. Wiesendanger, G. Bihlmayer, and S. Blugel, Spontaneous atomic-scale magnetic skyrmion lattice in two dimensions, Nat. Phys. **7**, 713 (2011).

[4] I. Dzyaloshinskii, A thermodynamic theory of "weak" ferromagnetism of antiferromagnetics, J. Phys. Chem. Solids **4**, 241 (1958).

[5] T. Moriya, Anisotropic superexchange interaction and weak ferromagnetism, Phys. Rev. **120**, 91 (1960).

[6] S. Muhlbauer, B. Binz, F. Jonietz, C. Pfleiderer, A. Rosch, A. Neubauer, R. Georgii, and P. Boni, Skyrmion lattice in a chiral magnet, Science **323**, 915 (2009).

[7] X. Yu, N. Kanazawa, Y. Onose, K. Kimoto, W. Zhang, S. Ishiwata, Y. Matsui, and Y. Tokura, Near room-temperature

formation of a skyrmion crystal in thin-films of the helimagnet FeGe, Nat. Mater. **10**, 106 (2011).

[8] W. Münzer, A. Neubauer, T. Adams, S. Muhlbauer, C. Franz, F. Jonietz, R. Georgii, P. Boni, B. Pedersen, M. Schmidt, A. Rosch, and C. Pfleiderer, Skyrmion lattice in the doped semiconductor $Fe_{1-x}Co_xSi$, Phys. Rev. B **81**, 041203(R) (2010).

[9] X. Yu, Y. Onose, N. Kanazawa, J. Park, J. Han, Y. Matsui, N. Nagaosa, and Y. Tokura, Real-space observation of a two-dimensional skyrmion crystal, Nature (London) **465**, 901 (2010).

[10] Y. Tokunaga, X. Yu, J. White, H. Rønnow, D. Morikawa, Y. Taguchi, and Y. Tokura, A new class of chiral materials hosting magnetic skyrmions beyond room temperature, Nat. Commun. **6**, 7638 (2015).

[11] S. Seki, X. Yu, S. Ishiwata, and Y. Tokura, Observation of Skyrmions in a Multiferroic Material, Science **336**, 198 (2012).

[12] J. Bos, C. Colin, and T. Palstra, Magnetoelectric coupling in the cubic ferrimagnet Cu_2OSeO_3, Phys. Rev. B **78**, 094416 (2008).

[13] E. Ruff, P. Lunkenheimer, A. Loidl, H. Berger, and S. Krohns, Magnetoelectric effects in the skyrmion host material Cu_2OSeO_3, Sci. Rep. **5**, 15025 (2015).

[14] J. White, I. Levatić, A. Omrani, N. Egetenmeyer, K. Prša, I. Živković, J. Gavilano, J. Kohlbrecher, M. Bartkowiak, H. Berger, and H. Rønnow, Electric field control of the skyrmion lattice in Cu_2OSeO_3, J. Phys.: Condens. Matter **24**, 432201 (2012).

[15] T. Adams, A. Chacon, M. Wagner, A. Bauer, G. Brandl, B. Pedersen, H. Berger, P. Lemmens, and C. Pfleiderer, Long-Wavelength Helimagnetic Order and Skyrmion Lattice Phase in Cu_2OSeO_3, Phys. Rev. Lett. **108**, 237204 (2012).

[16] N. Khanh, T. Nakajima, X. Yu, S. Gao, K. Shibata, M. Hirschberger, Y. Yamasaki, H. Sagayama, H. Nakao, L. Peng, K. Nakajima, R. Takagi, T. Arima, Y. Tokura, and S. Seki, Nanometric square skyrmion lattice in a centrosymmetric tetragonal magnet, Nat. Nanotechnol. **15**, 444 (2020).

[17] K. Shimizu, S. Okumura, Y. Kato, and Y. Motome, Phase transitions between helices, vortices, and hedgehogs driven by spatial anisotropy in chiral magnets, Phys. Rev. B **103**, 054427 (2021).

[18] O. Janson, I. Rousochatzakis, A. Tsirlin, M. Belesi, A. Leonov, U. Rößler, J. Brink, and H. Rosner, The quantum nature of skyrmions and half-skyrmions in Cu_2OSeO_3, Nat. Commun. **5**, 5376 (2014).

[19] R. Evans, *Atomistic Spin Dynamics*, Handbook of Materials Modeling: Applications: Current and Emerging Materials (Springer, New York, 2018), pp. 1–23.

[20] R. Evans, W. Fan, P. Chureemart, T. Ostler, M. Ellis, and R. Chantrell, Atomistic spin model simulations of magnetic nanomaterials, J. Phys.: Condens. Matter **26**, 103202 (2014).

[21] A. Belemuk and S. Stishov, Monte Carlo modeling the phase diagram of magnets with the Dzyaloshinskii-Moriya interaction, Solid State Commun. **267**, 6 (2017).

[22] G. Kresse and J. Furthmüller, Efficient iterative schemes for *ab initio* total-energy calculations using a plane-wave basis set, Phys. Rev. B **54**, 11169 (1996).

[23] H. Xiang, E. Kan, S. Wei, M. Whangbo, and X. Gong, Predicting the spin-lattice order of frustrated systems from first principles, Phys. Rev. B **84**, 224429 (2011).

[24] D. Šabani, C. Bacaksiz, and M. Milosevic, *Ab initio* methodology for magnetic exchange parameters: Generic four-state energy mapping onto a Heisenberg spin Hamiltonian, Phys. Rev. B **102**, 014457 (2020).

[25] J. Perdew, K. Burke, and M. Ernzerhof, Generalized Gradient Approximation Made Simple, Phys. Rev. Lett. **77**, 3865 (1996).

[26] S. Dudarev, G. Botton, S. Savrasov, C. Humphreys, and A. Sutton, Electron-energy-loss spectra and the structural stability of nickel oxide: An LSDA+U study, Phys. Rev. B **57**, 1505 (1998).

[27] V. Anisimov, J. Zaanen, and O. Andersen, Band theory and Mott insulators: Hubbard U instead of stoner I, Phys. Rev. B **44**, 943 (1991).

[28] N. Metropolis and S. Ulam, The Monte Carlo method, J. Am. Stat. Assoc. **44**, 335 (1949).

[29] W. Hastings, Monte Carlo sampling methods using Markov chains and their applications, Biometrika **57**, 97 (1970).

[30] T. Preis, P. Virnau, W. Paul, and J. Schneider, GPU accelerated Monte Carlo simulation of the 2D and 3D Ising model, J. Comput. Phys. **228**, 4468 (2009).

[31] See Supplemental Material at http://link.aps.org/supplemental/10.1103/PhysRevB.107.024417 for details on the parallel checkerboard algorithm.

[32] J. Yang, Z. Li, X. Lu, M. Whangbo, S. Wei, X. Gong, and H. Xiang, Strong Dzyaloshinskii-Moriya Interaction and Origin of Ferroelectricity in Cu_2SeO_3, Phys. Rev. Lett. **109**, 107203 (2012).

[33] P. Mohn, *Magnetism in the Solid State*, Solid-State Sciences (Springer-Verlag, Berlin, 2003).

[34] V. Sidorov, A. Petrova, P. Berdonosov, V. Dolgikh, and S. Stishov, Comparative study of helimagnets MnSi and Cu_2OSeO_3 at high pressures, Phys. Rev. B **89**, 100403 (2014).

[35] H. Chauhan, B. Kumar, J. Tiwari, and S. Ghosh, Multiple phases with a tricritical point and a Lifshitz point in the skyrmion host Cu_2OSeO_3, Phys. Rev. B **100**, 165143 (2019).

[36] M. Janoschek, M. Garst, A. Bauer, P. Krautscheid, R. Georgii, P. Böni, and C. Pfleiderer, Fluctuation-induced first-order phase transition in Dzyaloshinskii-Moriya helimagnets, Phys. Rev. B **87**, 134407 (2013).

[37] S. Brazovskǐ, Phase transition of an isotropic system to a nonuniform state, Sov. JETP **41**, 85 (1975).

[38] K. Wilson, The renormalization group and critical phenomena, Rev. Mod. Phys. **55**, 583 (1983).

[39] I. Živković, J. S. White, H. M. Rønnow, K. Prsa, and H. Berger, Critical scaling in the cubic helimagnet Cu_2OSeO_3, Phys. Rev. B **89**, 060401(R) (2014).

[40] R. Hornreich, M. Luban, and S. Shtrikman, Critical Behavior at the Onset of $\vec{k}$-Space Instability on the λ Line, Phys. Rev. Lett. **35**, 1678 (1975).

[41] N. Kanazawa, S. Seki, and Y. Tokura, Noncentrosymmetric magnets hosting magnetic skyrmions, Adv. Mater. **29**, 1603227 (2017).

[42] W. Zhong, D. Vanderbilt, and K. Rabe, First-principles theory of ferroelectric phase transitions for perovskites: The case of $BaTiO_3$, Phys. Rev. B **52**, 6301 (1995).

[43] http://mesocentre.centralesupelec.fr/.